

AD-A243 698



AFIT/GE/ENG/91D-39

DTIC
ELECTE
DEC 27 1991
S C D

DEVELOPMENT OF HIGH ANGLE OF ATTACK
CONTROL LAWS FOR AN UNSTABLE, NON-
MINIMUM PHASE AIRCRAFT USING VARIATIONS
OF THE QUANTITATIVE FEEDBACK TECHNIQUE

THESIS

Mark A. McClure
Captain, USAF

AFIT/GE/ENG/91D-39

Approved for public release; distribution unlimited

91-19040



91 12 24 072

REPORT DOCUMENTATION PAGE			Form Approved OMB No 0704-0188	
Public reporting burden for this collection of information is estimated to average 1 hour per response, including the time for reviewing instructions, searching existing data sources, gathering and maintaining the data needed, and completing and reviewing the collection of information. Send comments regarding this burden estimate or any other aspect of this collection of information, including suggestions for reducing this burden, to Washington Headquarters Services, Directorate for Information Operations and Reports, 1215 Jefferson Davis Highway, Suite 1204, Arlington, VA 22202-4302, and to the Office of Management and Budget, Paperwork Reduction Project (0704-0188), Washington, DC 20503.				
1. AGENCY USE ONLY (Leave blank)	2. REPORT DATE December 1991	3. REPORT TYPE AND DATES COVERED Master's Thesis		
4. TITLE AND SUBTITLE Development of High Angle-of-Attack Control Laws for an Unstable, Non-Minimum Phase Aircraft Using Variations of the Quantitative Feedback Technique		5. FUNDING NUMBERS		
6. AUTHOR(S) Mark A. McClure Captain, USAF				
7. PERFORMING ORGANIZATION NAME(S) AND ADDRESS(ES) Air Force Institute of Technology WPAFB OH 45433-6583		8. PERFORMING ORGANIZATION REPORT NUMBER AFIT/GE/ENG/91D-39		
9. SPONSORING / MONITORING AGENCY NAME(S) AND ADDRESS(ES) X-29 Advanced Development Program Office WL/FIMT Wright Patterson AFB, OH 45433		10. SPONSORING / MONITORING AGENCY REPORT NUMBER		
11. SUPPLEMENTARY NOTES				
12a. DISTRIBUTION / AVAILABILITY STATEMENT Approved for Public Release; Distribution Unlimited.			12b. DISTRIBUTION CODE	
13. ABSTRACT (Maximum 200 words)				
<p style="text-align: center;">Abstract</p> <p>This thesis discusses the application of variations of the Quantitative Feedback Technique to a control problem with unstable, non-minimum phase plants. The X-29A research aircraft is used as the basis for developing a set of <i>representative</i> linearized aircraft dynamics models, which are modified to allow for the use of differential canard control inputs for enhanced maneuverability at extreme angles of attack. A specialized design approach is presented to develop frequency dependent weighting matrices, and the shortcomings of traditional methods are discussed.</p> <p>Four independent longitudinal compensators are developed by first designing loop transmission functions. Discussion is provided that addresses the limitations imposed on the designer by the numerous right half plane poles and zeros of the effective plants. The optimal blending method is applied in one case to achieve a marginally stable system for a virtually impossible problem. Prefilters are designed and their effects on closed-loop time responses are discussed. The singular-G method is used to improve the achievable stability characteristics of a multi-input multi-output lateral-directional controller. The optimal blending method is then applied to develop an optimal loop transmission function. Finally, the required steps for completing the MIMO design are presented to aid future research efforts.</p>				
14. SUBJECT TERMS Quantitative Feedback Technique (QFT), Unstable Plant, Non-Minimum Phase Plant, Weighting Matrix, X-29, Canard, Linearized Aircraft Models			15. NUMBER OF PAGES 266	
			16. PRICE CODE	
17. SECURITY CLASSIFICATION OF REPORT Unclassified	18. SECURITY CLASSIFICATION OF THIS PAGE Unclassified	19. SECURITY CLASSIFICATION OF ABSTRACT Unclassified	20. LIMITATION OF ABSTRACT UL	

AFIT/GE/ENG/91D-39

DEVELOPMENT OF HIGH ANGLE OF ATTACK CONTROL
LAWS FOR AN UNSTABLE, NON-MINIMUM PHASE
AIRCRAFT USING VARIATIONS OF THE
QUANTITATIVE FEEDBACK TECHNIQUE

THESIS

Presented to the Faculty of the School of Engineering
of the Air Force Institute of Technology

Air University

In Partial Fulfillment of the
Requirements for the Degree of
Master of Science in Electrical Engineering

Mark A. McClure, B.S.E.E.

Captain, USAF

December 1991



Accession For	
NTIS GRA&I	<input checked="" type="checkbox"/>
DTIC TAB	<input type="checkbox"/>
Unannounced	<input type="checkbox"/>
Justification	
By	
Distribution/	
Availability Codes	
Dist	Avail and/or Special
A-1	

Approved for public release; distribution unlimited

Preface

I wish to express my sincere thanks to my instructors and colleagues from whom I have learned so much. While all of the AFIT instructors are true professionals in every sense, several are worthy of special mention. Professor Constantine Houpis, Major Robert Riggins, and Dr Meir Pachter have patiently guided me through the world of automatic flight control. Although all of my Guidance & Control colleagues have been helpful and supportive throughout, I must give special thanks to Captain Jeff Bradley, whose positive attitude and willingness to help were instrumental in helping me through the control sequence. Thanks also to Mr Terry Christian, Dr Larry Walchli, and Mr Bill Gillard from the Flight Dynamics Directorate for their continued support on X-29 related matters.

Two people, however, deserve my highest praise and most sincere thanks. Professor Isaac Horowitz possesses the enviable attributes of extreme intelligence and unlimited patience. Working closely with him, I have been able to learn at least a working knowledge of the powerful control theory known as *Quantitative Feedback*. He is truly the master of this subject. Finally, my extra special thanks to my advisor, Captain Randy Paschall. Randy has been my primary guiding source throughout the AFIT experience. When I ran into problems, which happened often, Randy would spend whatever time was needed to get me back on track with a positive attitude. Thanks again for everything, Randy!

Last, but certainly not least, I would like to thank my wonderful wife, Karen, and our two boys, Chris and Mike for their understanding and patience over the past eighteen months. I hope my long hours and seven day a week schedule have not scared the boys off from college. It is such a rewarding experience in so many ways that it is *well* worth the effort!

Mark A. McClure

Table of Contents

	Page
Preface	ii
Table of Contents	iii
List of Figures	vi
List of Symbols	xii
List of Tables	xv
Abstract	xvi
 I. Introduction	 1-1
1.1 Introduction	1-1
1.2 Background	1-3
1.3 Problem Description	1-4
1.4 Assumptions	1-5
1.5 Scope	1-7
1.6 Design Method	1-8
1.7 Organization	1-10
 II. Development of Mathematical Aircraft Models	 2-1
2.1 Introduction	2-1
2.2 Aircraft Description	2-2
2.3 Control Surfaces	2-5
2.4 Actuator and Sensor Models	2-7
2.5 Linearized Aircraft Model Equations	2-10

	Page
2.6 Modification of Aircraft Model Equations	2-16
2.7 Summary	2-23
III. Weighting Matrix Development	3-1
3.1 Introduction	3-1
3.2 Weighting Matrix Design Approach	3-2
3.3 Unsuccessful Compensation Attempts	3-6
3.4 Pitch Channel Compensation	3-10
3.5 Roll Channel Compensation	3-19
3.6 Yaw Channel Compensation	3-37
3.7 Combined Roll and Yaw Channel Compensation	3-53
3.8 Final Weighting Matrices	3-57
3.9 Summary	3-59
IV. Longitudinal Control System Design	4-1
4.1 Introduction	4-1
4.2 Analysis of Effective Plants	4-3
4.3 Design of Loop Transmission Functions	4-6
4.4 Prefilter Designs and Responses	4-27
4.5 Summary	4-46
V. Lateral-Directional Control System Design	5-1
5.1 Introduction	5-1
5.2 Analysis of Effective Plants	5-1
5.3 Singular-G Modification of Effective Plants . . .	5-10
5.4 Application of Optimal Blending to One Case .	5-18
5.5 Summary	5-27

	Page
VI. Conclusions and Recommendations	6-1
6.1 Conclusions	6-1
6.2 Recommendations	6-3
Appendix A. Original State Space Matrices	A-1
Appendix B. Open-Loop System Eigenvalues	B-1
Appendix C. Differential Canard Stability Derivatives	C-1
Appendix D. Translation of Longitudinal Stability Derivatives	D-1
Appendix E. Modified B Matrices	E-1
Appendix F. Final State Space Models	F-1
Appendix G. Matrix _x Executable Files - Weighting Matrix .	G-1
G.1 Development of Frequency Dependent Terms . .	G-1
G.2 Verification of Phase Compensation	G-6
G.3 Inclusion of Gain Compensation	G-8
Appendix H. Lateral-Directional Effective Plants	H-1
Appendix I. Matrix _x Executable Files - Singular-G	I-1
Bibliography	BIB-1
Vita	VITA-1

List of Figures

Figure	Page
1.1. X-29A Advanced Technology Demonstrator	1-2
2.1. X-29A Advanced Aircraft Technologies	2-2
2.2. Comparison Between Stabilator and Canard	2-4
2.3. Pitch Control Surfaces	2-6
2.4. Block Diagram Representation of State Space	2-11
2.5. Definition of α and θ	2-12
2.6. Definition of ϕ	2-12
2.7. Definition of β	2-13
2.8. Translation of Lift and Drag into Longitudinal Forces	2-18
3.1. Block Diagram of Flight Control System	3-1
3.2. S-plane Region of Convergence for LaPlace Integral	3-5
3.3. Uncompensated Open-Loop Yaw Rate Step Responses ($\alpha = 50$)	3-6
3.4. Initial Uncompensated Yaw Rate Frequency Response ($\alpha = 50$)	3-7
3.5. Initial Compensated Yaw Rate Frequency Response ($\alpha = 50$)	3-7
3.6. Initial Yaw Rate Compensation Block Diagram ($\alpha = 50$)	3-8
3.7. Initial Compensated Open-Loop Yaw Rate Step Responses ($\alpha = 50$)	3-8
3.8. Padé Compensated Yaw Rate Block Diagram ($\alpha = 50$)	3-9
3.9. Padé Compensated Open-Loop Yaw Rate Step Responses ($\alpha = 50$)	3-10
3.10. Uncompensated Open-Loop Pitch Rate Step Response ($\alpha = 20$)	3-11
3.11. Pitch Rate Compensation Block Diagram ($\alpha = 20$)	3-12
3.12. Compensated Open-Loop Pitch Rate Step Response ($\alpha = 20$)	3-13
3.13. Uncompensated Open-Loop Pitch Rate Step Response ($\alpha = 40$)	3-13
3.14. Pitch Rate Compensation Block Diagram ($\alpha = 40$)	3-14

Figure	Page
3.15. Compensated Open-Loop Pitch Rate Step Response ($\alpha = 40$) . .	3-15
3.16. Uncompensated Open-Loop Pitch Rate Step Response ($\alpha = 50$) .	3-15
3.17. Pitch Rate Compensation Block Diagram ($\alpha = 50$)	3-16
3.18. Compensated Open-Loop Pitch Rate Step Response ($\alpha = 50$) . .	3-16
3.19. Uncompensated Open-Loop Pitch Rate Step Response ($\alpha = 60$) .	3-17
3.20. Pitch Rate Compensation Block Diagram ($\alpha = 60$)	3-18
3.21. Compensated Open-Loop Pitch Rate Step Response ($\alpha = 60$) . .	3-18
3.22. Uncompensated Open-Loop Roll Rate Step Responses ($\alpha = 20$) .	3-19
3.23. Uncompensated <i>Shifted</i> Roll Rate Frequency Response ($\alpha = 20$) .	3-21
3.24. Compensated <i>Shifted</i> Roll Rate Frequency Response ($\alpha = 20$) . .	3-21
3.25. Compensated Open-Loop Roll Rate Step Responses ($\alpha = 20$) . .	3-23
3.26. Roll Rate Compensation Block Diagram ($\alpha = 20$)	3-24
3.27. Final Compensated Open-Loop Roll Rate Step Responses ($\alpha = 20$)	3-24
3.28. Uncompensated Open-Loop Roll Rate Step Responses ($\alpha = 40$) .	3-25
3.29. Uncompensated <i>Shifted</i> Roll Rate Frequency Response ($\alpha = 40$) .	3-26
3.30. Compensated <i>Shifted</i> Roll Rate Frequency Response ($\alpha = 40$) . .	3-26
3.31. Compensated Open-Loop Roll Rate Step Responses ($\alpha = 40$) . .	3-27
3.32. Roll Rate Compensation Block Diagram ($\alpha = 40$)	3-27
3.33. Final Compensated Open-Loop Roll Rate Step Responses ($\alpha = 40$)	3-28
3.34. Uncompensated Open-Loop Roll Rate Step Responses ($\alpha = 50$) .	3-29
3.35. Uncompensated <i>Shifted</i> Roll Rate Frequency Response ($\alpha = 50$) .	3-30
3.36. Compensated <i>Shifted</i> Roll Rate Frequency Response ($\alpha = 50$) . .	3-30
3.37. Compensated Open-Loop Roll Rate Step Responses ($\alpha = 50$) . .	3-31
3.38. Roll Rate Compensation Block Diagram ($\alpha = 50$)	3-31
3.39. Final Compensated Open-Loop Roll Rate Step Responses ($\alpha = 50$)	3-32
3.40. Uncompensated Open-Loop Roll Rate Step Responses ($\alpha = 60$) .	3-33
3.41. Uncompensated <i>Shifted</i> Roll Rate Frequency Response ($\alpha = 60$) .	3-34

Figure	Page
3.42. Compensated <i>Shifted</i> Roll Rate Frequency Response ($\alpha = 60$) . .	3-34
3.43. Compensated Open-Loop Roll Rate Step Responses ($\alpha = 60$) . .	3-35
3.44. Roll Rate Compensation Block Diagram ($\alpha = 60$)	3-35
3.45. Final Compensated Open-Loop Roll Rate Step Responses ($\alpha = 60$)	3-36
3.46. Uncompensated Open-Loop Yaw Rate Step Responses ($\alpha = 20$) .	3-37
3.47. Uncompensated <i>Shifted</i> Yaw Rate Frequency Response ($\alpha = 20$) .	3-38
3.48. Compensated <i>Shifted</i> Yaw Rate Frequency Response ($\alpha = 20$) . .	3-38
3.49. Compensated Open-Loop Yaw Rate Step Responses ($\alpha = 20$) . .	3-39
3.50. Yaw Rate Compensation Block Diagram ($\alpha = 20$)	3-39
3.51. Final Compensated Open-Loop Yaw Rate Step Responses ($\alpha = 20$)	3-40
3.52. Uncompensated Open-Loop Yaw Rate Step Responses ($\alpha = 40$) .	3-41
3.53. Uncompensated <i>Shifted</i> Yaw Rate Frequency Response ($\alpha = 40$) .	3-42
3.54. Compensated <i>Shifted</i> Yaw Rate Frequency Response ($\alpha = 40$) . .	3-42
3.55. Compensated Open-Loop Yaw Rate Step Responses ($\alpha = 40$) . .	3-43
3.56. Yaw Rate Compensation Block Diagram ($\alpha = 40$)	3-43
3.57. Final Compensated Open-Loop Yaw Rate Step Responses ($\alpha = 40$)	3-44
3.58. Uncompensated Open-Loop Yaw Rate Step Responses ($\alpha = 50$) .	3-45
3.59. Uncompensated <i>Shifted</i> Yaw Rate Frequency Response ($\alpha = 50$) .	3-46
3.60. Compensated <i>Shifted</i> Yaw Rate Frequency Response ($\alpha = 50$) . .	3-46
3.61. Compensated Open-Loop Yaw Rate Step Responses ($\alpha = 50$) . .	3-47
3.62. Yaw Rate Compensation Block Diagram ($\alpha = 50$)	3-47
3.63. Final Compensated Open-Loop Yaw Rate Step Responses ($\alpha = 50$)	3-48
3.64. Uncompensated Open-Loop Yaw Rate Step Responses ($\alpha = 60$) .	3-49
3.65. Uncompensated <i>Shifted</i> Yaw Rate Frequency Response ($\alpha = 60$) .	3-50
3.66. Compensated <i>Shifted</i> Yaw Rate Frequency Response ($\alpha = 60$) . .	3-50
3.67. Compensated Open-Loop Yaw Rate Step Responses ($\alpha = 60$) . .	3-51
3.68. Yaw Rate Compensation Block Diagram ($\alpha = 60$)	3-51

Figure	Page
3.69. Final Compensated Open-Loop Yaw Rate Step Responses ($\alpha = 60$)	3-52
3.70. Unadjusted Lateral-Directional Plants with Roll Rate Input . . .	3-55
3.71. Final Gain Adjusted Lateral-Directional Plants with Roll Rate Input	3-55
3.72. Unadjusted Lateral-Directional Plants with Yaw Rate Input . . .	3-56
3.73. Final Gain Adjusted Lateral-Directional Plants with Yaw Rate Input	3-56
4.1. Basic QFT Standard Control System Notation	4-1
4.2. Basic QFT Alternate Control System Notation	4-2
4.3. Nichols Plot - Pitch Rate Loop Transmission 1 ($\alpha = 20$)	4-7
4.4. Bode Plot - Pitch Rate Loop Transmission 1 ($\alpha = 20$)	4-8
4.5. Bode Plot - Pitch Rate Closed Loop Transmission 1 ($\alpha = 20$) . .	4-9
4.6. Nichols Plot - Pitch Rate Loop Transmission 2 ($\alpha = 20$)	4-11
4.7. Bode Plot - Pitch Rate Loop Transmission 2 ($\alpha = 20$)	4-12
4.8. Bode Plot - Pitch Rate Closed Loop Transmission 2 ($\alpha = 20$) . .	4-12
4.9. Nichols Plot - Pitch Rate Loop Transmission 1 ($\alpha = 40$)	4-13
4.10. Bode Plot - Pitch Rate Loop Transmission 1 ($\alpha = 40$)	4-14
4.11. Bode Plot - Pitch Rate Closed Loop Transmission 1 ($\alpha = 40$) . .	4-14
4.12. Nichols Plot - Pitch Rate Loop Transmission 2 ($\alpha = 40$)	4-16
4.13. Bode Plot - Pitch Rate Loop Transmission 2 ($\alpha = 40$)	4-17
4.14. Bode Plot - Pitch Rate Closed Loop Transmission 2 ($\alpha = 40$) . .	4-17
4.15. Root Locus Sketch of Optimal Blending (Marginal Stability) . . .	4-19
4.16. Root Locus Sketch of Shifted Optimal Blending (Stable)	4-20
4.17. Nichols Plot - Pitch Rate Loop Transmission ($\alpha = 50$)	4-21
4.18. Detailed Nichols Plot - Pitch Rate Loop Transmission ($\alpha = 50$) .	4-22
4.19. Bode Plot - Pitch Rate Loop Transmission ($\alpha = 50$)	4-23
4.20. Bode Plot - Pitch Rate Closed Loop Transmission ($\alpha = 50$) . . .	4-23
4.21. Nichols Plot - Pitch Rate Loop Transmission ($\alpha = 60$)	4-24
4.22. Bode Plot - Pitch Rate Loop Transmission ($\alpha = 60$)	4-25

Figure	Page
4.23. Bode Plot - Pitch Rate Closed Loop Transmission ($\alpha = 60$) . . .	4-26
4.24. Bode Plot - Pitch Rate Design 1 with Prefilter ($\alpha = 20$)	4-28
4.25. Pitch Rate Step Response - Design 1 {5-sec}($\alpha = 20$)	4-29
4.26. Pitch Rate Step Response - Design 1 {20-sec}($\alpha = 20$)	4-30
4.27. Pitch Rate Step Response - Design 1 {500-sec}($\alpha = 20$)	4-30
4.28. Bode Plot - Pitch Rate Design 2 with Prefilter ($\alpha = 20$)	4-31
4.29. Pitch Rate Step Response - Design 2 {5-sec}($\alpha = 20$)	4-32
4.30. Pitch Rate Step Response - Design 2 {20-sec}($\alpha = 20$)	4-32
4.31. Pitch Rate Step Response - Design 2 {500-sec}($\alpha = 20$)	4-33
4.32. Bode Plot - Pitch Rate Design 1 with Prefilter ($\alpha = 40$)	4-34
4.33. Pitch Rate Step Response - Design 1 {5-sec}($\alpha = 40$)	4-34
4.34. Pitch Rate Step Response - Design 1 {20-sec}($\alpha = 40$)	4-35
4.35. Pitch Rate Step Response - Design 1 {500-sec}($\alpha = 40$)	4-35
4.36. Bode Plot - Pitch Rate Design 2 with Prefilter ($\alpha = 40$)	4-37
4.37. Pitch Rate Step Response - Design 2 {5-sec}($\alpha = 40$)	4-37
4.38. Pitch Rate Step Response - Design 2 {20-sec}($\alpha = 40$)	4-38
4.39. Pitch Rate Step Response - Design 2 {500-sec}($\alpha = 40$)	4-38
4.40. Bode Plot - Pitch Rate with Prefilter Design 1 ($\alpha = 50$)	4-39
4.41. Pitch Rate Step Response - Prefilter Design 1 ($\alpha = 50$)	4-40
4.42. Bode Plot - Pitch Rate with Prefilter Design 2 ($\alpha = 50$)	4-41
4.43. Pitch Rate Step Response - Prefilter Design 2 ($\alpha = 50$)	4-42
4.44. Bode Plot - Pitch Rate with Prefilter Design 1 ($\alpha = 60$)	4-43
4.45. Pitch Rate Step Response - Prefilter Design 1 ($\alpha = 60$)	4-43
4.46. Bode Plot - Pitch Rate with Prefilter Design 2 ($\alpha = 60$)	4-44
4.47. Pitch Rate Step Response - Prefilter Design 2 ($\alpha = 60$)	4-45
5.1. Singular-G Compensator	5-10
5.2. Root Locus of Modified Effective Plant ($\alpha = 20$)	5-13

Figure	Page
5.3. Root Locus of Modified Effective Plant ($\alpha = 40$)	5-15
5.4. Root Locus of Modified Effective Plant ($\alpha = 50$)	5-16
5.5. Root Locus of Modified Effective Plant ($\alpha = 60$)	5-17
5.6. Initial Optimal Blending Loop Transmission ($\alpha = 50$)	5-23
5.7. Final Optimal Blending Loop Transmission ($\alpha = 50$)	5-24
5.8. Singular-G Compensator with Prefilter	5-26
H.1. $P_{eff}(1,1)$ Final Compensation Block Diagram ($\alpha = 20$)	H-1
H.2. $P_{eff}(1,1)$ Final Compensation Block Diagram ($\alpha = 40$)	H-1
H.3. $P_{eff}(1,1)$ Final Compensation Block Diagram ($\alpha = 50$)	H-2
H.4. $P_{eff}(1,1)$ Final Compensation Block Diagram ($\alpha = 60$)	H-2
H.5. $P_{eff}(2,1)$ Final Compensation Block Diagram ($\alpha = 20$)	H-3
H.6. $P_{eff}(2,1)$ Final Compensation Block Diagram ($\alpha = 40$)	H-3
H.7. $P_{eff}(2,1)$ Final Compensation Block Diagram ($\alpha = 50$)	H-4
H.8. $P_{eff}(2,1)$ Final Compensation Block Diagram ($\alpha = 60$)	H-4
H.9. $P_{eff}(1,2)$ Final Compensation Block Diagram ($\alpha = 20$)	H-5
H.10. $P_{eff}(1,2)$ Final Compensation Block Diagram ($\alpha = 40$)	H-5
H.11. $P_{eff}(1,2)$ Final Compensation Block Diagram ($\alpha = 50$)	H-6
H.12. $P_{eff}(1,2)$ Final Compensation Block Diagram ($\alpha = 60$)	H-6
H.13. $P_{eff}(2,2)$ Final Compensation Block Diagram ($\alpha = 20$)	H-7
H.14. $P_{eff}(2,2)$ Final Compensation Block Diagram ($\alpha = 40$)	H-7
H.15. $P_{eff}(2,2)$ Final Compensation Block Diagram ($\alpha = 50$)	H-8
H.16. $P_{eff}(2,2)$ Final Compensation Block Diagram ($\alpha = 60$)	H-8

List of Symbols

Symbol	Page
AOA	1-1
WL/FIMT	1-4
AFIT	1-5
QFT	1-7
M	1-9
X	1-9
Z	1-9
Y	1-9
L	1-9
N	1-9
Q	1-9
P	1-9
R	1-9
FSW	2-2
TED	2-6
ζ	2-7
ω_n	2-7
S	2-10
$x(t)$	2-10
A	2-10
B	2-10
$u(t)$	2-10
$y(t)$	2-10
C	2-10

Symbol	Page
D	2-10
LTI	2-11
$v(t)$	2-11
$\alpha(t)$	2-11
$q(t)$	2-11
$\theta(t)$	2-11
$x_{lon}(t)$	2-11
$\beta(t)$	2-12
$p(t)$	2-12
$r(t)$	2-12
$\phi(t)$	2-12
$x_{lat}(t)$	2-13
$u_{lon}(t)$	2-13
$\delta_c(t)$	2-13
$\delta_{sf}(t)$	2-13
$\delta_{str}(t)$	2-13
$\delta_{th}(t)$	2-13
$u_{lat}(t)$	2-14
$\delta_{df}(t)$	2-14
$\delta_r(t)$	2-14
RHP	2-14
λ	2-15
LHP	2-15
C_L	2-16
C_D	2-16
C_M	2-16
C_Y	2-16

Symbol	Page
C_N	2-16
C_l	2-16
Δ	3-1
P_{eff}	3-1
$P_{eff}(1,1)$	3-54
$P_{eff}(2,2)$	3-54
$P_{eff}(1,2)$	3-54
$P_{eff}(2,1)$	3-54
$Y(s)$	4-1
$R(s)$	4-1
$G(s)$	4-1
$F(s)$	4-2
$L(s)$	4-2
ζ_{sp}	4-27
ω_{sp}	4-27
t_r	4-27
t_s	4-27
Ψ	5-11
Λ	5-12
δ_p	5-19
δ_z	5-19
δ_{pc}	5-19
δ_{zc}	5-19
$\phi(s)$	5-19

List of Tables

Table	Page
2.1. Control Surface Characteristics	2-7
2.2. Fourth Order Actuator Models	2-8
2.3. First Order Actuator Models	2-9
2.4. Sensor Models	2-9
2.5. Final Differential Canard Stability Derivatives	2-19
3.1. Uncompensated Roll Rate System Roots ($\alpha = 20$)	3-20
3.2. Compensated Roll Rate System Roots ($\alpha = 20$)	3-22
3.3. Compensated Roll Rate System Roots ($\alpha = 40$)	3-28
3.4. Compensated Roll Rate System Roots ($\alpha = 50$)	3-32
3.5. Compensated Roll Rate System Roots ($\alpha = 60$)	3-36
3.6. Compensated Yaw Rate System Roots ($\alpha = 20$)	3-40
3.7. Compensated Yaw Rate System Roots ($\alpha = 40$)	3-44
3.8. Compensated Yaw Rate System Roots ($\alpha = 50$)	3-48
3.9. Compensated Yaw Rate System Roots ($\alpha = 60$)	3-52
4.1. Roots of Longitudinal Effective Plant ($\alpha = 20$)	4-4
4.2. Roots of Longitudinal Effective Plant ($\alpha = 40$)	4-4
4.3. Roots of Longitudinal Effective Plant ($\alpha = 50$)	4-5
4.4. Roots of Longitudinal Effective Plant ($\alpha = 60$)	4-5
5.1. Roots of Lateral-Directional P_{eff} (1,1) ($\alpha = 20$)	5-2
5.2. Roots of Lateral-Directional P_{eff} (1,2) ($\alpha = 20$)	5-2
5.3. Roots of Lateral-Directional P_{eff} (2,1) ($\alpha = 20$)	5-3
5.4. Roots of Lateral-Directional P_{eff} (2,2) ($\alpha = 20$)	5-3

Table	Page
5.5. Roots of Lateral-Directional P_{eff} (1,1) ($\alpha = 40$)	5-4
5.6. Roots of Lateral-Directional P_{eff} (1,2) ($\alpha = 40$)	5-4
5.7. Roots of Lateral-Directional P_{eff} (2,1) ($\alpha = 40$)	5-5
5.8. Roots of Lateral-Directional P_{eff} (2,2) ($\alpha = 40$)	5-5
5.9. Roots of Lateral-Directional P_{eff} (1,1) ($\alpha = 50$)	5-6
5.10. Roots of Lateral-Directional P_{eff} (1,2) ($\alpha = 50$)	5-6
5.11. Roots of Lateral-Directional P_{eff} (2,1) ($\alpha = 50$)	5-7
5.12. Roots of Lateral-Directional P_{eff} (2,2) ($\alpha = 50$)	5-7
5.13. Roots of Lateral-Directional P_{eff} (1,1) ($\alpha = 60$)	5-8
5.14. Roots of Lateral-Directional P_{eff} (1,2) ($\alpha = 60$)	5-8
5.15. Roots of Lateral-Directional P_{eff} (2,1) ($\alpha = 60$)	5-9
5.16. Roots of Lateral-Directional P_{eff} (2,2) ($\alpha = 60$)	5-9
5.17. Roots of Modified Lateral-Directional Effective Plant ($\alpha = 20$) . .	5-14
5.18. Roots of Modified Lateral-Directional Effective Plant ($\alpha = 40$) . .	5-15
5.19. Roots of Modified Lateral-Directional Effective Plant ($\alpha = 50$) . .	5-16
5.20. Roots of Modified Lateral-Directional Effective Plant ($\alpha = 60$) . .	5-18
5.21. Roots of Equivalent Loop Transmission Function ($\alpha = 50$)	5-25

Abstract

^A This thesis discusses the application of variations of the Quantitative Feed-back Technique to a control problem with unstable, non-minimum phase plants. The X-29A research aircraft is used as the basis for developing a set of *representative* linearized aircraft dynamics models, which are modified to allow for the use of differential canard control inputs for enhanced maneuverability at extreme angles of attack. A specialized design approach is presented to develop frequency dependent weighting matrices, and the shortcomings of traditional methods are discussed.

Four independent longitudinal compensators are developed by first designing loop transmission functions. Discussion is provided that addresses the limitations imposed on the designer by the numerous right half plane poles and zeros of the effective plants. The optimal blending method is applied in one case to achieve a marginally stable system for a virtually impossible problem. Prefilters are designed and their effects on closed-loop time responses are discussed. The singular-G method is used to improve the achievable stability characteristics of a multi-input multi-output lateral-directional controller. The optimal blending method is then applied to develop an optimal loop transmission function. Finally, the required steps for completing the MIMO design are presented to aid future research efforts. ⁷

DEVELOPMENT OF HIGH ANGLE OF ATTACK CONTROL LAWS FOR AN UNSTABLE, NON-MINIMUM PHASE AIRCRAFT USING VARIATIONS OF THE QUANTITATIVE FEEDBACK TECHNIQUE

I. Introduction

1.1 Introduction

This thesis investigates a proposed modification to the flight control system of the X-29A research aircraft. The X-29A (Figure 1.1) was designed for the expressed purpose of demonstrating several advanced technologies. These technologies combine to give the aircraft a *unique* capability to fly in unusual attitudes [11]. Such a capability has long been desired for modern fighter aircraft, to improve both mission effectiveness and survivability. As anticipated, the flight test program revealed some expected problems in the aircraft's handling qualities, while flying at high angles-of-attack (AOA). The desire was to demonstrate improved aircraft maneuverability in high AOA flight conditions by using differential canards.

From the start, it should be noted that due to the limited amount of differential canard wind tunnel data, it is not expected that this effort will result in a *flight-worthy* control system design. Further, since the model developed in this thesis is based on such limited data, it is not expected that this model reflects the X-29's actual performance. However, sufficient data is available to develop a representative non-minimum phase aircraft model, and to synthesize a flight control system design. Such a design at the very least, demonstrates the potential performance of the proposed modification, and the limitations of the design methodology in the presence of non-minimum phase characteristics. In addition, this design provides a useful starting point for a flight control system design capable of operating across a full range of flight conditions. To perform a complete design would require a substantial amount of additional wind tunnel testing to provide the necessary aerodynamic data

for all flight conditions within the X-29 flight envelope. A more complete set of aerodynamic data could also be used to verify or deny the models developed for this research.

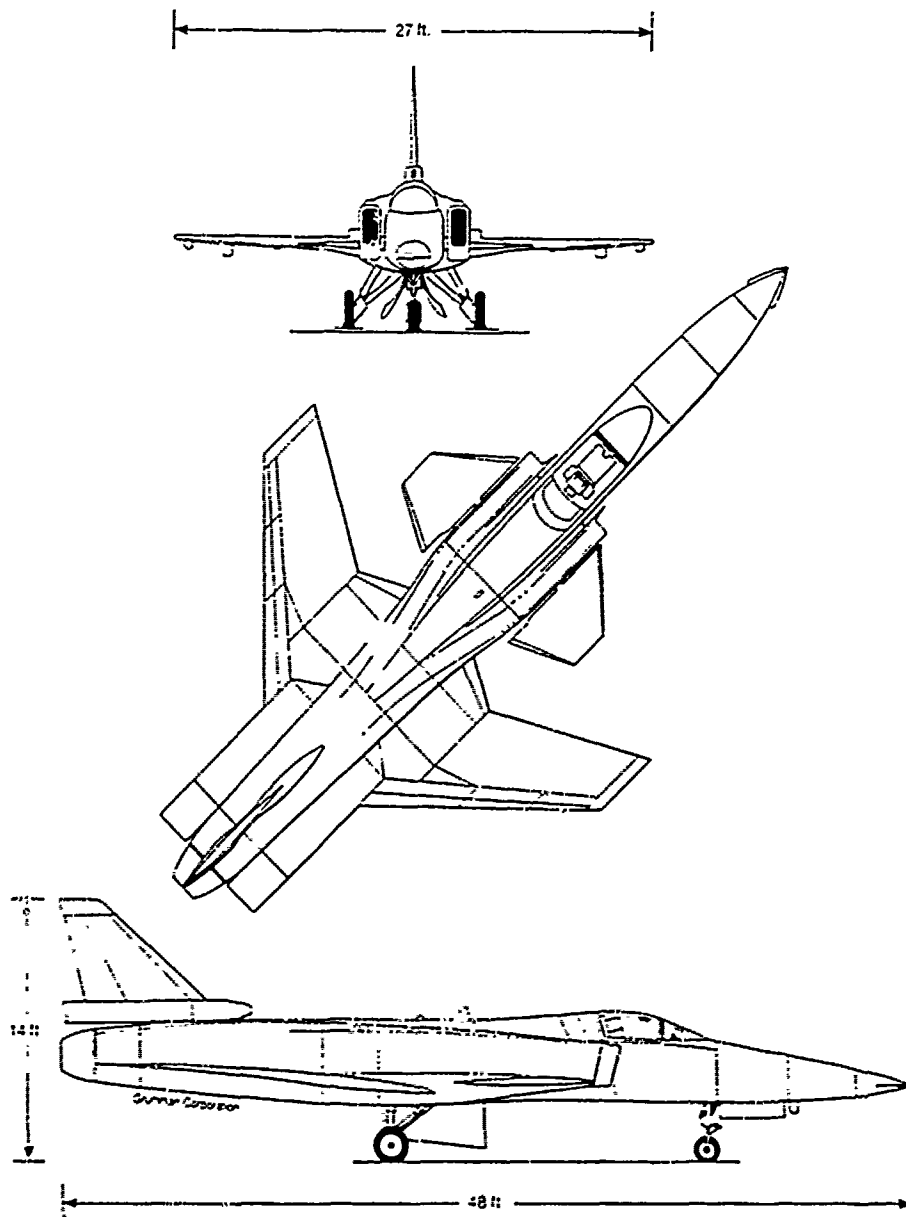


Figure 1.1. X-29A Advanced Technology Demonstrator [21]

Flight tests of the X-29A, overall, have been quite successful [24]. However, it has been noted that the aircraft in its present configuration experiences a problem while flying at high AOAs. The X-29 has flown and remained completely controllable at relatively high AOAs (20 to 30 degrees). However, the aircraft was designed to fly at extreme AOAs (in excess of 60 degrees) while still maintaining a reasonably high degree of maneuverability [5].

Flight test information obtained for the X-29 reveals the following problem. While flying at extreme AOAs, the aircraft is controllable in the longitudinal axis (pitching motions), but it shows some undesirable tendencies in the lateral-directional axes. These tendencies are wing rock about the roll axis and yaw oscillation about the aircraft's vertical axis. The undesirable motions can be controlled with the present flight control system, but an excessive amount of the available control authority is expended in so doing. It is desirable to control such unwanted motions while retaining sufficient control authority to perform additional commanded flight maneuvers at these high AOAs. Other studies are being performed to address this problem, such as vortex flow control through the use of bleed air ports in the aircraft's nose [5].

1.2 Background

A review of pertinent government documents revealed that this problem was predicted prior to the initiation of the X-29 flight test program. Early wind tunnel tests predicted noticeable wing rock at AOAs in excess of 20 degrees. Following the initial wind tunnel tests, NASA's Langley Research Center conducted numerous drop tests of a 22-percent dynamically scaled replica of the X-29. This unpowered model is equipped with fully functional control surfaces that can be operated by a pilot through radio control [26]. The model was carried by a helicopter to an altitude of 6000 feet and released for its controlled descent. On repeated flights with the AOA greater than 20 degrees, the model was difficult to control and the wing rock behavior eventually resulted in roll departure. The wing rock oscillations were attributed to unfavorable roll damping [26].

The yaw instability was also predicted in the wind tunnel tests and noted during the scale model drop tests [26]. The primary cause of the yaw oscillation is thought to be asymmetric vortex shedding off the aircraft's nose [24]. The X-29

was designed from the start to be a relatively low cost test bed aircraft whose sole purpose was to demonstrate advanced technologies. Since only two were to be built and cost was a concern, Grumman decided to use existing aircraft subsystems to the maximum extent possible. Perhaps the most notable single example of this design philosophy is the X-29's nose section. In fact, the entire aircraft forward of the intakes is a slightly modified nose section of a Northrop F-5A fighter [10].

The F-5, an early 1960's design fighter, was not designed for flight at high AOAs. Consequently, it was not surprising when early wind tunnel tests of the X-29A revealed the existence of asymmetric vortices being shed from the nose at high AOAs. A *quick fix* solution was tried in an attempt to alleviate this problem. Small fixed strakes were added to both sides of the nose to direct the airflow in predictable symmetric fashion [10]. While this may have helped slightly, the problem still existed at the more extreme AOAs.

During the flight test program, X-29A1 did not fly above 20 degrees AOA. X-29A2 was to be the high AOA demonstrator. Aircraft number two differs from aircraft number one in two primary ways. First, number two's subtle change is a modification to the flight control system gain scheduling to make the control surfaces more effective at high AOAs. This was not a complete re-design of the flight control system software, and thus only a limited improvement in handling qualities was expected. The second, and more visible modification to aircraft number two is the addition of a spin recovery parachute assembly at the base of the rudder. This precautionary measure is frequently added to experimental test aircraft for a practical reason. Should the pilot lose control of the aircraft during flight testing, in most instances he would not be forced to eject and lose the aircraft [21]. X-29A2 has flown at AOAs over 60 degrees, and as expected, both wing rock and yaw oscillations occurred above 40 degrees AOA [24]. The aircraft was controllable, but the problem was noted by the test pilots [21].

1.3 Problem Description

The specific problem addressed by this effort is the development of high AOA flight control laws for a non-minimum phase aircraft. The control system is designed to make the most effective use of the aircraft's control surfaces. This project was recommended by the Flight Dynamics Directorate of the Air Force Wright Laboratory (WL/FIMT), located at Wright-Patterson AFB, OH. FIMT proposed the use

of differential inputs to the aircraft's canards [5]. Canards are control surfaces that perform a function similar to that of a conventional elevator. What distinguishes the canard from a conventional elevator is the canard's placement in front of the wing. The current flight control system uses only symmetric inputs to the canards, thus enabling them to control attitude only in the pitch axis.

Roll is controlled by differentially commanded flaperons on the wings, and yaw is controlled primarily by the rudder [21]. FIMT hypothesizes that in addition to performing their primary pitch control function, the canards could also be differentially commanded to aid in both roll and yaw control [5]. While this idea seems reasonable, to date, no in-depth design study has been performed to address this proposed solution, due to program funding limitations. Consequently, FIMT asked the Air Force Institute of Technology (AFIT) to investigate the idea.

The objective of this thesis is to develop high AOA flight control laws for an unstable non-minimum phase aircraft. A secondary objective is to demonstrate improved performance potential at high AOA flight conditions, by using differential canards. In order to accomplish these objectives, linearized aircraft dynamics models based on such control capability are developed. Since no flight test data involving differential canards is available, the models are developed based on the limited amount of differential canard wind tunnel data available. Following this, the next major task is to develop complex weighting matrices to distribute the control inputs in the appropriate relative weightings, and ensure maximum synergistic effectiveness from the control surfaces. Finally, the flight control system transfer functions are developed and the time responses are evaluated with step inputs to determine the systems's performance potential.

1.4 Assumptions

As with any effort of this type, certain simplifying assumptions must be made to make the project realizable. Such assumptions are necessary due to limitations in the student's level of knowledge, available man-hours, computer support, etc. However, the assumptions made for this effort have been discussed at length with experienced flight control specialists at AFIT and FIMT, and the assumptions discussed below have been determined to be both reasonable and valid.

The first assumption is that the control system can be properly designed using a linearized state space model to describe the aircraft's dynamics. This is necessary

because most control techniques are based on the mathematics of linear system theory. It is a generally accepted engineering practice to use linearized models to describe a non-linear system, provided such a system is operated in a *relatively small linear range* about the nominal operating condition. For the case of aircraft dynamics, this assumption is reasonable when the aircraft is operated around the specific flight conditions for which the linear model is developed. For example, a specified speed and altitude may be chosen as a nominal operating point about which to vary the AOA (or other parameter of interest). Once a nominal operating point is defined, a linearized state space model of the aircraft dynamics may be obtained using simulations, wind tunnel tests, or flight tests.

Other flight conditions can also be chosen as nominal operating points, with each nominal point yielding a different state space model. It should be noted that some models are more sensitive to certain parameter variations than others. For example, the effectiveness of control surfaces is highly dependent on the dynamic pressure, which is greatest at high speed and low altitude. With the nominal point based on high speed and low altitude, the aircraft response is very sensitive to the slightest control surface inputs. This sensitivity is drastically reduced when operating at low speed and high altitude.

The next assumption is that the available wind tunnel data for differential canard effects is sufficient. This assumption is necessary due to the lack of any differential canard flight test data and the very limited number of wind tunnel test runs that were made with the canards positioned differentially. FINT provided all the differential canard wind tunnel data that was generated from the NASA-Langley tests, but due to limited funding to perform this effort, the data is not representative of the full flight envelope. Further, the limited data has large jumps in it, and therefore requires interpolation. The differential canard aerodynamic data must be incorporated into the linearized state space models. This is discussed in Chapter II. Specifically, this data contains the aerodynamic coefficients that result from various differential canard settings on the X-29. Before a control system can be effectively designed, these coefficients are needed to predict the aircraft motions in response to various control surface configurations.

A third simplifying assumption is that the engine thrust is fixed at a set value for each of the operating points. Thus, only the aerodynamic control surfaces are used to control the aircraft motions. This is a reasonable assumption, even in the real

test flight scenarios. Frequently, a test aircraft is flown in a specified flight condition and then the pilot *perturbs* one or more of his available controls to determine specific aspects of the aircraft handling qualities in response to the desired input(s).

A fourth assumption results from the choice of nominal operating condition. In order to fly at extreme AOA with an acceptable wing loading, the aircraft must not fly in the supersonic or transonic regions of the flight envelope. For this study, the aircraft models are based on an airspeed of three-tenths Mach [9]. At this comparatively slow speed (approximately 310 feet/second), the atmospheric compressibility effects may be neglected.

In addition, the aircraft is assumed to be a rigid body, constant mass vehicle. That is, stability and control effects resulting from structural flexing or consumption of fuel are neglected. This aircraft, like most fighter aircraft, is small enough so that structural flexing is minimal, and changes in mass due to fuel consumption are not significant over the period of interest for each commanded maneuver.

1.5 Scope

This effort is limited to developing a set of control laws for a high AOA flight control system which implements differential commands to the aircraft's canard control surfaces. The system design entails extensive use of computer aided design and analysis programs. The result is a *paper design* consisting of detailed block diagrams with pertinent parameters identified. Such block diagrams are typically used as a blueprint for programming the flight control computers on modern aircraft. As discussed before, actual implementation of this design would not be practical due to the limited aerodynamic data, but the methodology discussed in this thesis can be applied to similar design problems.

The development begins with the modification of the linearized aircraft dynamics models to account for the aerodynamic effects due to the use of differential canards. The next task is the development of the complex weighting matrices to be used in the design process. Each weighting matrix ensures that when multiple control surfaces are commanded to produce a desired aircraft response, they work together in direction and phase. This is discussed at length in Chapter III. The control system design is accomplished using variations of a control method known as the Quantitative Feedback Technique (QFT). This is discussed in greater detail in the

next section of this chapter. After the control laws are developed, they are combined with the developed aircraft dynamics models to obtain system time responses by use of computer simulations. Finally, the achieved results are analyzed and conclusions are drawn.

This study demonstrates that it is possible to design a flight control system for a non-minimum phase aircraft that utilizes canards in a differential manner to control the aircraft at high AOAs. In addition, this thesis provides useful insight to the application and limitations of using QFT for designing a flight control system for any unstable, non-minimum phase aircraft. Chapter II discusses this further.

Finally, the research is performed entirely with resources available at AFIT and FIMT. The principle design work is accomplished on AFIT's Sun work-station computers, and the principle design software package is *MatrixX* [19].

1.6 Design Method

There are several well proven methods currently used in designing multi-variable flight control systems. As mentioned above, the method employed in this thesis is known as the Quantitative Feedback Technique (QFT). This method has been used for other flight control system designs, and is chosen for this project in part because of QFT's ability to account for parameter uncertainties in the system design. It is determined that such a capability is especially important for this project due to the limited amount of available wind tunnel data. In addition, the Flight Dynamics Directorate has expressed an ongoing interest in sponsoring flight control work using QFT as the principle design method. An earlier AFIT thesis discussed the application of QFT to the longitudinal channel of the X-29 flight control system. That particular study did not involve high AOA flight conditions or differential canards [27]. QFT is a frequency design technique that may be applied to either analog (continuous time) or digital (discrete time) control systems. The design for this effort is performed for an analog flight control system. The principle objectives of this thesis are met by performing the design entirely in the continuous time domain [23].

Before describing the design procedure used in this thesis, a brief discussion of flight control dynamics may help to clarify the reasons for treating the overall design as two separate design problems. Aircraft flight control systems are typically

designed around two primary modes: longitudinal and lateral-directional. These modes result from the partial decoupling of the basic aircraft dynamics equations of motion. Detailed derivations and analyses of these equations are provided in several references [2] [8] [20].

To briefly summarize, there are three force equations and three moment equations. The longitudinal mode involves the pitching moment (M) about the lateral axis and the two forces confined to the plane of symmetry: longitudinal force (X) and vertical force (Z). The lateral-directional mode involves the side force (Y), and the rolling (L) and yawing (N) moments about the longitudinal and vertical axes, respectively. These two primary modes have been shown to be virtually decoupled for conventional aircraft [2]. Examples where this is not true would be unconventional aircraft such as lifting bodies and cruciform wing missiles.

The aircraft models developed in this thesis are based on the X-29A, which, though unusual, is still considered a conventional aircraft, so its flight control systems are divided into the two primary modes described above [3]. Consequently, the design method used in this thesis treats the two modes independently.

The overall flight control system developed in this research is a three-by-three system, with three inputs and three outputs. Three control variables are frequently chosen when designing flight control systems [23]. QFT's design methods are based on a square system, so the number of inputs equals the number of outputs. A four-by-four system could be designed, but would result in significant computational difficulties when performing such operations as matrix inversion, and such a system *in most cases* does not inherently perform any better than a properly designed three-by-three system. It should be noted, however, that choosing to use four or more control variables *may* result in a more effective control system design.

In this design, the three outputs are fed back to the inputs in the conventional manner. The control variables are chosen to be pitch rate (Q), roll rate (P), and yaw rate (R). It should be noted that the nominal angular rates are denoted by capital letters. The time-varying perturbations of these variables, to be used in the state space models discussed in Chapter II, are denoted by lower case letters.

There are numerous other choices that can be used for the feedback control variables, such as; pitch, roll, and yaw angles, AOA, sideslip angle, forces, or linear combinations of such variables. The feedback variables chosen for this effort were

recommended by FIMT [1]. It was recommended that feeding back any variables containing force terms would not be ideal for this application since the aircraft speed is relatively slow, and changes in linear forces would be quite small. However, feeding back and controlling the angular rates is quite effective even for slow speeds.

It is recognized that this combination may not be the optimum choice of control variables when dealing with a non-minimum phase aircraft. However, for a study such as this, with limited data for aircraft model development, the choice is reasonable and all three control variables are directly accessible state variables. Pitch rate is the only longitudinal control variable, so the longitudinal controller is a SISO design. The remaining two control variables, roll rate and yaw rate, are in the lateral-directional control mode and that controller is a two-by-two MIMO design.

Before the actual design process can commence, the appropriate linearized aircraft dynamics models must be defined. In this case, existing aircraft models are modified to account for the differential canard aerodynamic effects. The QFT designs commence with the development of the complex weighting matrices. The weighting matrices match-up, in correct proportions, the number of desired control inputs with the larger number of control surfaces, and ensure that the control surfaces are working in phase with each other. Following this, variations of QFT methods are used to design the compensator and prefilter transfer functions for the longitudinal and lateral-directional controllers. The particular variations used are known as the *optimal blending method* and the *singular-G compensation method*. The unstable, non-minimum phase characteristics of these aircraft models require the use of such specialized design techniques.

Finally, due to extreme variations encountered in the aircraft dynamics at the different flight conditions, a different set of control laws is developed for each AOA. A single controller that can handle such extreme variations in plant parameters cannot be readily designed with the chosen technique [15].

1.7 Organization

This thesis is presented in six chapters. Chapter II addresses the aircraft model development by first briefly describing the X-29A, and then discussing how the linearized state space models are developed and modified, based on limited amounts of X-29 wind tunnel data. Next, Chapter III discusses the development of the complex

weighting matrices. Due to the very unusual characteristics of the aircraft's flight dynamics, the weighting matrix development presents a significant challenge. Several approaches are tried before the desired results are finally obtained. A specialized *shifting* technique is finally used to obtain the desired results, and a brief explanation of the reason for using such a technique is provided. The unsuccessful results are also discussed briefly, to show why conventional compensation techniques did not work well with this system.

The next two chapters describe the actual control system design procedures, and discuss in detail the application of the specialized QFT design techniques mentioned earlier. The longitudinal flight control systems are discussed in Chapter IV, and following an in-depth discussion of the design process, simulated responses to a step input are shown and analyzed. Chapter V discusses the lateral-directional (MIMO) controller design. Once again, due to the aircraft's unstable, non-minimum phase characteristics, numerous problems are encountered and specialized design techniques are presented to handle them in an optimal fashion. A complete lateral-directional controller is not designed, but the material covered in the chapter provides useful information for design work involving such difficult to handle systems. Finally, Chapter VI presents conclusions based on the results obtained, and recommendations for future research efforts.

II. Development of Mathematical Aircraft Models

2.1 Introduction

This chapter discusses the development and modification of the mathematical aircraft models used in this design. The X-29A technology demonstration aircraft is the basis for these models. It is mentioned in Chapter I that due to the availability of only limited amounts of wind tunnel data, the models developed here do not represent the X-29's actual performance. However, since the overall flight control configuration used in this thesis is most like that of the X-29, it is useful to understand the effects of some of that aircraft's advanced technologies. Following a general overview of the aircraft, the aerodynamic control surfaces are discussed in greater detail.

The second half of this chapter is devoted to the linearized aircraft model equations. First, the state space model is discussed and the state variables are defined. The initial aircraft dynamic model coefficients were obtained from the Air Force Flight Dynamics Directorate (WL/FIMT). FIMT obtained the data from the NASA Ames-Dryden Research Center, located at Edwards AFB, CA. These original state space models are based on the use of *symmetric* canard positions. The aircraft dynamics models are modified in this thesis to account for the aerodynamic effects resulting from the use of *differential* canard positions. The modifications are performed using wind tunnel data obtained from NASA's Langley Research Center in Hampton, VA.

Due to the limited amount of differential canard wind tunnel data, only four flight conditions are chosen as nominal design points. Specifically, four different AOAs are selected for a single speed and altitude condition. It is recognized that a single operating condition (speed and altitude) does not account for the effects of changing dynamic pressure. However, demonstrating the development of high AOA control laws utilizing differential canards is possible based on a few carefully selected nominal design points. Design of a control system capable of operating across the full flight envelope would require much more aerodynamic data and is well beyond the scope of this effort.

2.2 Aircraft Description

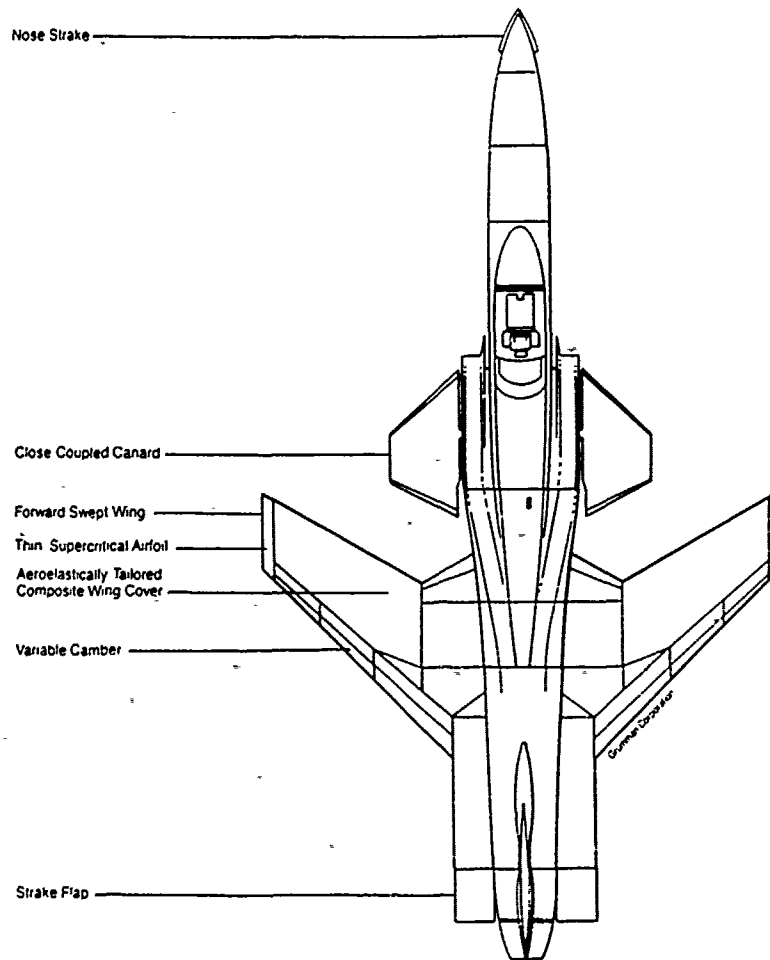


Figure 2.1. X-29A Advanced Aircraft Technologies [21]

Chapter I described the X-29A's primary purpose; that of an advanced technology demonstrator. Some of these unusual technologies are evident by looking at the aircraft. Others, however, are not so obvious. The aircraft's most striking feature is the forward swept wing (FSW). As shown in Figure 2.1, the wing has a high degree

of forward sweep, with the center of lift clearly aft of the aircraft's midpoint. The reasons for designing an aircraft with such an unusual planform may not be obvious. The overriding reason is greatly increased aerodynamic efficiency. When compared with a conventional aft swept wing, the FSW results in drag reductions of at least 20 percent, and in the transonic speed range (0.8 to 1.2 Mach), this figure may be as high as 45 percent. The benefits are clear; for a desired performance level, a fighter using the FSW may be designed around a smaller, lighter, more fuel efficient power plant.

Another key benefit of the FSW is the fact that the airflow is directed from the wing tips toward the fuselage. This means that when the wing stalls (loss of lift under extreme AOA), the ailerons remain effective for roll control. Aircraft with aft swept wings stall from the tips first, resulting in early loss of control. On the X-29A, the stall initiates at the wing root. This aerodynamic characteristic, combined with the use of close-coupled canards, enables the X-29A to fly and remain controllable at AOAs greater than sixty degrees. Prolonged *controlled* flight at such extreme values of AOA has been virtually impossible for conventional aircraft designs.

The close-coupled canards are another readily distinguishable feature of the aircraft. The term close-coupled refers to the aerodynamic interactions that take place between the canard and wing, due to their close proximity to each other. The principle function of the canards, that of primary pitch control surfaces, is discussed in Chapter I. The canards also contribute substantially to the aerodynamic efficiency of this aircraft. On a conventional aircraft with aft mounted stabilators, the stabilator must actually provide a negative lift to counteract the downward pitching moment caused by the center of gravity being forward of the center of lift. This is shown in Figure 2.2.

On the X-29A, this downward pitching moment is counteracted by placing the canards in front of the wing. This enables the canards to *balance* the aircraft by providing a positive lift, thus working *with* the wing to provide lift for the aircraft. Unfortunately, this benefit is not without penalty. With the canards contributing a substantial portion of the total lift, the overall center of lift is well forward of the center of gravity. This condition results in an aircraft that is inherently unstable in the pitch axis. Indeed, the X-29A would be completely impossible to fly if it were not for the highly advanced flight control system.

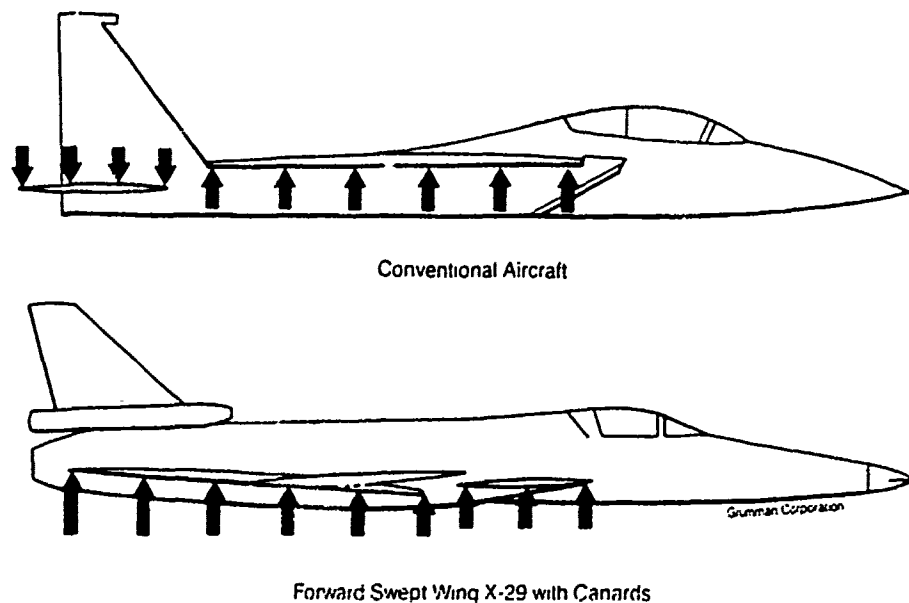


Figure 2.2. Comparison Between Stabilator and Canard [21]

Due to the extreme importance of the flight control system, this aspect of the aircraft is highly redundant. There are, in fact, three independent flight control systems that work simultaneously. Each of these systems has both a primary digital computer and an analog backup computer (with independent power supplies). Further, should one of the systems fail, the other two systems would take over and switch off the failed unit. In the extremely unlikely event of two systems failing, the pilot would still be able to land the aircraft with one system operating. The flight control system usually controls the longitudinal and lateral-directional modes in what is termed the *normal digital* mode.

A backup mode termed the *analog reversion* mode is available to get the aircraft safely home with very limited maneuvering capability. In addition, the normal digital and analog reversion modes are each capable of operating in two flight control configurations known as *up and away* and *powered approach*. These two configurations differ in the gain scheduling applied to the various control surfaces.

The flight control system is continuously updated by sensors providing information such as attitude, speed, air temperature, AOA, and side-slip angle. The flight control system compares the actual parameters with the desired ones and minimizes the error by sending commands to all the control surfaces at a 40 Hertz rate. This high speed control process occurs continuously just to maintain aircraft stability. The flight control system also responds to pilot commands (stick, rudder, and throttle inputs), and simultaneously sends the appropriate electronic control signals to the control surface actuators to accomplish the commanded flight maneuver(s). Since there is no mechanical connection between the pilot's flight controls and the aircraft's control surfaces, the system is termed *fly-by-wire*.

One of the less obvious technologies is the use of advanced composite materials in the construction of the wing. It is readily apparent that a wing with this radical design would tend to twist excessively near the tips, especially under relatively high loading conditions. Conventional materials are simply not able to provide the required strength, while at the same time being sufficiently thin and light weight. The composite material enabled the engineers to demonstrate another advanced technology; the thin supercritical wing section. This NASA developed design is only one-third as thick as a conventional wing of comparable size. The aerodynamic benefit is a softening of the transonic shock waves, and a significant reduction of buffeting and drag in the transonic speed range.

Another unusual feature of the wing is the use of full span flaperons. The unique feature noted here is that the flaperons are not conventional hinged control surfaces. Rather, these surfaces actually *bend* the shape of the wing's trailing edge by altering the camber, or curvature. A feature of the flight control system known as *automatic camber control* changes the symmetric position of the flaperons at the 40 Hertz rate to minimize drag for the current flight condition. The flaperons' use as pitch and roll control surfaces is discussed in the next section.

2.3 Control Surfaces

The longitudinal mode is controlled by three sets of control surfaces, as shown in Figure 2.3. The principle pitch control surfaces are the canards. A noteworthy feature of the canards is their extreme amount of travel. Capable of ranging from +30 to -60 degrees, the canards can remain parallel to the relative wind for nearly all

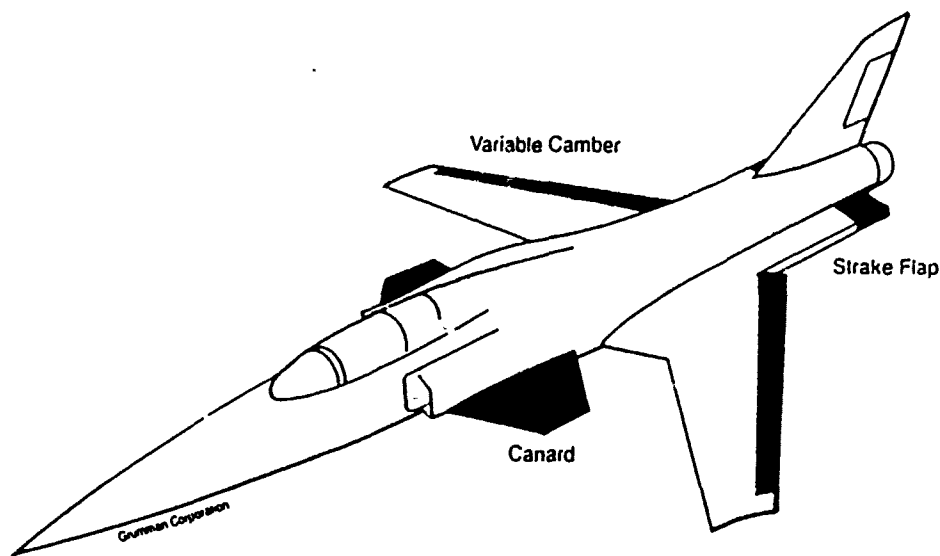


Figure 2.3. Pitch Control Surfaces [21]

achievable AOAs. Positive deflection is defined with the surface's trailing edge down (TED). With the present flight control system design, the canards have essentially no effect on the lateral-directional mode.

In addition to the canards, the variable camber flaperons contribute to pitch control when driven symmetrically. The *total* range of flaperon travel is 35 degrees. However, because of the variable camber function, these surfaces are asymmetrically limited to +25 and -10 degrees. Again, positive deflection is defined with the control surface TED. The flaperons contribute only a small amount of the total pitch control, since they lie roughly along the lateral axis, and the moment arm is quite short. Conversely, the small strakes near the exhaust nozzle contribute a substantial portion of the total pitch control, because their moment arm is relatively long. Currently, these surfaces are commanded to move a great deal in the powered approach mode to help control pitch under low speed conditions, when the canards are less effective. The strakes have a travel range of ± 30 degrees, again with positive deflection of the control surface defined with TED.

Lateral-directional control is currently provided by a combination of differentially commanded flaperons and the rudder. The sign conventions for the differential flaperons (acting like ailerons in this mode) and rudder are the same as for other

aircraft; positive deflections result in right wing down and left turn, respectively [21]. The focus of this thesis is to investigate the use of differential canards to aid the differential flaperons and rudder in controlling the lateral-directional modes (roll and yaw). The differential canard sign convention is chosen to be the same as that of the differential flaperons, with positive deflection being defined with the left surface TED. The control surface characteristics are summarized in Table 2.1.

Control Surface	Position Limit (deg)	Rate Limit (deg/sec)	Area (ft ²)
Canard	+30, -60	± 100	37.0
Symmetric Flaperon	+25, -10	± 70	14.32
Differential Flaperon	± 17.5	± 70	14.32
Rudder	± 30	± 125	7.31
Strake	± 30	± 30	5.21

Table 2.1. Control Surface Characteristics [3]

2.4 Actuator and Sensor Models

All of the control surfaces are controlled by electro-mechanical servo-actuators. The actuators receive electrical signals from the flight control system and deflect the control surfaces accordingly. Since the actuators are an integral part of any aircraft flight control system, they must be mathematically modeled along with the aircraft dynamics. The mathematical models may be in the form of either time domain or frequency domain transfer functions. Manufacturers typically provide frequency domain transfer functions for their actuators. Fourth order models of these actuators are shown in Table 2.2. Note that the denominators have been factored to show the first order exponential terms, and the second order oscillatory terms. Also, the second order terms have been written in such a way to clearly show the damping coefficient (ζ) and the natural frequency (ω_n). The standard form is given by $[s^2 + 2\zeta\omega_n + \omega_n^2]$.

For the most part, the actuators act like an exponential delay in the time domain, due to the effects of the *dominant* roots. Therefore, aircraft control surface actuators are usually represented by first order approximations, in the frequency

Canard	$\frac{(0.885)(20.2)(71.4)^2(144.9)}{(s+20.2)[s^2+2(0.736)(71.4)s+(71.4)^2](s+144.9)}$
Symmetric Flaperon	$\frac{(20.2)(71.4)^2(144.9)}{(s+20.2)[s^2+2(0.736)(71.4)s+(71.4)^2](s+144.9)}$
Differential Flaperon & Rudder	$\frac{(54.1)^2(71.4)^2}{[s^2+2(1.53)(54.1)s+(54.1)^2][s^2+2(0.735)(71.4)s+(71.4)^2]}$
Strake	$\frac{(50)(100)(325)^2}{(s+50)(s+100)[s^2+2(0.7)(325)s+(325)^2]}$

Table 2.2. Fourth Order Actuator Models [3]

domain. By using such approximations, the order of the overall control system is decreased significantly. First order approximations are used in this thesis, and are shown in Table 2.3. When comparing these approximations with the original fourth order models in Table 2.2, the dominant roots are readily seen for the canard, symmetric flaperon, and strake. The dominant root at $s = -20$ for the differential flaperon and rudder comes from factoring the first quadratic term in each denominator. In all cases, the non-dominant roots are sufficiently far away from the origin to have a negligible effect on the response characteristics.

These approximations have been validated in a recent AFIT thesis by Captain Tom Cox [6]. For one of his tasks, Capt Cox entered the aircraft dynamics models with the current flight control system design into both *MatrixX* and *SIMSTAR* computer simulations programs at AFIT. Capt Cox ran his simulations with the fourth order actuator models and again with the first order approximations, and noted that the results were virtually identical. Further, FIMT [9] notes that these approximations are commonly used to model the control actuators for simulation and design purposes.

Canard, Symmetric Flaperon, Differential Flaperon, & Rudder	$\frac{20}{s+20}$
Strake	$\frac{50}{s+50}$

Table 2.3. First Order Actuator Models [3]

The feedback signals (pitch rate, roll rate, and yaw rate), are sensed by rate gyros. The rate sensing gyros are modeled by second order transfer functions as shown in Table 2.4. For the control system design in this thesis, the frequency range of interest is roughly 0.1 to 100 rad/sec. Long term drift characteristics below 0.1 rad/sec are easily controlled by the autopilot, and frequencies above 100 rad/sec are attenuated in the feedback system to avoid exciting structural modes. Further, the *effective bandwidth* of the human pilot ranges from approximately 1 to 10 rad/sec. The natural frequencies of the rate gyros are high enough so that their gain attenuation in the frequency range of interest is negligible. Therefore, the sensors are modeled as unity gain functions for this design effort.

Pitch Rate Gyro & Yaw Rate Gyro	$\frac{(137)^2}{s^2+2(0.704)(137)s+(137)^2}$
Roll Rate Gyro	$\frac{(157)^2}{s^2+2(0.701)(157)s+(157)^2}$

Table 2.4. Sensor Models [3]

2.5 Linearized Aircraft Model Equations

The linearized aircraft dynamics models used in this effort are based on state space models provided by FIMT. The original models were generated by NASA's X-29A six-degree-of-freedom non-linear simulation program, and represented a wide range of flight conditions. The models were provided in the form of **A**, **B**, **C**, and **D** matrices. These matrices form the System matrix (**S**) shown in Equation 2.1. This matrix contains all the coefficients of the system's differential equations written in the standard state space form shown in Equations 2.2 and 2.3.

$$\mathbf{S} = \begin{bmatrix} \mathbf{A} & \vdots & \mathbf{B} \\ \dots & \dots & \dots \\ \mathbf{C} & \vdots & \mathbf{D} \end{bmatrix} \quad (2.1)$$

$$\dot{\mathbf{x}}(t) = \mathbf{A} \mathbf{x}(t) + \mathbf{B} \mathbf{u}(t) \quad (2.2)$$

$$\mathbf{y}(t) = \mathbf{C} \mathbf{x}(t) + \mathbf{D} \mathbf{u}(t) \quad (2.3)$$

Equation 2.2 is the *state* equation which relates the time rate of change of the state vector to the control vector. Equation 2.3 is the *output* equation which relates the system output vector to the state vector, and also the control vector when a feed-forward path is present in the control system. Figure 2.4 is the block diagram representation of Equations 2.2 and 2.3.

The state vector $\mathbf{x}(t)$ contains all the variables needed to completely describe the system's behavior. These variables are discussed in greater detail in the next paragraph. The **A** matrix is known as the system dynamics matrix, and the **B** matrix is known as the control matrix. Both relate the state variables to the input vector $\mathbf{u}(t)$.

The output vector $\mathbf{y}(t)$ is determined by using the output matrix **C** to form a linear combination of the state variables. The feed-forward matrix **D** is used to relate outputs directly to inputs. For most flight control systems, the **D** matrix

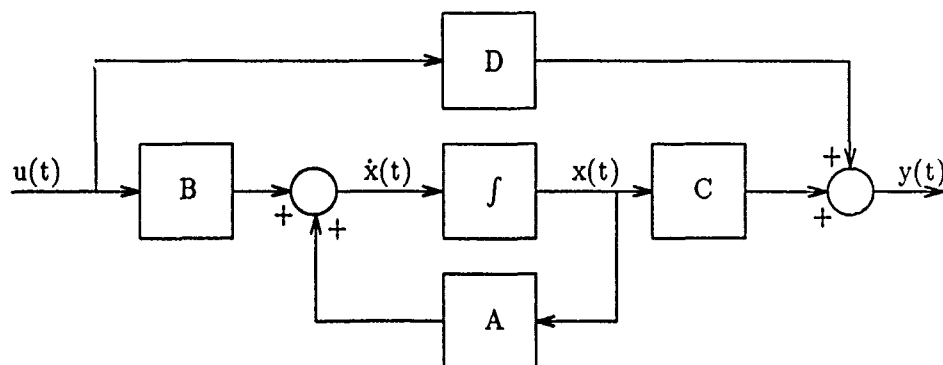


Figure 2.4. Block Diagram Representation of State Space

is zero-valued, as is the case in this design. Finally, it should be noted that since this design is based on linear time-invariant (LTI) analysis and design methods, the elements of the system matrix are not time varying. This condition holds for small perturbations about each nominal point, as discussed in Chapter I.

The models provided by NASA include a total of eight states; four longitudinal and four lateral-directional. The longitudinal states are forward velocity $[v(t)]$, AOA $[\alpha(t)]$, pitch rate $[q(t)]$, and pitch angle $[\theta(t)]$. Angle of attack is defined as the angle between the aircraft's longitudinal axis and the velocity vector as projected onto the vertical plane of symmetry (defined by X and Z). Pitch angle is defined with positive deflection corresponding to a *nose up* attitude relative to the local level defined in inertial coordinates. Figure 2.5 pictorially defines these angles in relation to the aircraft.

Having defined the state variables associated with the longitudinal mode, the longitudinal state vector $\mathbf{x}_{lon}(t)$ is:

$$\mathbf{x}_{lon}(t) = \begin{bmatrix} v(t) \\ \alpha(t) \\ q(t) \\ \theta(t) \end{bmatrix} \begin{array}{l} \text{forward velocity (ft/sec)} \\ \text{angle of attack (deg)} \\ \text{pitch rate (deg/sec)} \\ \text{pitch angle (deg)} \end{array} \quad (2.4)$$

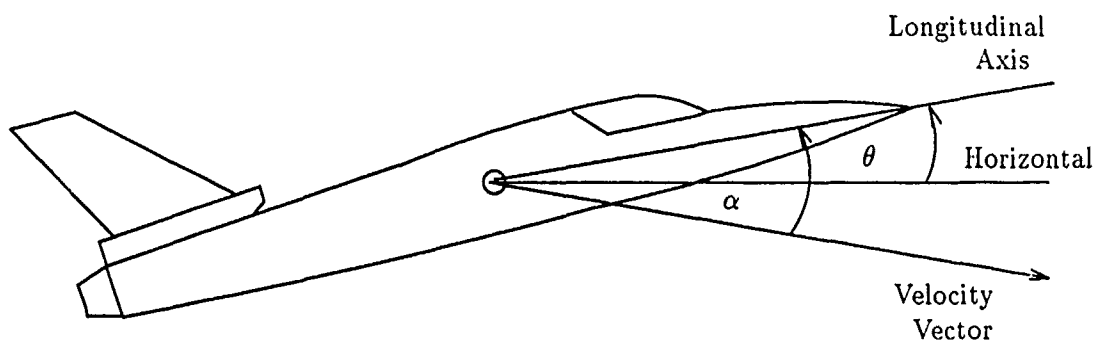


Figure 2.5. Definition of α and θ

The four lateral-directional states are side slip angle $[\beta(t)]$, roll rate $[p(t)]$, yaw rate $[r(t)]$, and bank angle $[\phi(t)]$. Positive bank angle is defined with the right wing down relative to the local level coordinate frame, as shown in Figure 2.6. Side slip angle is defined as the angle between the aircraft's longitudinal axis and the velocity vector as projected down onto the local level plane (defined by X and Y). Positive side slip is sometimes referred to as *having wind in the right ear*. This is shown in Figure 2.7.

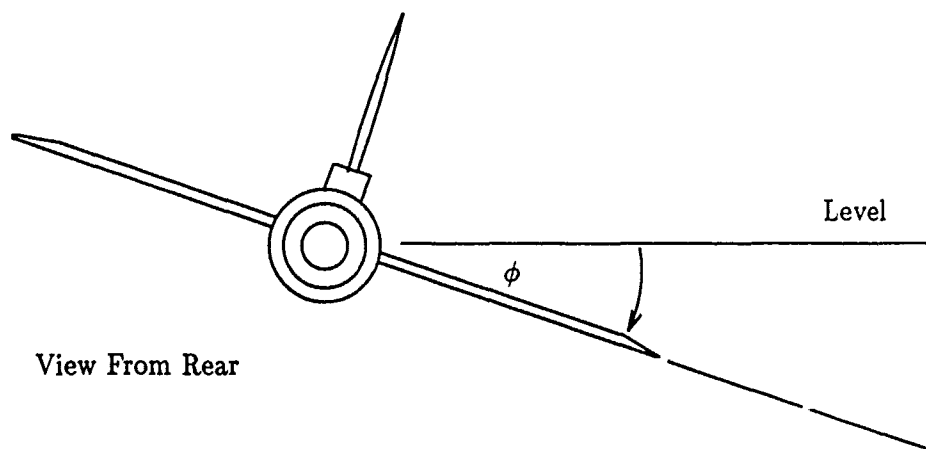


Figure 2.6. Definition of ϕ

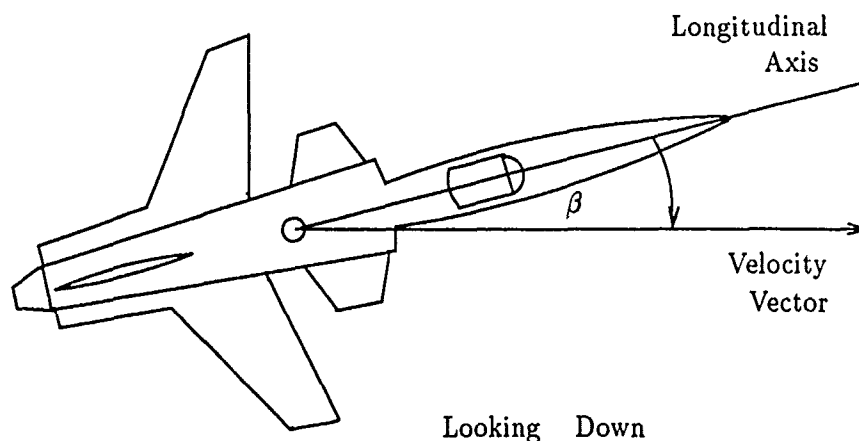


Figure 2.7. Definition of β

With the remaining state variables defined, the lateral-directional state vector $\mathbf{x}_{lat}(t)$ is:

$$\mathbf{x}_{lat}(t) = \begin{bmatrix} \beta(t) \\ p(t) \\ r(t) \\ \phi(t) \end{bmatrix} \quad \begin{array}{l} \text{side slip angle (deg)} \\ \text{roll rate (deg/sec)} \\ \text{yaw rate (deg/sec)} \\ \text{bank angle (deg)} \end{array} \quad (2.5)$$

The input vectors, like the state vectors above, are defined in the two primary flight control modes. The longitudinal input vector $\mathbf{u}_{lon}(t)$ originally provided contains four elements corresponding to control perturbations. Three of these correspond to small control surface deflections and the remaining element corresponds to small variations in engine thrust. Specifically, the four elements of the original input vector are symmetric canard $[\delta_c(t)]$, symmetric flaperon $[\delta_{sf}(t)]$, strake flap $[\delta_{str}(t)]$, and engine thrust $[\delta_{th}(t)]$. The next section discusses the modification of the input vectors to incorporate differential canard effects. The longitudinal input vector as initially defined is:

$$\mathbf{u}_{lon}(t) = \begin{bmatrix} \delta_c(t) \\ \delta_{sf}(t) \\ \delta_{str}(t) \\ \delta_{th}(t) \end{bmatrix} \begin{array}{l} \text{symmetric canard (deg)} \\ \text{symmetric flaperon (deg)} \\ \text{strake flap (deg)} \\ \text{thrust (lbs)} \end{array} \quad (2.6)$$

The original lateral-directional input vector $\mathbf{u}_{lat}(t)$ contains only two elements. These are differential flaperon $[\delta_{df}(t)]$, and rudder $[\delta_r(t)]$. Again, the modification of this vector is discussed in the next section. The original lateral-directional input vector is:

$$\mathbf{u}_{lat}(t) = \begin{bmatrix} \delta_{df}(t) \\ \delta_r(t) \end{bmatrix} \begin{array}{l} \text{differential flaperon (deg)} \\ \text{rudder (deg)} \end{array} \quad (2.7)$$

Having defined the state and input vectors, the design analysis proceeds with the examination of the complete state space models originally generated by the NASA simulation. Although the original models were provided for a wide range of flight conditions, only four nominal points are chosen for this design effort, due in part to the limited amount of available differential canard wind tunnel data. The wind tunnel data is based on a low speed and low altitude flight condition with varying AOAs. For this design, one specific speed and altitude pair is chosen as the nominal flight condition about which to vary the AOA. It was determined that a representative flight control system can be designed using only four properly selected nominal points. The four AOA values selected for this design are 20, 40, 50, and 60 degrees. The reasons for selecting these specific values are discussed in greater detail in the next section.

The original longitudinal and lateral-directional **A**, **B**, **C**, and **D** matrices for each of the four flight conditions are given in Appendix A. The state space models, after being modified, are transformed into high order transfer functions known as open-loop *plants*. The plants are the basis of the QFT design process to be described in subsequent chapters.

Finally, the aircraft considered in this research is unstable and non-minimum phase. These characteristics result from the system plants having poles and zeros in the right half of the complex *s-plane*. The right-half-plane (RHP) poles cause the

open loop system to be unstable, and the RHP zeros result in the non-minimum phase characteristics (i.e. they add excess phase lag). The physical properties that result in these mathematical characteristics are due to aerodynamic phenomena resulting from such considerations as the relative placement of control surfaces, their relative sizes, and the locations of rate sensing gyros. An in-depth aerodynamic study of this aircraft is well beyond the scope of this thesis, but the principle reasons for the longitudinal static instability were discussed previously.

The undesirable effects resulting from these mathematical characteristics are discussed in detail in Chapters IV and V. However, it is useful to examine the poles of the initial dynamics models, to verify the expected open loop instability characteristics for each of the flight conditions. This is accomplished by obtaining the *eigenvalues* (λ) of each A matrix [8]. The task is performed using *MatrixX* and the results are shown in Appendix B. The longitudinal mode's eigenvalues for the first flight condition ($\alpha = 20$) are repeated here for discussion.

$$\lambda_{lon20} = \begin{bmatrix} -0.0203 + 0.1257j \\ -0.0203 - 0.1257j \\ 0.7080 + 0.0000j \\ -1.0302 + 0.0000j \end{bmatrix} \quad (2.8)$$

It is noted that one of the four poles is in the RHP, and thus causes the system to be unstable. Complex poles in the RHP add oscillatory instability characteristics, while an RHP pole on the real axis contributes a purely exponential form of instability, as is the case here.

Using a similar analysis procedure for the remaining cases, it is noted that the open loop dynamics become slightly more stable in the pitch axis as the AOA increases. This is seen by the fact that the RHP poles, for the longitudinal cases, approach the origin as the AOA increases and finally become left-half-plane (LHP) poles for the 60 degree case. However, in the lateral-directional modes, the open loop aircraft dynamics are clearly unstable for all four of the chosen flight conditions, as evidenced by the RHP poles present in all cases. These results were shared with FIMT and it was verified that the actual aircraft tends to behave in this manner [9].

2.6 Modification of Aircraft Model Equations

This section discusses how the wind tunnel data generated by the NASA Langley Research Center is used to modify the linearized state space models to account for the aerodynamic effects due to differential canard positions. The raw data is in the form of coefficients of lift, drag, side force, and pitch, roll, and yaw moments. These coefficients were obtained over a wide range of AOAs. The data was obtained for a constant dynamic pressure. FIMT stated that the data is reasonably accurate up to a speed of 0.5 Mach and an altitude of 30,000 feet, based on information provided by NASA. For this design study, FIMT recommended a single flight condition of 0.3 Mach and 20,000 feet, to use as the nominal trim condition. This trim condition allows the AOA to vary up to sixty degrees without introducing concern over excessive structural loading [9].

The first wind tunnel runs were made with symmetric canard settings of 0, -25, and -40 degrees. Recall that *positive* canard deflection is defined with the trailing edge down. The initial runs were followed by similar runs with the canards set at ± 20 degrees about the nominal symmetric deflections. This resulted in differential values of -5 & -45, and -20 & -60 degrees, respectively.

The coefficients obtained from each symmetric deflection run are subtracted from the coefficients produced during the corresponding differential deflection run. These results are then divided by the nominal differential amount of 20 degrees to obtain the stability derivatives with respect to differential canard inputs. This procedure was provided by the Air Force Flight Dynamics Laboratory [5]. While this procedure is an accepted method used to obtain stability derivatives, it is recognized that the expected accuracy of these results is quite limited. This is due primarily to having only a single differential deflection, and the fact that this deflection is perhaps unrealistically large for many flight maneuvers. It is likely that with such large differential deflections one of the canards might be stalled (loss of lift resulting from disrupted airflow) under certain flight conditions.

Appendix C lists the two symmetric and the two differential coefficient matrices. Each matrix has six columns, corresponding to the aerodynamic coefficients, and 13 rows, corresponding to AOAs ranging from zero to sixty degrees in five degree increments. The side slip angle is zero for all cases. The order of the aerodynamic coefficients as listed in the matrices is: lift (C_L), drag (C_D), pitching moment (C_M), side force (C_Y), yawing moment (C_N), and rolling moment (C_l). The general method

used to obtain the stability derivatives is discussed in the previous paragraph. The most efficient way to obtain the desired results is to subtract the appropriate symmetric coefficient matrix from its corresponding differential coefficient matrix and divide the result by 20. Since there are two nominal symmetric deflections, this results in two complete sets of stability derivatives from which the desired values are chosen as discussed below. The matrix calculations are performed using *MatrixX*, and the results are included in Appendix C.

As an example, in order to obtain the C_M stability derivative for 20 degrees AOA, the symmetric value is subtracted from the differential value and divided by 20. Referring to the first set of wind tunnel coefficients (based on 25 degree symmetric deflection), the symmetric value (-0.2023) is read from the (5,3) position of the 'sim25' matrix. This is subtracted from the corresponding value (-0.2076) from the 'diff25' matrix, and the result is divided by 20 to obtain the result shown in the (5,3) position of the 'stabder25' matrix (-2.650E-4).

At this point the choice is made to use the four previously defined AOAs. Since the focus of this thesis is to investigate controlled flight at extreme values of AOA, a reasonable selection of nominal points includes 40, 50, and 60 degrees. In addition, a moderate AOA value of 20 degrees is chosen to possibly demonstrate the potential robustness of the QFT design process.

To minimize adverse effects resulting from extrapolating data, the 20 degree AOA coefficients are taken from the results based on 25 degree symmetric deflections (i.e. row five of the first stability derivative matrix 'stabder25' shown in Appendix C). Similarly, the three high AOA coefficient sets are taken from the matrix based on 40 degree symmetric deflections (i.e. rows 9, 11, & 13 of the second stability derivative matrix 'stabder40'.) This is clarified by examining the 20 degree AOA C_M stability derivative once again. Since the ideal (minimum drag) flight condition is to have the canards positioned so that they are aligned with the relative wind, a symmetric deflection of 25 degrees for an AOA of 20 degrees is reasonable. However, a symmetric canard deflection of 40 degrees while flying at 20 degrees AOA would result in a high drag configuration, and any results based on such extreme operating conditions would not be expected to be reasonable. The result of this can be seen by noting the calculated value in the (5,3) position of the 'stabder40' matrix (+7.350E-4) and comparing this with the value previously obtained from the 'stabder25' matrix.

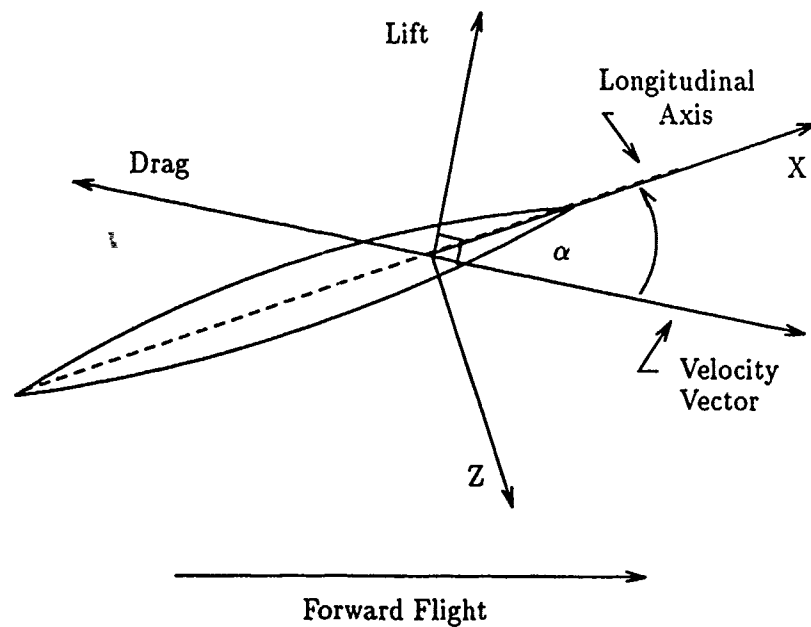


Figure 2.8. Translation of Lift and Drag into Longitudinal Forces

Before modifying the **B** matrices, it is necessary to translate two of the six aerodynamic coefficients for each of the chosen flight conditions. It is standard practice to obtain lift and drag coefficients from wind tunnel test runs. However, the aircraft dynamics equations that form the state space models are based on the three orthogonal forces and three orthogonal moments defined in Section 1.6. Lift and drag must therefore be translated into the **X** and **Z** forces. The translation is required when the AOA is not zero, as shown in Figure 2.8. Simple trigonometric calculations based on the figure are used to perform the translation. Equations 2.9 and 2.10 are the general equations and the values for the 20 degree case are calculated from Equations 2.11 and 2.12.

$$C_Z = -C_L \cos(\alpha) - C_D \sin(\alpha) \quad (2.9)$$

$$C_X = C_L \sin(\alpha) - C_D \cos(\alpha) \quad (2.10)$$

$$C_{Z20} = (4.000E - 5) * \cos(20) - (3.550E - 3) * \sin(20) = -3.229E - 3 \quad (2.11)$$

$$C_{X20} = (-4.000E - 5) * \sin(20) - (3.550E - 3) * \cos(20) = -1.487E - 3 \quad (2.12)$$

Appendix D lists the four sets of stability derivatives obtained from the calculations performed in Appendix C. For each flight condition, the first two entries (C_L & C_D) are used to calculate the translated X and Z force stability derivatives, and those results are also shown in the appendix. Finally, the four sets of differential canard stability derivatives are listed in Table 2.5. These are now used to define the modified state space models.

AOA	C_X	C_Z	C_M	C_Y	C_N	C_l
20	-1.487D-03	-3.229D-03	-2.650D-04	-5.250D-03	4.050D-04	-2.305D-03
40	2.609D-03	-2.255D-03	2.345D-03	-6.420D-03	-1.550D-04	-1.530D-03
50	3.504D-04	4.490D-03	-7.700D-04	-3.675D-03	3.150D-04	-2.145D-03
60	1.960D-03	-5.305D-03	-3.555D-03	-3.290D-03	4.550D-04	-1.125D-03

Table 2.5. Final Differential Canard Stability Derivatives

Now properly defined, the four sets of stability derivatives need to be incorporated into the B matrices, since the original control vectors do not contain any terms accounting for differential canard effects. Following extensive discussions with Dr Meir Pachter [22], the following approach is decided upon.

The original longitudinal control vector contained a term for delta thrust, which related to the corresponding entries in the fourth column of the original B matrix. However, for this simulation the thrust is assumed to be constant, so the original fourth column entries in the B matrix are not needed. This means that the longitudinal B matrix can retain its original dimensionality by replacing the fourth column with the coefficients obtained using differential canard control inputs. The longitudinal B matrix is then modified by deleting the fourth column, moving the second

and third columns to the third and fourth column positions, and inserting the appropriate differential canard longitudinal stability derivatives into the second column. The two longitudinal **B** matrices for the 20 degree flight condition are shown below. The modified matrix is denoted with a tilde.

$$\mathbf{B}_{lon20} = \begin{bmatrix} -8.8250D-02 & -8.5710D-02 & -2.3390D-02 & 1.0280D-01 \\ -3.3100D-04 & -3.4930D-04 & -2.1030D-04 & -1.2020D-04 \\ 1.2410D-02 & -2.7310D-03 & -9.6810D-03 & -9.0470D-04 \\ 0.0000D+00 & 0.0000D+00 & 0.0000D+00 & 0.0000D+00 \end{bmatrix} \quad (2.13)$$

$$\tilde{\mathbf{B}}_{lon20} = \begin{bmatrix} -8.8250D-02 & -1.4872D-03 & -8.5710D-02 & -2.3390D-02 \\ -3.3100D-04 & -3.2292D-03 & -3.4930D-04 & -2.1030D-04 \\ 1.2410D-02 & -2.6500D-04 & -2.7310D-03 & -9.6810D-03 \\ 0.0000D+00 & 0.0000D+00 & 0.0000D+00 & 0.0000D+00 \end{bmatrix} \quad (2.14)$$

In each case, the **X** force coefficient is in the forward velocity equation, the **Z** force coefficient is in the AOA equation, and the pitching moment coefficient is in the pitch rate equation. The modification is required to match up the longitudinal **B** matrix with the modified longitudinal control vector, which is defined below.

$$\tilde{\mathbf{u}}_{lon}(t) = \begin{bmatrix} \delta_c(t) \\ \delta_{dc}(t) \\ \delta_{df}(t) \\ \delta_{str}(t) \end{bmatrix} \begin{array}{l} \text{symmetric canard (deg)} \\ \text{differential canard (deg)} \\ \text{differential flaperon (deg)} \\ \text{strake flap (deg)} \end{array} \quad (2.15)$$

The dimensionality of the lateral-directional **B** matrix, and its corresponding control vector, is increased by one. In this case, the lateral-directional stability derivatives associated with the differential canard control inputs are augmented as a third column in the lateral-directional **B** matrix. The original and modified lateral-directional **B** matrices for the 20 degree flight condition are shown below.

$$\mathbf{B}_{lat20} = \begin{bmatrix} -8.8650D-05 & 2.0300D-04 \\ 1.3280D-01 & 1.0630D-02 \\ 7.1400D-03 & -9.8750D-03 \\ 0.0000D+00 & 0.0000D+00 \end{bmatrix} \quad (2.16)$$

$$\tilde{\mathbf{B}}_{lat20} = \begin{bmatrix} -8.8650D-05 & 2.0300D-04 & -5.2500D-03 \\ 1.3280D-01 & 1.0630D-02 & -2.3050D-03 \\ 7.1400D-03 & -9.8750D-03 & 4.0500D-04 \\ 0.0000D+00 & 0.0000D+00 & 0.0000D+00 \end{bmatrix} \quad (2.17)$$

The side force coefficient is in the side slip angle equation, and the yaw and roll moments are each in their corresponding rate equations. Finally, the modified lateral-directional control vector is defined below.

$$\tilde{\mathbf{u}}_{lat}(t) = \begin{bmatrix} \delta_{df}(t) \\ \delta_r(t) \\ \delta_{dc}(t) \end{bmatrix} \begin{array}{l} \text{differential flaperon (deg)} \\ \text{rudder (deg)} \\ \text{differential canard (deg)} \end{array} \quad (2.18)$$

The modified \mathbf{B} matrices for all four flight conditions are shown in Appendix E. Finally, the original \mathbf{C} matrix is modified in all cases to transmit only the desired state variables, $p(t)$, $q(t)$, and $r(t)$ to the system outputs. Since there is no feed-forward path in this control system, the \mathbf{D} matrices are all zero-valued. The longitudinal and lateral-directional \mathbf{C} matrices are shown in Equations 2.19 and 2.20.

$$\mathbf{C}_{lon} = \begin{bmatrix} 0 & 0 & 0 & 0 \\ 0 & 0 & 0 & 0 \\ 0 & 0 & 1 & 0 \\ 0 & 0 & 0 & 0 \end{bmatrix} \quad (2.19)$$

$$C_{lat} = \begin{bmatrix} 0 & 0 & 0 & 0 \\ 0 & 1 & 0 & 0 \\ 0 & 0 & 1 & 0 \\ 0 & 0 & 0 & 0 \end{bmatrix} \quad (2.20)$$

Appendix F lists the final state space system matrices for all four flight conditions. In each case, the **S** matrix is used to generate the open loop plant transfer functions from the appropriate *System Build* files. The longitudinal and lateral-directional **S** matrices for the 20 degree flight condition are given below.

S_{lon20} =

Columns	1 thru	6
-6.7320D-02	-1.9190D+01	-5.8320D-01 -3.2110D+01 -8.8250D-02 -1.4872D-03
-6.0200D-04	-1.4980D-01	9.9480D-01 -3.9770D-09 -3.3100D-04 -3.2292D-03
4.9390D-04	7.3440D-01	-1.4560D-01 -2.2720D-09 1.2410D-02 -2.6500D-04
0.0000D+00	0.0000D+00	1.0000D+00 0.0000D+00 0.0000D+00 0.0000D+00
0.0000D+00	0.0000D+00	0.0000D+00 0.0000D+00 0.0000D+00 0.0000D+00
0.0000D+00	0.0000D+00	0.0000D+00 0.0000D+00 0.0000D+00 0.0000D+00
0.0000D+00	0.0000D+00	1.0000D+00 0.0000D+00 0.0000D+00 0.0000D+00
0.0000D+00	0.0000D+00	0.0000D+00 0.0000D+00 0.0000D+00 0.0000D+00

Columns	7 thru	8
-8.5710D-02	-2.3390D-02	
-3.4930D-04	-2.1030D-04	
-2.7310D-03	-9.6810D-03	
0.0000D+00	0.0000D+00	
0.0000D+00	0.0000D+00	
0.0000D+00	0.0000D+00	
0.0000D+00	0.0000D+00	
0.0000D+00	0.0000D+00	

$$S_{lat20} =$$

Columns	1 thru	6			
-6.8010D-02	3.4030D-01	-9.3810D-01	9.7000D-02	-8.8650D-05	2.0300D-04
-1.8850D+01	1.4380D-02	1.2860D-01	1.4200D-06	1.3280D-01	1.0630D-02
1.0090D+00	-3.3750D-02	-1.3520D-02	4.3340D-07	7.1400D-03	-9.8750D-03
0.0000D+00	1.0000D+00	3.6400D-01	6.6800D-03	0.0000D+00	0.0000D+00
0.0000D+00	0.0000D+00	0.0000D+00	0.0000D+00	0.0000D+00	0.0000D+00
0.0000D+00	1.0000D+00	0.0000D+00	0.0000D+00	0.0000D+00	0.0000D+00
0.0000D+00	0.0000D+00	1.0000D+00	0.0000D+00	0.0000D+00	0.0000D+00
0.0000D+00	0.0000D+00	0.0000D+00	0.0000D+00	0.0000D+00	0.0000D+00

Columns	7 thru	7
-5.2500D-03		
-2.3050D-03		
4.0500D-04		
0.0000D+00		
0.0000D+00		
0.0000D+00		
0.0000D+00		
0.0000D+00		

2.7 Summary

This chapter presents a brief overview of the X-29A technology demonstration aircraft, since that aircraft is used as the basis for the aircraft models developed in this design problem, and then provides an in-depth look at the control surfaces. The reduced order actuator models are developed, and the models of the pertinent flight control sensors are discussed. The next section begins with a brief discussion of how state space models are used to represent a system of linear differential equations in a more convenient form. Following this, the initial linearized aircraft model equations are described. The system state vectors are defined, and the system control vectors

are presented in their original form. As an interim check, the system eigenvalues are obtained and examined to verify the expected open-loop instability characteristics.

The final section of this chapter describes the modifications made to the original state space models. The modifications are required to account for the aerodynamic effects resulting from the use of differential canard positions. The control matrices and input vectors are modified accordingly, and the output matrices are re-defined to obtain the desired control variables for feedback. Finally, the open-loop system matrices are presented. These state space models are used along with the actuator models and weighting matrices to form the effective plant transfer functions in subsequent chapters. Chapter III discusses the development of the control system weighting matrices.

III. Weighting Matrix Development

3.1 Introduction

This chapter discusses the development of the weighting matrices that augment the open loop dynamics models. For each of the flight conditions, the weighting matrix (Δ) combines with the actuator matrix and the state space model to form the *effective plant* (P_{eff}), as shown in Figure 3.1. QFT design methods require that the effective plant matrix be square (i.e. with the same number of inputs and outputs) and be non-singular. These requirements are necessary for the matrix to be invertible. The weighting matrix accomplishes the squaring operation at the front end of the system, and distributes the commanded control inputs (three angular rates) among the seven aerodynamic control surface inputs in the proper relative weights.

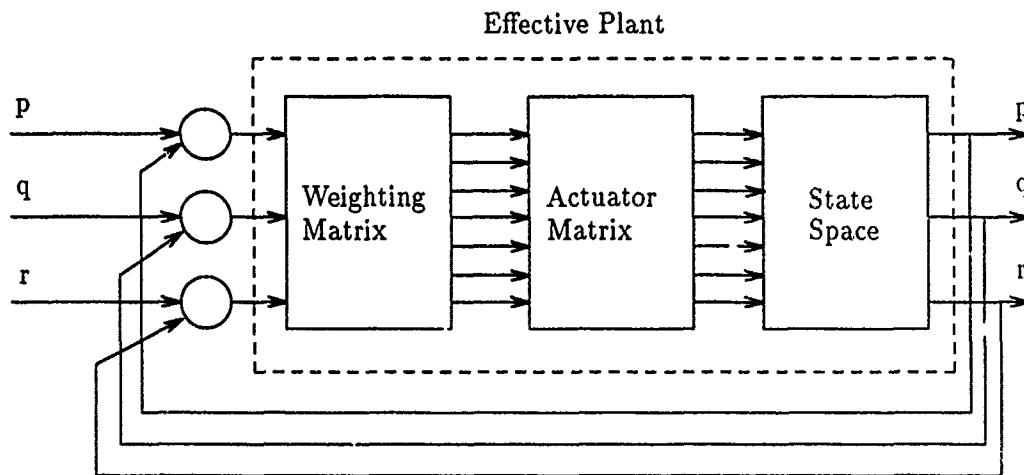


Figure 3.1. Block Diagram of Flight Control System

The next section describes the principle function of the weighting matrix in greater detail, and discusses the need to develop a *frequency dependent* weighting matrix for this particular application. This is followed by a brief overview of the techniques used to develop both constant and frequency dependent compensation terms. Some unusual problems arise due to the unstable, non-minimum phase state

space models discussed in the last chapter. As a result, special *shifting* methods are required to obtain the desired open loop response characteristics from the frequency dependent compensation terms.

Since a significant amount of effort was expended on unsuccessful methods to develop lateral-directional compensation terms, a brief discussion of those methods is included, along with results from one of the cases. Following this, the development of the individual compensation terms (weighting matrix elements) for each of the flight conditions is detailed in the pitch, roll, and yaw channels individually. The roll and yaw channels are then combined, along with cross terms and appropriate gains, to form the complete lateral-directional compensation matrices. Finally, the longitudinal (SISO) and lateral-directional (MIMO) weighting matrices are listed, along with a discussion of how they are incorporated into the effective plants.

3.2 Weighting Matrix Design Approach

The principle function of the weighting matrix is to distribute the desired control inputs among the appropriate control surfaces with specified relative weights. The relative weights are based on such considerations as the aerodynamic effectiveness of each control surface to perform a given flight maneuver at a particular flight condition. This includes inverting control surface inputs as necessary due to the sign conventions discussed in Chapter II. The weighting matrix ensures that the appropriate control surfaces are all working together to achieve a commanded flight maneuver. For most aircraft flight control systems, a simple weighting matrix with constant elements is sufficient. This turns out to be the case for the longitudinal channel on this aircraft, as well. However, the lateral-directional controls possess unusual response characteristics. In particular, the control surfaces used to control roll and yaw operate out of phase with each other without appropriate compensation. The required compensation involves frequency dependent terms, as well as constant gain values. Further, the compensation terms are a function of the particular flight condition. As a result, different weighting matrices are required for each flight condition considered in this design effort.

For the longitudinal channel, the compensation terms are developed by examining the uncompensated open-loop step responses, inverting the appropriate control inputs, and including the desired relative gains for each. This is discussed in detail

in the next section. Developing the frequency dependent compensation required for the lateral-directional channels presents quite a problem, due to the unusual characteristics of this aircraft. As before, the process begins with examination of the uncompensated open-loop step responses. From these plots, it is clear that the control surfaces are working out of phase with each other, and without compensation, would be inefficient in achieving a commanded flight maneuver.

The accepted technique for developing frequency dependent compensation terms is to obtain the relative phase characteristics from a Bode phase plot, and then include poles and zeros as needed to adjust the phase plots until they are nearly the same. With similar phase characteristics in the frequency domain, the time response plots would normally be expected to show that the control surfaces are working together. Unfortunately, this is not the case with the initial design attempts used to perform this task. This method is used to develop roll and yaw rate compensation terms for all four flight conditions. In most of the cases, the composite time response plots do not show the desired characteristics, even though the relative phase plots are in close agreement in the frequency domain.

An alternative approach was suggested by Captain Paschall [23]. Since the end goal for this task is to force the appropriate control surfaces to work together in response to a commanded maneuver, he suggested that the uncompensated open-loop time responses be analyzed for each case to determine what form of compensation might bring the time domain plots together. Initially, this is attempted on the problematic yaw channels, whose time responses are sinusoidally unstable, as expected. Since the sinusoids *appear* to lag or lead each other by a constant amount, Captain Paschall suggested using the simple first order Padé approximation to compensate for the relative time delay. This approximation uses a first order pole/zero combination and is given as [2]:

$$e^{-\tau s} = \frac{s - \frac{2}{\tau}}{s + \frac{2}{\tau}} \quad (3.1)$$

This method results in fewer and simpler compensation terms, and does achieve a *partial* improvement in the time response relationships. However, even after fine-tuning the Padé compensation terms, the time response plots reveal that the control surfaces are still not working together continuously, thus indicating that effective

compensation involves more than simply accounting for the relative time delays. Both this and the previous design method are discussed further, along with selected results, in Section 3.3.

Professor Horowitz finally determined the probable reason for the two previous techniques' failures to yield the desired results. While one would normally expect a good correlation between the time and frequency domain phase characteristics, it should be remembered that such a correlation is based upon the transformation between the two domains. That transformation is given by the LaPlace integral:

$$F(s) \equiv \int_0^{\infty} f(t) e^{-st} dt \quad (3.2)$$

$$s = \sigma + j\omega \quad (3.3)$$

For the definition to hold, the integral must exist (i.e. the solution is not ∞). If $f(t)$ contains a term $e^{\alpha t}$ (where $\alpha > 0$), and $\sigma = 0$, then the equation becomes:

$$F(j\omega) = \int_0^{\infty} e^{\alpha t} e^{-j\omega t} dt \quad (3.4)$$

The solution of this equation is infinite. In order for the integral to converge to a finite solution, σ must be chosen to be greater than α . Therefore, the integral exists only for all σ values to the right of α as shown in Figure 3.2.

Consequently, for the time and frequency domains to correlate, as desired for phase compensation purposes, Professor Horowitz recommended shifting the roots of the open-loop plants (state space models), so that all the poles are in the LHP. Then, pole/zero compensation is added to improve the frequency domain phase characteristics. After shifting back the compensated systems by the same amount they were initially shifted, the time response plots are obtained and show the desired results. As is seen in Sections 3.5 and 3.6, some degree of fine-tuning is necessary to match the relative time responses sufficiently (i.e. the shifted Bode phase plots are not all perfectly matched).

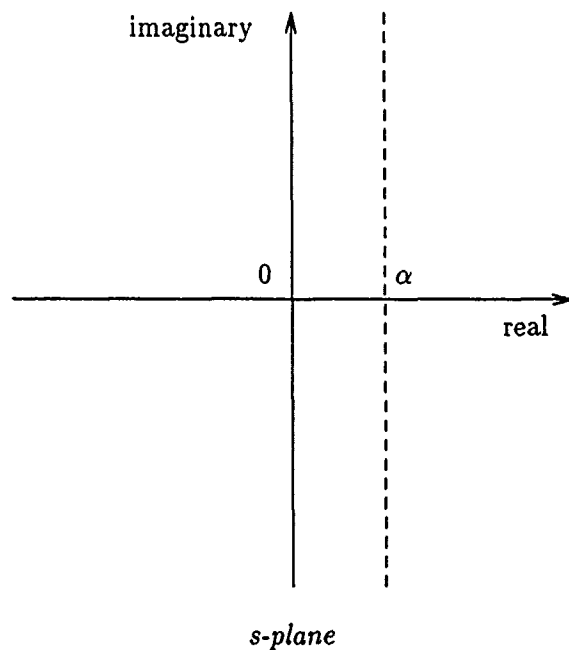


Figure 3.2. S-plane Region of Convergence for Laplace Integral

With the phase characteristics properly matched by the frequency dependent compensation terms, the desired relative control surface weightings are included. The weights are determined from a combination of open-loop time response analysis and knowledge of the actual aircraft aerodynamic performance characteristics.

The overall weighting matrix for this control system distributes three control inputs among seven control surfaces. However, the development is performed independently for the longitudinal and lateral-directional control systems, as previously discussed. Therefore, the longitudinal weighting matrix relates one control input $[q(t)]$ to four control surfaces. Similarly, the lateral-directional weighting matrix relates the remaining two control inputs $[p(t)]$ and $[r(t)]$ to the three remaining control surfaces. This is clearly shown throughout the remainder of this chapter in the appropriate block diagrams and open-loop response plots.

3.3 Unsuccessful Compensation Attempts

Before discussing the final weighting matrix compensation for each of the cases, it would be useful to examine selected results of the two unsuccessful compensation methods. The purpose of this section is to show the failings of using conventional methods (without shifting roots) to develop frequency dependent compensation terms for unstable plants. Section 3.2 briefly discussed the procedures used in both of these methods. The 50 degree yaw rate case has been chosen to demonstrate the ineffectiveness of these two methods. The uncompensated open-loop step responses for this case are shown in Figure 3.3.

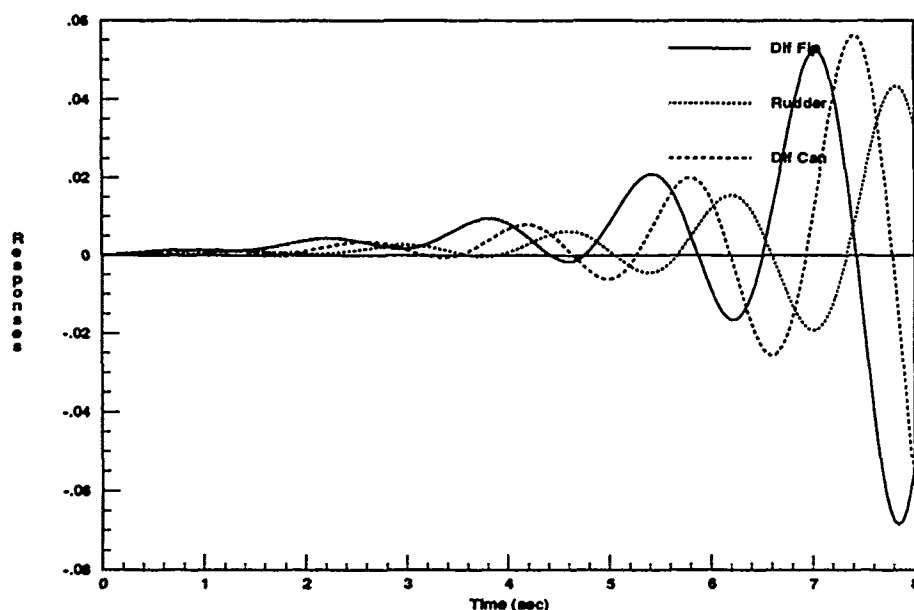


Figure 3.3. Uncompensated Open-Loop Yaw Rate Step Responses ($\alpha = 50$)

The original method involves compensating the Bode phase responses with poles and zeros to align the plots as closely as possible. This is done without shifting the RHP poles into the LHP. As shown in Figures 3.4 and 3.5, the frequency domain compensation is quite successful in aligning the phase plots. However, as pointed out in Section 3.2, the existence of the RHP poles causes the transformation integral that relates the frequency and time domains to be non-convergent. Thus, there is no guarantee that proper phase matching in the frequency domain will yield the desired results in the time domain.

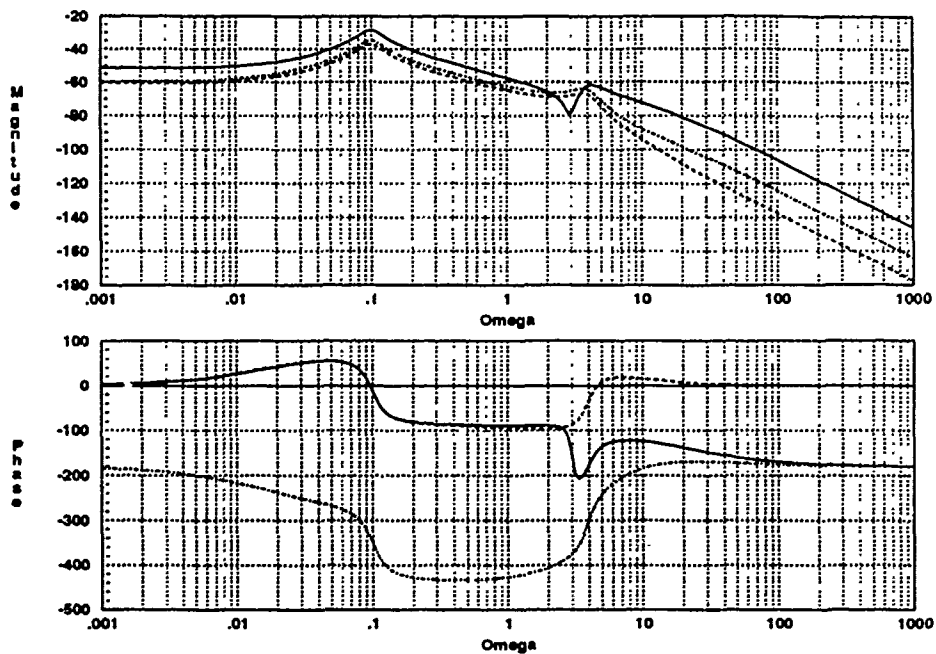


Figure 3.4. Initial Uncompensated Yaw Rate Frequency Response ($\alpha = 50$)

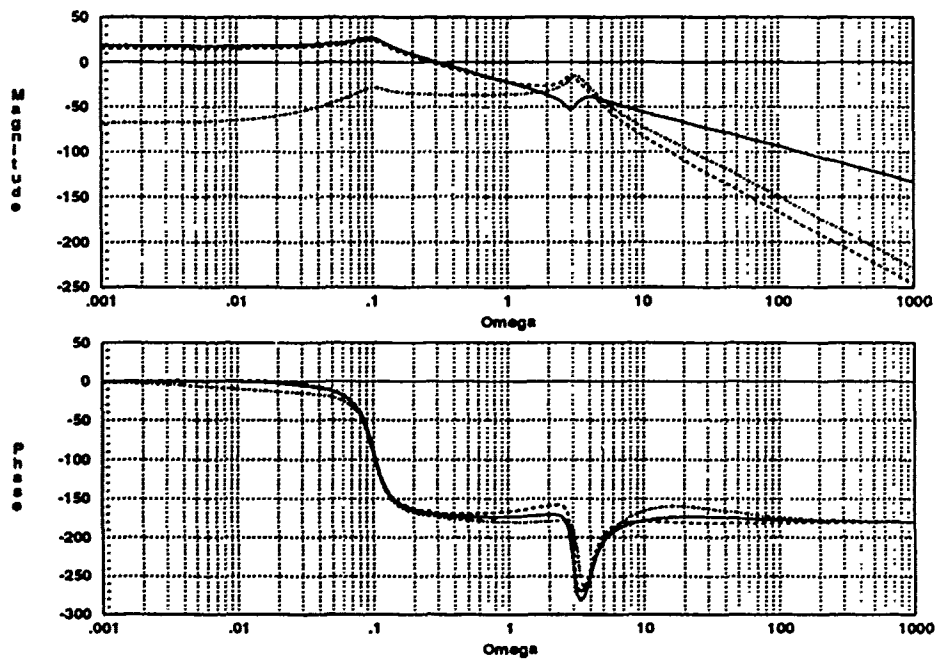


Figure 3.5. Initial Compensated Yaw Rate Frequency Response ($\alpha = 50$)

The final system resulting from the frequency domain compensation is shown in Figure 3.6. Finally, the resulting time domain responses shown in Figure 3.7 prove that good phase matching in the frequency domain is no guarantee that the time domain responses will be matched to any acceptable degree for unstable, non-minimum phase systems.

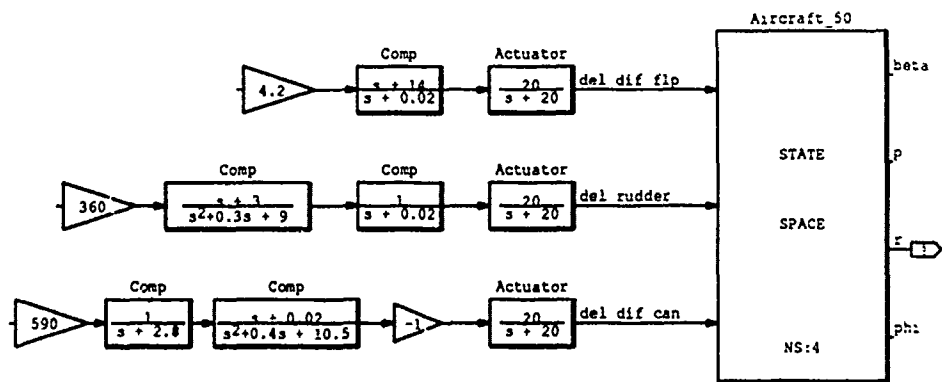


Figure 3.6. Initial Yaw Rate Compensation Block Diagram ($\alpha = 50$)

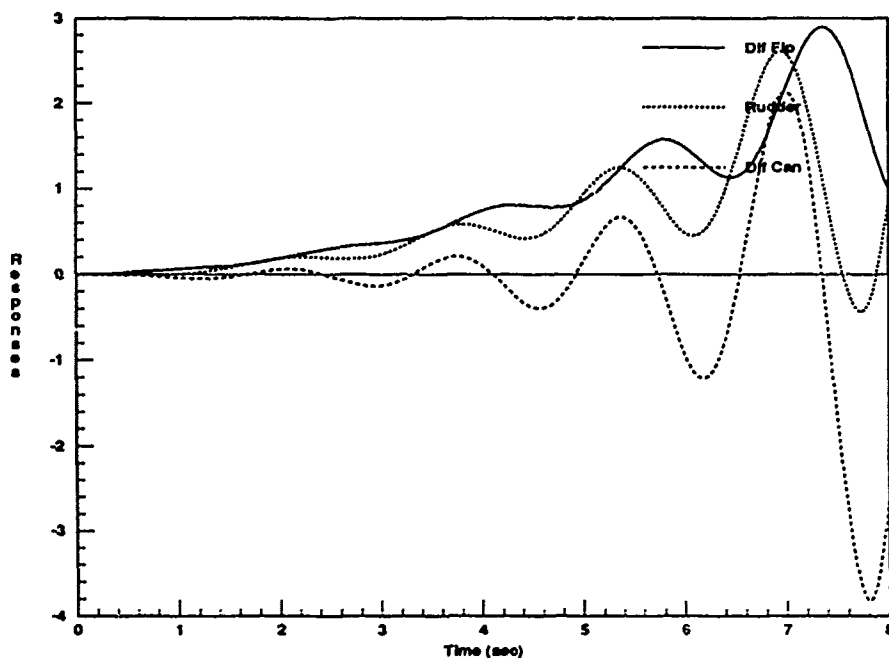


Figure 3.7. Initial Compensated Open-Loop Yaw Rate Step Responses ($\alpha = 50$)

The second method of phase compensation discussed in Section 3.2 is based on directly compensating the time response plots. Referring to Figure 3.3, the goal is to align the rudder and differential canard responses with the differential flaperon response. The rudder response is roughly 180 degrees out of phase with that of the differential flaperon. This is compensated with a negative gain value. The differential canard response is compensated by adding the Padé approximation as shown in the *System Build* block diagram (Figure 3.8). The determination of the relative weights shown in the figure is discussed in Section 3.6, and is independent of the method of phase compensation used.

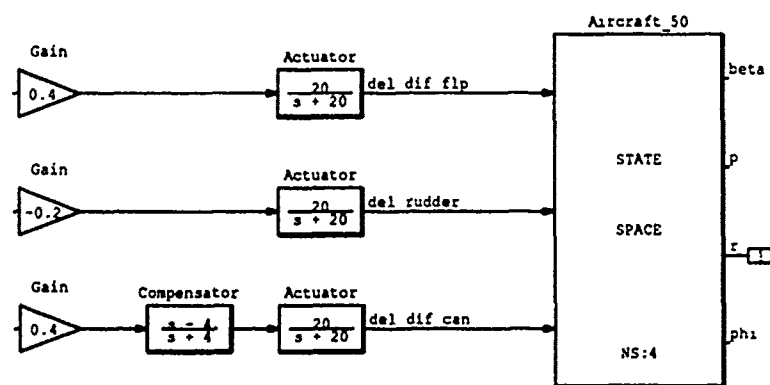


Figure 3.8. Padé Compensated Yaw Rate Block Diagram ($\alpha = 50$)

This compensation method results in fewer terms (none of which is higher than first order), and is far simpler to implement than the previously discussed frequency domain method. Furthermore, the results, at least in this case, come much closer to achieving the desired goal. However, examination of the compensated responses in Figure 3.9 reveals that the control surfaces are only working together part of the time. Note how the curves do not cross the axis simultaneously. Thus, there are times when one response takes on a positive value while another takes on a negative value. This appears to result from the drift characteristics noted earlier, indicating that there is more than just a relative time delay involved. The Padé approximation only shifts the phase of the sinusoid, but cannot compensate for a general positive or negative drift characteristic.

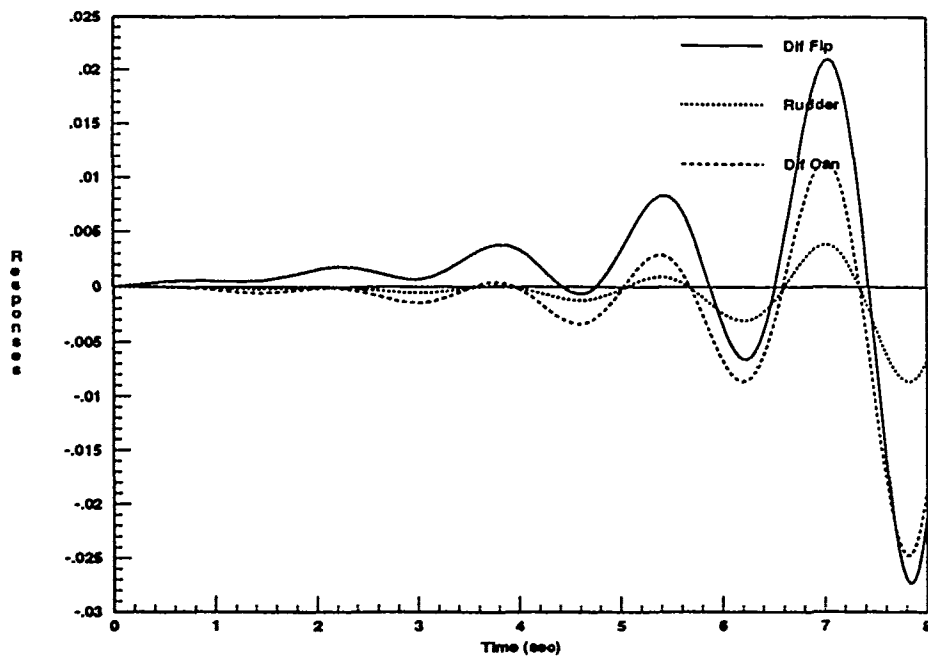


Figure 3.9. Padé Compensated Open-Loop Yaw Rate Step Responses ($\alpha = 50$)

It is useful to refer to the non-ideal composite response plots of Figures 3.7 and 3.9 when examining the successfully compensated responses for this case shown in Section 3.6. Both of the unsuccessful methods were used to develop compensation terms for the roll and yaw channels for each of the flight conditions. In general, the results are unacceptable, as shown in this one case.

3.4 Pitch Channel Compensation

For each of the flight conditions, development of the pitch channel compensation begins with analysis of the uncompensated open-loop time response plots. Throughout this task, the input is chosen to be a one degree step applied to the control surface of interest. In this section, the control input of interest is the pitch rate $[q(t)]$. Plots are obtained of the pitch rate response for each of the control surface inputs; those being symmetric canards, differential canards, symmetric flaperons, and strakes. Open-loop response plots indicate that differential canard positions have some effect (in most cases relatively small) on the aircraft's longitudinal dynamics. However, when commanded differentially, the canards have a much greater effect on

the lateral-directional modes, as would conventional ailerons. Since the most effective use of the canards as pitch control surfaces is obtained by commanding them symmetrically, it is decided to give the differential canard inputs zero weighting in the longitudinal control system. Thus, the only inputs used for controlling pitch rate are the symmetric canards and flaps, and strakes.

The uncompensated open-loop pitch rate responses for the 20 degree AOA flight condition are shown in Figure 3.10. Careful examination of the figure reveals that the differential canard and symmetric flaperon responses are on top of each other. Both have a much smaller effect on the overall response than the other two sets of control surfaces. Also evident is the fact that the symmetric flaperons and strakes require inverted inputs to make them work in phase with the symmetric canards. This is expected based on analysis of the control surface sign conventions discussed in Chapter II. It is also noted that the open-loop responses are exponentially unstable. This too is expected based on the RHP eigenvalue located on the real axis (Appendix B).

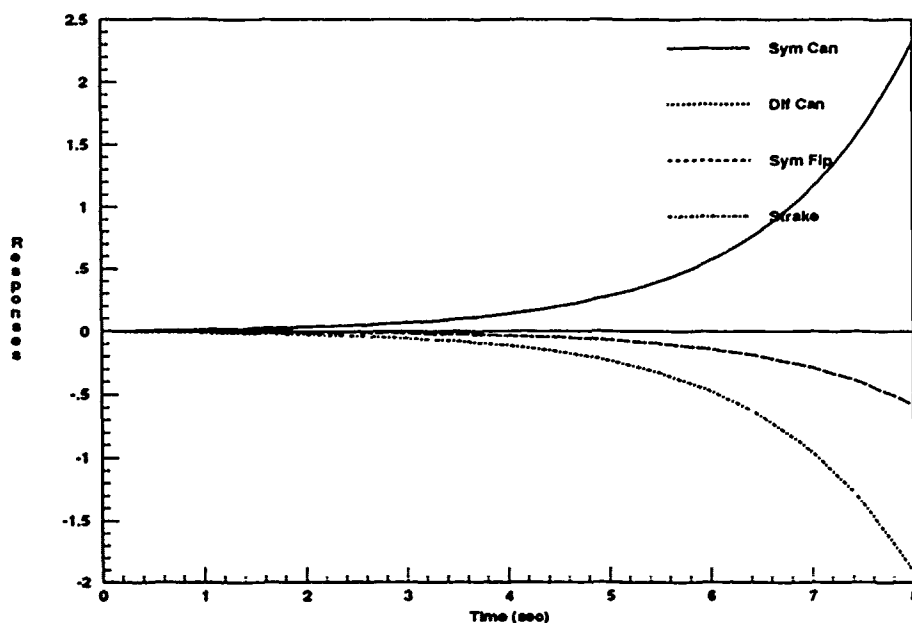


Figure 3.10. Uncompensated Open-Loop Pitch Rate Step Response ($\alpha = 20$)

The relative magnitudes chosen are roughly in proportion to those seen in the uncompensated responses, with the exception of the differential canard input which is given zero weighting. Normalizing the magnitudes, the symmetric canards are chosen to take on half of the task of pitch rate control, with the strakes picking up another 40 percent. The symmetric flaperons take care of the remaining ten percent. The qualitative analysis of the longitudinal controls presented in Section 2.3 mentions the fact that the flaperons lie roughly on the aircraft's lateral axis, and therefore have little effect on pitch control. Figure 3.11 is the *MatrixX System Build* diagram of the open-loop pitch rate control system for the 20 degree AOA flight condition. The weighting matrix compensation terms are shown preceding the actuator models and the aircraft dynamics state space model.

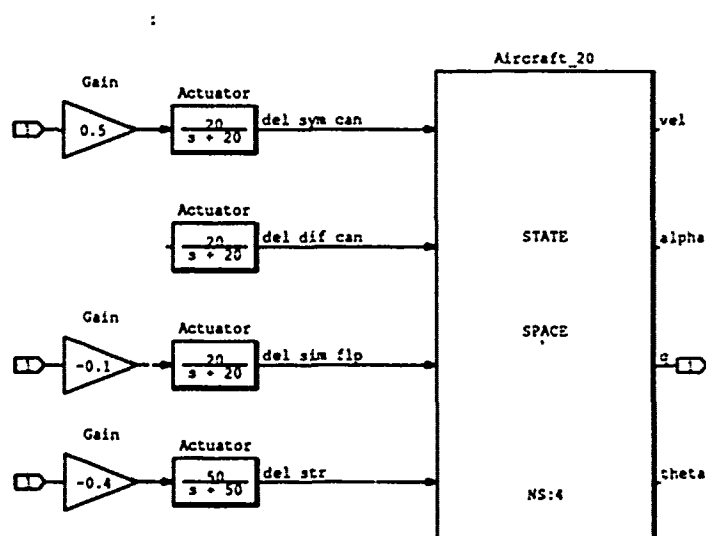


Figure 3.11. Pitch Rate Compensation Block Diagram ($\alpha = 20$)

Finally, Figure 3.12 shows the resulting *compensated* open-loop pitch rate responses for this flight condition. Clearly, the control surfaces are shown working together, and the relative magnitudes are in the desired proportions.

A similar procedure is used to develop the pitch rate compensation for the other three flight conditions. The 40 degree AOA uncompensated open-loop responses are shown in Figure 3.13. Again, the required sign changes are evident.

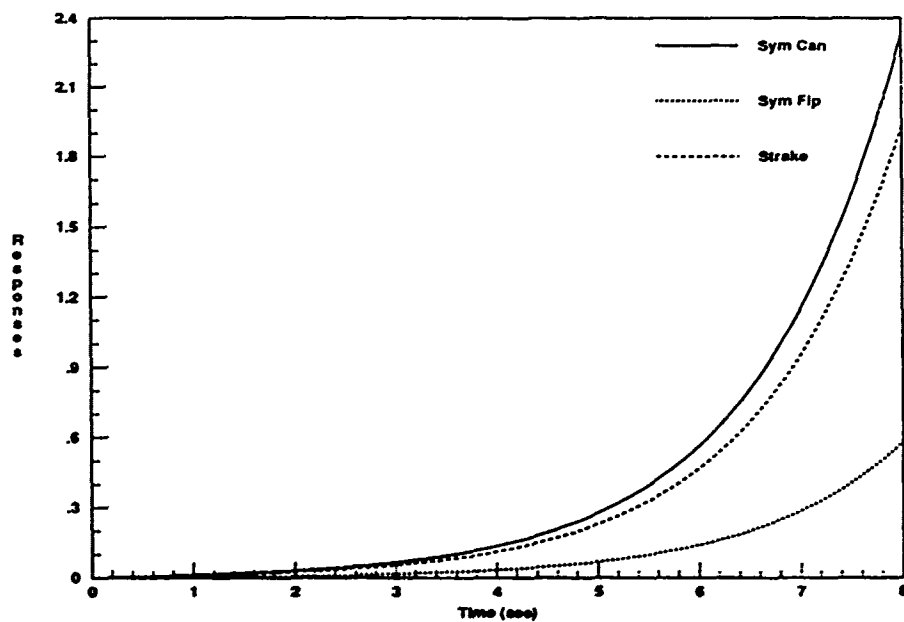


Figure 3.12. Compensated Open-Loop Pitch Rate Step Response ($\alpha = 20$)

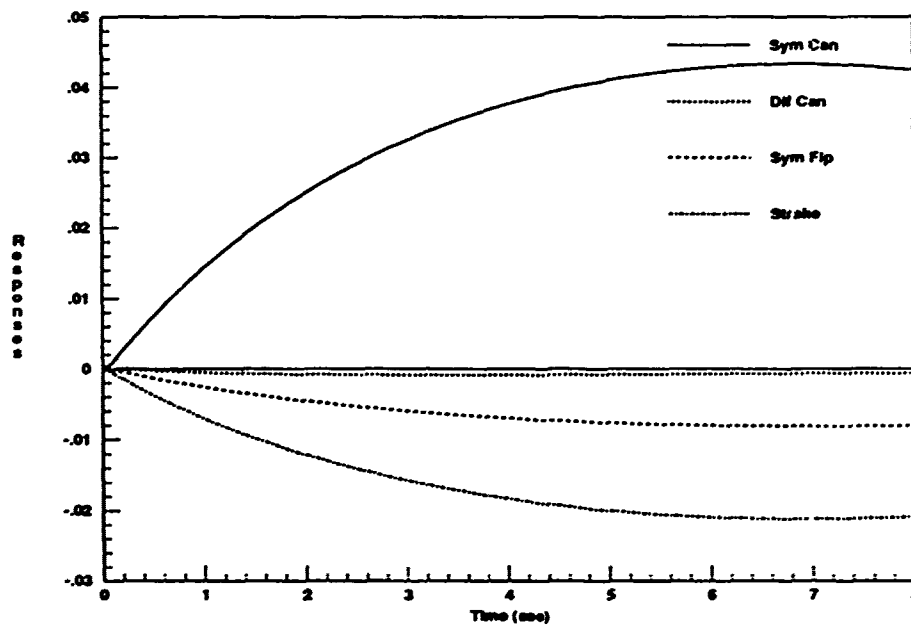


Figure 3.13. Uncompensated Open-Loop Pitch Rate Step Response ($\alpha = 40$)

The relative compensation gains are again normalized and based partially on analysis of the uncompensated response plots. For this flight condition, the strakes are noted to be slightly less effective than before, and their compensation gain is adjusted accordingly, as shown in Figure 3.14. The compensated open-loop responses for the 40 degree AOA flight condition are plotted in Figure 3.15, and show that the control surfaces are working together in the correct proportions. Note that although the compensation gain terms are normalized for each case, the magnitudes of the responses do not necessarily add to one. For this task, only the *relative* magnitudes are important.

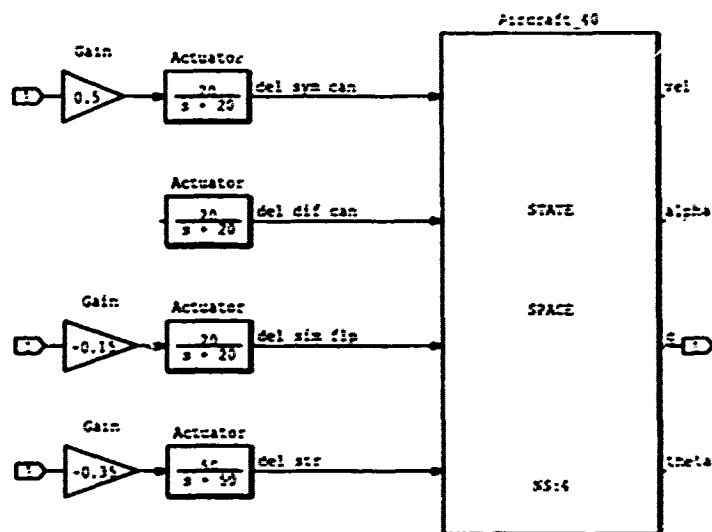


Figure 3.14. Pitch Rate Compensation Block Diagram ($\alpha = 40$)

The 50 degree AOA response plots look virtually the same as those of the previous flight condition. Again, a slight adjustment is made to the relative compensation gains, based on the analysis of the uncompensated response plots. Figures 3.16 through 3.18 pertain to this flight condition.

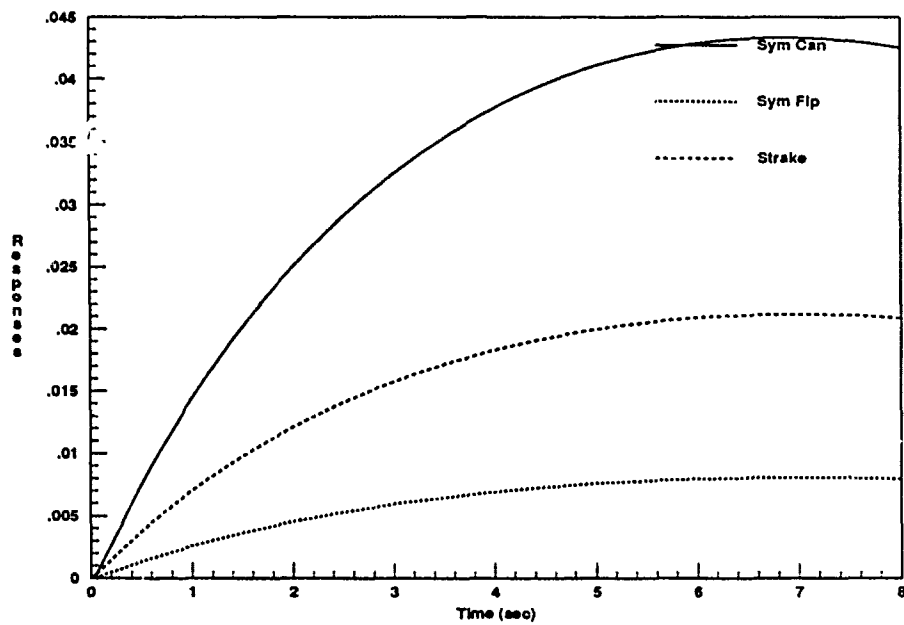


Figure 3.15. Compensated Open-Loop Pitch Rate Step Response ($\alpha = 40$)

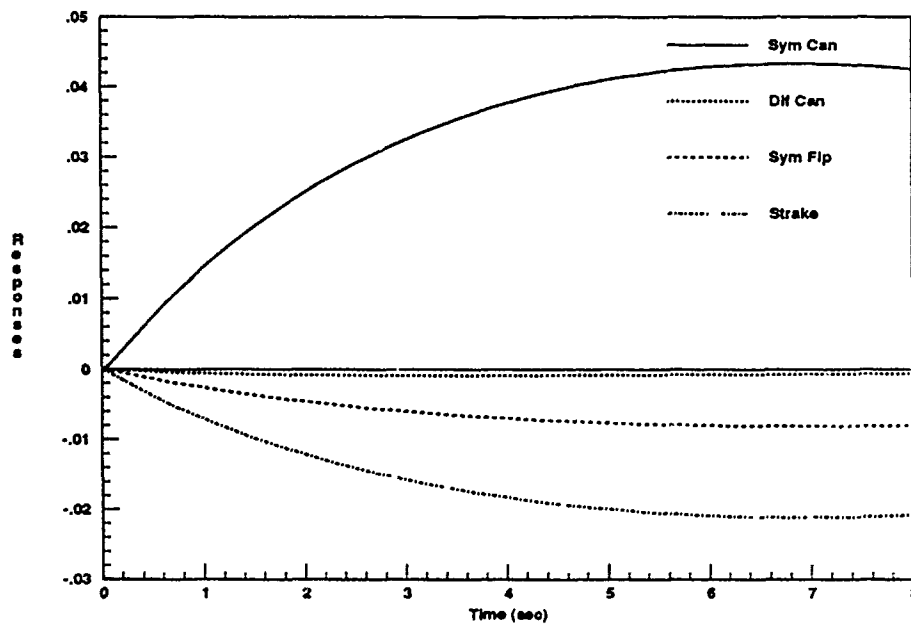


Figure 3.16. Uncompensated Open-Loop Pitch Rate Step Response ($\alpha = 50$)

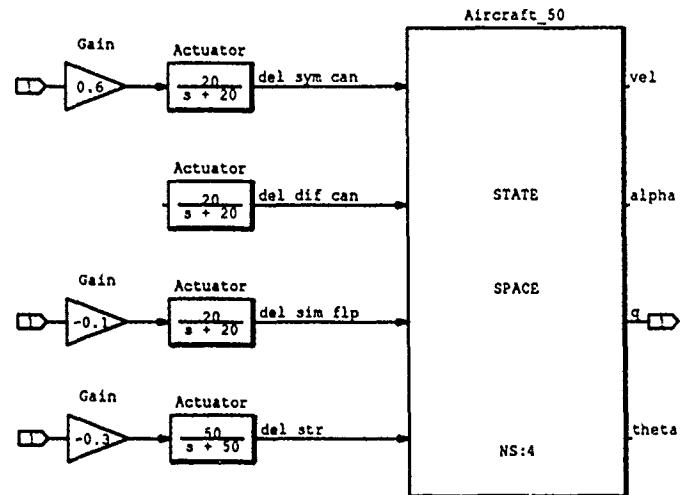


Figure 3.17. Pitch Rate Compensation Block Diagram ($\alpha = 50$)

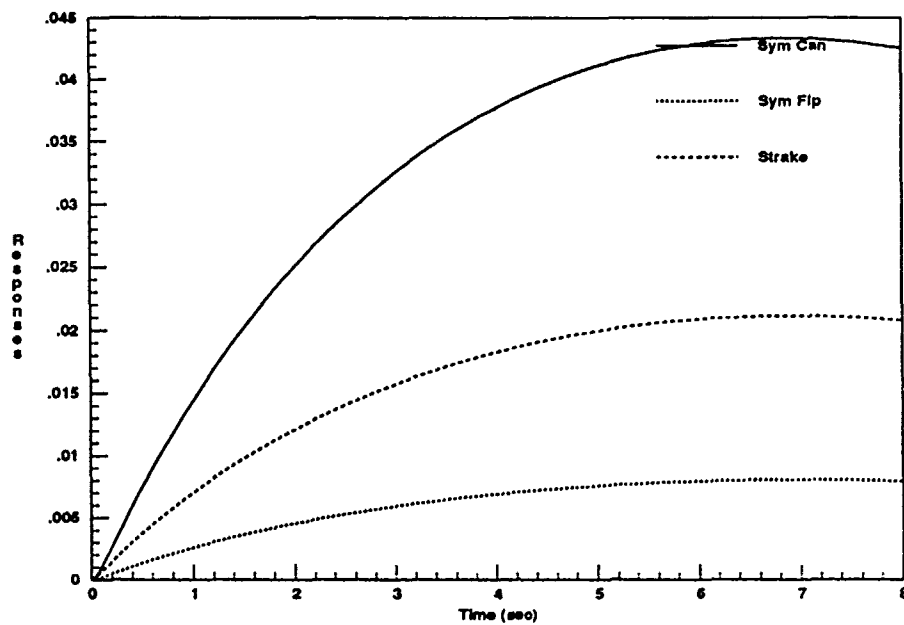


Figure 3.18. Compensated Open-Loop Pitch Rate Step Response ($\alpha = 50$)

The uncompensated response plots for the sixty degree flight condition are shown in Figure 3.19. Analysis of these plots indicates that the responses are highly sinusoidal in nature with a very slowly decreasing magnitude. Again, based on the eigenvalues listed in Appendix B, this is not surprising. For this condition, all four open-loop state space eigenvalues are just inside the LHP, and are expected to result in a stable system. Note that since the eigenvalues are so close to the $j\omega$ axis, the exponential decay time constant is extremely large, resulting in a very slow decay to steady state. The differential canard effects are more noticeable for this flight condition, but as previously discussed, this input is not commanded in the longitudinal flight control system. The remaining three longitudinal control inputs are used to control pitch rate, and are expected to have sufficient control authority to counteract unwanted coupling effects from the lateral-directional channels.

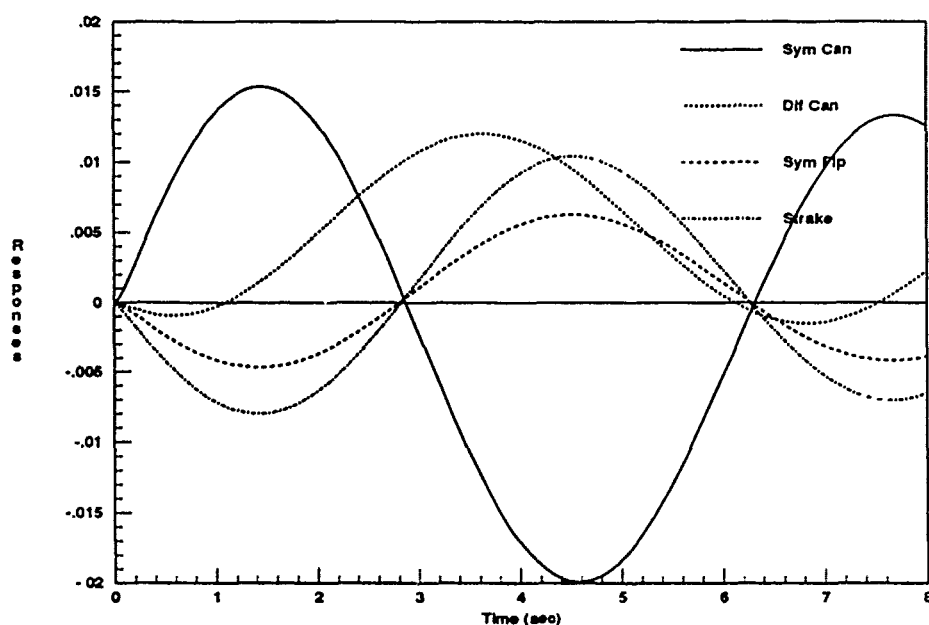


Figure 3.19. Uncompensated Open-Loop Pitch Rate Step Response ($\alpha = 60$)

The relative gain compensation is determined as before, and the compensated system block diagram is shown in Figure 3.20. The final step responses are shown working together in Figure 3.21. The character of the open-loop responses is not important; only the fact that all surfaces are either positive or negative valued at the same time.

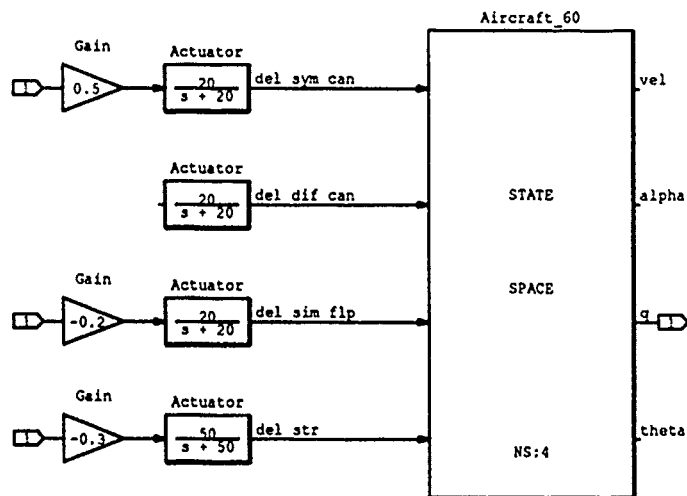


Figure 3.20. Pitch Rate Compensation Block Diagram ($\alpha = 60$)

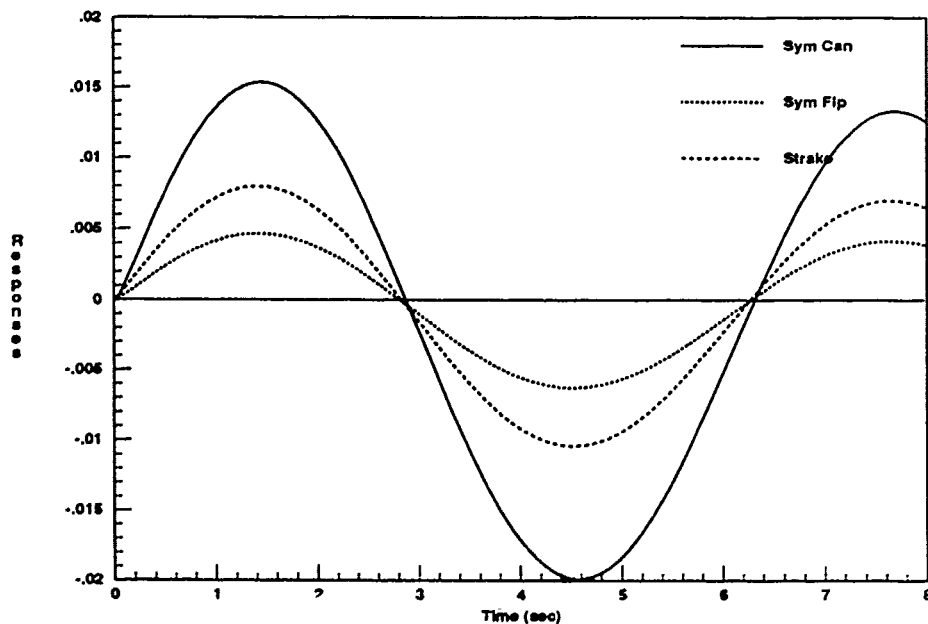


Figure 3.21. Compensated Open-Loop Pitch Rate Step Response ($\alpha = 60$)

3.5 Roll Channel Compensation

Although the roll and yaw channels are both in the lateral-directional control mode, they are discussed separately for the purposes of developing the weighting matrix. The compensation terms are developed independently for the two channels, since each term is based on the relationship between a single control variable and a single commanded control surface input. After all the individual compensation terms are developed, the roll and yaw channels are combined with overall gain adjustments to form the lateral-directional weighting matrices. This is discussed in Section 3.7.

As with the pitch channel, the roll channel compensation begins with analysis of the uncompensated open-loop time response plots. The control variable is the roll rate $[p(t)]$, and the three control surface inputs are differential flaperons, rudder, and differential canards. Examination of Figure 3.22 reveals the complexity of the lateral-directional compensation problems. Note that the exponentially unstable sinusoidal response plots are clearly out of phase with each other. In addition, the individual response magnitudes are not centered about zero. Thus, it would appear quite difficult to force the three responses to work together continuously.

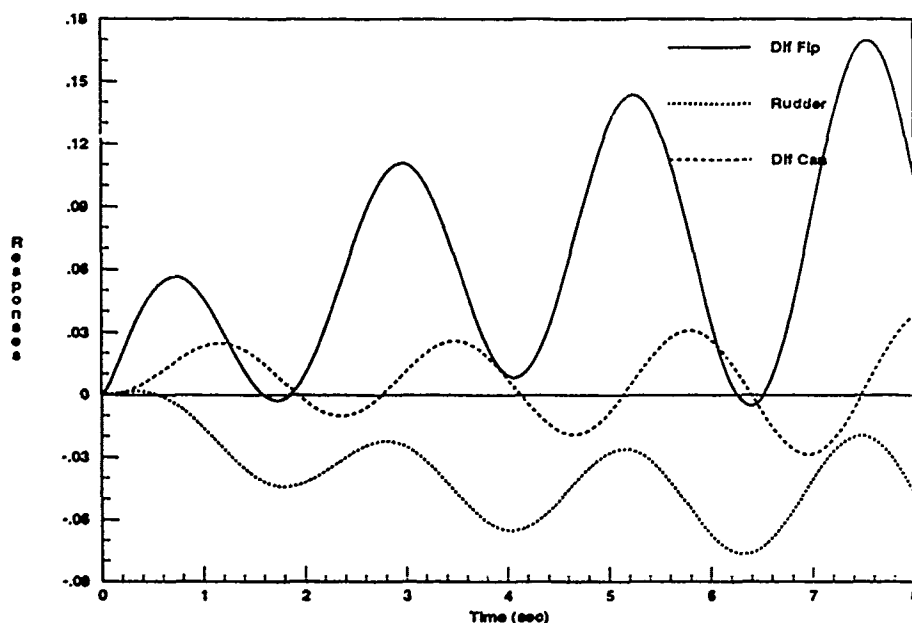


Figure 3.22. Uncompensated Open-Loop Roll Rate Step Responses ($\alpha = 20$)

The development of the 20 degree AOA roll rate compensation is now detailed in a step-by-step manner. The first step is to generate the combined state space model and obtain the roots of that system. These roots are those of the state space dynamics model with the actuator transfer functions included. The roots are obtained from *System Build*, and are listed in Table 3.1. Note that the numerator is different for each control input, but all three share a common denominator.

roots(n1)	roots(n2)	roots(n3)	roots(d)
0.0442	0.0443	0.0288	0.0058
-1.0	-1.0	-0.079	-0.3239
-0.0693±j1.3782	-3.0	-1.0	-1.0
-3.0	-3.7614	-3.0	.1288±j2.7262
-20.0	4.1217	-20.0	-3.0
-20.0	-20.0	-20.0	-20.0
	-20.0	42.9318	-20.0
			-20.0

Table 3.1. Uncompensated Roll Rate System Roots ($\alpha = 20$)

As discussed in Section 3.2, the phase compensation approach for such unstable plants is to shift the roots by an amount sufficient to temporarily eliminate all RHP poles. In this case, the roots are shifted to the left by subtracting 0.2 from the real portion of each. Reference to Table 3.1 indicates that shifting the roots by 0.13 results in a stable shifted system. The roots are shifted more than the minimum required amount to provide a slightly greater stability margin, thus allowing for possible roundoff or computational accuracy errors. The shifted roots, now representing a stable system, are used to generate a composite Bode plot (Figure 3.23). Next, pole/zero compensation terms are added as needed to match the three phase plots as closely as possible with each other (Figure 3.24).

The general procedure for adding phase compensation is now described for this particular case. Referring to Figure 3.23, the concern at this time is only with the phase portion of the Bode plots. Beginning at the low frequency end, it is seen that the second and third responses lag the first by 180 degrees. This is easily compensated with a negative gain value on the second and third inputs.

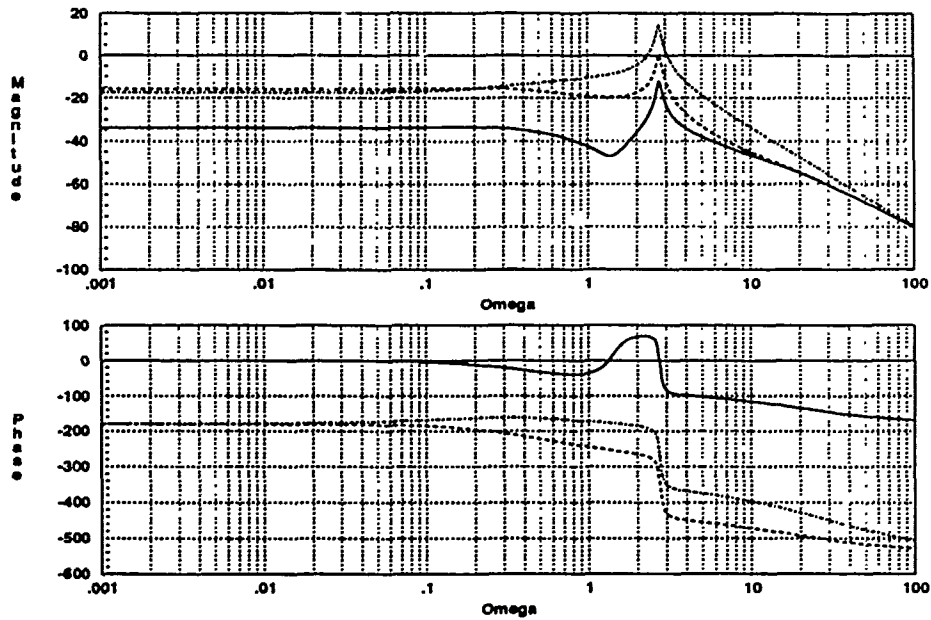


Figure 3.23. Uncompensated *Shifted* Roll Rate Frequency Response ($\alpha = 20$)

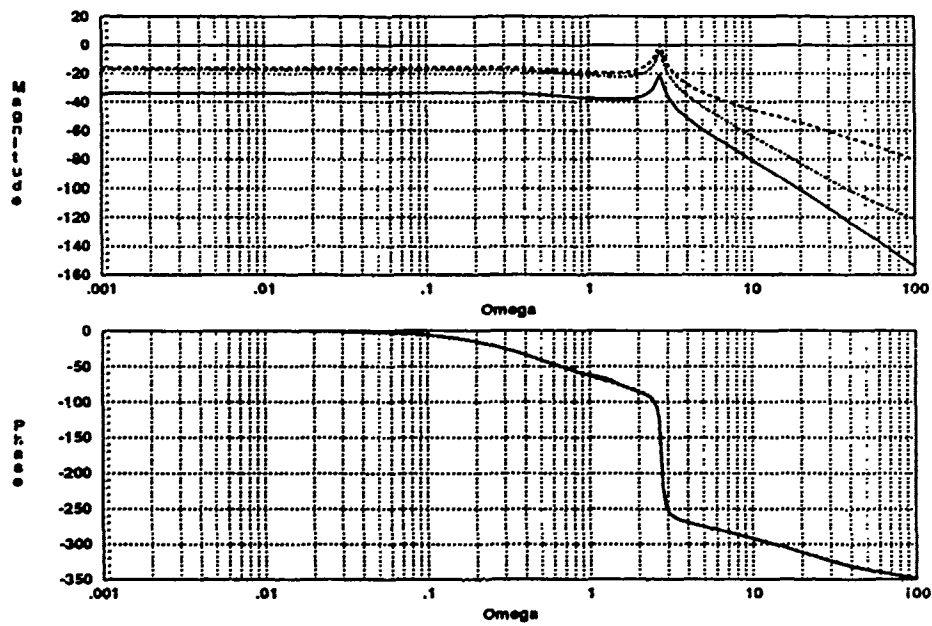


Figure 3.24. Compensated *Shifted* Roll Rate Frequency Response ($\alpha = 20$)

Next, the third input needs to be *bent down* to coincide with the second. This is accomplished by adding a pole (giving phase lag) at $\omega = 0.3$ and a zero (giving phase lead) at $\omega = 40$. By introducing phase lag at one frequency and cancelling that amount with phase lead at a higher frequency, the phase plot is bent down slightly without changing the steady state value. The specific values of the compensator poles and zeros are obtained in an iterative fashion as required to achieve the desired results.

The first response is somewhat more difficult to compensate. It is noted that this response requires 180 degrees of additional phase lag in steady state. This can be accomplished by adding a second order pair of poles. By using a second order compensator, the ζ and ω_n values can be adjusted in such a way to virtually eliminate the *hump* centered around $\omega = 2$. In this case, it is found that using $(s^2 + 0.5s + 2)$ for the compensator poles results in the desired response shape. Since the system is shifted into the LHP, only LHP compensation elements are added. However, when the system is shifted back to the original reference frame, in some cases the compensator elements *may* become RHP elements.

The roots of the compensated *shifted* system are obtained and shifted back by adding 0.2 to the real portion of each. The resulting compensated system roots are listed in Table 3.2. Note that due to the compensation terms, the three transfer functions no longer share a common denominator.

roots(n1)	roots(n2)	roots(n3)	roots(d1)	roots (d2)	roots (d3)
0.0442	0.0443	0.0288	0.0058	0.0058	0.0058
-1.0	-1.0	-0.079	-0.3239	-.3239	-.3239
-0.0693±j1.3782	-3.0	-1.0	-1.0	-1.0	-1.0
-3.0	-3.7614	-3.0	.1288±j2.7262	.1288±j2.7262	.1288±j2.7262
-20.0	4.1217	-20.0	-3.0	-3.0	-3.0
-20.0	-20.0	-20.0	-20.0	-20.0	-20.0
	-20.0	42.9318	-20.0	-20.0	-20.0
		-39.8	-20.0	-20.0	-20.0
			-0.05±j1.3919		-0.1

Table 3.2. Compensated Roll Rate System Roots ($\alpha = 20$)

The compensated system roots are convolved into polynomial transfer functions and the step responses are obtained. After including necessary sign corrections, the response plots are generated in a *strip* format without gain correction (Figure 3.25). As a check, the phase compensation terms are included into the *System Build* diagram and a similar set of step response plots is obtained. These responses look like those in Figure 3.25, but are generated directly from the *System Build* simulation, rather than the derived transfer functions.

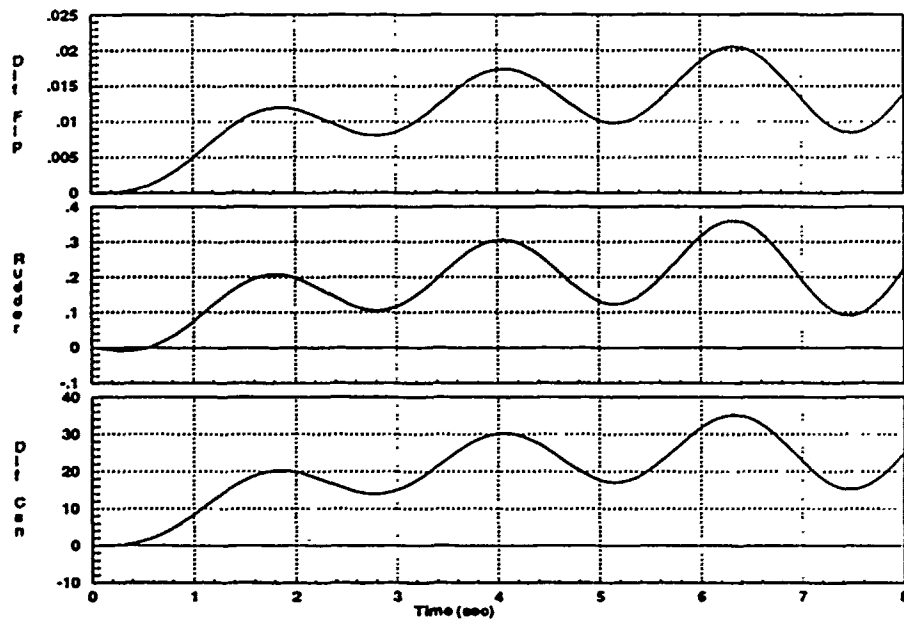


Figure 3.25. Compensated Open-Loop Roll Rate Step Responses ($\alpha = 20$)

The final step is to develop the relative gain terms. The responses shown in Figure 3.25 are first individually normalized, and then multiplied by the desired relative weighting factors. In this case, the differential flaperons and differential canards each handle 40 percent of the task, and the rudder takes on the remaining 20 percent. Note that the rudder has limited effect on roll rate control, as is typical of most aircraft. The block diagram of the final compensated system is shown in Figure 3.26. The final composite step responses reveal that all three control surfaces are working together continuously, and in the desired relative proportions (Figure 3.27). The effectiveness of this compensation technique is demonstrated by comparing the compensated responses shown in Figure 3.27 with the uncompensated ones shown in Figure 3.22.

Finally, to aid others who may need to accomplish similar phase compensation, Appendix G describes a sample *MatrixX* executable file that may be used to perform some of the steps discussed in this section. What is listed is not computer code: simply a brief, commented list of standard commands. A general working knowledge of *MatrixX* and *System Build* is assumed.

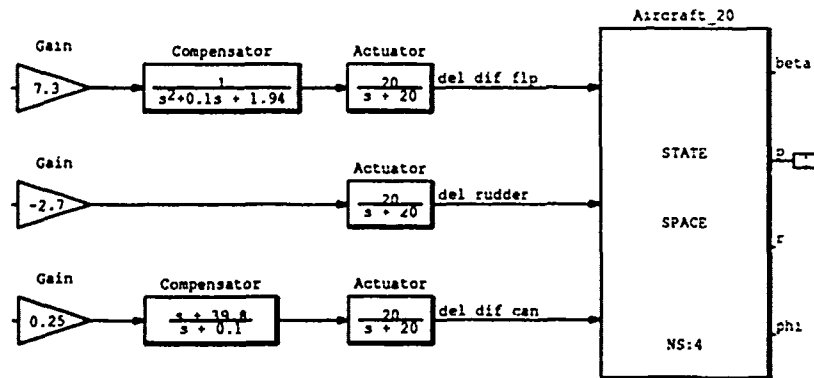


Figure 3.26. Roll Rate Compensation Block Diagram ($\alpha = 20$)

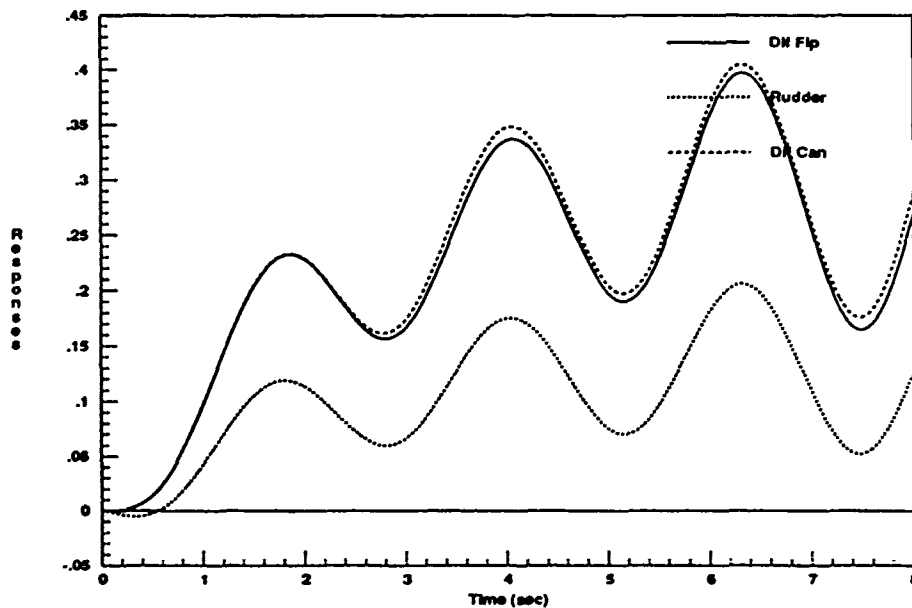


Figure 3.27. Final Compensated Open-Loop Roll Rate Step Responses ($\alpha = 20$)

The other flight conditions are handled in a similar manner. However, it is useful to provide a brief discussion of each case, due to some of the differences encountered. For instance, it is noted in Figure 3.28 that the uncompensated responses have a somewhat different appearance from those previously seen. Based on the different aerodynamic characteristics of the higher AOA flight condition, this is not surprising. Here the responses are shown to rapidly increase exponentially, and again, the sinusoids are out of phase with each other. However, the responses for this flight condition are at least relatively symmetric about zero.

The roots are shifted as before, and the necessary pole/zero compensation terms are added to align the Bode phase plots (Figures 3.29 & 3.30). The roots of the compensated system are shifted back and the strip plots are obtained to verify the phase characteristics. The relative gains are obtained as before, except that the desired relative weights are altered slightly (Figure 3.31). For this flight condition (as well as the 50 and 60 degree cases), the rudder is only used to control 10 percent of the commanded roll rate, with the other two surfaces handling 45 percent each. The final compensation is shown in Figure 3.32, and the desired responses appear in Figure 3.33. Finally, the compensated roll rate system roots for this flight condition are listed in Table 3.3.

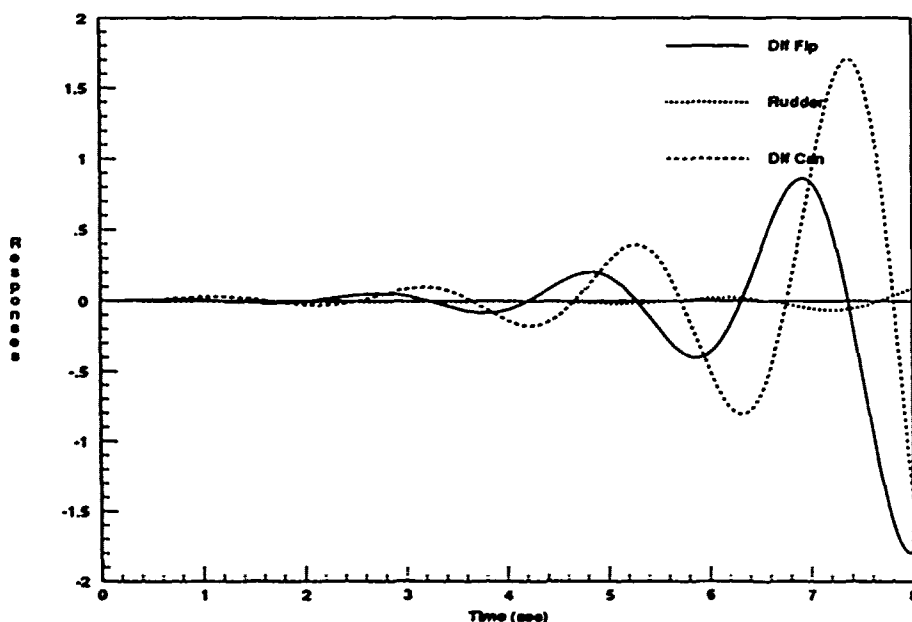


Figure 3.28. Uncompensated Open-Loop Roll Rate Step Responses ($\alpha = -40$)

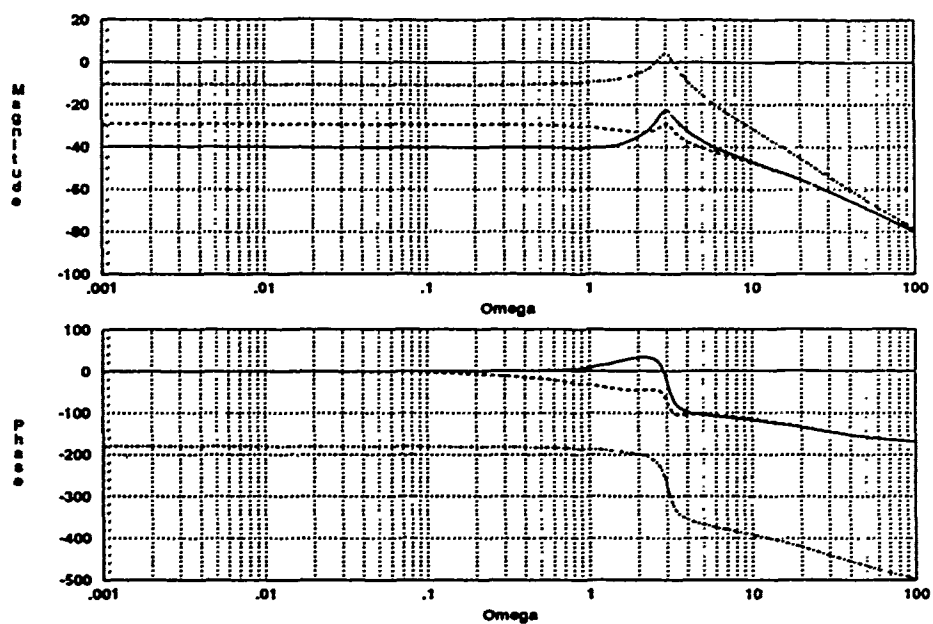


Figure 3.29. Uncompensated *Shifted* Roll Rate Frequency Response ($\alpha = 40$)

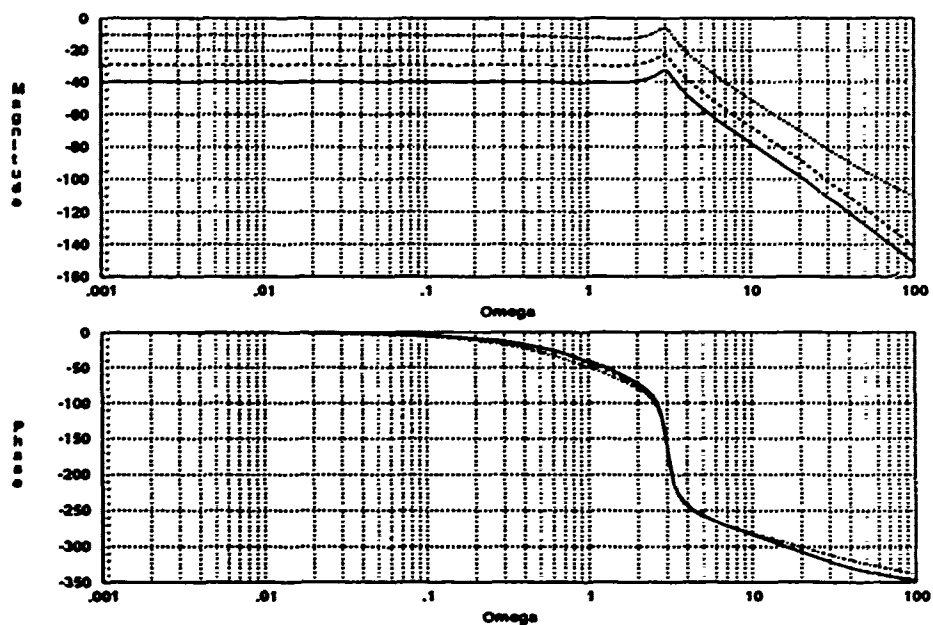


Figure 3.30. Compensated *Shifted* Roll Rate Frequency Response ($\alpha = 40$)

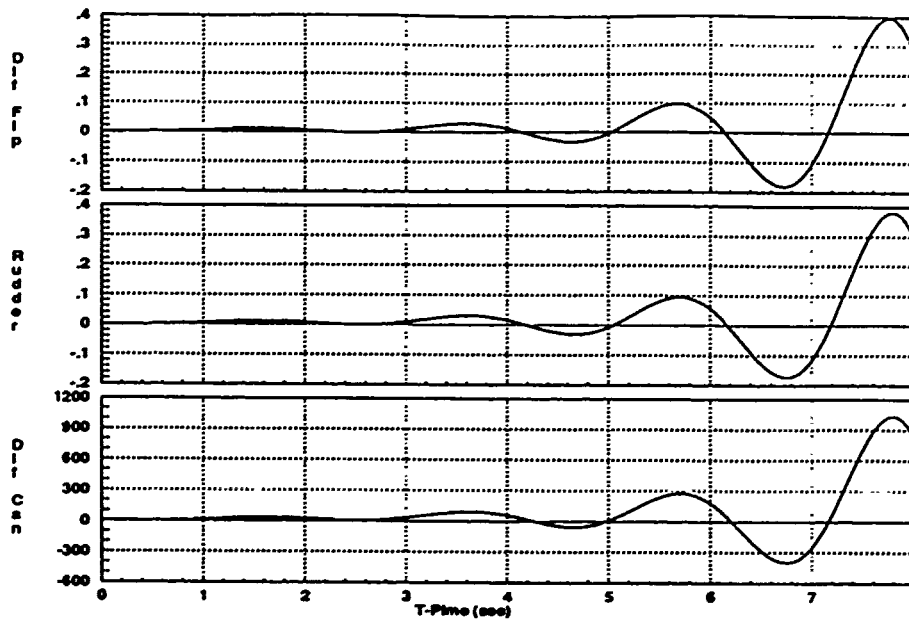


Figure 3.31. Compensated Open-Loop Roll Rate Step Responses ($\alpha = 40$)

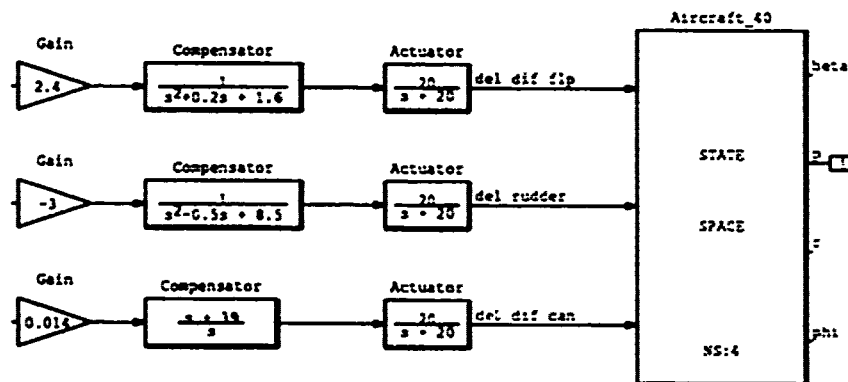


Figure 3.32. Roll Rate Compensation Block Diagram ($\alpha = 40$)

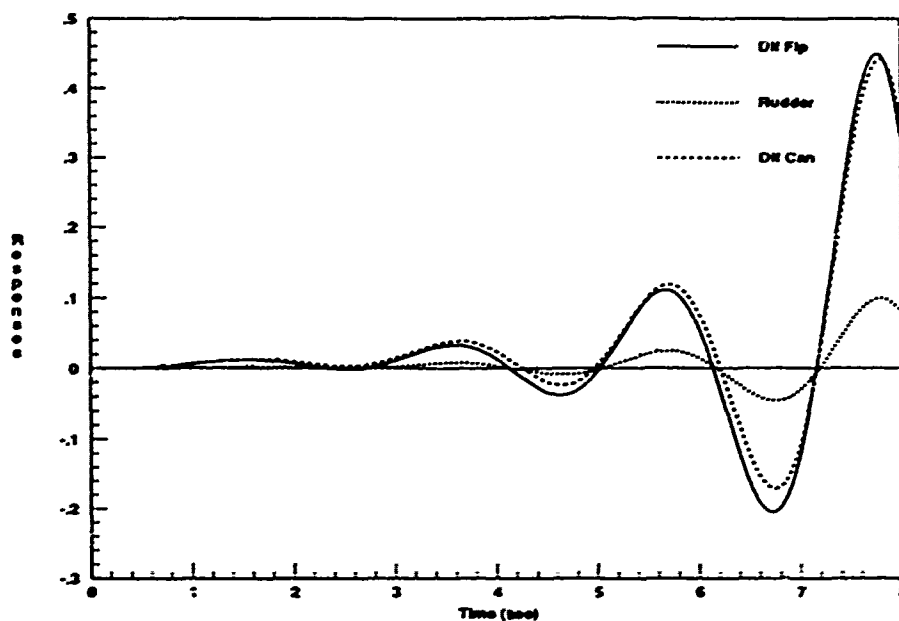


Figure 3.33. Final Compensated Open-Loop Roll Rate Step Responses ($\alpha = 40$)

roots(n1)	roots(n2)	roots(n3)
0.1304	0.1325	0.0363
$-0.0731 \pm j1.2303$	$0.2767 \pm j2.9412$	-0.1768
-20.0	-20.0	-20.0
-20.0	-20.0	-20.0
		-39.0
		60.0083
roots(d1)	roots (d2)	roots (d3)
$-0.0808 \pm j0.1561$	$-0.0808 \pm j0.1561$	0
$-0.1 \pm j1.2610$	$0.25 \pm j2.9047$	$-0.0808 \pm j0.1561$
$0.7098 \pm j3.0081$	$0.7098 \pm j3.0081$	$0.7098 \pm j3.0081$
-20.0	-20.0	-20.0
-20.0	-20.0	-20.0
-20.0	-20.0	-20.0

Table 3.3. Compensated Roll Rate System Roots ($\alpha = 40$)

The 50 degree uncompensated roll rate responses are similar in form to those obtained for the 40 degree case. Again, the sinusoids are out of phase with each other, but symmetric about zero (Figure 3.34). The uncompensated Bode plots are shown in Figure 3.35. Initially, the compensation terms are added to match the Bode phase plots precisely, as before. However, the phase response characteristics shown in the strip response plots are not as close as desired. Since the relative time responses are used as the criteria for developing effective compensation, the responses in Figure 3.37 have been *optimized* by fine-tuning the compensation parameters. This is done at the expense of the frequency response phase characteristics (Figure 3.36) by varying the ζ and ω_n parameters while observing the strip responses so that the plots are all positive and negative at the same time.

The same relative weightings are applied to this case as used for the 40 degree flight condition. Figure 3.38 shows the compensated open-loop system, and the compensated responses are shown in Figure 3.39. Table 3.4 lists the compensated system roots for this case.

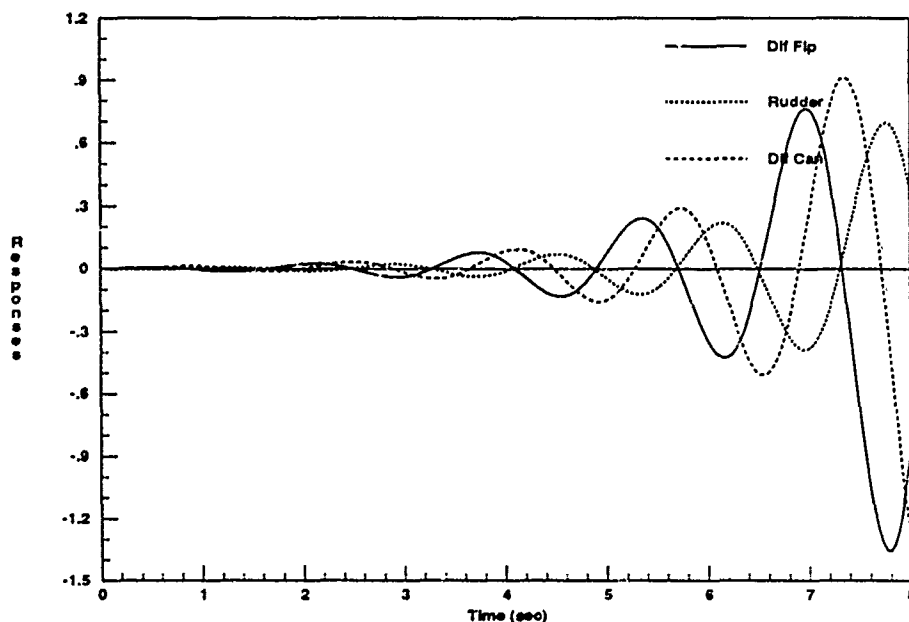


Figure 3.34. Uncompensated Open-Loop Roll Rate Step Responses ($\alpha = 50$)

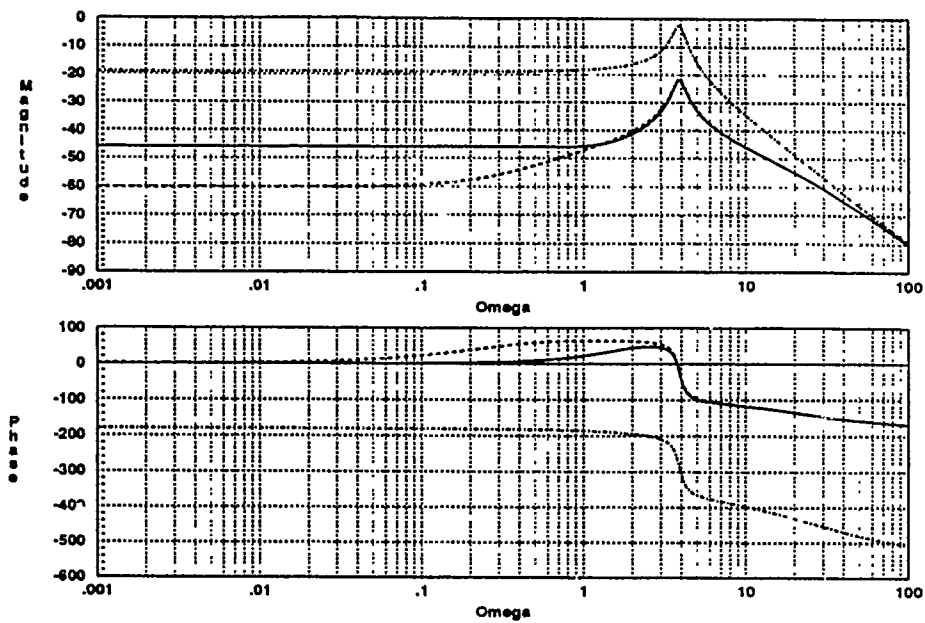


Figure 3.35. Uncompensated *Shifted* Roll Rate Frequency Response ($\alpha = 50$)

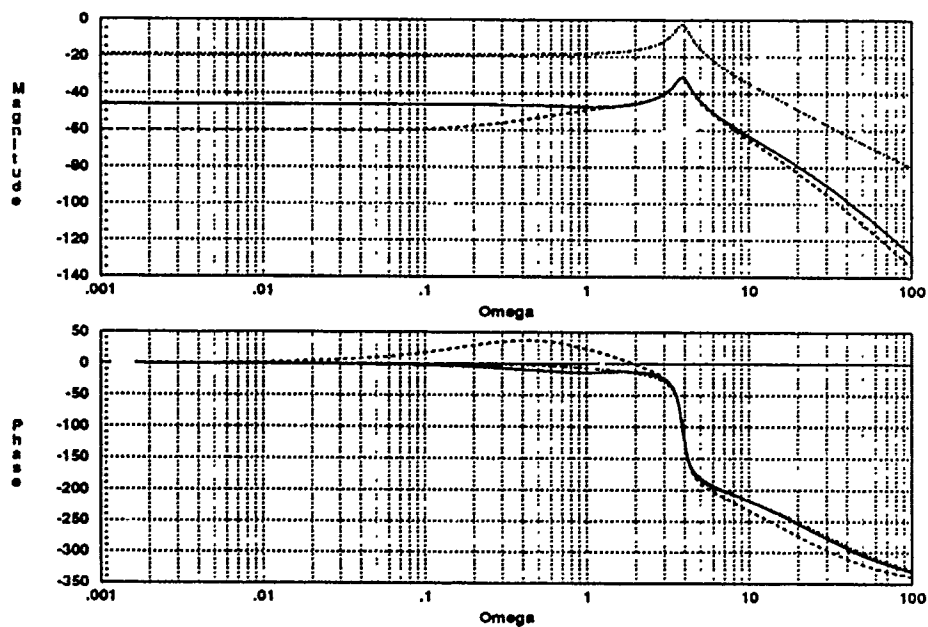


Figure 3.36. Compensated *Shifted* Roll Rate Frequency Response ($\alpha = 50$)

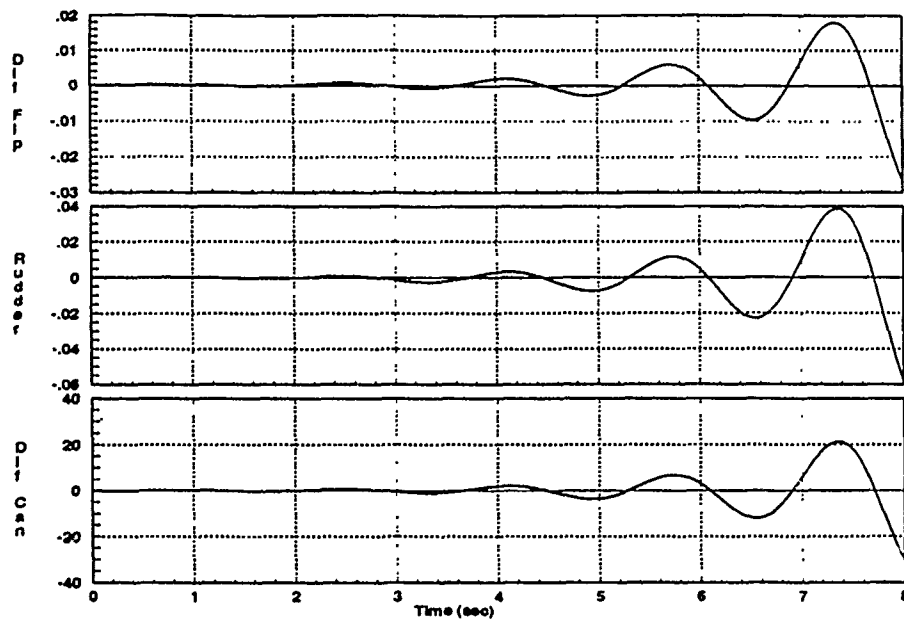


Figure 3.37. Compensated Open-Loop Roll Rate Step Responses ($\alpha = 50$)

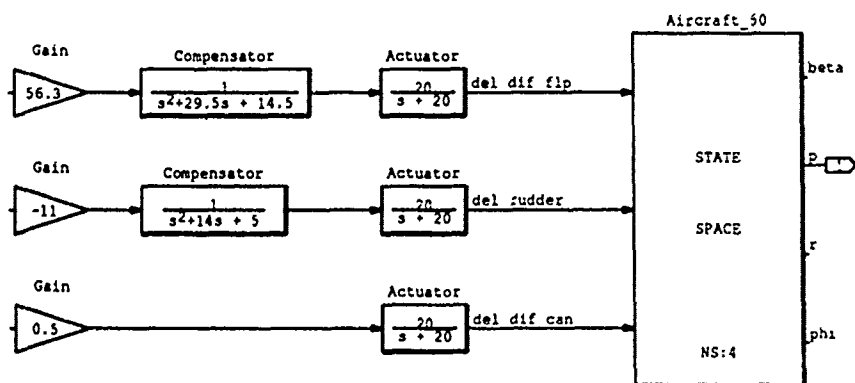


Figure 3.38. Roll Rate Compensation Block Diagram ($\alpha = 50$)

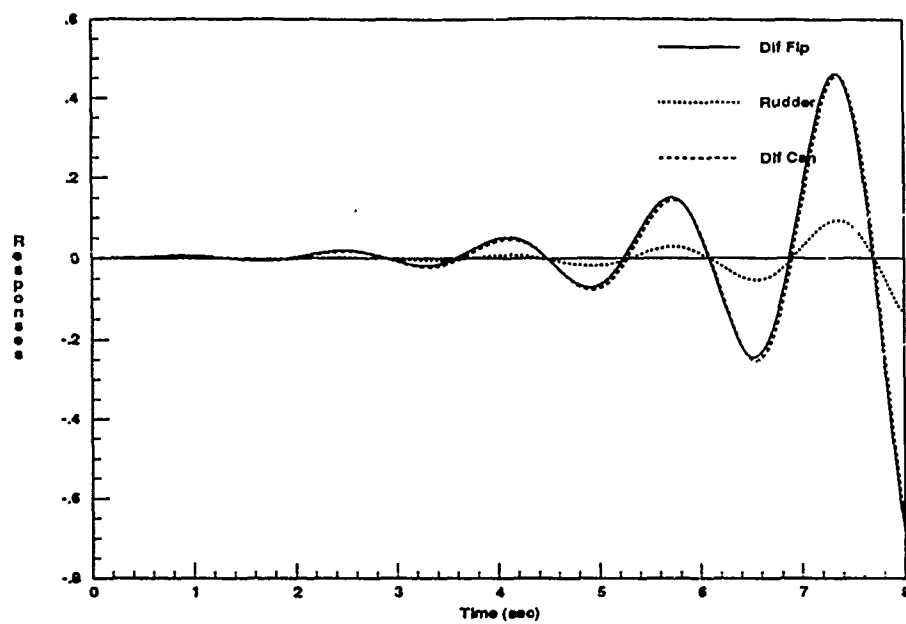


Figure 3.39. Final Compensated Open-Loop Roll Rate Step Responses ($\alpha = 50$)

roots(n1)	roots(n2)	roots(n3)
0.1862	0.7720	0.1075
-0.1064±j0.9131	0.1956	-0.1628
-20.0	-0.7837	-20.0
-20.0	-20.0	-20.0
	20.0	36.9255
roots(d1)	roots (d2)	roots (d3)
-0.0190±j0.0977	-0.0190±j0.0977	-0.0190±j0.0977
-0.5	-0.3668	0.7143±j3.8832
0.7143±j3.8832	0.7143±j3.8832	-20.0
-20.0	-13.6332	-20.0
-20.0	-20.0	-20.0
-20.0	-20.0	
-29.0	-20.0	

Table 3.4. Compensated Roll Rate System Roots ($\alpha = 50$)

The uncompensated 60 degree roll rate responses look quite different from any of those previously encountered (Figure 3.40). There is very little exponential growth of the sinusoids. This is not surprising when one examines the eigenvalues for this case (Appendix B). The real portions of the RHP roots are very small in magnitude, so the system is only slightly unstable, but highly oscillatory. The shifted Bode plots (Figures 3.41 & 3.42) reveal that once again, the *optimal* design for the time response characteristics results in a non-optimal set of phase plots in the frequency domain.

Close examination of the strip response plots in Figure 3.43 reveals that even though the third plot appears quite different from the other two, the waves are all in phase with each other and take on positive and negative values at the same times. The same relative control surface weighting is used as before, and the compensated system is shown in Figure 3.44. The composite response plots in Figure 3.45 show that the control surfaces are working together, and the compensated system roots are listed in Table 3.5.

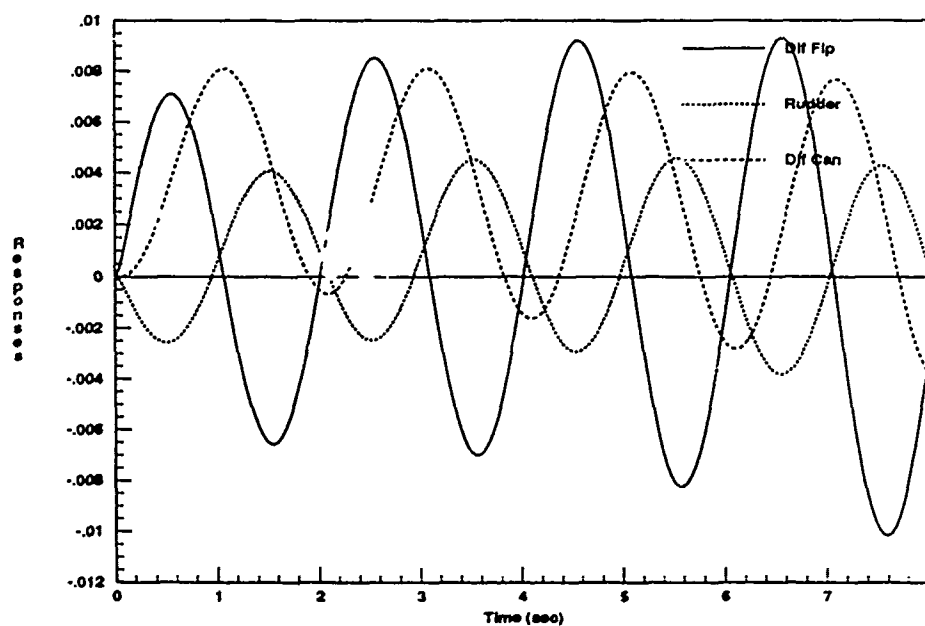


Figure 3.40. Uncompensated Open-Loop Roll Rate Step Responses ($\alpha = 60$)

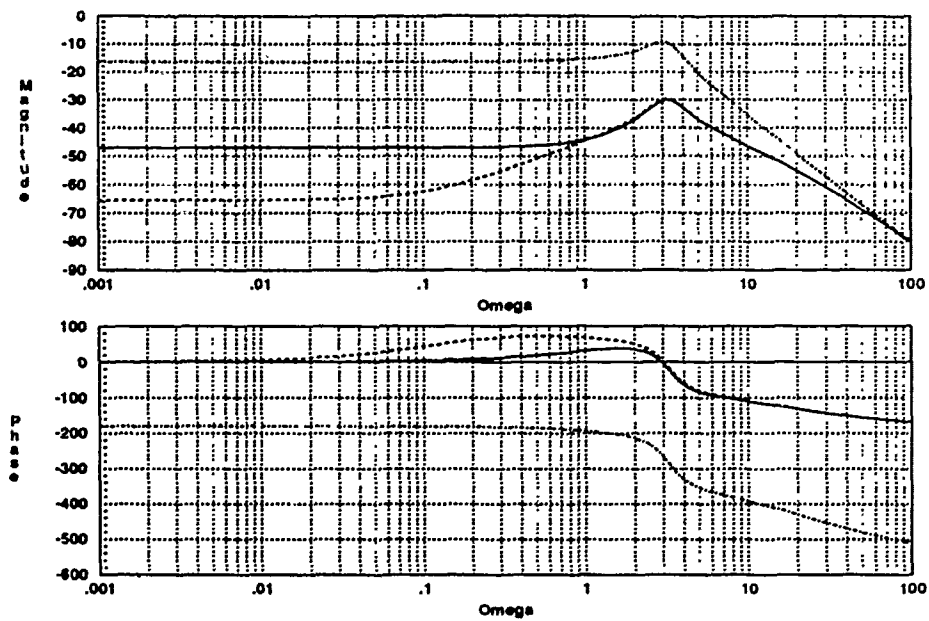


Figure 3.41. Uncompensated *Shifted* Roll Rate Frequency Response ($\alpha = 60$)

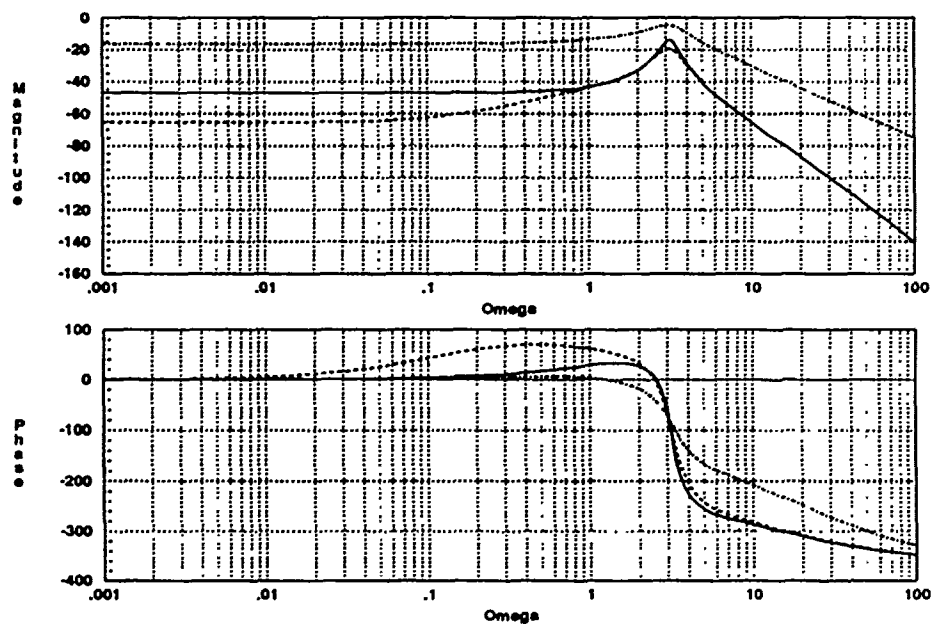


Figure 3.42. Compensated *Shifted* Roll Rate Frequency Response ($\alpha = 60$)

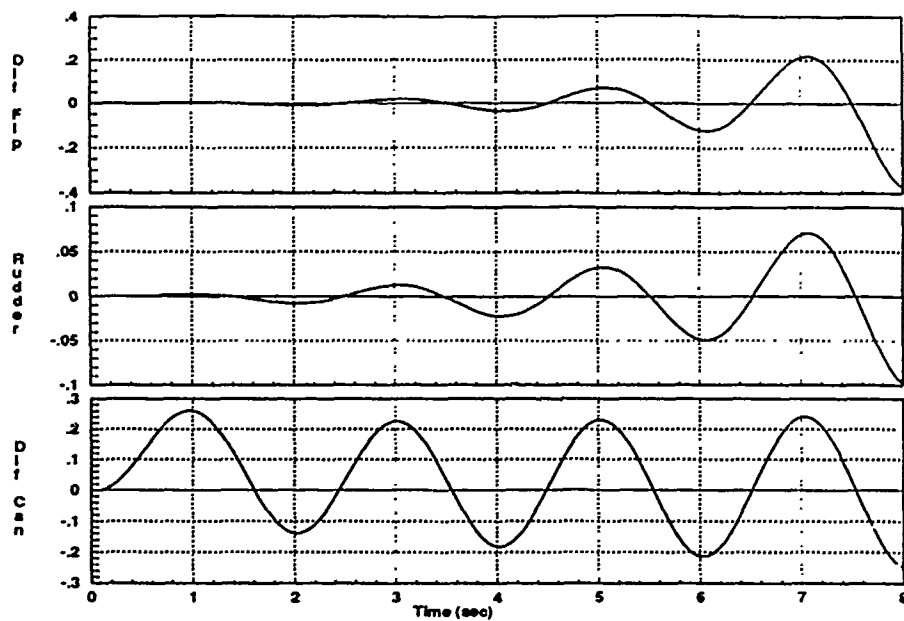


Figure 3.43. Compensated Open-Loop Roll Rate Step Responses ($\alpha = 60$)

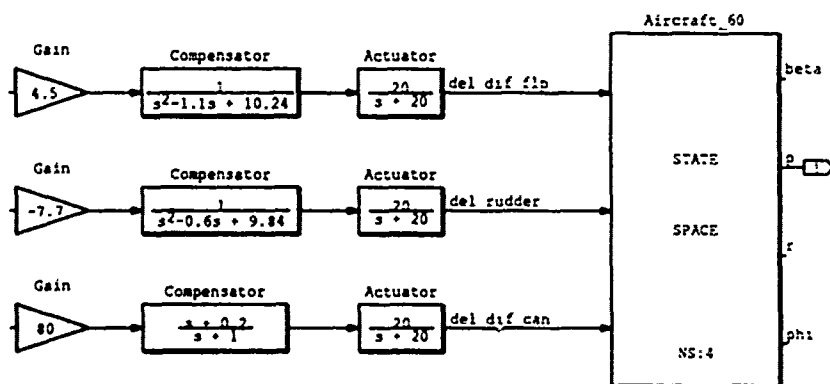


Figure 3.44. Roll Rate Compensation Block Diagram ($\alpha = 60$)

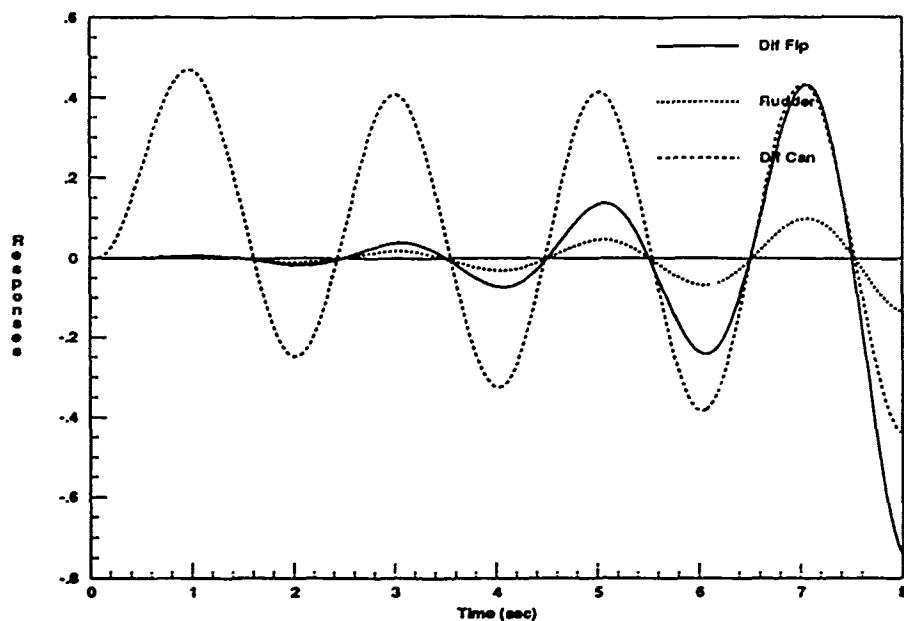


Figure 3.45. Final Compensated Open-Loop Roll Rate Step Responses ($\alpha = 60$)

roots(n1)	roots(n2)	roots(n3)
0.2287	0.6966	0.1221
$-0.1290 \pm j0.5965$	0.2657	-0.2000
-20.0	-0.7122	-0.21
-20.0	-20.0	-20.0
	-20.0	-20.0
		34.9727
roots(d1)	roots (d2)	roots (d3)
0.0459	0.0459	0.0459
-0.1554	-0.1554	-0.1554
$0.5500 \pm j3.1524$	$0.3000 \pm j3.1225$	-1.0
$0.0477 \pm j3.1259$	$0.0477 \pm j3.1259$	$0.0477 \pm j3.1259$
-20.0	-20.0	-20.0
-20.0	-20.0	-20.0
-20.0	-20.0	-20.0

Table 3.5. Compensated Roll Rate System Roots ($\alpha = 60$)

3.6 Yaw Channel Compensation

The same techniques used for the roll channels are used to develop compensation terms for the yaw channels. Beginning with the 20 degree flight condition. Figure 3.46 reveals another interesting form of responses. In this case, the sinusoidal nature is barely distinguishable, but it is clear that the control surfaces are not working together. The shifted Bode plots are shown in Figures 3.47 and 3.48. Note that the *kink* in one of the Bode phase responses cannot be removed without adversely affecting the phase at nearby frequencies. However, its effective variation is minimized and made symmetric about the nominal value.

The strip response plots in Figure 3.49 show that the controls are always working together. Also, the relative phases of the sinusoids are aligned, although that may not be absolutely necessary for these forms of responses, whose values are always positive. Since the rudder is the primary yaw control surface up through moderately high AOAs, it is chosen to handle 60 percent of the task for this flight condition. The other surfaces equally divide the remaining 40 percent. The compensated system is shown in Figure 3.50. Figure 3.51 shows the composite responses with the proper relative weights, and the compensated system roots are listed in Table 3.6.

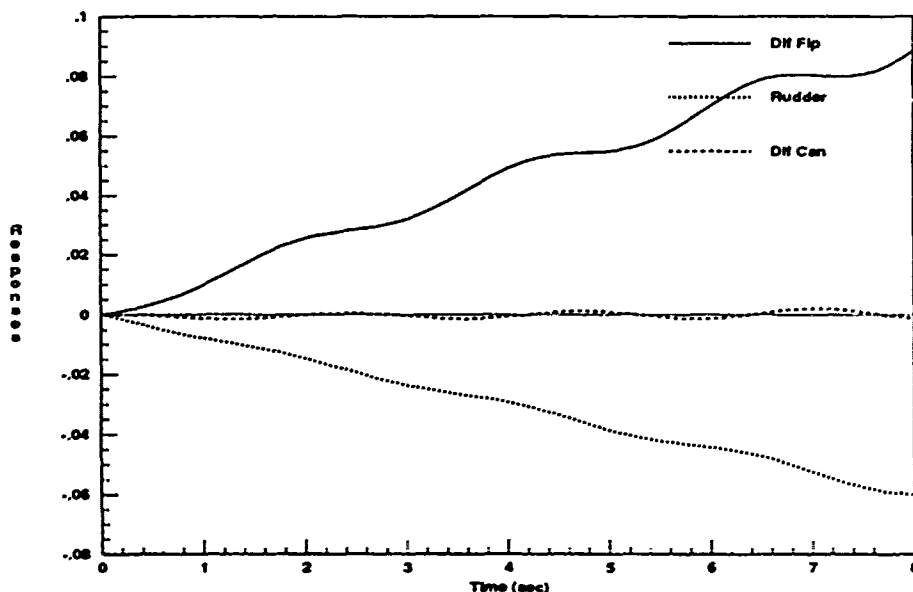


Figure 3.46. Uncompensated Open-Loop Yaw Rate Step Responses ($\alpha = 20$)

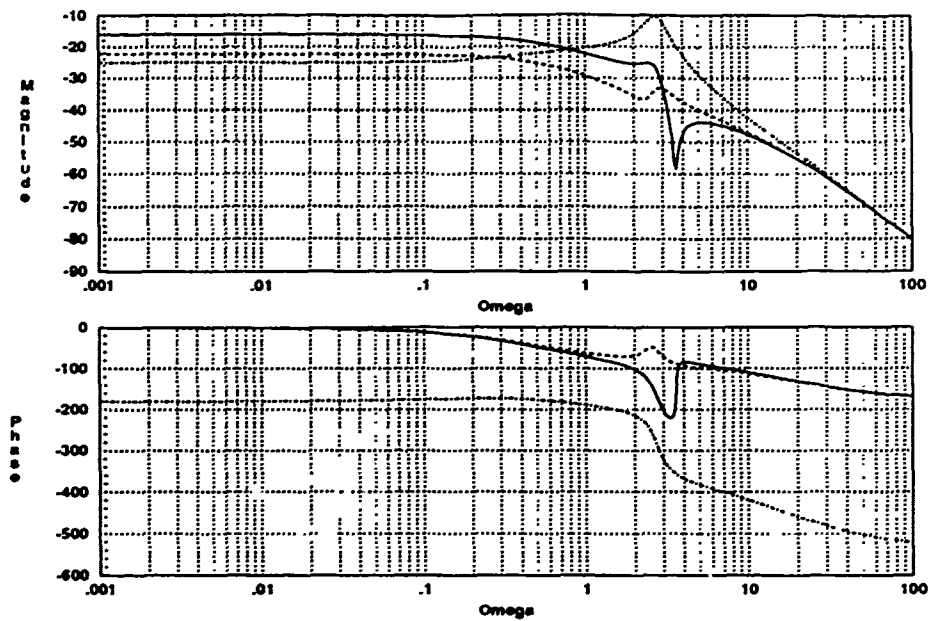


Figure 3.47. Uncompensated *Shifted* Yaw Rate Frequency Response ($\alpha = 20$)

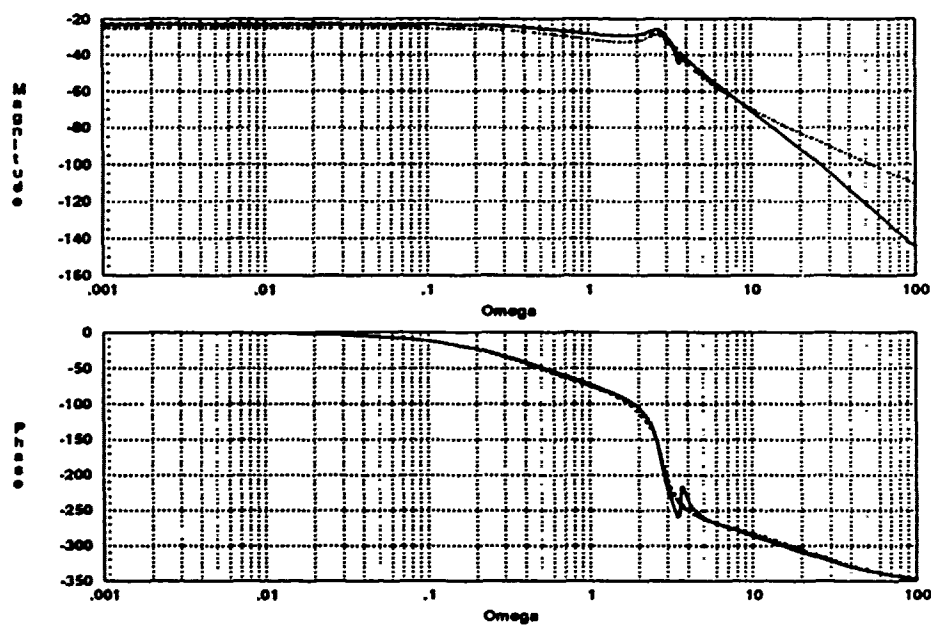


Figure 3.48. Compensated *Shifted* Yaw Rate Frequency Response ($\alpha = 20$)

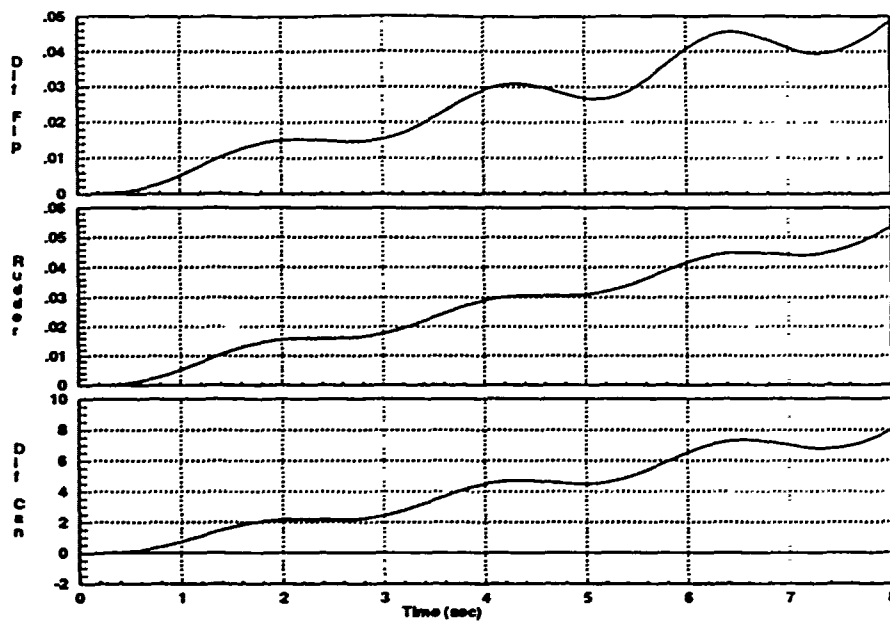


Figure 3.49. Compensated Open-loop Yaw Rate Step Responses ($\alpha = 20$)

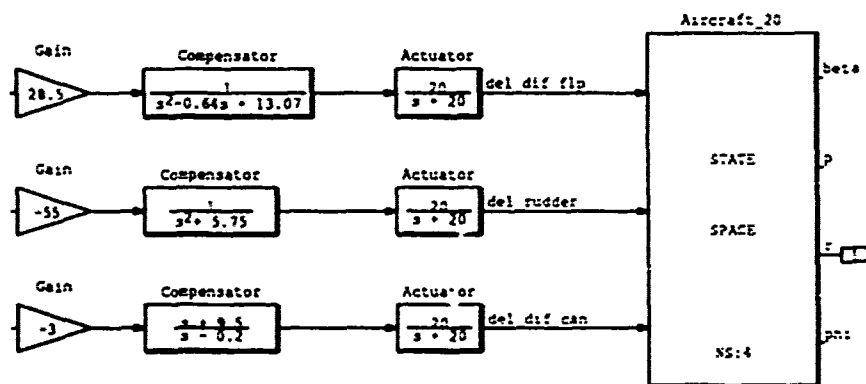


Figure 3.50. Yaw Rate Compensation Block Diagram ($\alpha = 20$)

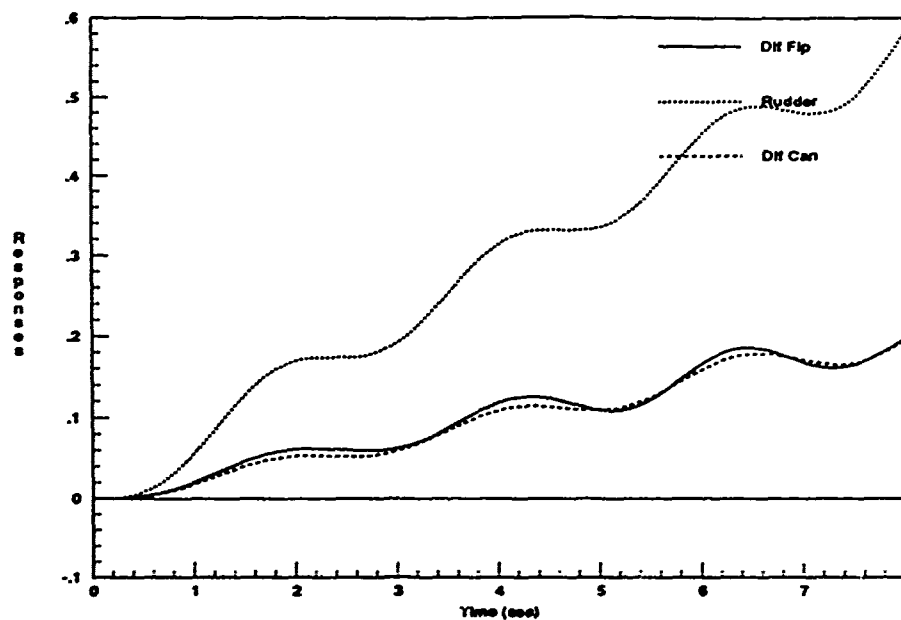


Figure 3.51. Final Compensated Open-Loop Yaw Rate Step Responses ($\alpha = 20$)

roots(n1)	roots(n2)	roots(n3)
-0.2743	-0.2762	0.2104
$0.4338 \pm j3.5782$	$0.1068 \pm j2.4659$	-0.4700
-20.0	-20.0	-9.5000
-20.0	-20.0	13.1003
		-20.0
		-20.0
roots(d1)	roots (d2)	roots (d3)
0.0058	0.0058	0.2000
-0.3239	-0.3239	0.0058
$0.1288 \pm j2.7262$	$0.0000 \pm j2.3979$	-0.3239
$0.3200 \pm j3.6011$	$0.1288 \pm j2.7262$	$0.1288 \pm j2.7262$
-20.0	-20.0	-20.0
-20.0	-20.0	-20.0
-20.0	-20.0	-20.0

Table 3.6. Compensated Yaw Rate System Roots ($\alpha = 20$)

Figure 3.52 reveals an unusual set of response characteristics for the 40 degree yaw case. The rudder response appears to behave roughly as it did in the last case, and the differential canard response looks similar to those observed in the 40 and 50 degree roll channel cases. However, the differential flaperon response, although generally an exponentially increasing sinusoid, appears to have a slight drift, somewhat like that seen in the 20 degree yaw case.

After compensating the shifted Bode responses (Figures 3.53 & 3.54), the strip response plots are obtained and optimized, as before. The unusually high gains seen in Figure 3.55 are normalized with the small gains shown in the system diagram (Figure 3.56). The relative weights chosen for yaw rate control in the 40, 50, and 60 degree conditions all have the same values. The rudder loses most of its effectiveness at such high AOAs due to aerodynamic effects. Therefore, the rudder is chosen to handle only 20 percent of the task, and the other two control surfaces take on the remaining 80 percent in equal proportions. Finally, the composite response plots are shown in Figure 3.57 and the system roots are listed in Table 3.7.

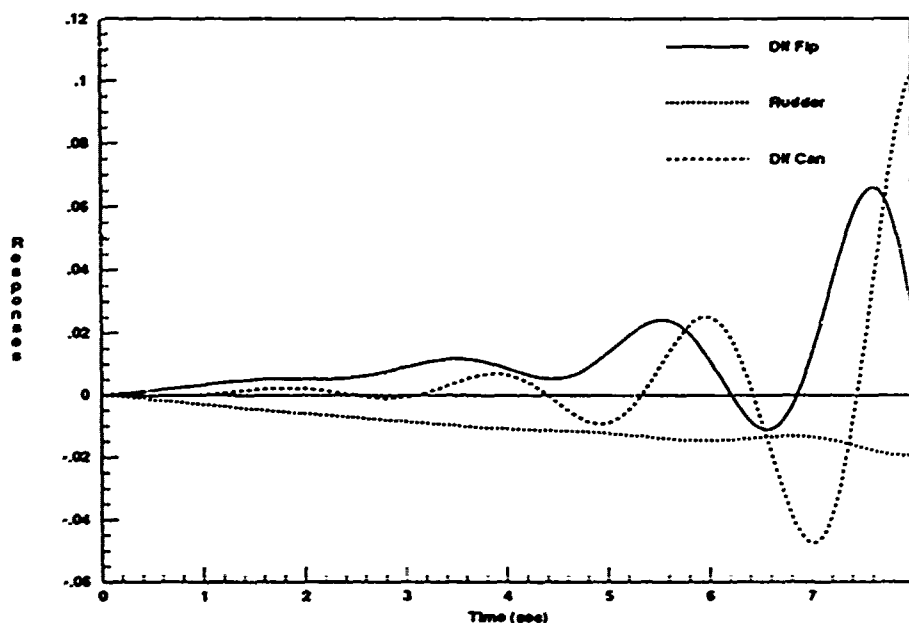


Figure 3.52. Uncompensated Open-Loop Yaw Rate Step Responses ($\alpha = 40$)

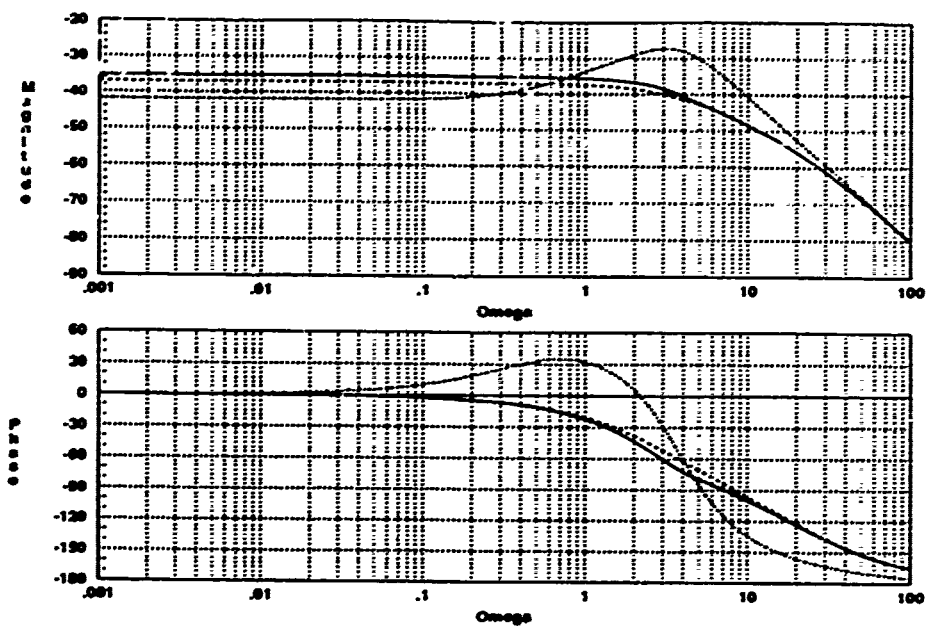


Figure 3.53. Uncompensated *Shifted* Yaw Rate Frequency Response ($\alpha = -10$)

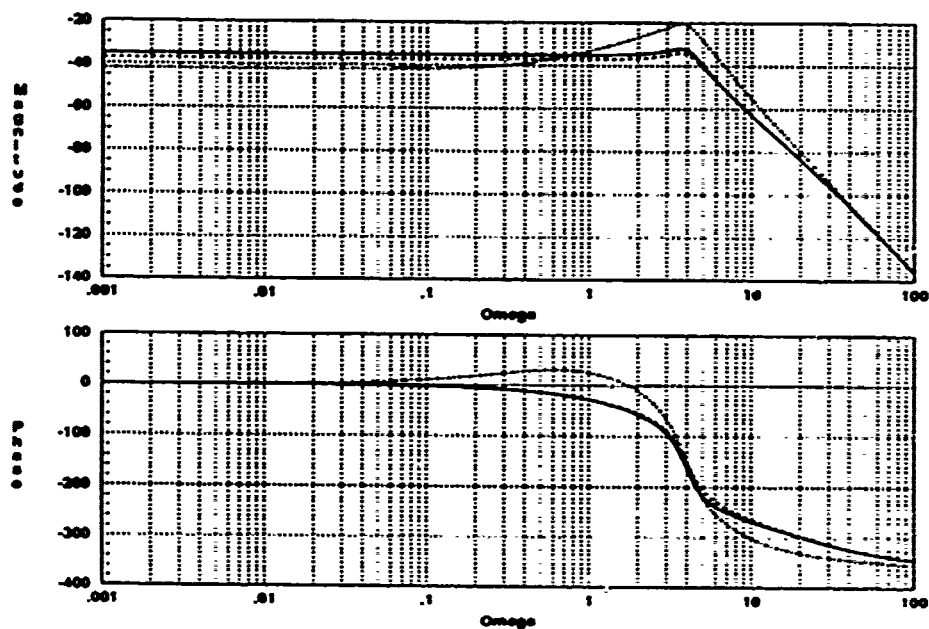


Figure 3.54. Compensated *Shifted* Yaw Rate Frequency Response ($\alpha = -10$)

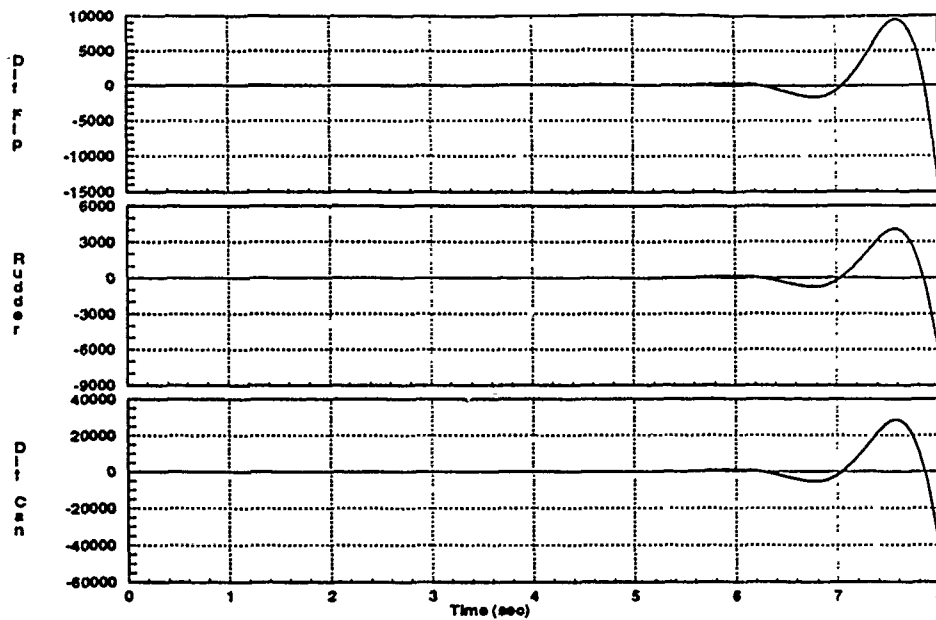


Figure 3.55. Compensated Open-Loop Yaw Rate Step Responses ($\alpha = 40$)

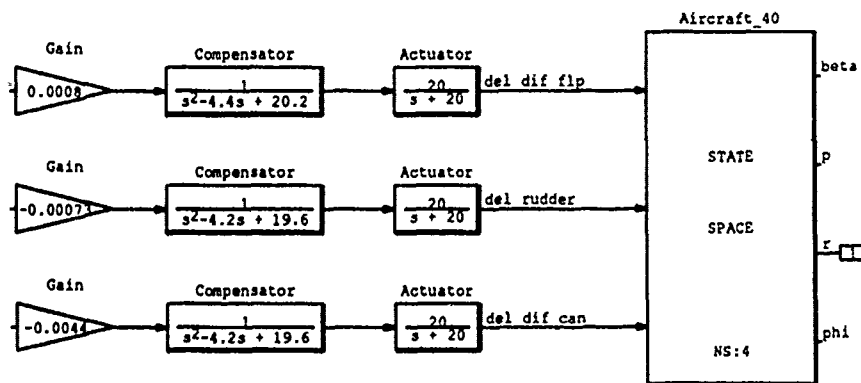


Figure 3.56. Yaw Rate Compensation Block Diagram ($\alpha = 40$)

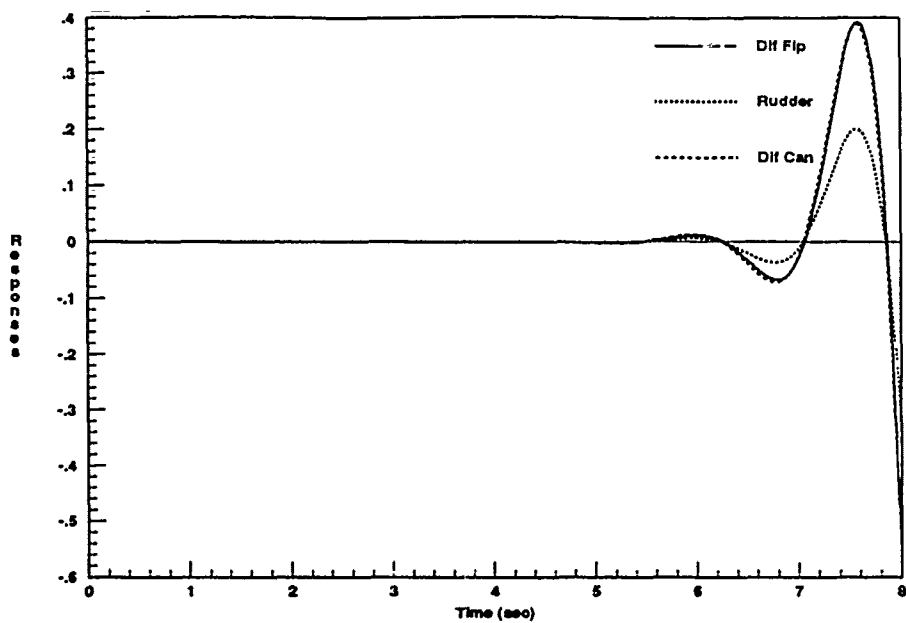


Figure 3.57. Final Compensated Open-Loop Yaw Rate Step Responses ($\alpha = 40$)

roots(n1)	roots(n2)	roots(n3)
-0.0766	-0.0760	2.5933
$0.4731 \pm j3.3759$	$0.7170 \pm j3.0272$	0.0767
-20.0	-20.0	-18.2664
-20.0	-20.0	-20.0
		-20.0
roots(d1)	roots (d2)	roots (d3)
$-0.0808 \pm j0.1561$	$-0.0808 \pm j0.1561$	$-0.0808 \pm j0.1561$
$0.7098 \pm j3.0081$	$0.7098 \pm j3.0081$	$0.7098 \pm j3.0081$
$2.2000 \pm j3.9192$	$2.1000 \pm j3.8974$	$2.1000 \pm j3.8974$
-20.0	-20.0	-20.0
-20.0	-20.0	-20.0
-20.0	-20.0	-20.0

Table 3.7. Compensated Yaw Rate System Roots ($\alpha = 40$)

Figure 3.58 shows that the uncompensated yaw rate responses for the 50 degree flight condition resemble those encountered in several previous cases. At first glance, these responses appear almost identical to those of the 50 degree roll rate case. However, unlike those responses, these are not symmetric about zero. This characteristic presents a significant problem when attempting to use the unsuccessful compensation techniques discussed in Sections 3.2 and 3.3. Section 3.3 uses this case to demonstrate the failings of those earlier methods in achieving the desired time response characteristics.

The shifted Bode plots in Figures 3.59 and 3.60 are used to obtain the required compensation needed to generate the strip response plots shown in Figure 3.61. Using the previously defined relative weights, the gains are computed and shown in the system diagram (Figure 3.62). It is interesting to note that the negative signs are not required on the last two inputs as before. The net compensation is effective as shown in Figure 3.63. The compensated system roots for this case are listed in Table 3.3.

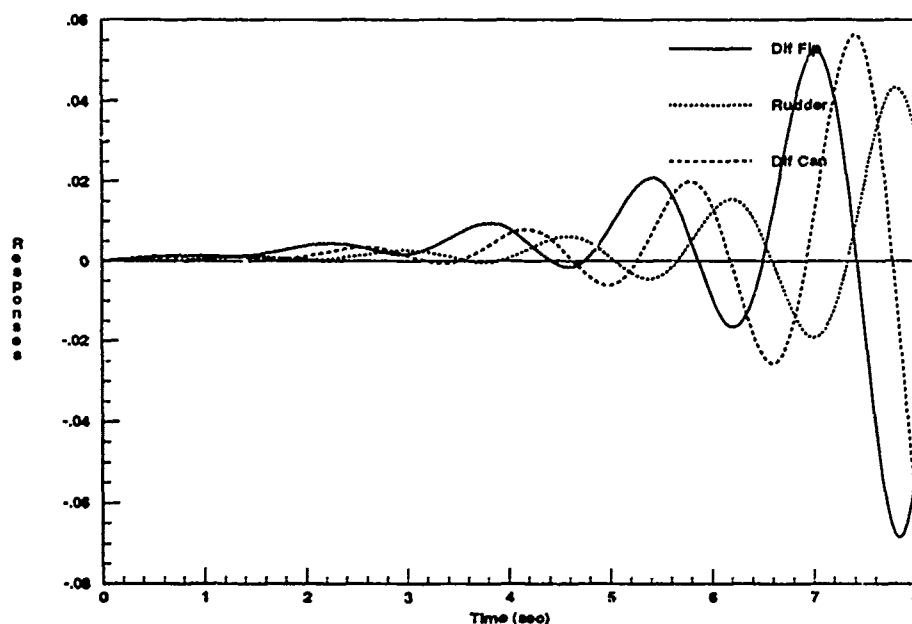


Figure 3.58. Uncompensated Open-Loop Yaw Rate Step Responses ($\alpha = 50$)

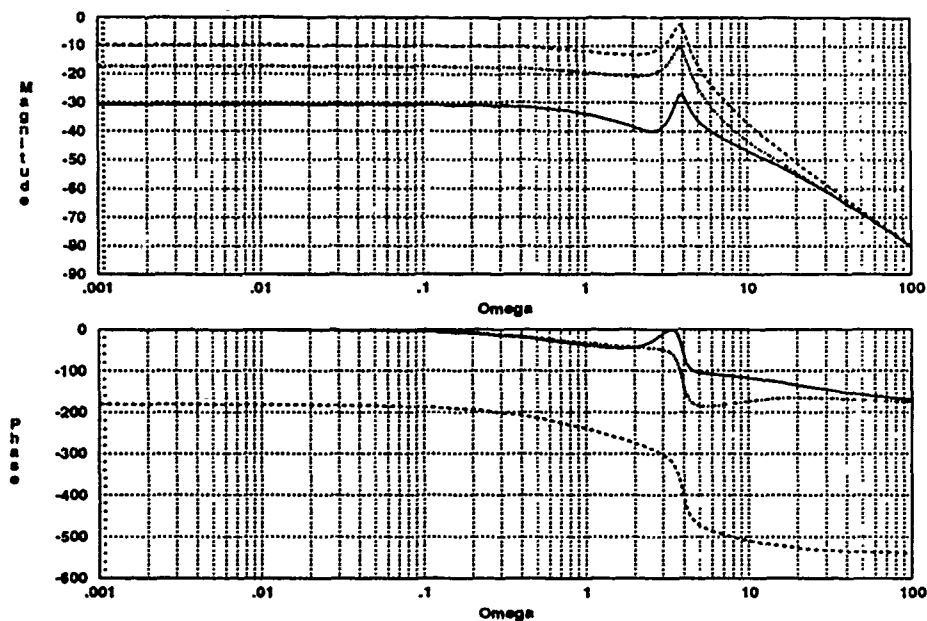


Figure 3.59. Uncompensated *Shifted* Yaw Rate Frequency Response ($\alpha = 50$)

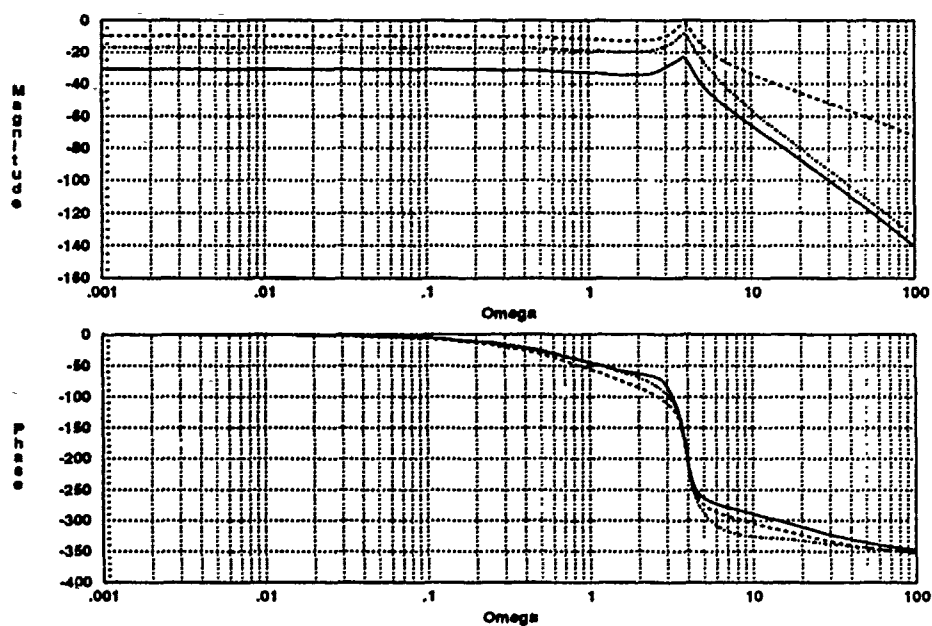


Figure 3.60. Compensated *Shifted* Yaw Rate Frequency Response ($\alpha = 50$)

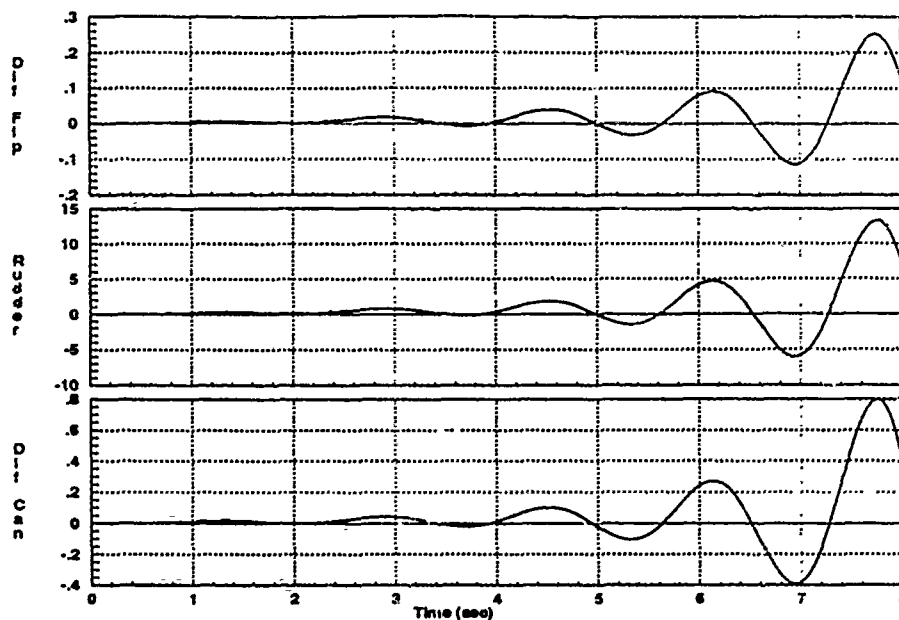


Figure 3.61. Compensated Open-Loop Yaw Rate Step Responses ($\alpha = 50$)

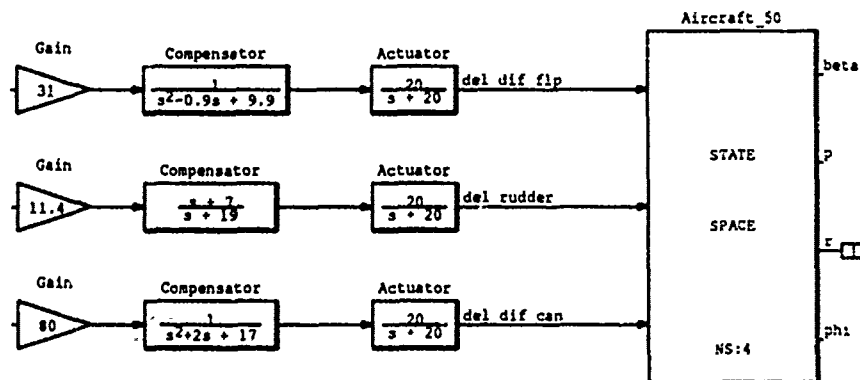


Figure 3.62. Yaw Rate Compensation Block Diagram ($\alpha = 50$)

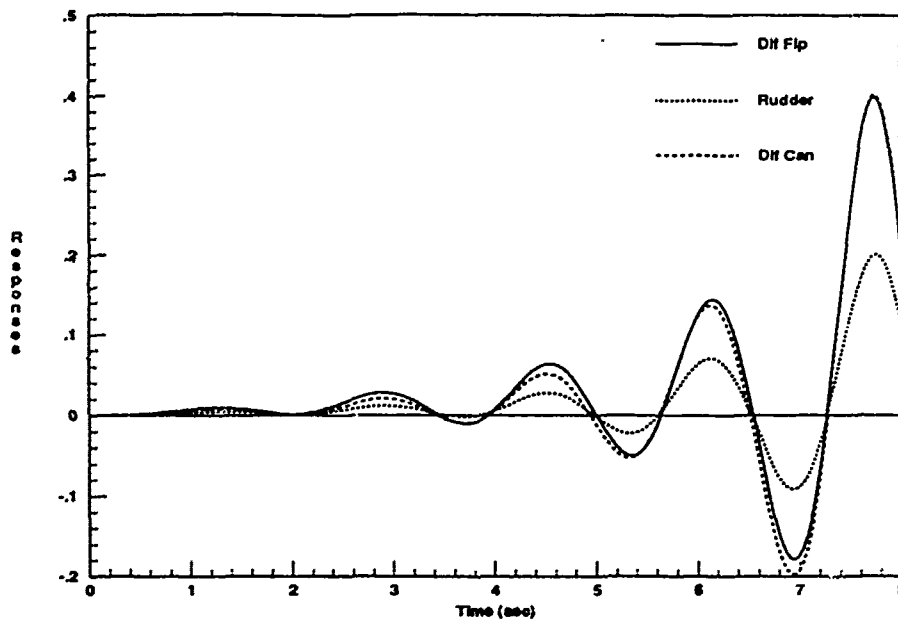


Figure 3.63. Final Compensated Open-Loop Yaw Rate Step Responses ($\alpha = 50$)

roots(n1)	roots(n2)	roots(n3)
-0.0184	-0.0173	0.0148
$0.1683 \pm j2.9641$	5.4230	$-5.2933 \pm j2.5594$
-20.0	-7.0	-20.0
-20.0	-20.0	-20.0
	-20.0	
	-23.0596	
roots(d1)	roots (d2)	roots (d3)
$-0.0190 \pm j0.0977$	$-0.0190 \pm j0.0977$	$-0.0190 \pm j0.0977$
$0.4500 \pm j3.1141$	$0.7143 \pm j3.8832$	$0.7143 \pm j3.8832$
$0.7143 \pm j3.8832$	-19.0	$-1.0000 \pm j4.0000$
-20.0	-20.0	-20.0
-20.0	-20.0	-20.0
-20.0	-20.0	-20.0

Table 3.8. Compensated Yaw Rate System Roots ($\alpha = 50$)

The final case is the 60 degree yaw rate compensation. Perhaps surprisingly, the uncompensated responses shown in Figure 3.64 do not appear all that bad. Though the relative phases of the sinusoids require some alignment, all three responses have positive values for all time. However, the usual method of phase compensation in the shifted frequency domain is used once again to yield the desired strip response plots (Figures 3.65 through 3.66). The small gains noted in the strip response plots (Figure 3.67) are normalized with fairly large gain terms as shown in the system diagram (Figure 3.68). The final compensated responses are shown in Figure 3.69, and the compensated system roots are listed in Table 3.9.

One other point worth noting is the fact that some of the compensation terms developed in the last two sections have poles or zeros in the RHP. Typically, one would not desire to add RHP terms, since they introduce additional instability and non-minimum phase characteristics. Horowitz points out that such characteristics limit the benefits of feedback and make it extremely difficult to achieve reasonable gain and phase margins [14]. These limitations are discussed further in Chapter IV. The RHP compensation terms introduced here result from the inverse shifting procedure. Since these uncompensated state space models already contained a large number of RHP terms, the addition of a few more makes little difference.

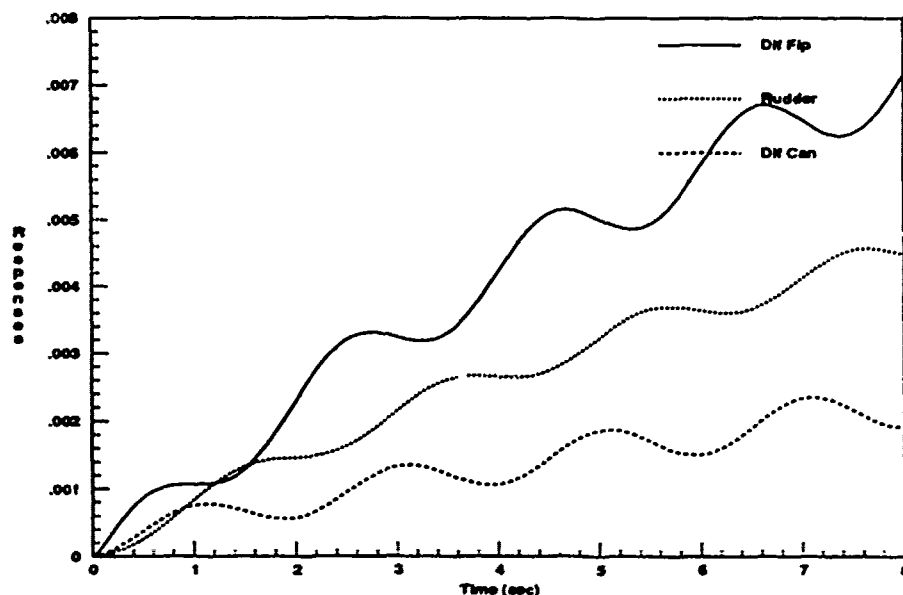


Figure 3.64. Uncompensated Open-Loop Yaw Rate Step Responses ($\alpha = 60$)

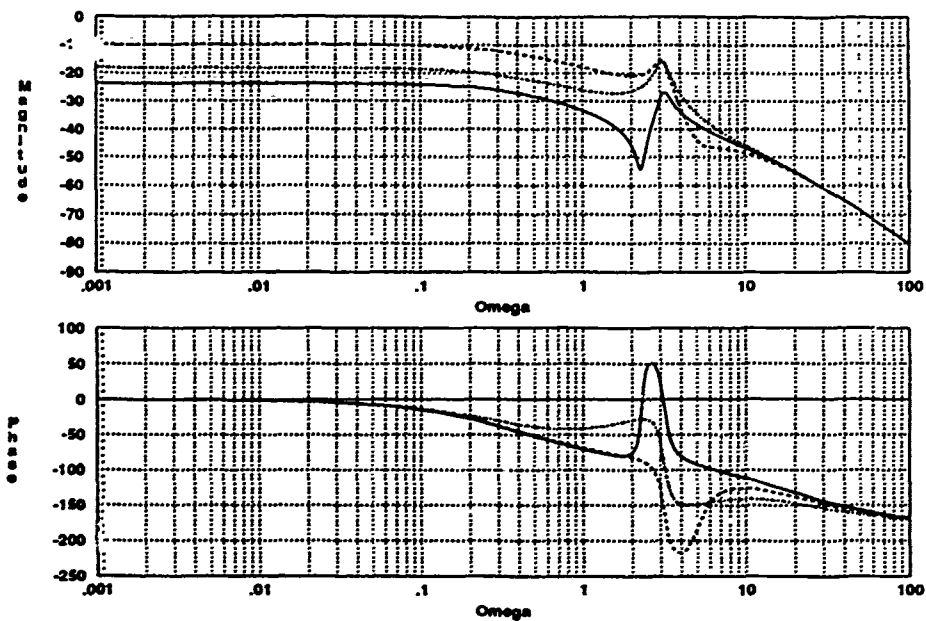


Figure 3.65. Uncompensated *Shifted* Yaw Rate Frequency Response ($\alpha = 60$)

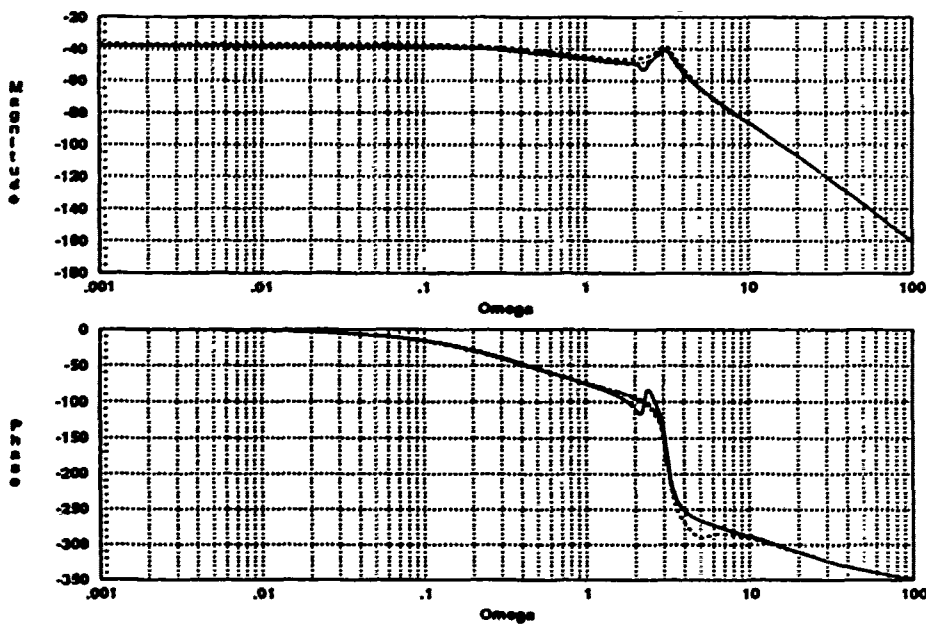


Figure 3.66. Compensated *Shifted* Yaw Rate Frequency Response ($\alpha = 60$)

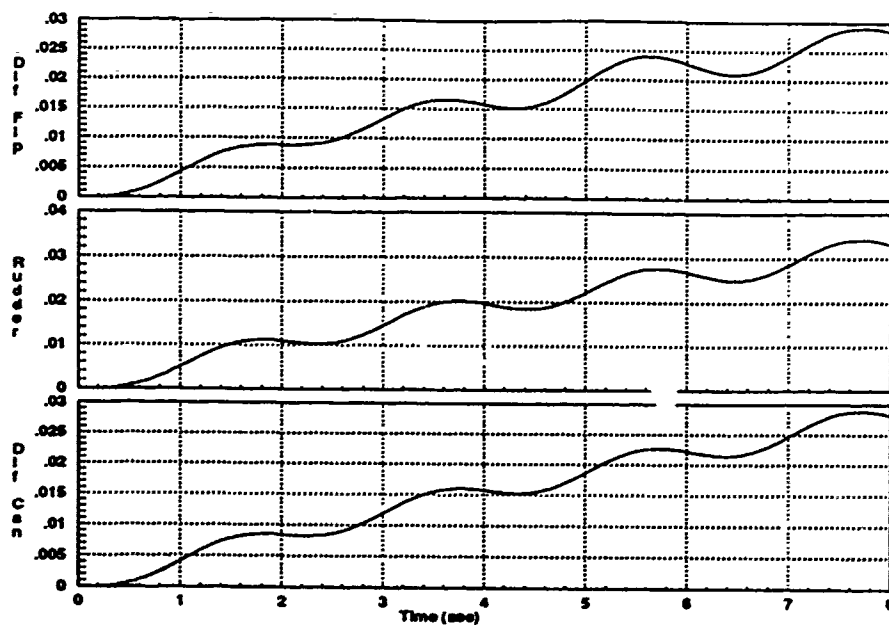


Figure 3.67. Compensated Open-Loop Yaw Rate Step Responses ($\alpha = 60$)

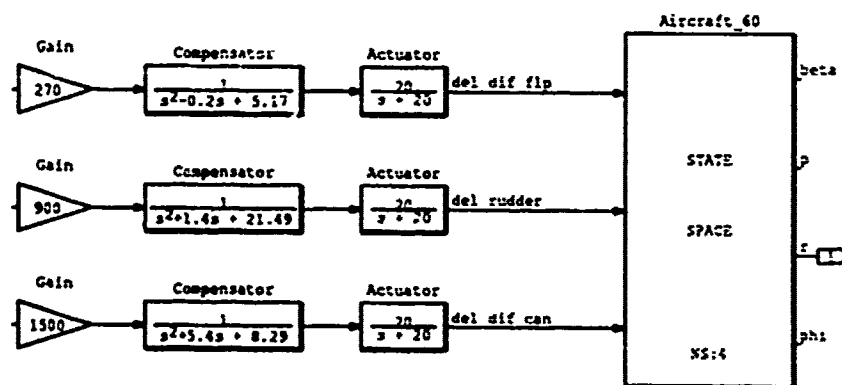


Figure 3.68. Yaw Rate Compensation Block Diagram ($\alpha = 60$)

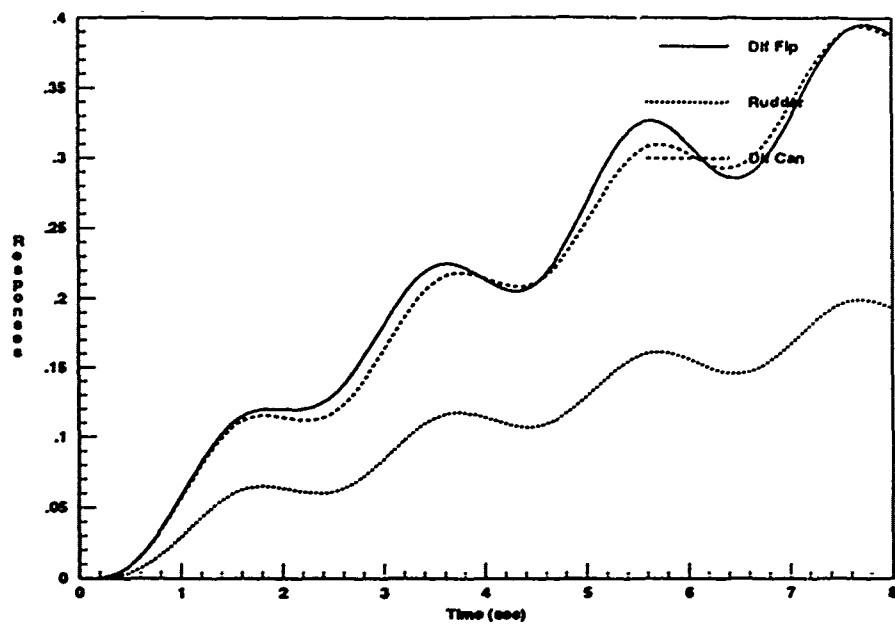


Figure 3.69. Final Compensated Open-Loop Yaw Rate Step Responses ($\alpha = 60$)

roots(n1)	roots(n2)	roots(n3)
0.0146	0.0140	-0.0111
$0.2038 \pm j2.2783$	$-0.7383 \pm j4.9687$	$-2.3667 \pm j1.3988$
-20.0	-20.0	-20.0
-20.0	-20.0	-20.0
roots(d1)	roots (d2)	roots (d3)
0.0459	0.0459	0.0459
-0.1554	-0.1554	-0.1554
$0.1000 \pm j2.2716$	$0.0477 \pm j3.1259$	$0.0477 \pm j3.1259$
$0.0477 \pm j3.1259$	$-0.7000 \pm j4.5826$	$-2.7000 \pm j1.000$
-20.0	-20.0	-20.0
-20.0	-20.0	-20.0
-20.0	-20.0	-20.0

Table 3.9. Compensated Yaw Rate System Roots ($\alpha = 60$)

3.7 Combined Roll and Yaw Channel Compensation

The weighting matrix compensation terms are developed individually and the individual transfer functions representing the effective plants are obtained from *System Build*. However, due to the inherent cross-coupling between the roll and yaw channels, the individual lateral-directional effective plants for each case must be combined into a 2X2 MIMO effective plant. The relationship of the longitudinal (SISO) and lateral-directional (MIMO) effective plants to the overall effective plant is shown in Equations 3.5 and 3.6. The zero valued cross terms result from the assumption of no cross-coupling between the two modes, as discussed in Chapter I.

$$P_{eff} = \begin{bmatrix} P_{eff}(1,1) & \vdots & 0 & 0 \\ \dots\dots\dots & \dots & \dots\dots\dots & \dots\dots\dots \\ 0 & \vdots & P_{eff}(2,2) & P_{eff}(2,3) \\ 0 & \vdots & P_{eff}(3,2) & P_{eff}(3,3) \end{bmatrix} \quad (3.5)$$

$$P_{eff} = \begin{bmatrix} P_{eff}(lon) & \vdots & 0 \\ \dots\dots\dots & \dots & \dots\dots\dots \\ 0 & \vdots & P_{eff}(lat) \end{bmatrix} \quad (3.6)$$

The SISO longitudinal compensation is complete and requires no further discussion. However, the MIMO lateral-directional portion does require additional work to complete the weighting matrix development. Since the lateral-directional mode is treated as a completely separate 2X2 MIMO system, the individual elements are numbered as shown in Equation 3.7.

$$P_{eff}(lat) = \begin{bmatrix} P_{eff}(1,1) & P_{eff}(1,2) \\ P_{eff}(2,1) & P_{eff}(2,2) \end{bmatrix} \quad (3.7)$$

$P_{eff}(1,1)$ is the effective plant representing the relationship between a commanded roll rate input and roll rate output. $P_{eff}(2,2)$ represents a similar relationship between a commanded yaw rate input and yaw rate output. The cross terms arise from the inherent coupling in the lateral-directional control modes. $P_{eff}(1,2)$ represents the relationship between a commanded yaw rate input and the resulting roll rate output. Likewise, $P_{eff}(2,1)$ represents the relationship between a commanded roll rate input and the resulting yaw rate output. The standard notation is used for each effective plant, where the first number refers to the output and the second number refers to the input. For this particular usage, the numbers one and two refer to the roll rate and yaw rate, respectively.

The final gain adjustment for the lateral-directional compensation involves adjusting the gains for each of the effective plants across all four flight conditions. This is done to minimize computational errors resulting from extreme variations in magnitude. In the first case, $P_{eff}(1,1)$ is generated from *System Build* and a composite plot of the Bode *magnitudes* is obtained, representing the four flight conditions.

Next, a similar composite magnitude plot is obtained for the four $P_{eff}(2,1)$ systems. Finally, overall system gains are included for the 40, 50, and 60 degree conditions so that the four Bode magnitude plots for each effective plant are brought within one or two orders of magnitude, across the frequency range of interest. The same gain factors are used for $P_{eff}(1,1)$ and $P_{eff}(2,1)$ at a given flight condition. The reason for this is the fact that these two plants share a common input channel, and thus common weighting matrix compensation terms. Figures 3.70 and 3.71 show the magnitude plots before and after final gain adjustment.

A similar procedure is used to generate the final gain adjustments for the $P_{eff}(1,2)$ and $P_{eff}(2,2)$ systems for all four flight conditions. The magnitude plots before and after final gain adjustment are shown in Figure 3.72 and 3.73. Again, for any one flight condition, the gain factors are the same for $P_{eff}(1,2)$ and $P_{eff}(2,2)$. However, there is no need to match the gains used in these cases with those used for $P_{eff}(1,1)$ and $P_{eff}(2,1)$, since the input channels are different.

Finally, Appendix H shows the *System Build* block diagrams of each of the effective plants for all four flight conditions after final gain adjustment. The overall relative gains are shown on the diagrams. Note that each of these block diagrams represents an individual element of Equation 3.7 for a given flight condition.

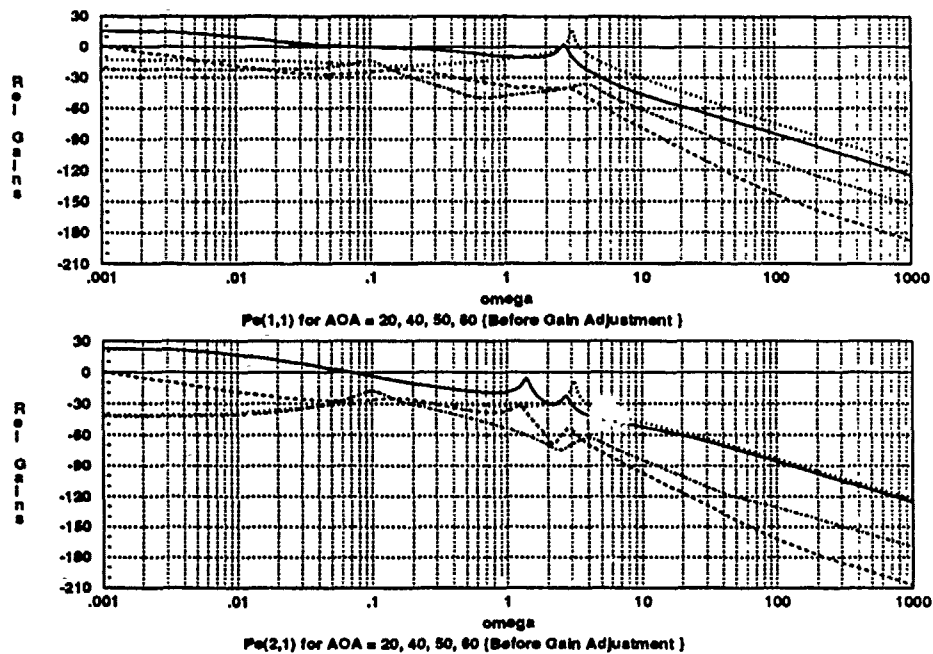


Figure 3.70. Unadjusted Lateral-Directional Plants with Roll Rate Input

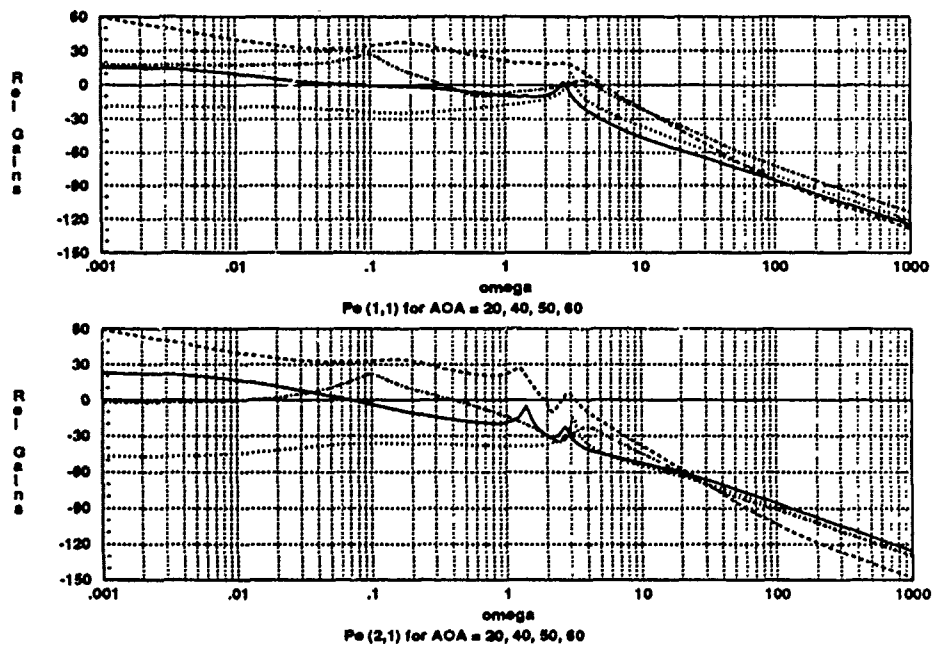


Figure 3.71. Final Gain Adjusted Lateral-Directional Plants with Roll Rate Input

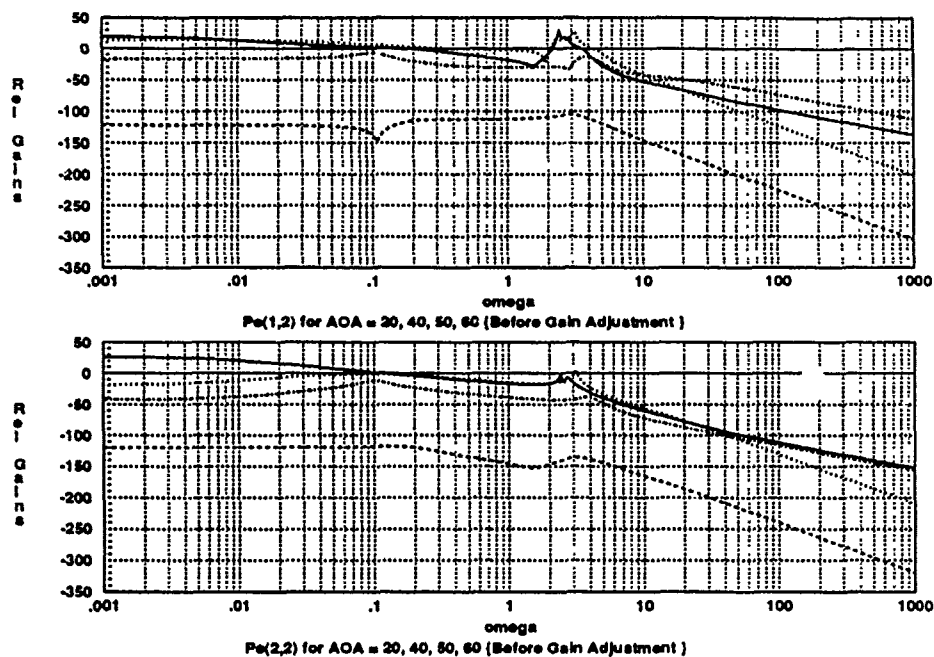


Figure 3.72. Unadjusted Lateral-Directional Plants with Yaw Rate Input

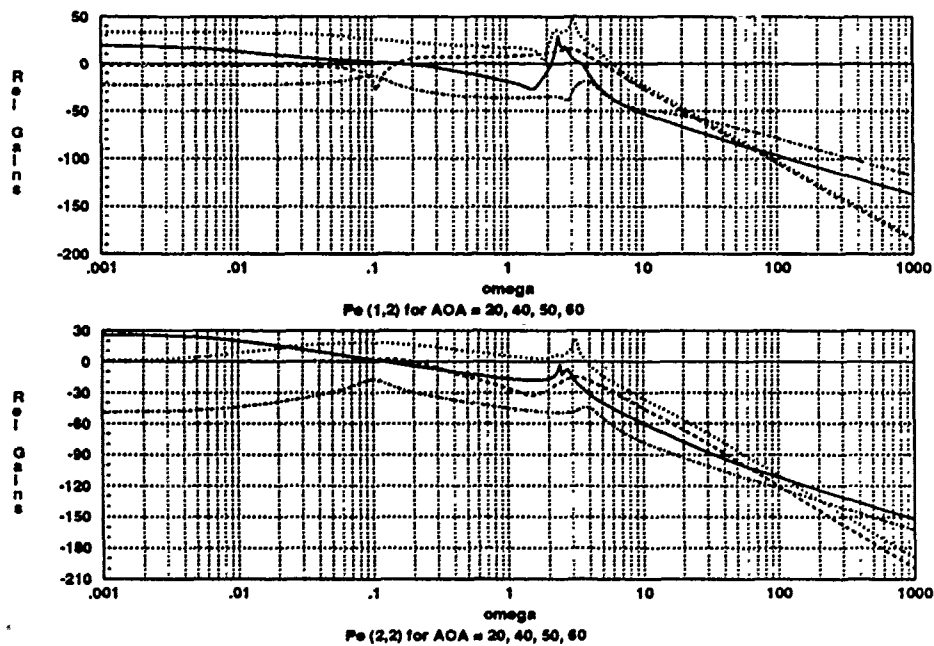


Figure 3.73. Final Gain Adjusted Lateral-Directional Plants with Yaw Rate Input

3.8 Final Weighting Matrices

The final weighting matrices are listed in this section. For each system, the effective plant (see Figure 3.1) is obtained algebraically by post-multiplying the state space dynamics model by the actuator and weighting matrices, respectively. However, with *Matrixx System Build*, the effective plants are already defined for each flight condition (Section 3.4 for the longitudinal control modes and Sections 3.5 through 3.7 for the lateral-directional control modes). Even though the computer performs the combining operation, it is useful to organize the compensation terms into the actual weighting matrices to understand the input/output relationships. In each case, the rows correspond to the state variables and the columns correspond to the control inputs (see Sections 2.5 & 2.6).

The individual longitudinal weighting matrices are shown below. Note that the non-zero entries appear only in row three (corresponding to the pitch rate). Also, note that the differential canard input (column two) entries are zero. These matrix elements are obtained from Figures 3.11, 3.14, 3.17, and 3.20.

$$\Delta_{lon20} = \begin{bmatrix} 0 & 0 & 0 & 0 \\ 0 & 0 & 0 & 0 \\ 0.5 & 0 & -0.1 & -0.4 \\ 0 & 0 & 0 & 0 \end{bmatrix} \quad (3.8)$$

$$\Delta_{lon40} = \begin{bmatrix} 0 & 0 & 0 & 0 \\ 0 & 0 & 0 & 0 \\ 0.5 & 0 & -0.15 & -0.35 \\ 0 & 0 & 0 & 0 \end{bmatrix} \quad (3.9)$$

$$\Delta_{lon50} = \begin{bmatrix} 0 & 0 & 0 & 0 \\ 0 & 0 & 0 & 0 \\ 0.6 & 0 & -0.1 & -0.3 \\ 0 & 0 & 0 & 0 \end{bmatrix} \quad (3.10)$$

$$\Delta_{lon60} = \begin{bmatrix} 0 & 0 & 0 & 0 \\ 0 & 0 & 0 & 0 \\ 0.5 & 0 & -0.2 & -0.3 \\ 0 & 0 & 0 & 0 \end{bmatrix} \quad (3.11)$$

The frequency dependent lateral-directional weighting matrices are now shown. In this case, the second row entries correspond to the roll rate and the third row entries correspond to the yaw rate. The system diagrams provided in Appendix H are used to obtain these weighting matrix elements.

$$\Delta_{lat20} = \begin{bmatrix} 0 & 0 & 0 \\ \frac{7.3}{s^2+0.1s+1.94} & -2.7 & \frac{0.25(s+39.8)}{s+0.1} \\ \frac{28.5}{s^2-0.64s+13.07} & \frac{-55}{s^2+5.75} & \frac{-3(s+9.5)}{s-0.2} \\ 0 & 0 & 0 \end{bmatrix} \quad (3.12)$$

$$\Delta_{lat40} = \begin{bmatrix} 0 & 0 & 0 \\ \frac{2160}{s^2+0.2s+1.6} & \frac{-2700}{s^2-0.5s+8.5} & \frac{12.6(s+39)}{s} \\ \frac{800}{s^2-4.4s+20.2} & \frac{-730}{s^2-4.2s+19.6} & \frac{-4400}{s^2-4.2s+19.6} \\ 0 & 0 & 0 \end{bmatrix} \quad (3.13)$$

$$\Delta_{lat50} = \begin{bmatrix} 0 & 0 & 0 \\ \frac{5630}{s^2+29.5s+14.5} & \frac{-1100}{s^2+14s+5} & 50 \\ \frac{15.5}{s^2-.9s+9.9} & \frac{5.7(s+7)}{s+19} & \frac{40}{s^2+2s+17} \\ 0 & 0 & 0 \end{bmatrix} \quad (3.14)$$

$$\Delta_{lat60} = \begin{bmatrix} 0 & 0 & 0 \\ \frac{2.25}{s^2-1.1s+10.24} & \frac{-3.85}{s^2-0.6s+9.84} & \frac{40}{s+1} \\ \frac{2700}{s^2-0.2s+5.17} & \frac{9000}{s^2+1.4s+21.49} & \frac{15000}{s^2+5.4s+8.29} \\ 0 & 0 & 0 \end{bmatrix} \quad (3.15)$$

Finally, as an example of how these matrices combine to form a single weighting matrix for each flight condition, Equations 3.8 and 3.12 (representing the 20 degree AOA condition) are combined in Equation 3.16. The resulting matrix has eight rows (corresponding to the eight state variables) and seven columns (corresponding to the seven control surface inputs). In this matrix, the third row corresponds to the pitch rate and the sixth and seventh rows correspond to the roll rate and yaw rate, respectively. If any other state variables had been chosen as control variables, their corresponding rows in this matrix would have non-zero elements.

3.9 Summary

This chapter presents an in-depth look at the weighting matrix development. It is clear that this is not a trivial task for an unstable, non-minimum phase problem such as this. The chapter begins with a definition of the weighting matrix and a discussion of how it is used to augment the state space and actuator matrices to form the effective plant. This is followed with a discussion of why a frequency dependent weighting matrix is required for the lateral-directional control modes.

$$\Delta_{20} = \begin{bmatrix} 0 & 0 & 0 & 0 & 0 & 0 & 0 \\ 0 & 0 & 0 & 0 & 0 & 0 & 0 \\ 0.5 & 0 & -0.1 & -0.4 & 0 & 0 & 0 \\ 0 & 0 & 0 & 0 & 0 & 0 & 0 \\ 0 & 0 & 0 & 0 & 0 & 0 & 0 \\ 0 & 0 & 0 & 0 & \frac{7.3}{s^2+0.1s+1.94} & -2.7 & \frac{0.25(s+39.8)}{s+0.1} \\ 0 & 0 & 0 & 0 & \frac{28.5}{s^2-0.64s+13.07} & \frac{-55}{s^2+5.75} & \frac{-3(s+9.5)}{s-0.2} \\ 0 & 0 & 0 & 0 & 0 & 0 & 0 \end{bmatrix} \quad (3.16)$$

The accepted design approach for frequency dependent weighting matrices is discussed briefly. Following this is a description of two design methods which both fail to achieve the desired results. A shifting method for handling the unstable roots is presented and the likely reason for the earlier methods' failings is discussed. A brief look at selected results of the unsuccessful compensation methods is also presented to demonstrate the problem of correlating the time and frequency domains for such functions.

Using the shifting technique, the individual weighting matrix compensation terms are developed in a step-by-step process for each of the primary channels and flight conditions. Open-loop step responses before and after compensation are included and provide dramatic evidence of the need and effectiveness of the frequency dependent compensation terms. The roll rate and yaw rate compensation terms are then combined with *System Build* to form the lateral-directional (MIMO) effective plants, and a final gain adjustment is performed. Finally, the actual weighting matrices are shown individually for each flight condition and a combined system weighting matrix is shown for one flight condition. The next two chapters use the effective plants developed here as a basis for the control system designs.

IV. Longitudinal Control System Design

4.1 Introduction

This chapter discusses the individual control system designs for each of the longitudinal cases. The X-29A uses a summation of pitch rate, normal acceleration, and canard position as the longitudinal control variable for the *normal digital* flight control system. The *analog reversion* system, however, uses only the pitch rate, as does this design.

The primary design goal in each case is to achieve closed-loop stability. A high degree of static instability causes control law designers to stress stability and robustness over handling qualities. Indeed, it has been stated that the primary task of the X-29A longitudinal control system is to stabilize the aircraft [4]. The stability of the system is assessed by the use of gain and phase margins, as discussed later in this chapter. Some basic QFT terms are now explained with the use of two simplified diagrams.

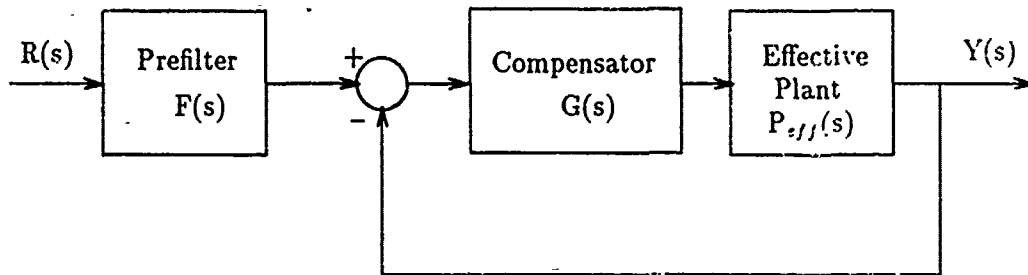


Figure 4.1. Basic QFT Standard Control System Notation

Figure 4.1 shows the simplified block diagram of a basic QFT SISO system, such as the ones discussed in this chapter. The closed-loop control ratio is given by $Y(s)/R(s)$, where $Y(s)$ is the LaPlace transform of the output and $R(s)$ is the LaPlace transform of the input. For each case, the compensator $G(s)$ is developed

in this chapter. The prefilter $F(s)$, is designed to achieve the desired closed-loop performance characteristics, once the system is stabilized.

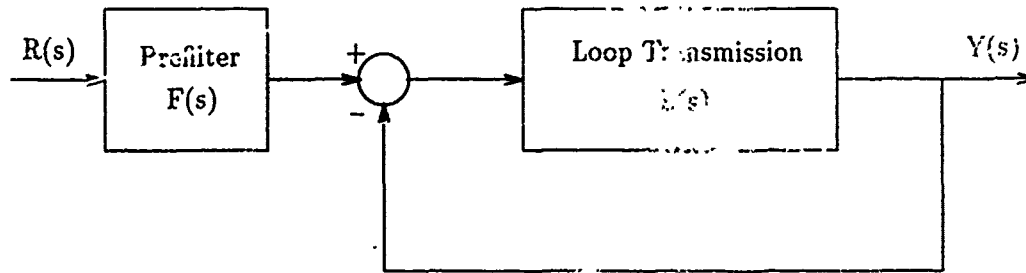


Figure 4.2. Basic QFT Alternate Control System Notation

Figure 4.2 shows the alternate notation for the same basic QFT SISO system. Note that the loop transmission function $L(s)$ is equal to the product of the compensator and the effective plant. The QFT method is based on achieving a desired loop transmission function and dividing the result by the effective plant to obtain the compensator transfer function. The design is accomplished using Nichols charts and Bode plots. For this reason, the transfer functions are expressed in terms of the complex frequency as shown below.

$$G(j\omega) = \frac{L(j\omega)}{P_{eff}(j\omega)} \quad (4.1)$$

Finally, a single compensator/prefilter design capable of controlling the system for all four flight conditions is deemed impractical [15]. This is due primarily to the wide variations of RHP poles and zeros in the effective plants. However, for the 20 and 40 degree cases, alternate designs are presented and the relative merits of each are discussed. The design of the loop transmission functions begins with an analysis of the effective plants, as discussed in the next section.

4.2 Analysis of Effective Plants

The longitudinal effective plants are represented by the block diagrams in Figures 3.11, 3.14, 3.17, and 3.20. The aircraft dynamics models are represented by the state space block in each diagram. In each case, the transfer function representing the effective plant is the ratio between the pitch rate output of the state space block and the simultaneous control input to the three control channels of interest. Note that the system is still termed SISO, since a single control input is applied, and then distributed among the three control surfaces of interest. Recall that the differential canard channel is not commanded for the longitudinal control systems. For clarity, the effective plant transfer functions are listed in this section, in both polynomial and factored forms. The polynomial forms are shown below. In each case, the numerator is sixth order and the denominator is eighth order.

$$P_{eff}(lon20) =$$

$$\frac{.8s^6 + 56.5s^5 + 1320.4s^4 + 10223s^3 + 2225.2s^2 - 14s}{s^8 + 110.4s^7 + 4239.2s^6 + 69446s^5 + 421720s^4 + 97374s^3 - 281760s^2 - 105 - 33s - 4728.2}$$

$$P_{eff}(lon40) =$$

$$\frac{.7s^6 + 53.8s^5 + 1271.1s^4 + 9936s^3 + 2497.6s^2 - 135.2s}{s^8 + 110.6s^7 + 4260.4s^6 + 70289s^5 + 436460s^4 + 203860s^3 - 99113s^2 - 104 - 84s - 2104.6}$$

$$P_{eff}(lon50) =$$

$$\frac{.9s^6 + 64.7s^5 + 1561.8s^4 + 12398s^3 + 2874.8s^2 - 336.3s}{s^8 + 110.7s^7 + 4271.1s^6 + 70715s^5 + 444000s^4 + 259570s^3 + 7434.1s^2 + 40 - 24.4s - 504.9}$$

$$P_{eff}(lon60) =$$

$$\frac{s^6 + 71.9s^5 + 1735.2s^4 + 13720s^3 + 2526.4s^2 - 609.8}{s^8 + 110.4s^7 + 4241.2s^6 + 69649s^5 + 429260s^4 + 218840s^3 + 443260s^2 + 13 - 4740s + 7145.7}$$

The roots of each effective plant, shown in Tables 4.1 through 4.4, are used as the basis for designing the loop transmission functions. In each case, note that the last four denominator roots result from the actuator transfer functions. All the other roots result from the open-loop aircraft dynamics models. Each of the first three flight conditions has an unstable RHP pole. This is also pointed out in Section 2.5.

roots(num20)	roots(den20)
0.0000	-0.0203±j0.1257
0.0061	0.7080
-0.2304	-1.0502
-20.0000	-20.0000
-20.0000	-20.0000
-31.5489	-20.0000
	-50.0000

Table 4.1. Roots of Longitudinal Effective Plant ($\alpha = 20$)

roots(num40)	roots(den40)
0.0000	-0.0534±j0.1193
0.0458	0.3756
-0.3076	-0.8200
-20.0000	-20.0000
-20.0000	-20.0000
-32.4259	-20.0000
	-50.0000

Table 4.2. Roots of Longitudinal Effective Plant ($\alpha = 40$)

roots(num50)	roots(den50)
0.0000	0.0785
0.0853	-.0377±j0.1528
-0.3280	-0.6490
-20.0000	-20.0000
-20.0000	-20.0000
-34.9758	-20.0000
	-50.0000

Table 4.3. Roots of Longitudinal Effective Plant ($\alpha = 50$)

roots(num60)	roots(den60)
0.0000	-0.0677
0.1373	-0.2586
-0.3318	-0.0193±j1.0103
-20.0000	-20.0000
-20.0000	-20.0000
-35.0064	-20.0000
	-50.0000

Table 4.4. Roots of Longitudinal Effective Plant ($\alpha = 60$)

All four transfer functions have one zero at the origin and one RHP zero. The RHP zeros add undesirable non-minimum phase characteristics in the form of excess phase lag. Also, when an RHP pole and zero are near each other, this limits the achievable gain margin. In the 50 degree case, it is noted that an RHP pole and zero are virtually on top of each other. The achievable gain margin for this plant is *severely* limited, as shown in the next section.

4.3 Design of Loop Transmission Functions

Section 4.1 mentioned that the compensator is designed by obtaining the desired loop transmission function and dividing the result by the effective plant. Obviously, one desirable goal is to achieve the desired stability with as simple a compensator as possible. To minimize the number of compensator terms, L is designed to contain some of the terms found in P_{eff} .

Starting with the 20 degree case, the loop transmission function is chosen to contain a zero at 0.0061 and a pole at 0.7080. Note that the effective plant has these same roots (Table 4.1). For the determination of the compensator transfer function, these terms *effectively* cancel out (Equation 4.1), thus reducing the number of terms in G . It should be pointed out that one may *not* cancel out poles or zeros in the RHP. This is because an exact cancellation can never be assured. Without an exact cancellation, a closed-loop pole would remain in the RHP and the system would be unstable. Such a cancellation has not occurred here. The *effective* cancellation discussed above results from using two of the P_{eff} terms to form part of the loop transmission function.

The next step is to determine the order of the loop transmission function. Since the effective plant has an excess of two poles over zeros, the loop transmission function must have at least this excess. To *ensure* the desired high-frequency characteristics [$L(\infty)=0$], it is decided that the loop transmission function should have an excess of three poles over zeros. Therefore, in addition to the pole at 0.7080, the denominator of L must contain a second order pair of poles and a single real pole. The second order pair may be real or complex, and the values of ζ and ω_n may be arbitrarily chosen. For simplicity, ζ is chosen to be unity. Using an iterative routine, the values of ω_n , the additional real pole, and the overall gain are adjusted while observing changes on the Nichols plot of the loop transmission function (Figure 4.3).

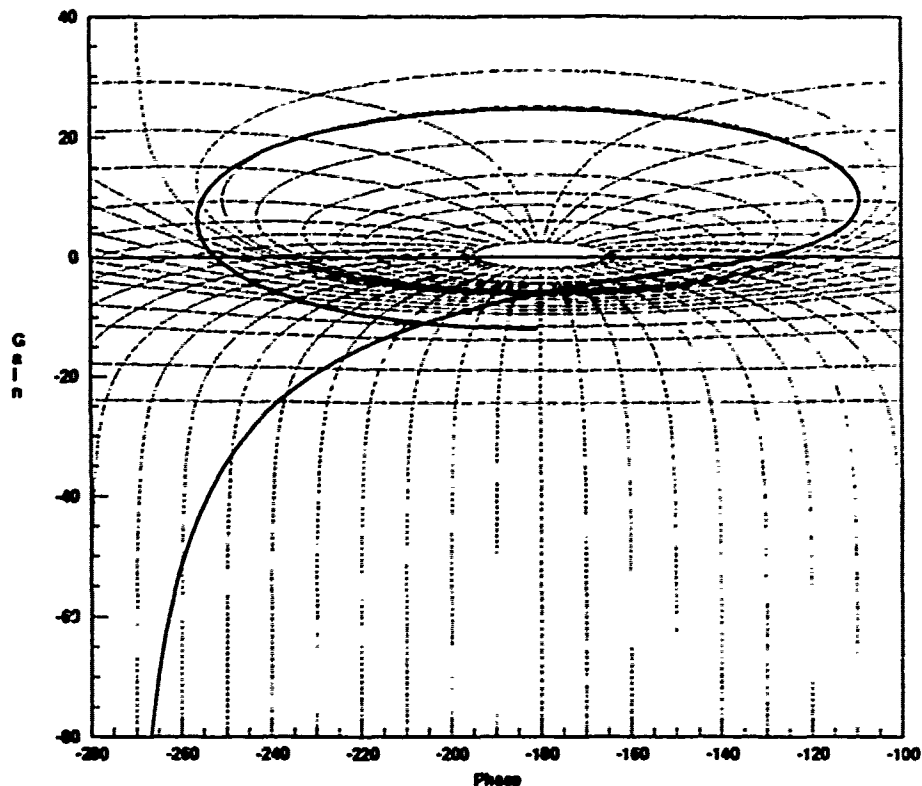


Figure 4.3. Nichols Plot - Pitch Rate Loop Transmission 1 ($\alpha = 20$)

The design philosophy is to maximize the amount of loop transmission gain in the mid-frequency range, while maintaining reasonable gain and phase margins. It is known that in order to maximize the benefits of feedback, the loop transmission gain must be made as great as possible [14]. Maximizing the benefits of feedback reduces the sensitivity to disturbances [15]. There is a tradeoff, however. The amount of allowable loop transmission gain is limited by the gain and phase margins. Referring to Figure 4.3, if one increases the loop transmission gain (thus raising the entire plot), the function will eventually cross the zero-dB/-180 degree point. If this occurs, the system becomes unstable [8].

Figure 4.4 is the Bode plot of the same function. The Nichols plot is the primary design tool, but the Bode plot clearly shows the magnitude and phase characteristics as a function of frequency. The units of gain and phase for both types of plot are dBs and degrees, respectively. They have been omitted from the plot labeling for neat appearance. The low-frequency portion of L ($\omega = 0.0001$) has a magnitude of approximately -13 dB and a phase of -180 degrees, which is easily read off the Bode plots. This is also seen on the Nichols plot and the function moves in a clockwise direction around the zero-dB/-180 degree point until finally falling off to the desired steady state value of zero gain and -270 degrees of phase lag.

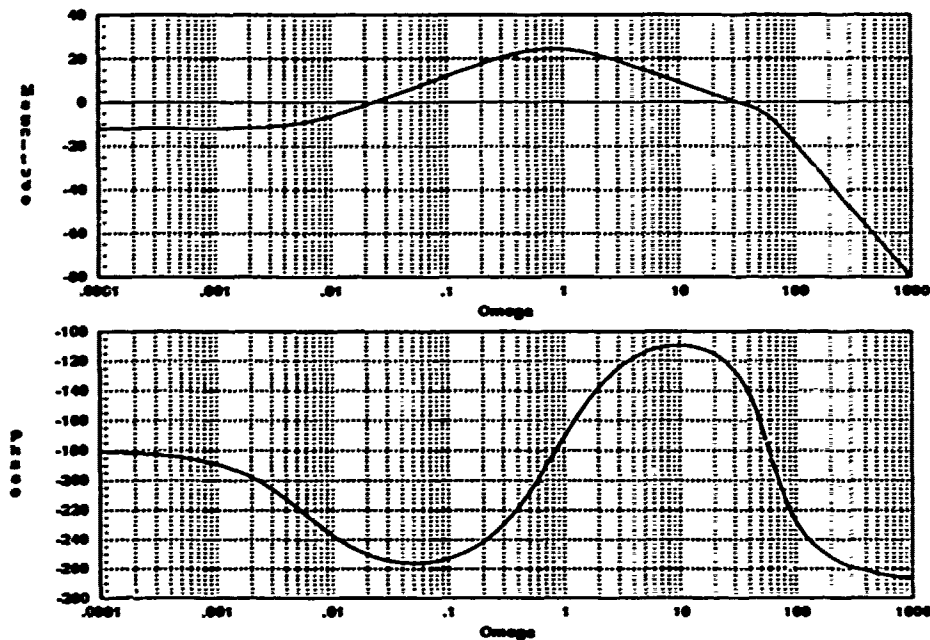


Figure 4.4. Bode Plot - Pitch Rate Loop Transmission 1 ($\alpha = 20$)

While the gain and phase margins can be read from either the Nichols or the Bode plot, the *Matrixx* *margin* command easily provides the values to a greater accuracy. In this case, the gain margin is +6.07 dB, and the phase margin is ± 49.35 degrees. These are considered reasonable values for stability margins, based on past experience in designing flight control systems [15].

A point worthy of mention is the effect of the non-minimum phase zero on the feedback performance. In a minimum phase system (no RHP zeros), the loop transmission gain is typically rather flat until ω reaches the desired roll-off frequency. In this system, however, the non-minimum phase zero has resulted in a lowering of the loop transmission gain in the low-frequency range (see Figure 4.4). The resulting lack of feedback benefits in this range is acceptable because it permits reasonably good feedback benefits in the more desirable mid frequency range [14].

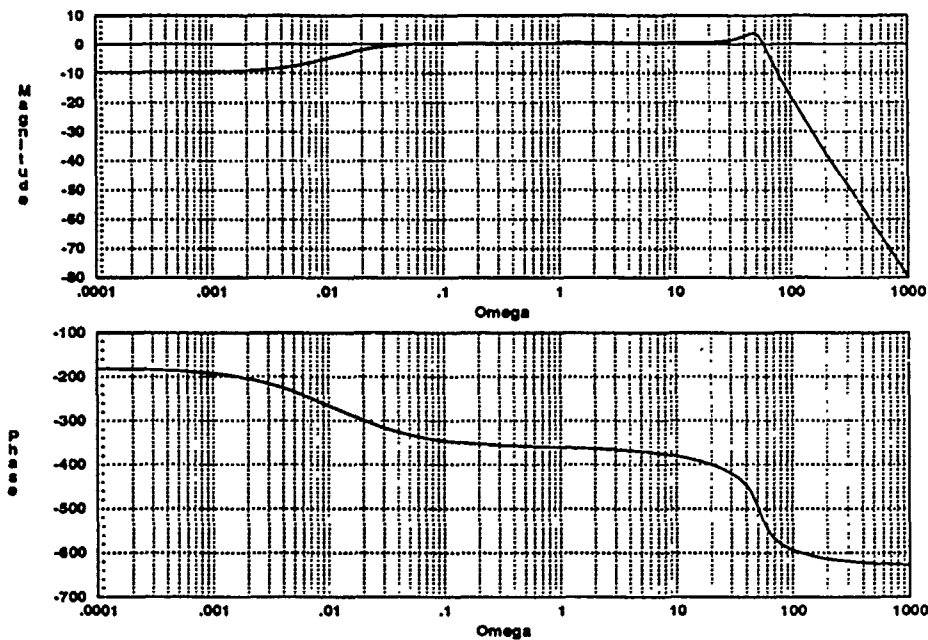


Figure 4.5. Bode Plot - Pitch Rate Closed Loop Transmission 1 ($\alpha = 20$)

The design process results in an ω_n value of 60, the additional pole being placed at -1, and an up front gain of 0.25. The final loop transmission function for this case is given in Equation 4.2. The additional gain terms are required to offset the steady state values of the individual poles and zeros.

$$L_{20q(1)} = \frac{(0.25)(0.7080)(3600)(s - 0.0061)}{(0.0061)(s - 0.7080)(s + 1)(s^2 + 60s + 3600)} \quad (4.2)$$

The closed-loop transmission function is given by Equation 4.3, and the resulting Bode plot is shown in Figure 4.5. This plot is to be modified by the prefilter transfer function to optimize the time response, as discussed in the next section of this chapter.

$$T_L = \frac{L}{1 + L} \quad (4.3)$$

Finally, the compensator transfer function is determined by use of Equation 4.1. In this case, Equation 4.2 is divided by the factored form of $P_{eff}(lon20)$, which is given by the roots in Table 4.1 multiplied by the polynomial gain of 0.8. The resulting compensator transfer function is shown below.

$$G_{20q(1)} = \frac{130,570(s^2 + 0.0406s + 0.0162)(s + 1.0302)(s + 20)(s + 50)}{s(s^2 + 60s + 3600)(s + 1)(s + .2304)(s + 31.5489)} \quad (4.4)$$

An alternative design is now shown that results in a simpler compensator transfer function. The loop transmission function is designed as before, except that the second order pair of poles is now chosen to be the convolution of $(s+20)$ and $(s+50)$. This results in an additional *effective* cancellation in the expression for G . Also, an additional gain factor of 0.5 is used to achieve a desirable stability margin. *MatrixX* gives the gain and phase margins as +12.59 dB and +37.35 degrees, respectively. The larger gain margin is required to ensure a reasonably high phase margin. The alternate loop transmission function is given by Equation 4.5 and the simpler compensator transfer function is given by Equation 4.6.

$$L_{20q(2)} = \frac{(0.25)(0.5)(0.7080)(1000)(s - 0.0061)}{(0.0061)(s - 0.7080)(s + 1)(s^2 + 70s + 1000)} \quad (4.5)$$

$$G_{20q(2)} = \frac{18,135(s^2 + 0.0406s + 0.0162)(s + 1.0302)}{s(s + 1)(s + .2304)(s + 31.5489)} \quad (4.6)$$

Figure 4.6 is the Nichols plot of the alternate loop transmission function and the corresponding Bode plot is shown in Figure 4.7. Finally, the closed-loop transmission function based on the alternative design is shown in Figure 4.8. Comparison of Figures 4.4 and 4.7 shows that the alternate design has slightly less loop transmission gain, which results in decreased feedback benefits. Also, the phase margin is somewhat lower in the second design. However, the trade-offs are probably acceptable, given the benefits of the reduced order compensator transfer function.

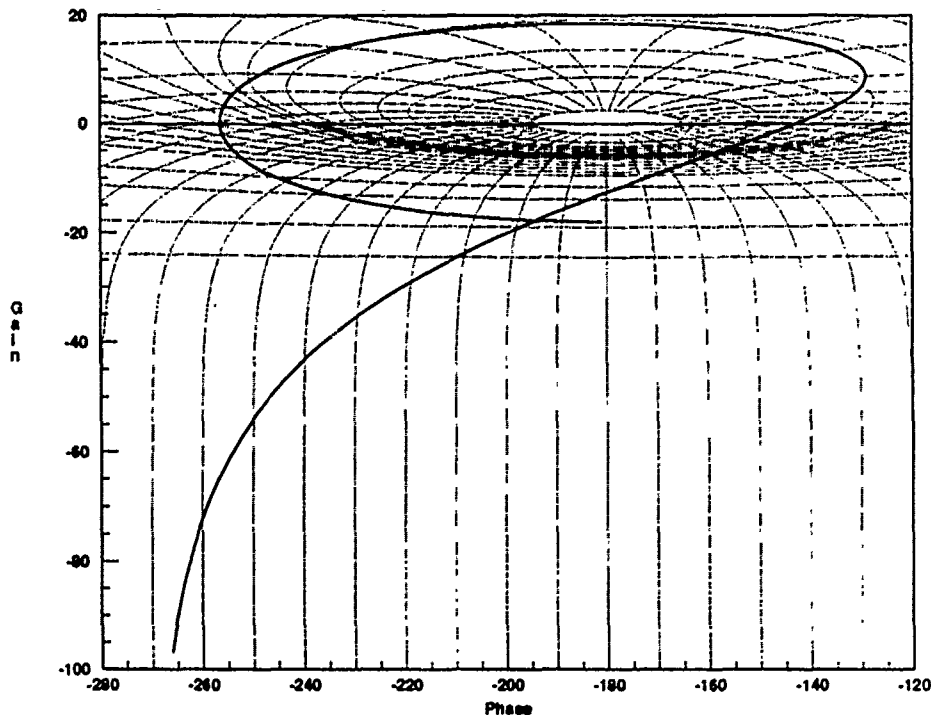


Figure 4.6. Nichols Plot - Pitch Rate Loop Transmission 2 ($\alpha = 20$)

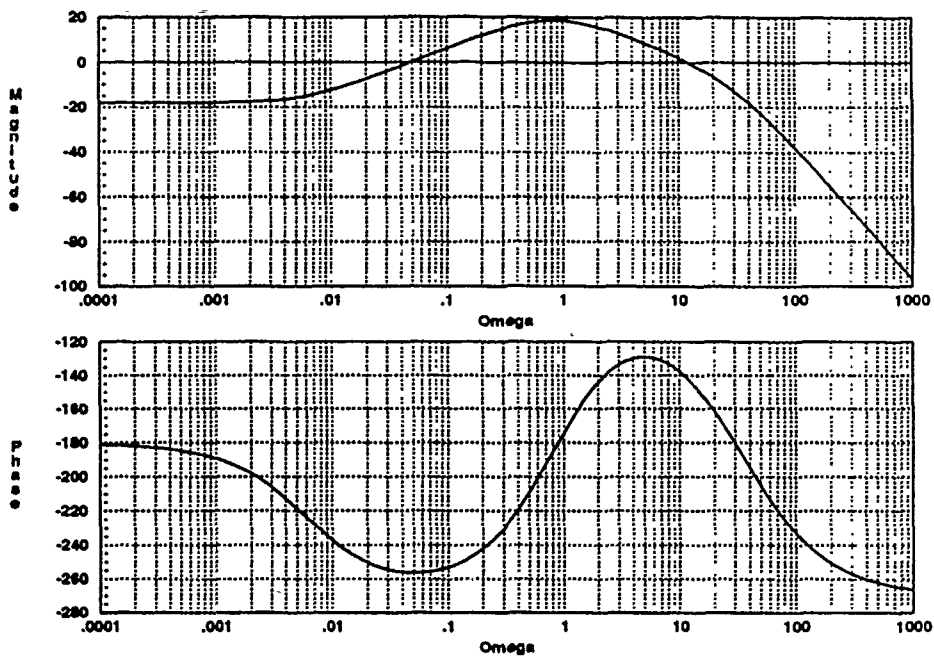


Figure 4.7. Bode Plot - Pitch Rate Loop Transmission 2 ($\alpha = 20$)

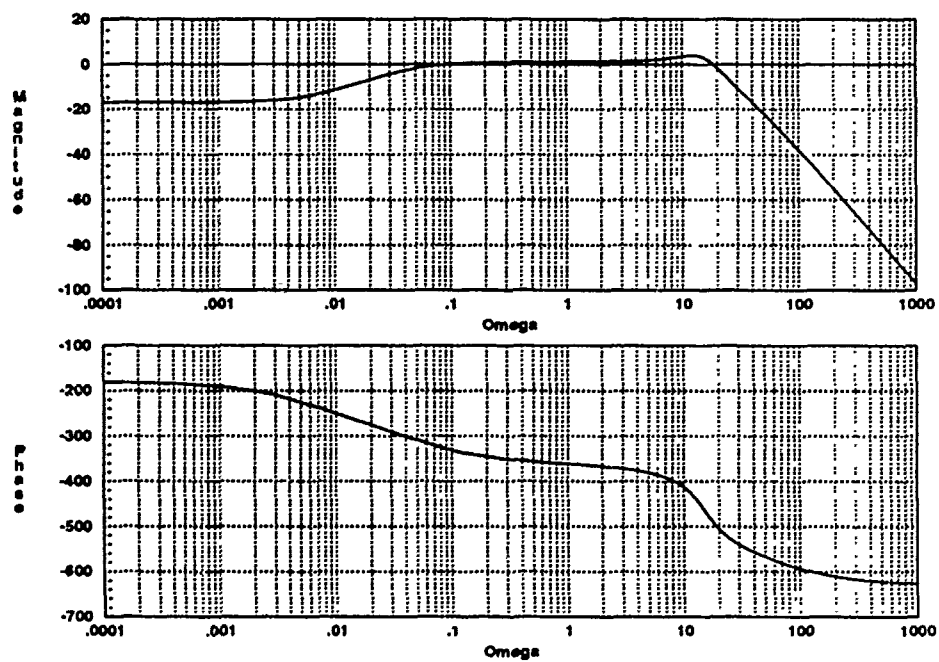


Figure 4.8. Bode Plot - Pitch Rate Closed Loop Transmission 2 ($\alpha = 20$)

The 40 degree loop transmission functions are designed just like the ones for the 20 degree case. In general, the same qualitative analysis applies to these cases, as well. The loop transmission gain is maximized in the mid-frequency range and the stability margins are again reasonable, based on past experience in designing aircraft flight control systems [15]. For the first design, the gain margin is +6.66 dB and the phase margin is +44.59 degrees. Figure 4.9 is the Nichols plot of the function and Figures 4.10 and 4.11 are the respective open and closed-loop Bode plots. Note that frequency responses are very similar to those shown in the 20 degree case.

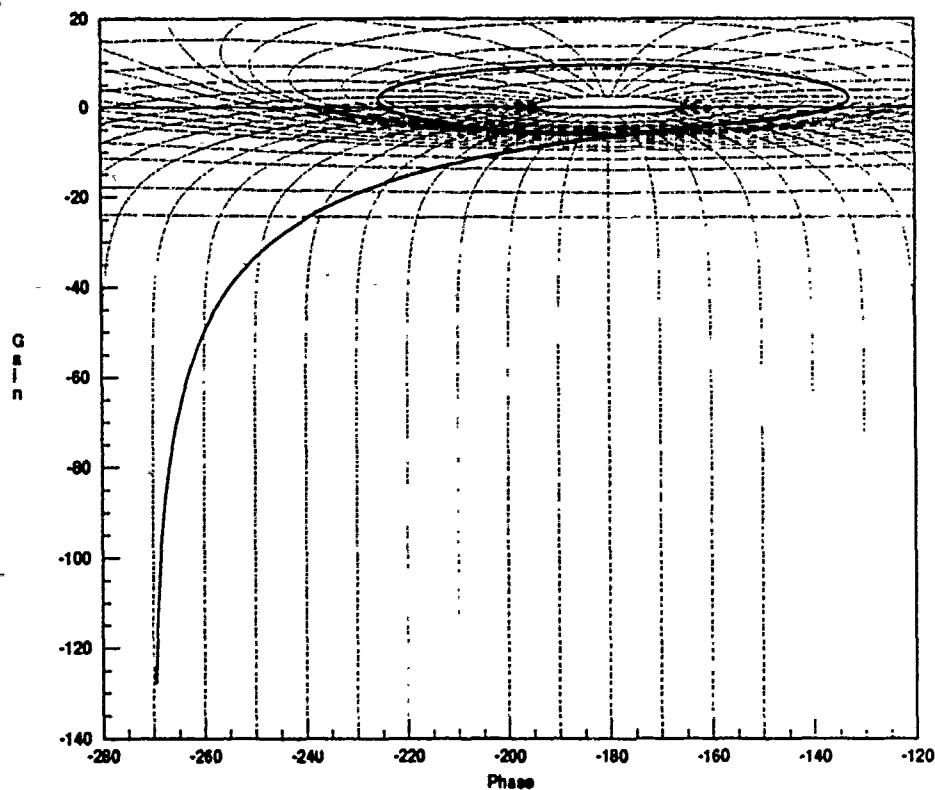


Figure 4.9. Nichols Plot - Pitch Rate Loop Transmission 1 ($\alpha = 40$)

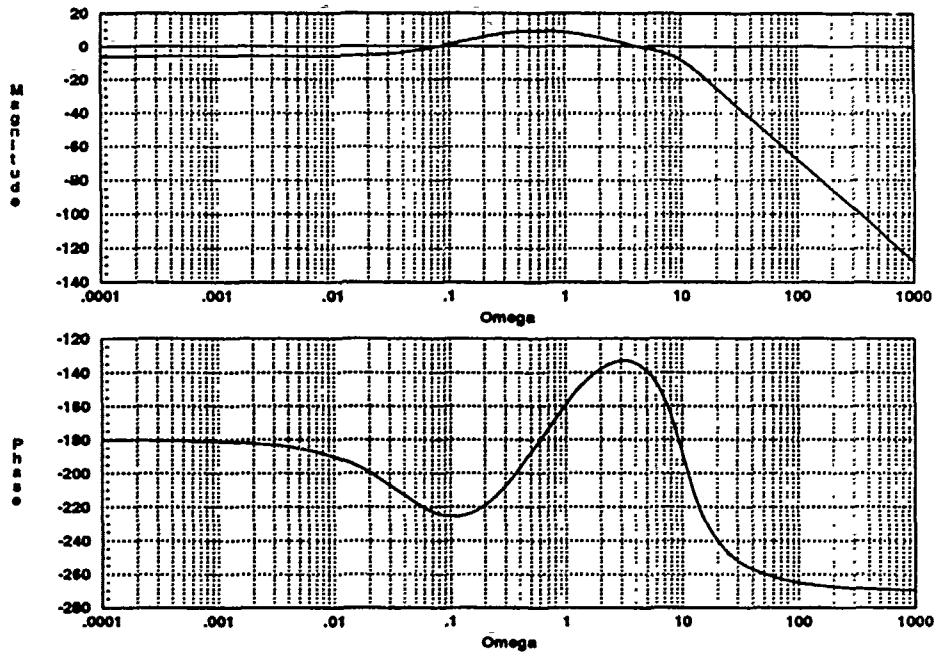


Figure 4.10. Bode Plot - Pitch Rate Loop Transmission 1 ($\alpha = 40$)

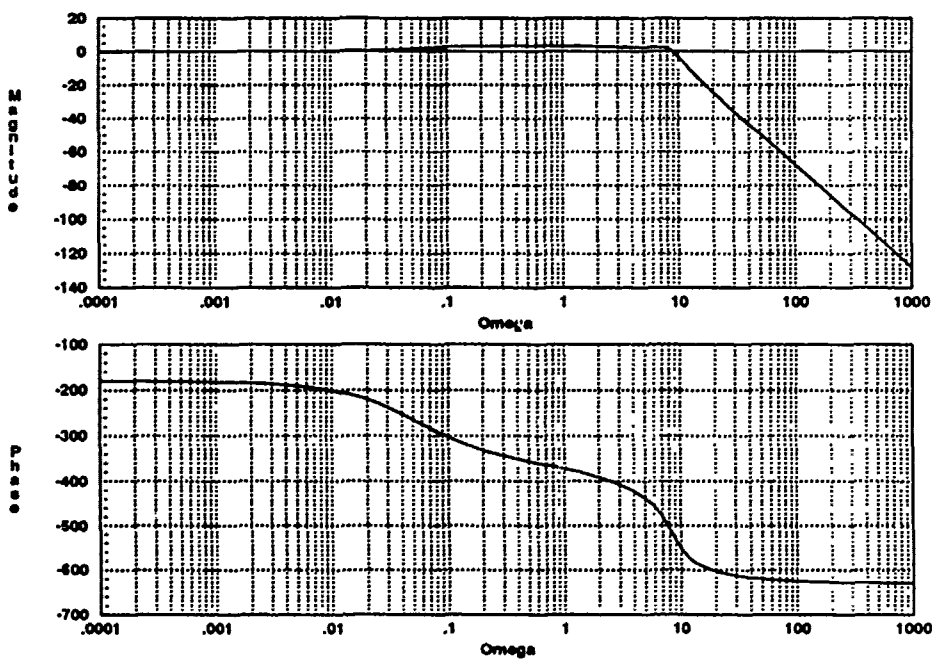


Figure 4.11. Bode Plot - Pitch Rate Closed Loop Transmission 1 ($\alpha = 40$)

The initial design loop transmission function for this flight condition is given by Equation 4.7, and after applying Equation 4.1, the resulting compensator transfer function is given by Equation 4.8.

$$L_{40q(1)} = \frac{(0.5)(0.3756)(100)(s - 0.0458)}{(0.0458)(s - 0.3756)(s + 1)(s^2 + 10s + 100)} \quad (4.7)$$

$$G_{40q(1)} = \frac{585(s^2 + 0.1068s + 0.0171)(s + 0.8200)(s + 20)(s + 50)}{s(s^2 + 10s + 100)(s + 1)(s + .3076)(s + 32.4259)} \quad (4.8)$$

Analogous to the twenty degree case, an alternate design is shown that takes advantage of an additional effective cancellation to simplify the compensator. As before, the second order pair of poles is designed to cancel out the $(s+20)$ and $(s+50)$ terms. In this case, the additional real pole is located at -3 , and the overall gain is not adjusted. The resulting gain margin is $+12.91$ dB and the phase margin is $+33.05$ degrees. As noted with the second design for the 20 degree case, excess gain margin is required to ensure a reasonable phase margin.

Figure 4.12 is the Nichols plot of this loop transmission function, and the corresponding open and closed-loop Bode plots are shown in Figures 4.13 and 4.14. Finally, the loop transmission function is given in Equation 4.9, and the resulting simpler compensator transfer function is given in Equation 4.10.

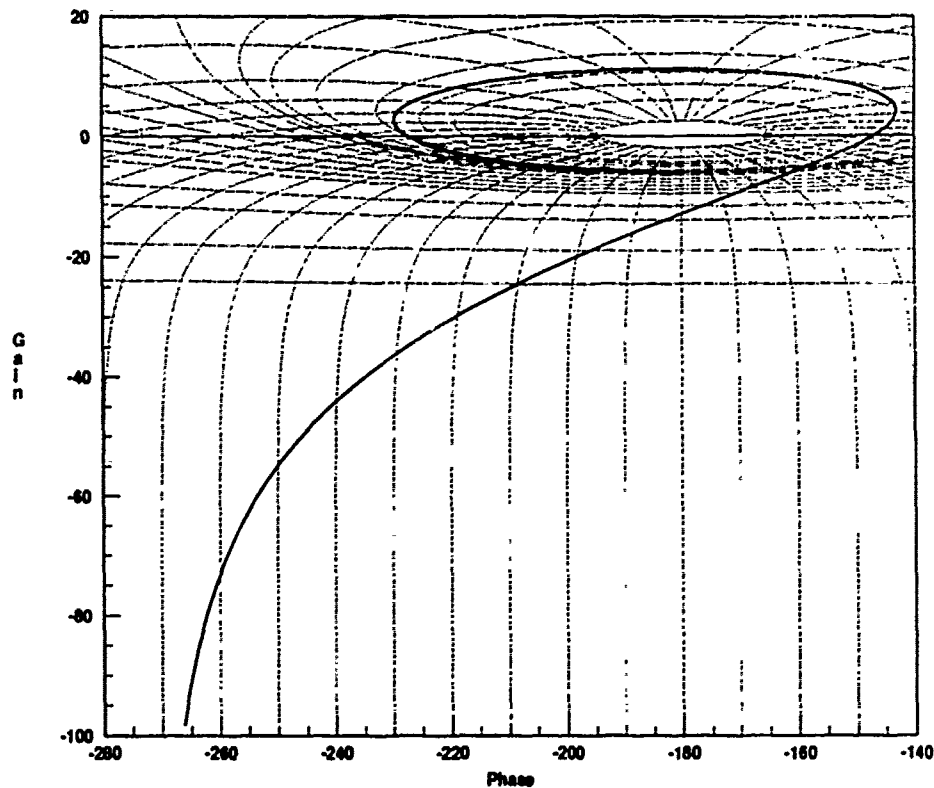


Figure 4.12. Nichols Plot - Pitch Rate Loop Transmission 2 ($\alpha = 40$)

$$L_{40q(2)} = \frac{(0.5)(0.3756)(1000)(s - 0.0458)}{(0.0458)(s - 0.3756)(s + 1)(s^2 + 70s + 1000)} \quad (4.9)$$

$$G_{40q(2)} = \frac{5850(s^2 + 0.1068s + 0.0171)(s + 0.8200)}{s(s + 1)(s + .3076)(s + 32.4259)} \quad (4.10)$$

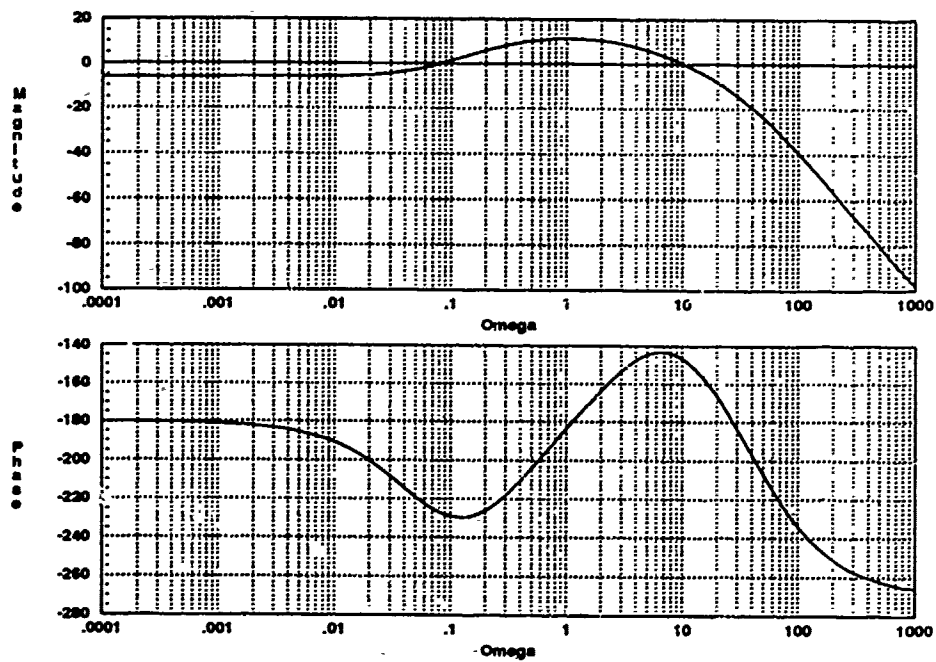


Figure 4.13. Bode Plot - Pitch Rate Loop Transmission 2 ($\alpha = 40$)

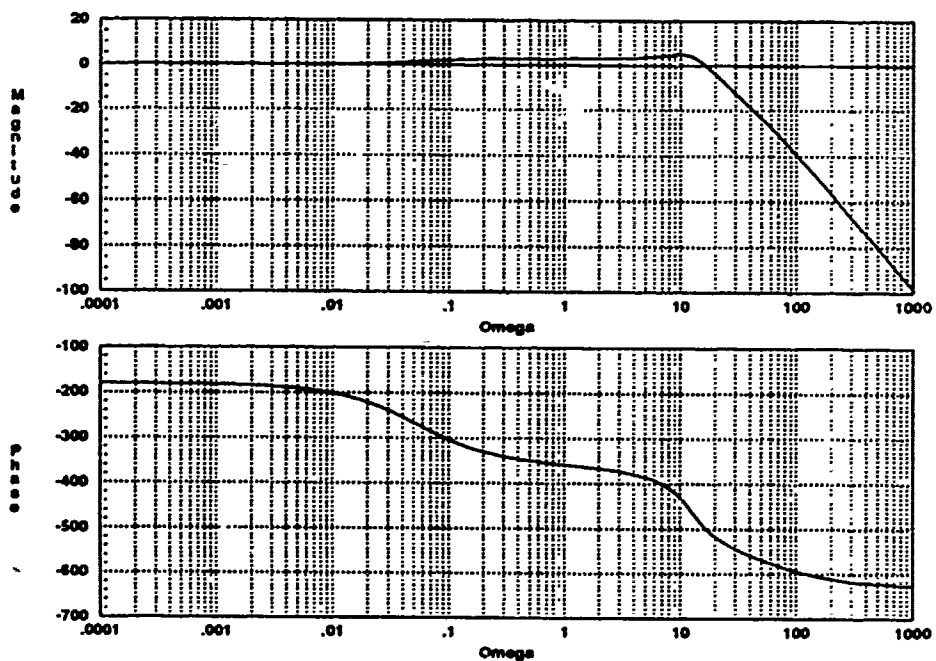


Figure 4.14. Bode Plot - Pitch Rate Closed Loop Transmission 2 ($\alpha = 40$)

As mentioned previously, the 50 degree longitudinal case poses a significant problem. Referring to Table 4.3, it is noted that the ratio of the RHP zero to pole is only 1.0866. This extremely close proximity severely limits the achievable gain margin. In fact, given the limitations of applying LTI design techniques to this particular problem, it is shown that the system stability margins cannot be made great enough to be practical. Nevertheless, the system can be made stable (though just barely) by use of the *optimal blending* method. Optimal blending is one of Professor Horowitz' variations of the basic QFT methods. This method is discussed, but not applied, in Walke's thesis [27].

The complete derivation of the optimal blending method is presented in a paper entitled *Design of Feedback Systems with Non-Minimum Phase Unstable Plants* [12]. The discussion presented here is only a brief look at the application of the method to this particular problem.

As before, the loop transmission function is designed to contain a pole at 0.0785 and a zero at 0.0853, to effectively cancel with the corresponding terms in the P_e . The optimal blending method derives its name from the fact that the design is optimal with respect toward achieving an acceptable gain margin. The optimality is measured by maximizing the ratio of allowable gains that result in a stable closed-loop system.

The optimal condition results from a forced *symmetry* in the s -plane. By *balancing* the RHP pole and zero with their equivalent LHP counterparts, a symmetry about the $j\omega$ axis is obtained. With increasing negative gain values, the poles migrate to the $j\omega$ axis and travel out to infinity, eventually coming back in on the real axis to terminate on the zeros. The root locus depicting this situation is sketched in Figure 4.15. Note that only the RHP poles and zeros of L are balanced by this method. There is no need to balance the LHP poles and zeros since they do not cause the closed-loop system to be unstable.

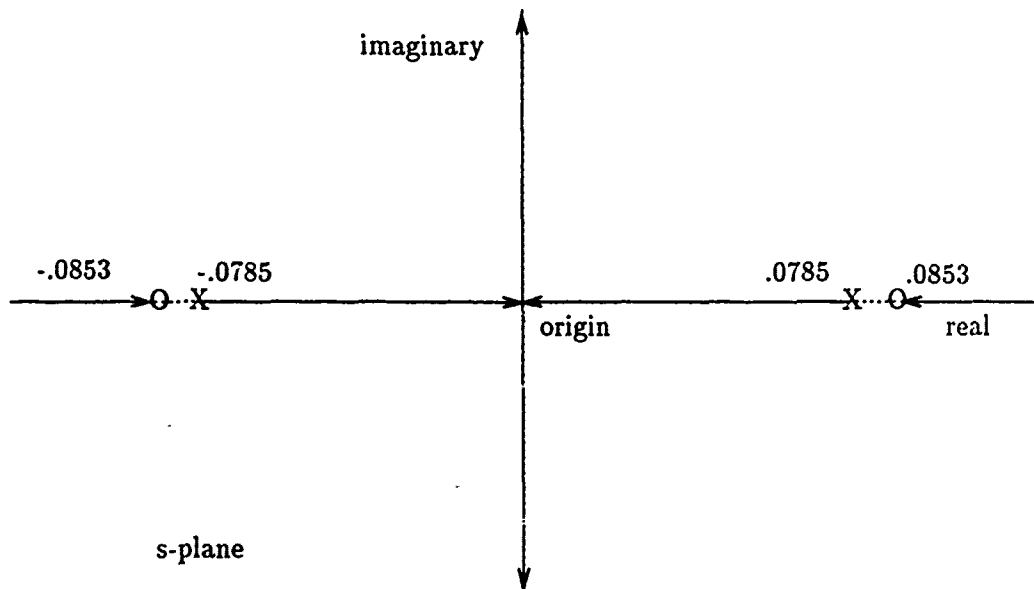


Figure 4.15. Root Locus Sketch of Optimal Blending (Marginal Stability)

From this it is clear that for some range of gain values, the closed loop poles are on the $j\omega$ axis, thus making the system *marginally* stable. Taking this one step further, if the symmetric axis is offset into the LHP by some σ value, there is a range of gain values for which the system is completely stable. For this case, σ is chosen to be -1 , and the resulting shifted root-locus is sketched in Figure 4.16. The upper limit of σ is limited by the fact that as the offset value is increased, the ratio of allowable gains for a stable closed-loop system decreases. The lower limit may be any value that places the line of symmetry *comfortably* within the LHP, and the *exact* value is somewhat arbitrary [15].

Thus, the optimal blending method has provided an LHP pole/zero pair to ensure the stability of the closed-loop system. Finally, the minimum excess of two poles over zeros is provided by the addition of a second order pair of poles. By

placing the extra poles far off in the LHP (i.e. large ω), the symmetry is not disturbed significantly. With a value of ω equal to 400, the 50 degree loop transmission function is defined by Equation 4.11.

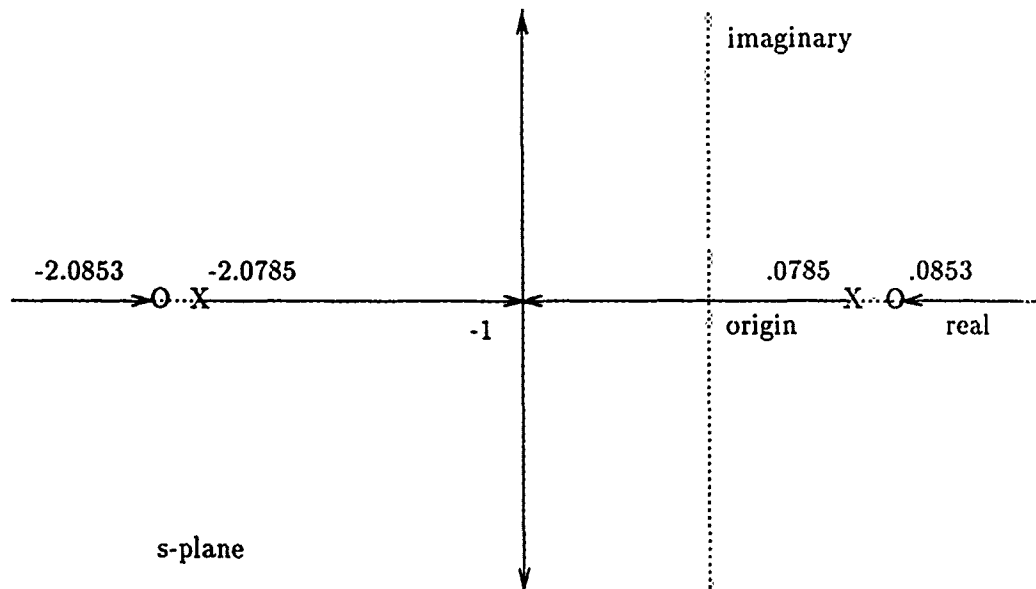


Figure 4.16. Root Locus Sketch of Shifted Optimal Blending (Stable)

$$L_{50q} = \frac{-(1.0785)^2(160,000)(s - 0.0853)(s + 2.0853)}{(1.0853)^2(s - 0.0875)(s + 2.0785)(s^2 + 400s + 160,000)} \quad (4.11)$$

The Nichols plot of this function is shown in Figure 4.17. Readily apparent is the way the loop transmission function *hooks* around the zero dB/-180 degree point. Figure 4.18 is a detail view of this region. The actual gain and phase margins are +0.09 dB and +1.45 degrees, respectively. Clearly, such stability margins are not acceptable for a realizable system. However, it has been shown that the optimal

blending method can result in a stable closed-loop system, even when based on a virtually unworkable open-loop problem.

Horowitz points out that in actual practice, the problem could be *re-defined* by using different combinations of control variables, that could result in a minimum phase open-loop plant. An unstable *minimum phase* system does not limit the designer by having RHP poles and zeros in close proximity to each other. Thus, it becomes far easier to stabilize the system over a relatively wide range of gain values [14]. An example of using different control variable combinations may be seen on the X-29. That aircraft's normal digital longitudinal control system feeds back a combination of pitch rate, normal acceleration, and canard position through several stages of frequency dependent filters and gain functions [3].

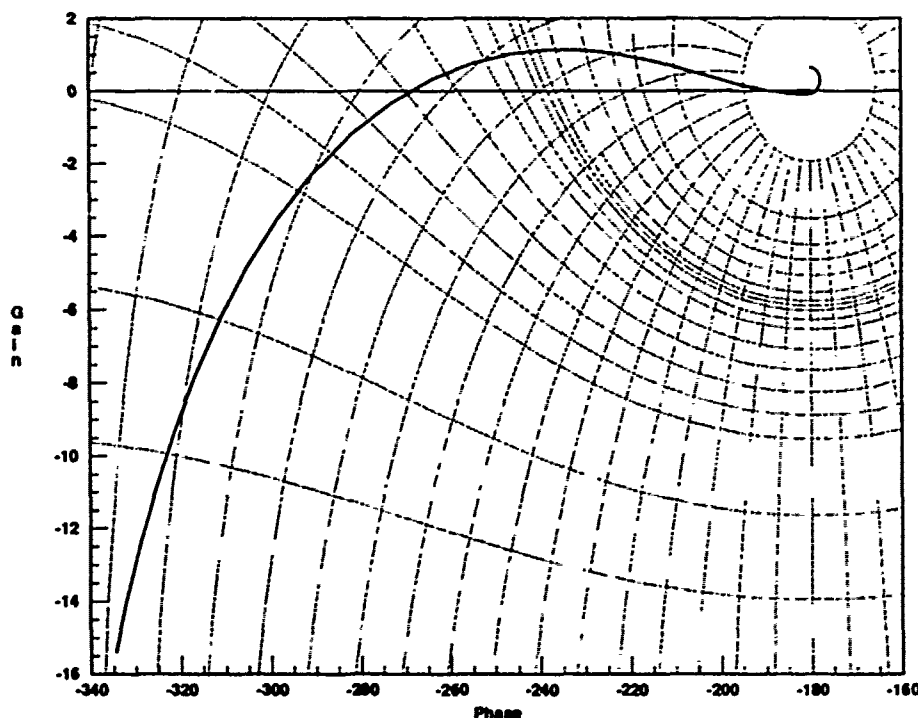


Figure 4.17. Nichols Plot - Pitch Rate Loop Transmission ($\alpha = 50$)

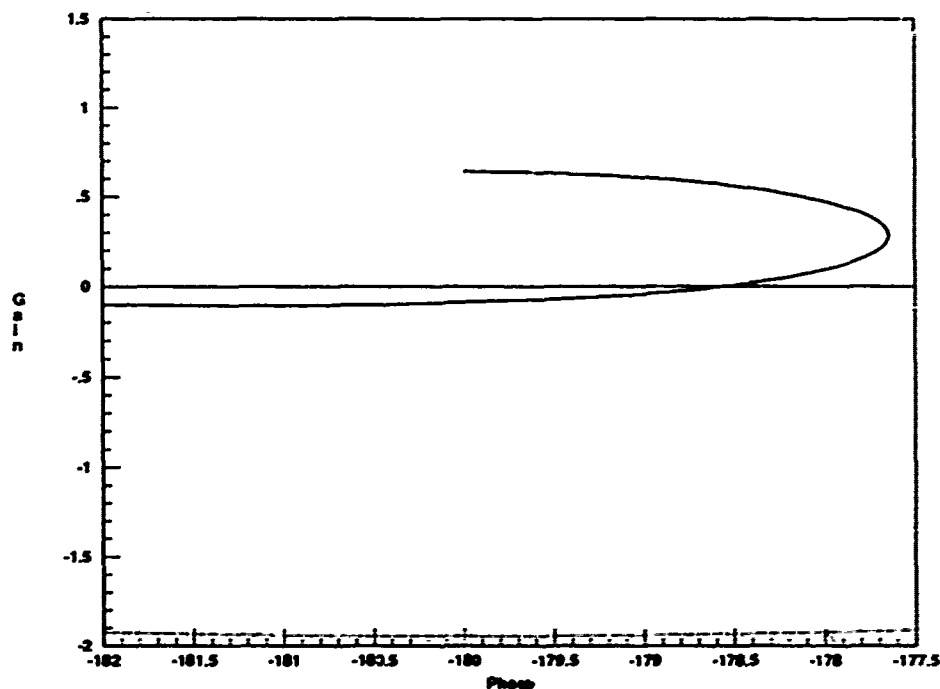


Figure 4.18. Detailed Nichols Plot - Pitch Rate Loop Transmission ($\alpha = 50$)

The open and closed-loop Bode plots of the 50 degree loop transmission function are shown in Figures 4.19 and 4.20, respectively. The resulting compensator transfer function is rather high order and is given by Equation 4.12.

$$G_{50q} = \frac{-175,560(s + 2.0853)(s^2 + 0.0754s + 0.0248)(s + 0.649)(s + 20)(s + 50)}{s(s + 2.0785)(s^2 + 400s + 160,000)(s + 0.3280)(s + 31.9758)} \quad (4.12)$$

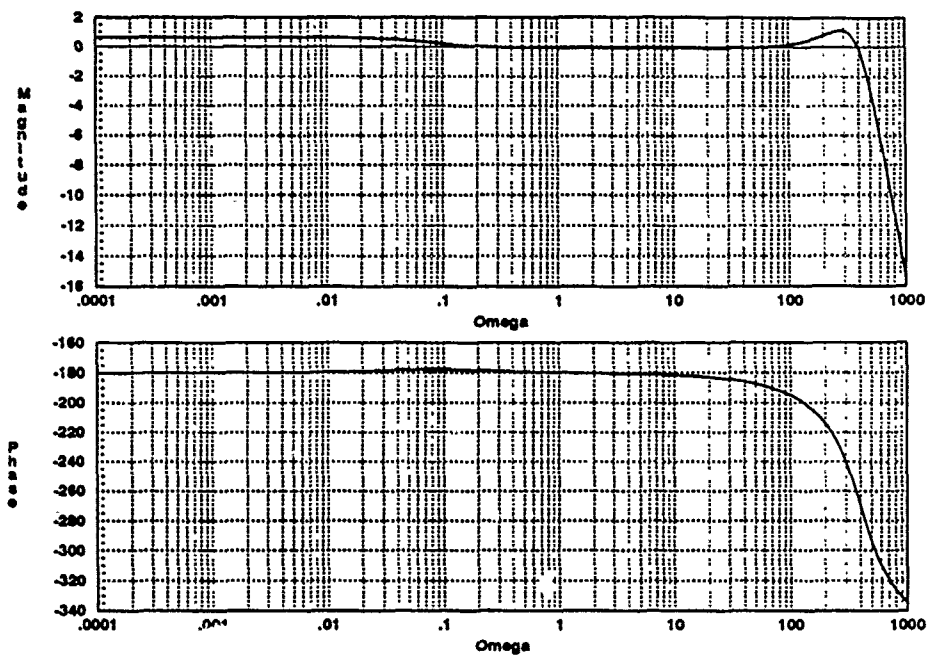


Figure 4.19. Bode Plot - Pitch Rate Loop Transmission ($\alpha = 50$)

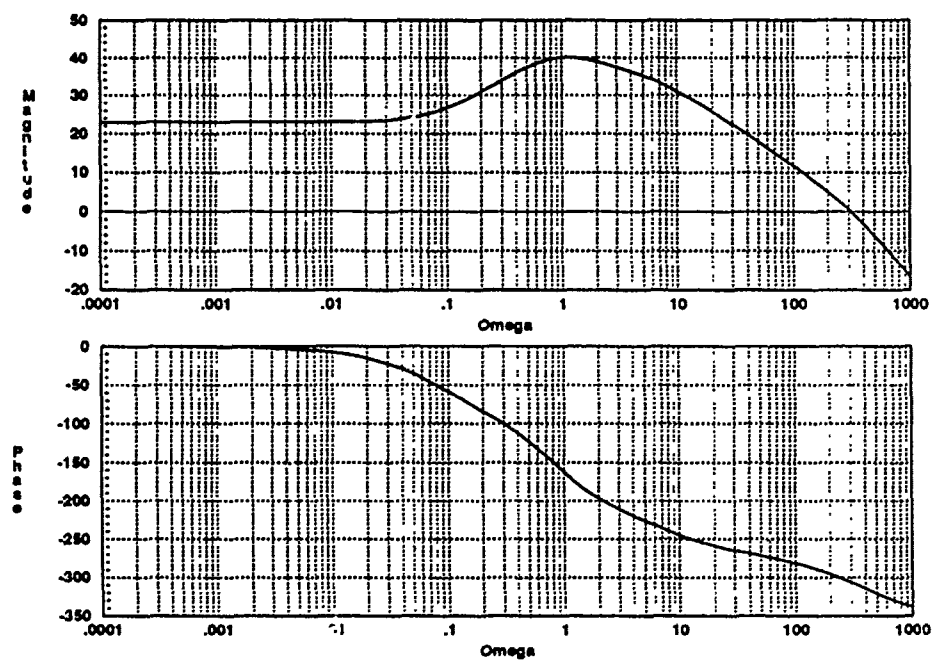


Figure 4.20. Bode Plot - Pitch Rate Closed Loop Transmission ($\alpha = 50$)

Finally, the 60 degree loop transmission function is designed from the start to maximize the number of effective cancellations, so that a relatively low order compensator may be realized. Referring to Table 4.4, it is decided to effectively cancel three zeros and two poles from the effective plant. With two additional real poles and another pair of complex poles, the resulting loop transmission function is given by Equation 4.13. The Nichols plot of this function is shown in Figure 4.21.

$$L_{60q} = \frac{4,453,630(s - 0.1373)(s + 0.3318)(s + 35)}{(s + 0.2586)(s + 20)(s + 10)(s + 5)(s^2 + 200s + 40,000)} \quad (4.13)$$

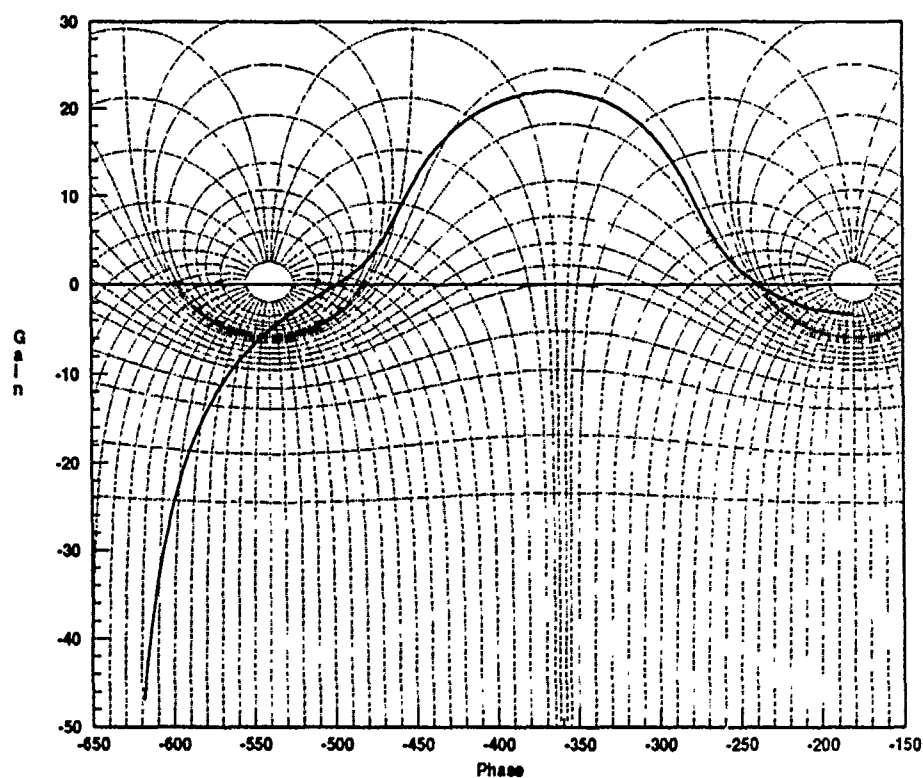


Figure 4.21. Nichols Plot - Pitch Rate Loop Transmission ($\alpha = 60$)

It is clearly evident on the Nichols plot that this particular loop transmission function has two cross-over frequencies. Horowitz points out that even moderate feedback benefits require some loop transmission gain to be significantly greater than one over some range of ω [13]. In this case, L has been maximized as much as possible in the mid-frequencies without diminishing the stability margins to unacceptable values. Note that there are two regions of instability to avoid in this case (zero-dB/-180 degrees and zero-dB/-540 degrees). Because of the large excess of poles over zeros and the additional phase lag contributed by the RHP zero, this function approaches -630 degrees of phase lag as ω goes to infinity. The actual gain and phase margins (based on the points closest to the instability regions) are +5.04 dB and +41.56 degrees, respectively.

The corresponding open-loop Bode plot is shown in Figure 4.22. The two cross-over frequencies are evident in this figure, and the cross-over frequencies are easily read off the plot.

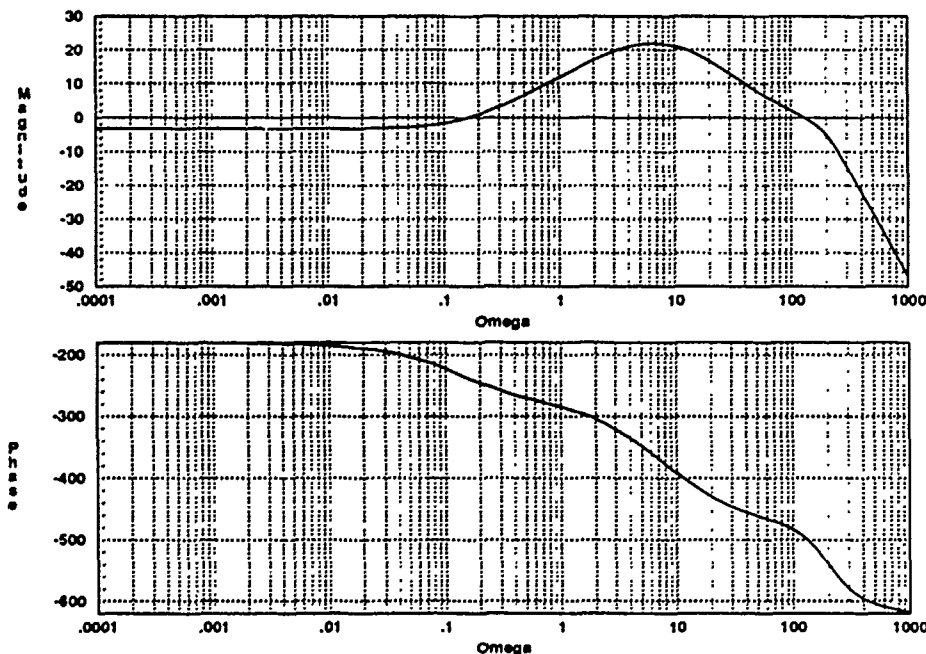


Figure 4.22. Bode Plot - Pitch Rate Loop Transmission ($\alpha = 60$)

The Bode plot of the closed-loop transmission function is shown in Figure 4.23. Note that this plot is quite similar to the closed-loop Bode plots obtained for the other flight conditions. In all but the 50 degree condition, the closed-loop responses approach -630 degrees of phase lag at $\omega = \infty$ regardless of the open-loop phase lag characteristics.

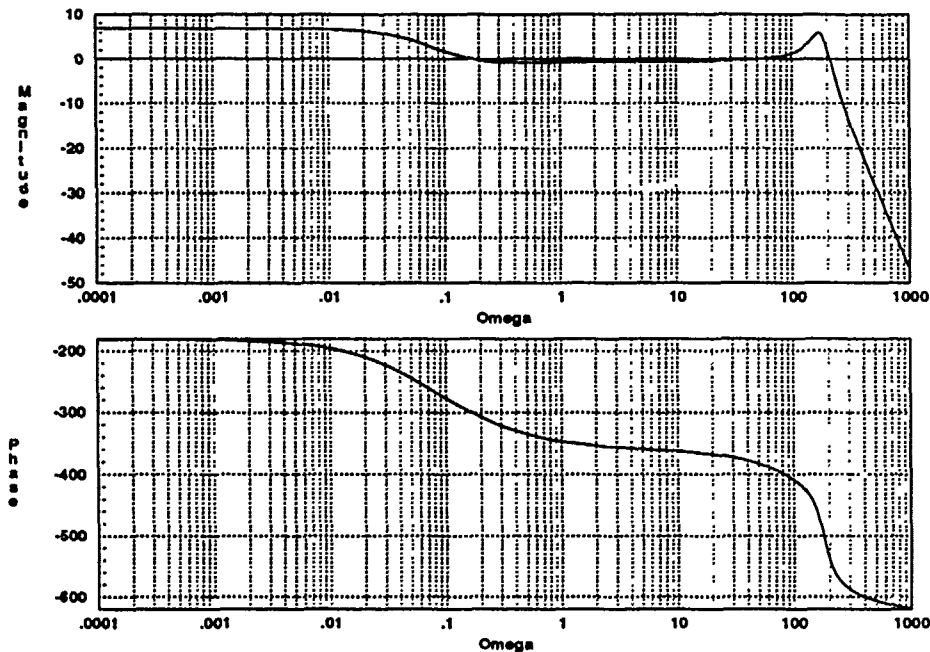


Figure 4.23. Bode Plot - Pitch Rate Closed Loop Transmission ($\alpha = 60$)

Finally, the compensator transfer function for the 60 degree flight condition is given by Equation 4.14. Note the relative simplicity, due to the number of effective cancellations.

$$G_{60q} = \frac{4,453,630(s + 0.0677)(s^2 + 0.0386s + 1.0211)(s + 50)}{(s + 10)(s + 5)(s^2 + 200s + 40,000)} \quad (4.14)$$

4.4 Prefilter Designs and Responses

This section discusses the prefilter designs and their effects on the system time responses. Specifications are not provided for this *academic* design study. However, it is desirable to work toward a realistic set of goals. Therefore, the appropriate military specification for flying qualities is referenced to provide a desired response characteristic. Without reproducing the detail of this entire specification, it is assumed that the models developed here represent a fighter type aircraft flying in category A. Based on these assumptions, the short period damping ratio (ζ_{sp}) for level 2 flying qualities may range from 0.25 to 2.00, according to the standard. For this design, a median value of one is chosen for ζ_{sp} . The short period natural frequency (ω_{sp}) is also chosen to be a median value from the allowable range given in the standard. For this design, a value of three radians/second is chosen for ω_{sp} .

With these values, the desired second order response is plotted with *MatrixX*, and the values of rise time (t_r) and settling time (t_s) are found to be approximately 1.3 seconds and 1.95 seconds, respectively. With a damping ratio of one, there is no overshoot. This type of response is often seen in control problems and experience has shown that to achieve such a response, the Bode magnitude plot should be nearly flat at zero dB up to a roll-off frequency of approximately one radian/second.

Beginning with the first loop transmission design for the 20 degree flight condition, the closed-loop Bode plot is examined (Figure 4.5). It is noted that for the mid-frequency range the magnitude is already zero-dB. Therefore, two portions of the plot require adjusting. The low-frequency range needs to be raised to the zero dB level and the magnitude needs to roll-off at around one radian/second. A pole/zero pair handles the low-frequency portion, and once again the values are obtained iteratively by observing the Bode plot as the parameters are varied. The desired roll-off is accomplished by adding a pole at $s = -2$. The prefilter for this condition is given by Equation 4.15. Note that the steady state gain value of this prefilter is not unity, as is typically the case for prefilter designs. This is because the steady state value of

T_L is less than one due to the limitations discussed previously. As a result, for this type of problem, the prefilter is used to compensate for the gain discrepancy in the low-frequency (steady state) range. Finally, the compensated Bode plot is shown in Figure 4.24.

$$F_{20-1} = \frac{1.875(s + 0.04)}{(s + 0.0125)(s + 2)} \quad (4.15)$$

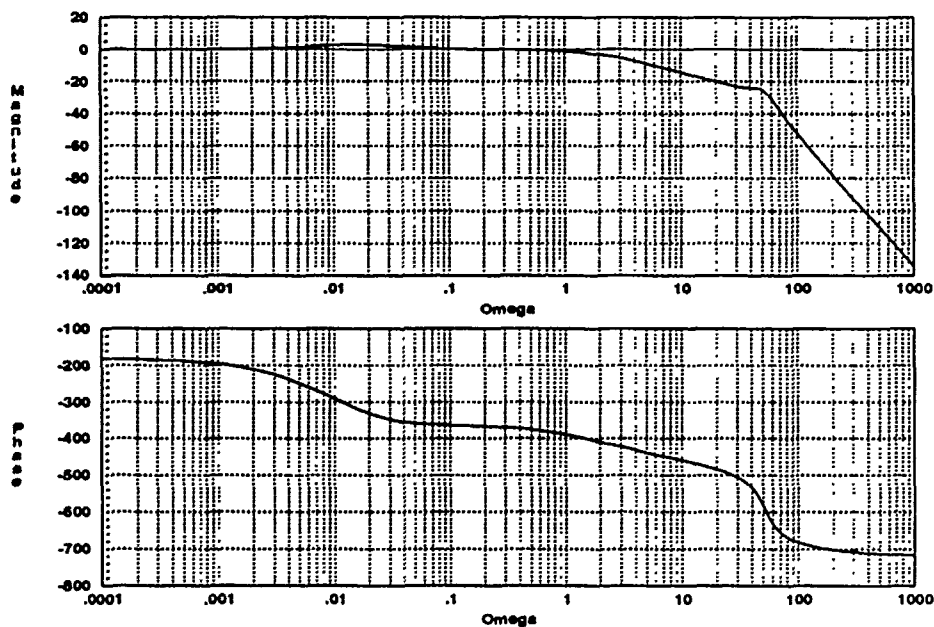


Figure 4.24. Bode Plot - Pitch Rate Design 1 with Prefilter ($\alpha = 20$)

It is known that the step response of a non-minimum phase system does not directly approach the steady state value. Instead, the response first goes in the opposite direction, before crossing the x-axis and then approaching the steady state value. Further, the amount of time spent in the opposite direction is inversely proportional to the magnitude of the RHP zero that caused the effect. In this case, the non-minimum phase zero is at $s = 0.0061$. The associated time constant is quite large so that the response does not cross the zero axis until approximately 120 seconds, and does not reach the steady state value until approximately 500 seconds.

Using this fact to advantage, the region of negative response is used as the desired transient control region. It is assumed that the slow decay in the opposite direction can easily be controlled by the closed-loop flight control system.

Figures 4.25 through 4.27 are the time response plots of the first case. The same response is plotted on three different time scales to show the effects just discussed. In all cases the response is the pitch rate with the units of degrees/second. The desired region of transient control has a slightly overdamped response with a rise time of approximately 1.2 seconds and a settling time of just over two seconds. These figures compare well with the desired response characteristics discussed above.

In the 20-second plot, the response can be seen falling off as it is heading for the crossover and steady state value. On the 500-second plot, the response has reached the steady state value and the crossover point is at approximately 120 seconds as noted. The steady state value is negative one, since the region of reverse response is chosen to be the transient control region. Thus, the response approaches positive one degree/second in the region of interest. The sign of the steady state value can easily be inverted by including a negative gain in the prefilter.

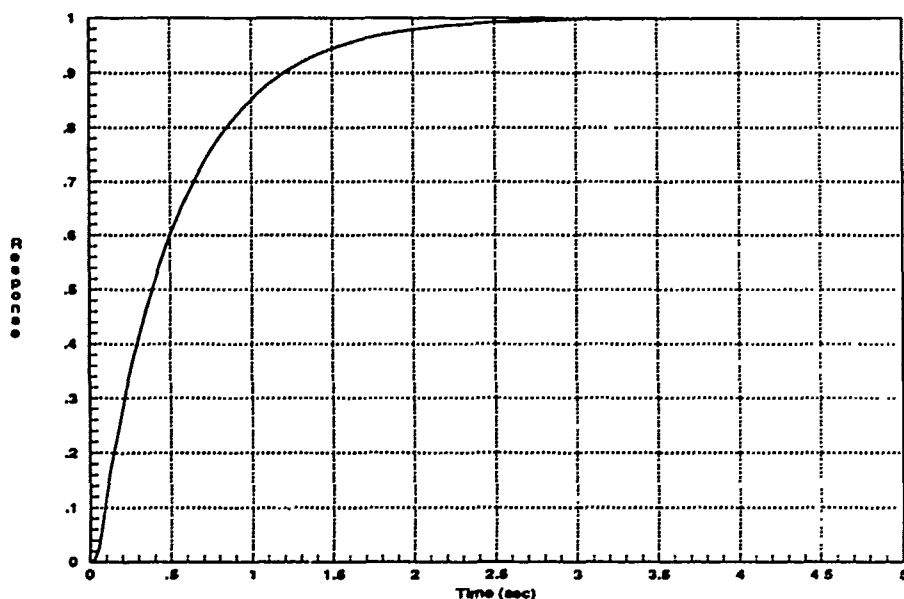


Figure 4.25. Pitch Rate Step Response - Design 1 {5-sec} ($\alpha = 20$)

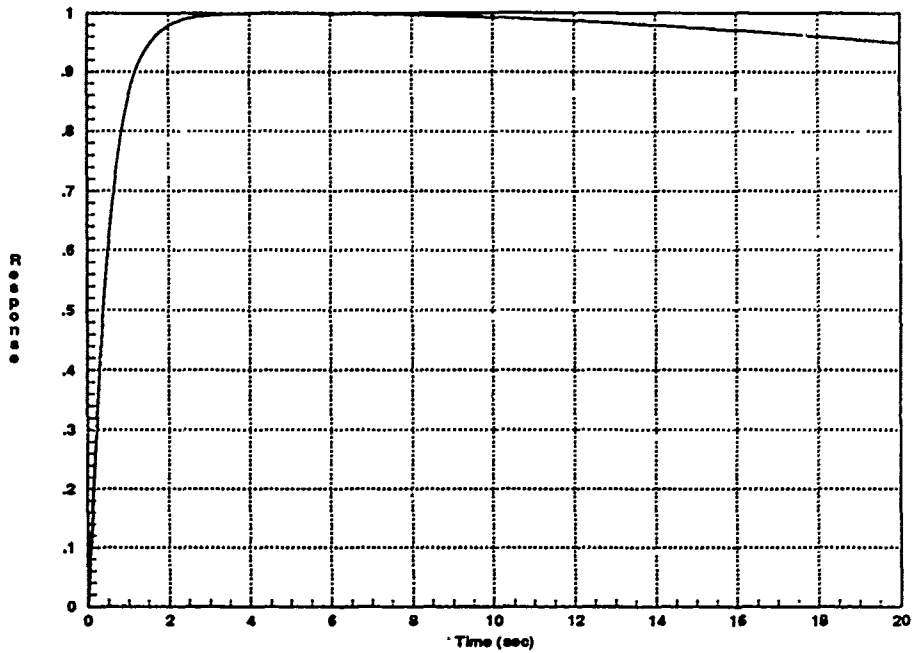


Figure 4.26. Pitch Rate Step Response - Design 1 {20-sec} ($\alpha = 20$)

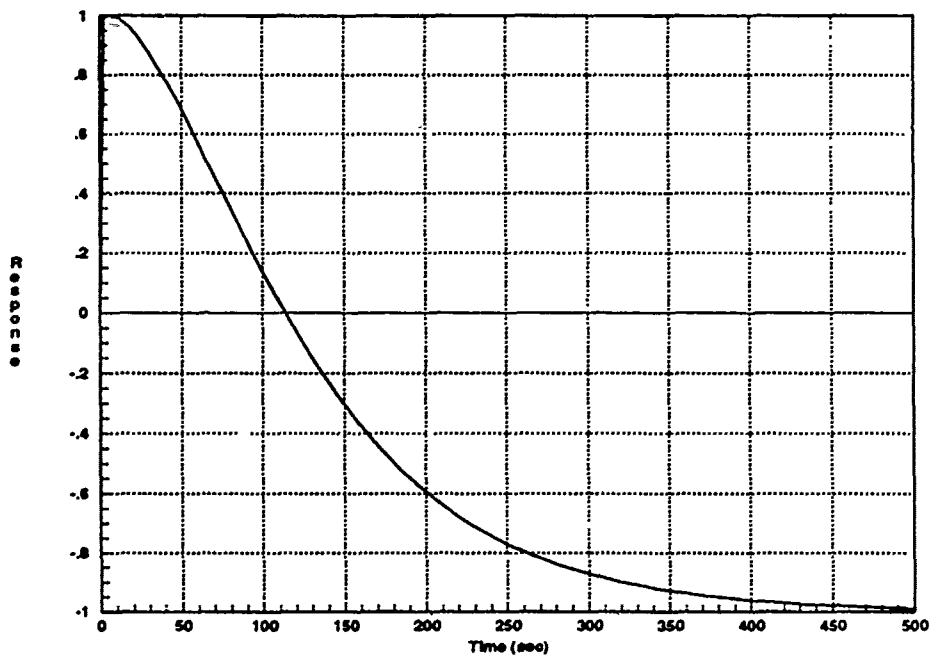


Figure 4.27. Pitch Rate Step Response - Design 1 {500-sec} ($\alpha = 20$)

The design for the alternate 20 degree loop transmission function is performed in an analogous manner. The closed-loop frequency response with prefilter is shown in Figure 4.28. Again, the response is made relatively flat up to the roll-off frequency. The prefilter for this condition is given by Equation 4.16.

$$F_{20-2} = \frac{1.768(s + 0.06)}{(s + 0.0068)(s + 2)} \quad (4.16)$$

Figures 4.29 through 4.31 are the corresponding time response plots for this system. The critical parameters of transient region settling time, crossover time, and steady state settling time are virtually the same as those seen in the last case.

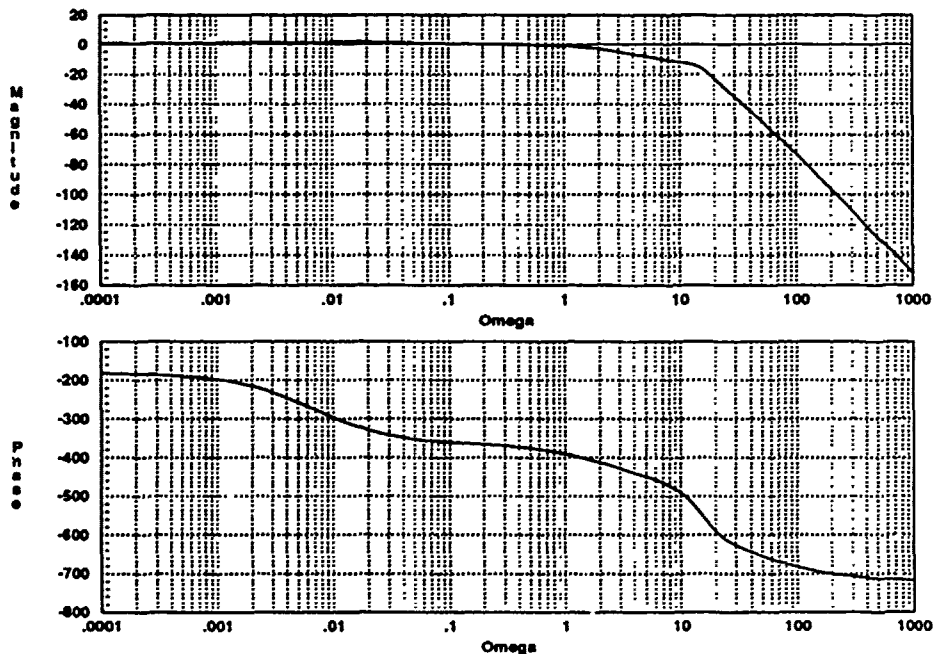


Figure 4.28. Bode Plot - Pitch Rate Design 2 with Prefilter ($\alpha = 20$)

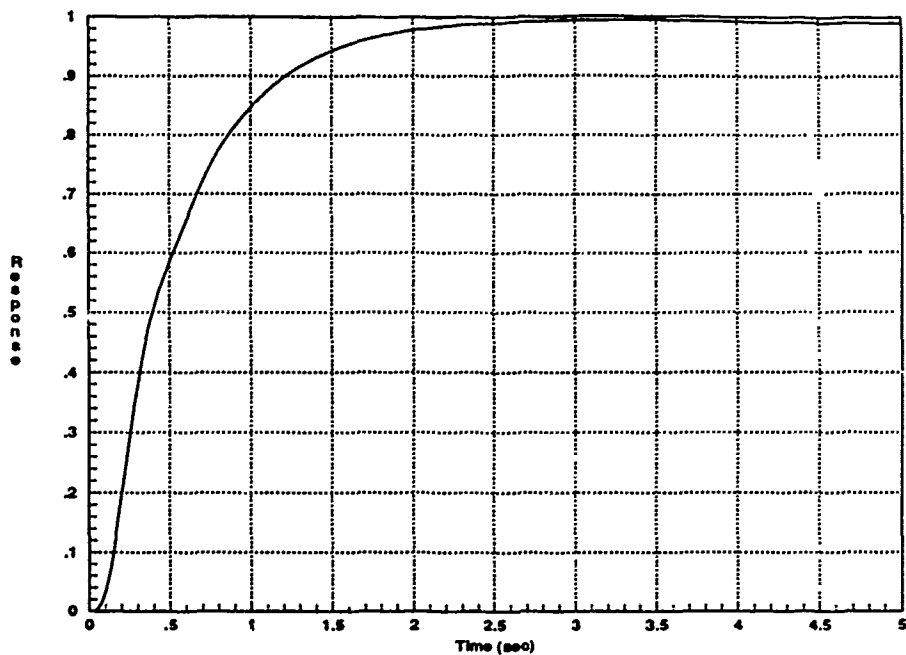


Figure 4.29. Pitch Rate Step Response - Design 2 {5-sec} ($\alpha = 20$)

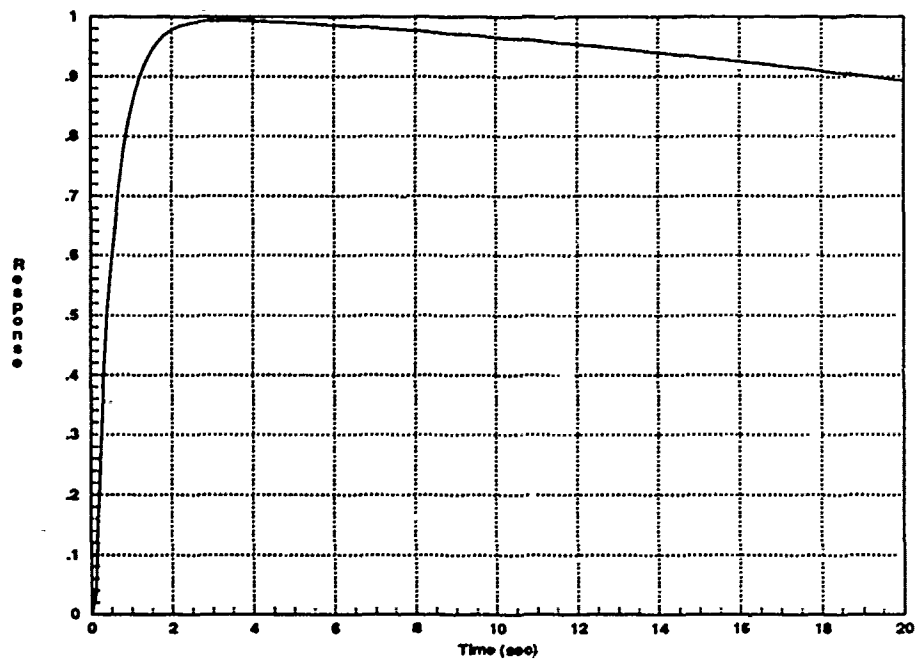


Figure 4.30. Pitch Rate Step Response - Design 1 {20-sec} ($\alpha = 20$)

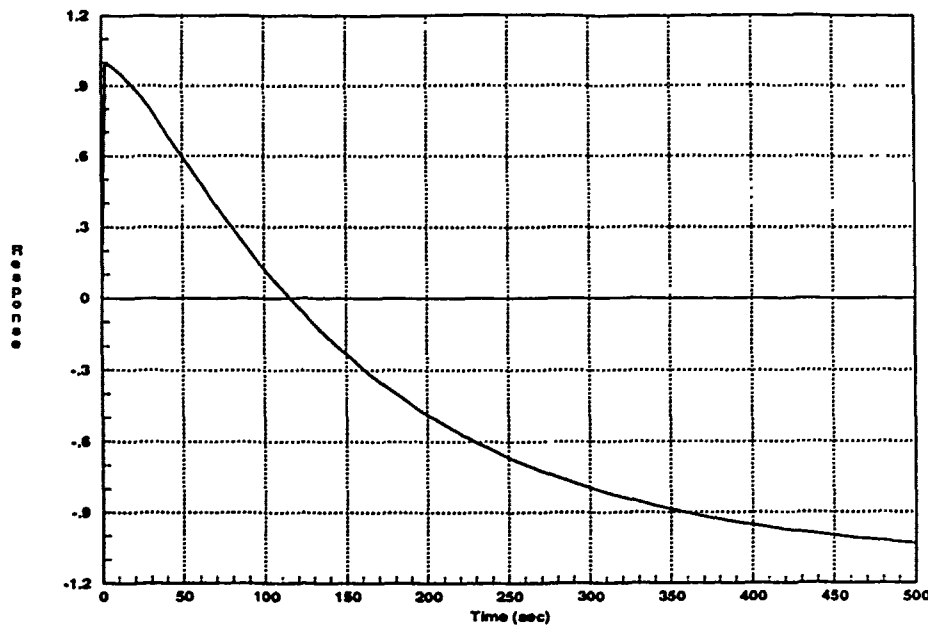


Figure 4.31. Pitch Rate Step Response - Design 1 {500-sec} ($\alpha = 20$)

The design for the first 40 degree prefilter is based on an analysis of Figure 4.11. It is seen that the magnitude in the low-frequency range is already approximately zero-dB. However, the roll-off frequency is a little too high (around eight radians/second) and must be brought back to approximately one radian/second. By developing the prefilter given by Equation 4.17, the desired frequency response is obtained and shown in Figure 4.32.

$$F_{40-1} = \frac{1.180(s + 0.3)}{(s + 0.1)(s + 2)} \quad (4.17)$$

The corresponding time responses are shown in Figures 4.33 through 4.35. The same general characteristics that are noted in the 20 degree cases are present in this case. However, this system, with its non-minimum phase zero farther to the right ($s=0.0458$), responds somewhat faster. Holding the magnitude of negative direction response to one, the transient settling time is approximately three seconds, with crossover and steady state settling times approximately 19 and 100 seconds, respectively.

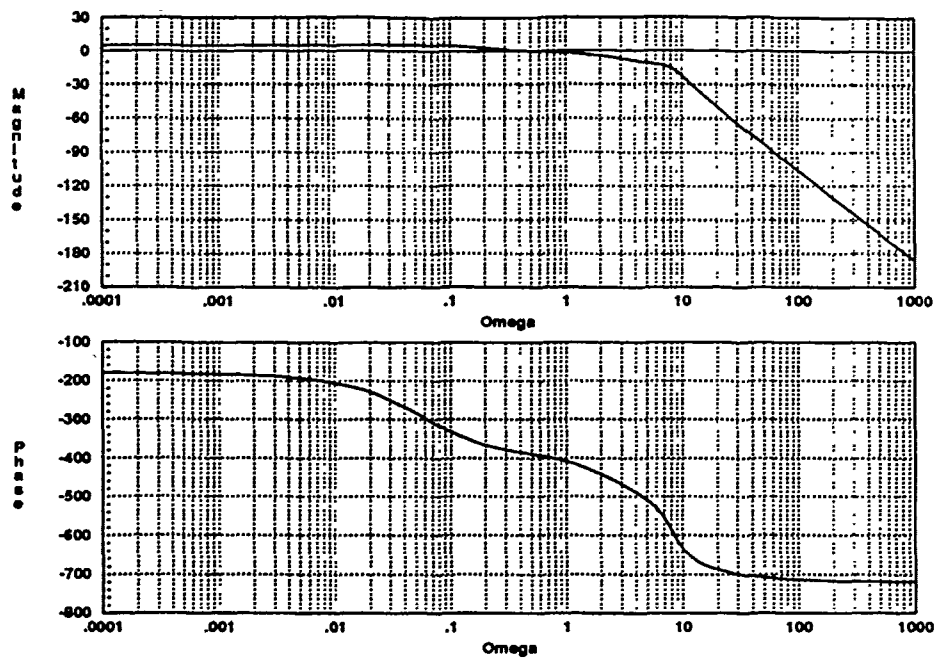


Figure 4.32. Bode Plot - Pitch Rate Design 1 with Prefilter ($\alpha = 40$)

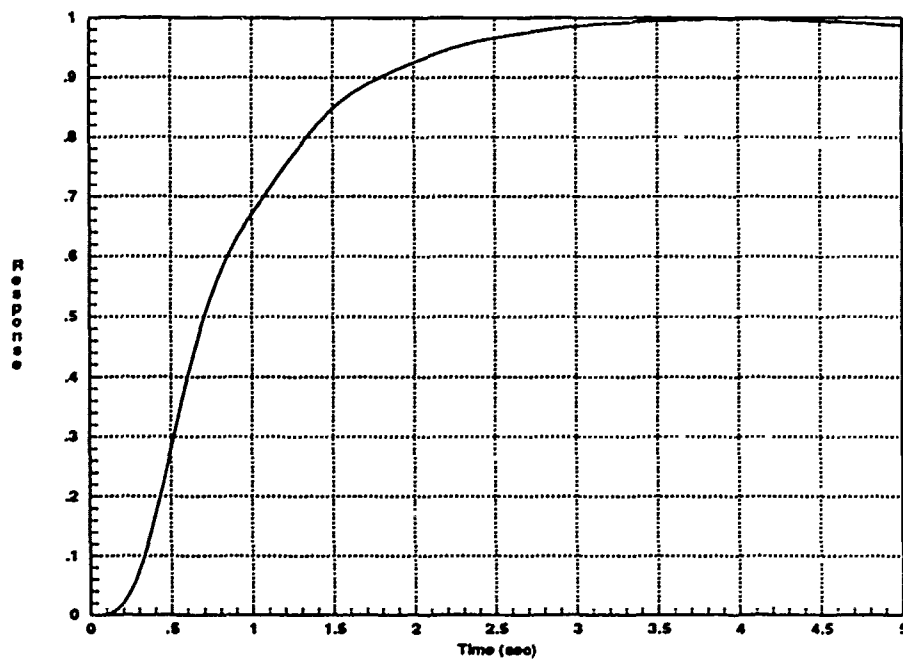


Figure 4.33. Pitch Rate Step Response - Design 1 {5-sec} ($\alpha = 40$)

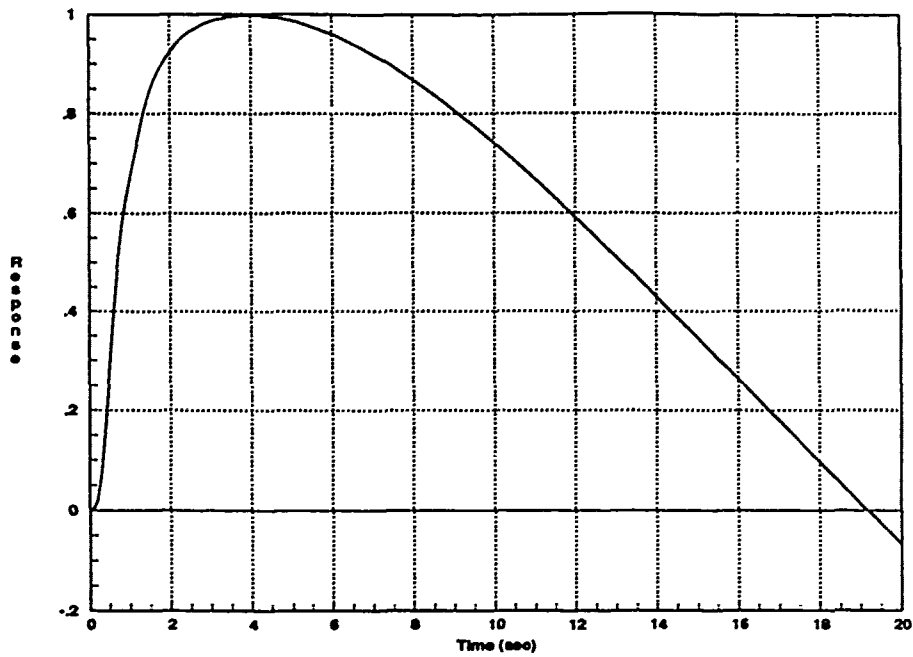


Figure 4.34. Pitch Rate Step Response - Design 1 {20-sec} ($\alpha = 40$)

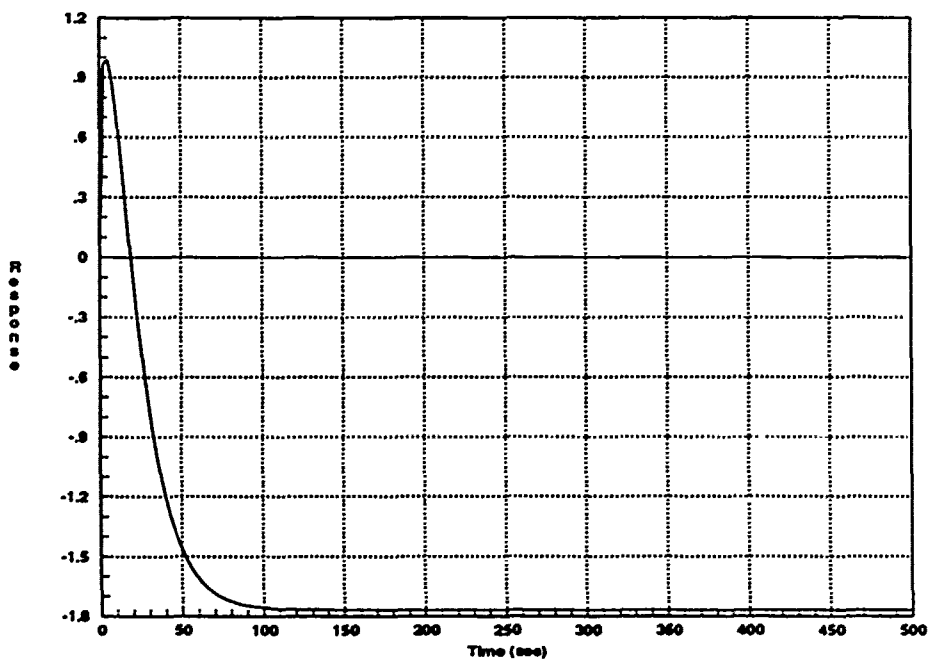


Figure 4.35. Pitch Rate Step Response - Design 1 {500-sec} ($\alpha = 40$)

As this is written, a problem is noted with the steady state value. Time does not permit a re-design, but a brief analysis of how to handle this situation may be useful for reference. While the steady state value should approach -1.0, it appears to approach -1.9. This is most likely due to an error in the overall system gain, which is used to cancel out the effects on the steady state value due to the poles and zeros. Qualitatively, one would expect that simply reducing the overall gain to correct this discrepancy would make the response somewhat slower. In addition, the magnitude in the transient region would be less than one. A reasonable way to handle this would be to increase the roll-off frequency by moving one of the prefilter poles slightly to the right (i.e. higher frequency). Alternatively, one could move the prefilter zero slightly to the left (i.e. lower frequency).

The prefilter design for the second 40 degree loop transmission function is very similar to the one obtained in the last case. The frequency response magnitude in Figure 4.14 is again relatively flat up to a roll-off frequency of approximately 10 radians/second. The prefilter for this case is given by Equation 4.18.

$$F_{40-2} = \frac{1.161(s + 0.36)}{(s + 0.11)(s + 2)} \quad (4.18)$$

The frequency response of the closed-loop system with prefilter is virtually identical to the previous case, as shown by Figure 4.36. The corresponding time responses (Figures 4.37 through 4.39) are also near duplicates of those seen in the last case. The same problem with the steady state value is noted in these plots, so a similar analysis and solution procedure could be used to correct the discrepancy.

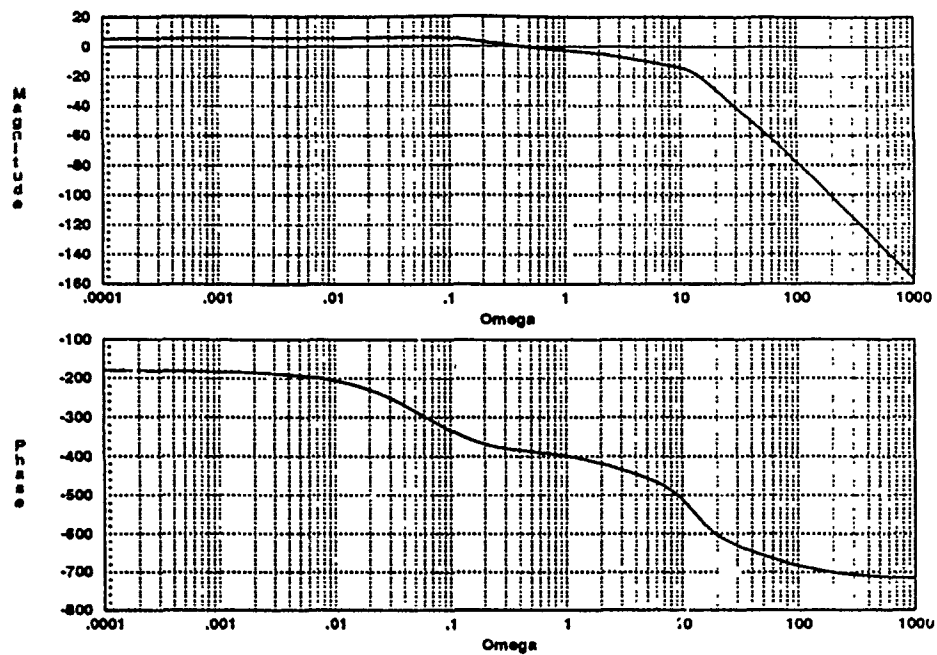


Figure 4.36. Bode Plot - Pitch Rate Design 2 with Prefilter ($\alpha = 40$)

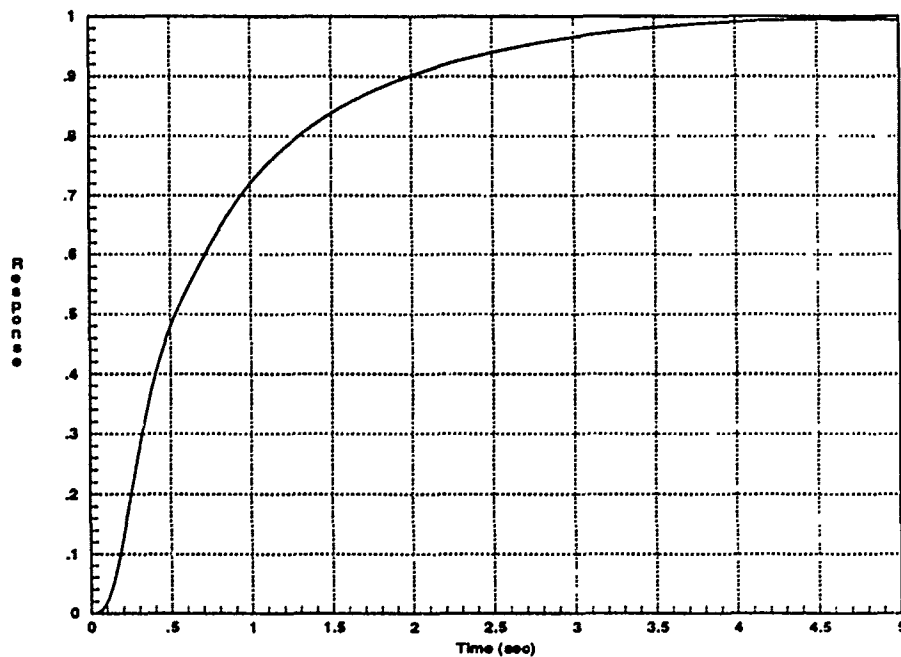


Figure 4.37. Pitch Rate Step Response - Design 2 {5-sec} ($\alpha = 40$)

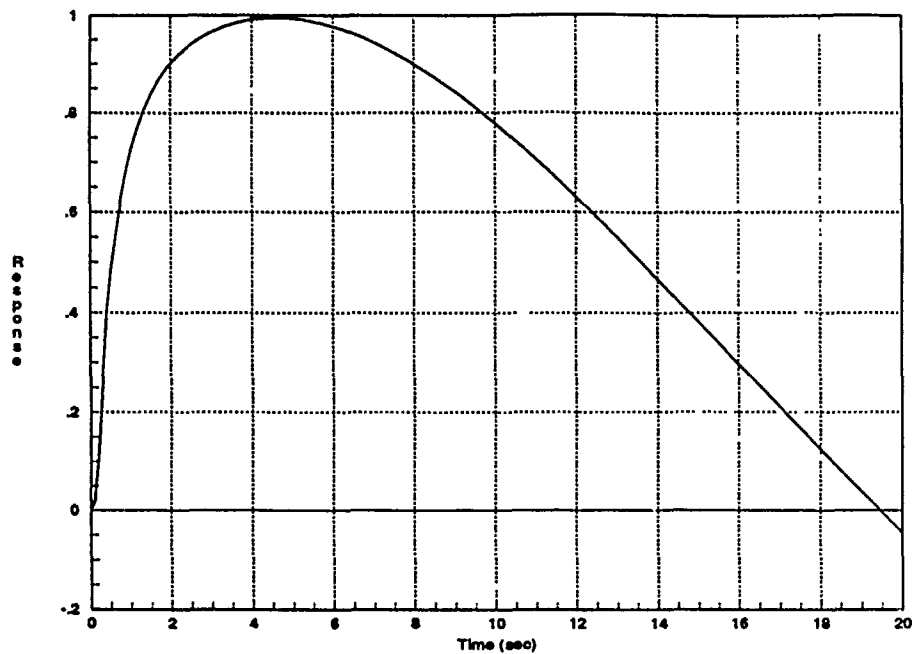


Figure 4.38. Pitch Rate Step Response - Design 2 {20-sec} ($\alpha = 40$)

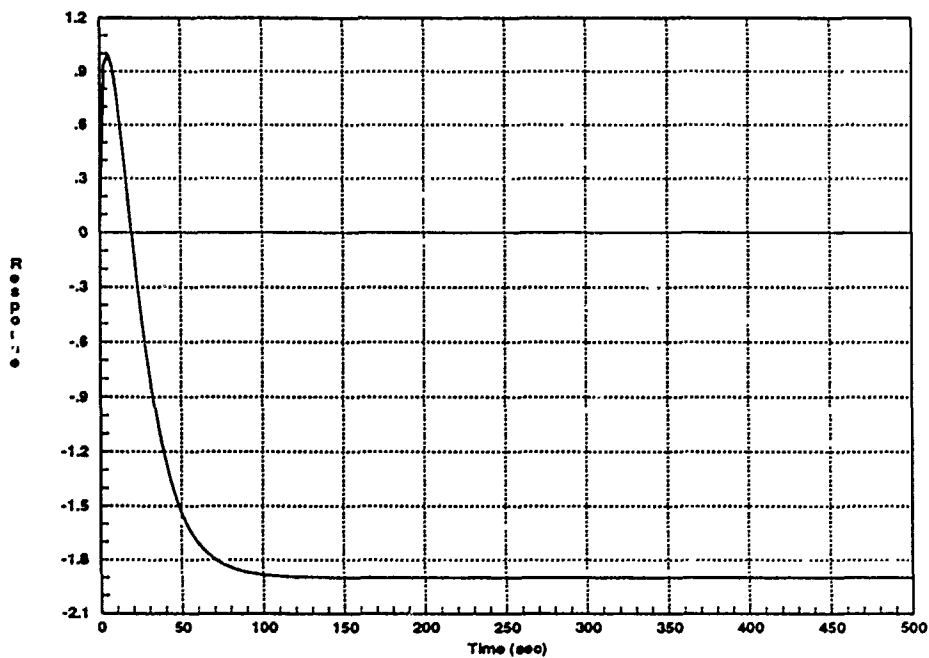


Figure 4.39. Pitch Rate Step Response - Design 2 {500-sec} ($\alpha = 40$)

The 50 degree case is discussed next. Recall that this flight condition resulted in a design that is just barely stable, and in fact is not practical. However, it is still useful to apply the prefilter design techniques to this case and analyze the results. Analysis of Figure 4.20 reveals that the closed-loop frequency response magnitude should be reduced to obtain the desired low-frequency value. Also, the initial roll-off frequency is approximately 300 radians/second. It is found that a simple prefilter pole with appropriate gain reduction results in the desired frequency response, as shown in Figure 4.40. The prefilter developed for this case is given by Equation 4.19.

$$F_{50-1} = \frac{0.0099}{(s + 0.14)} \quad (4.19)$$

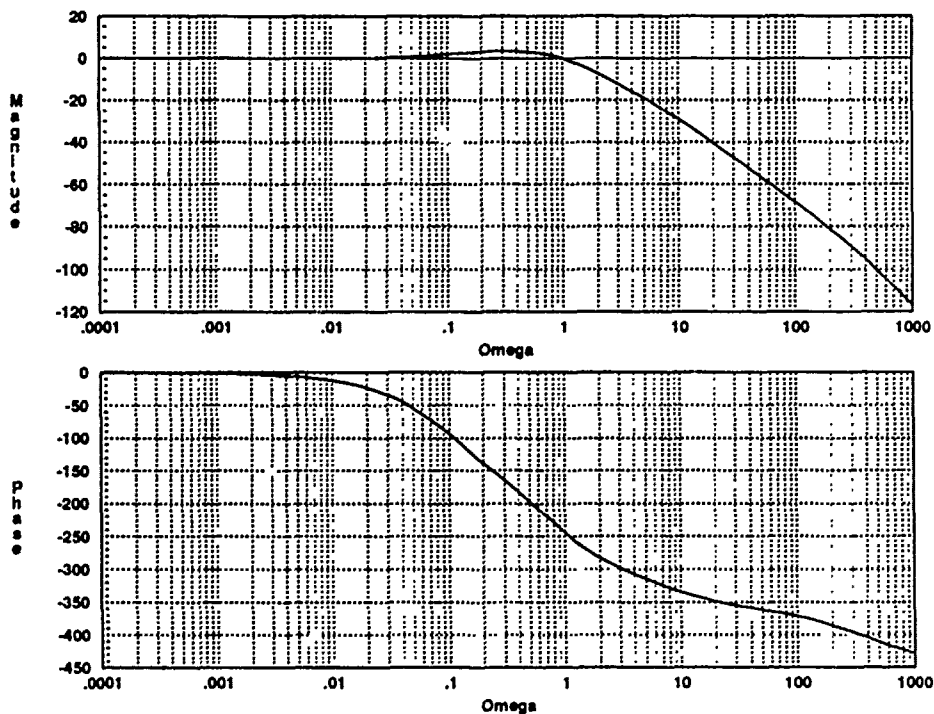


Figure 4.40. Bode Plot - Pitch Rate with Prefilter Design 1 ($\alpha = 50$)

The time response for this system is shown in Figure 4.41. In this case, it is not reasonable to choose the region of negative response for the desired transient response region. Due to the faster time constant from the RHP zero, this response rather quickly reverses direction to approach the steady state value. The prefilter design specified by Equation 4.19 results in the magnitude of the reverse response being no greater than one. The zero crossing is at approximately eight seconds and the final settling time is a rather slow 50 seconds.

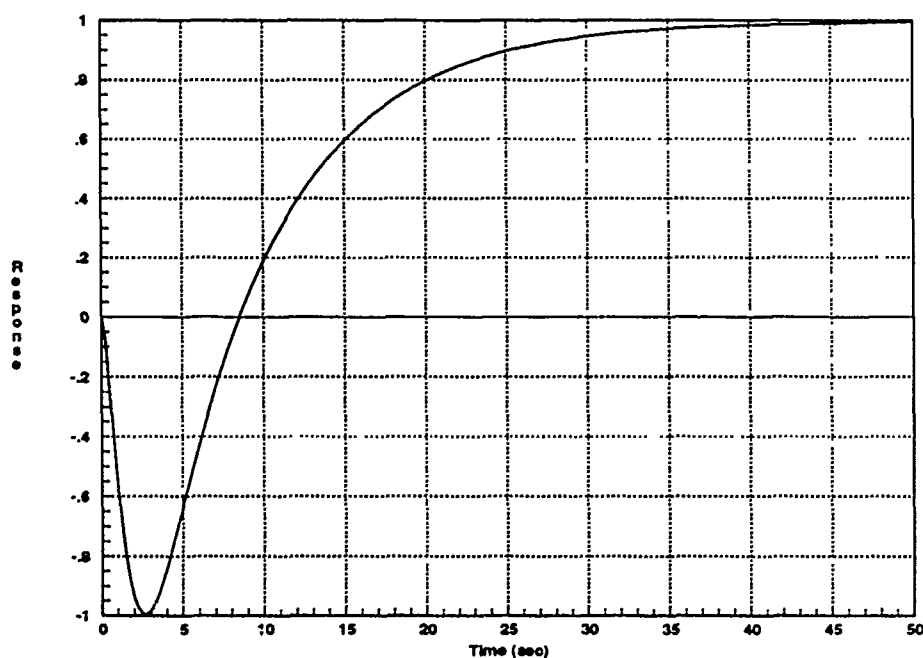


Figure 4.41. Pitch Rate Step Response - Prefilter Design 1 ($\alpha = 50$)

This response is completely unacceptable, so an alternate prefilter design is used to demonstrate an improved response. The prefilter design specified in Equation 4.20 results in a significantly faster time response. As before, the values of the compensation parameters have been selected based on observations of the response plots.

$$F_{50-2} = \frac{0.708}{(s + 10)} \quad (4.20)$$

The frequency response based on this design is shown in Figure 4.42. To speed up the response, excess gain is allowed near $\omega = 1$. The time response plot based on this design is shown in Figure 4.43. As is common in engineering designs, a trade-off is involved. By allowing the value of the negative response to reach a value of five, the crossover time is brought down to 3.5 seconds and the final settling time is a greatly improved six seconds. Again, it should be stressed that this is not an acceptable design, but the exercise has graphically demonstrated the effects of different prefilter designs on the system time response, based on a given closed loop transmission function.

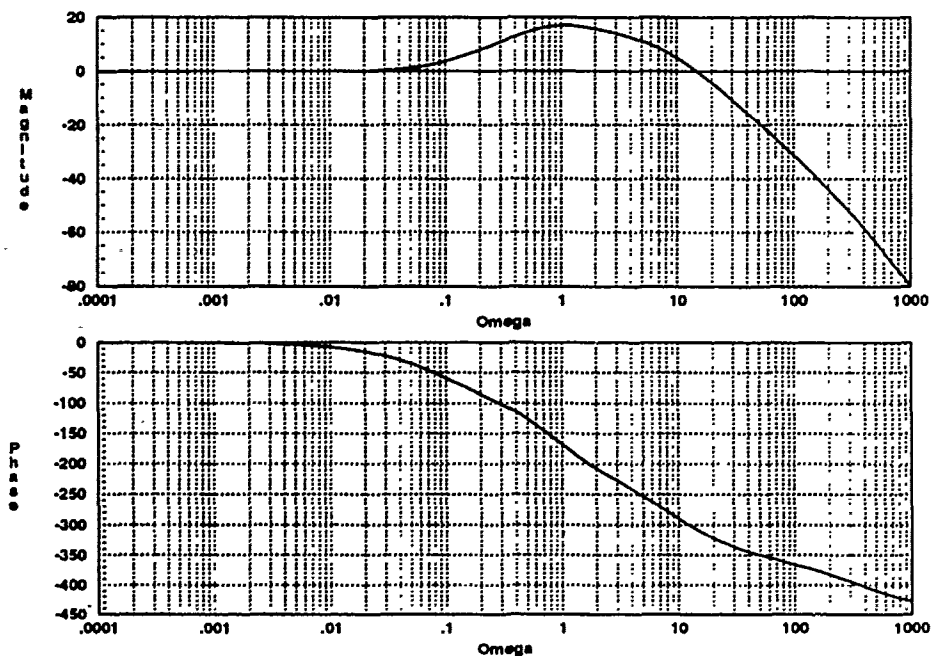


Figure 4.42. Bode Plot - Pitch Rate with Prefilter Design 2 ($\alpha = 50$)

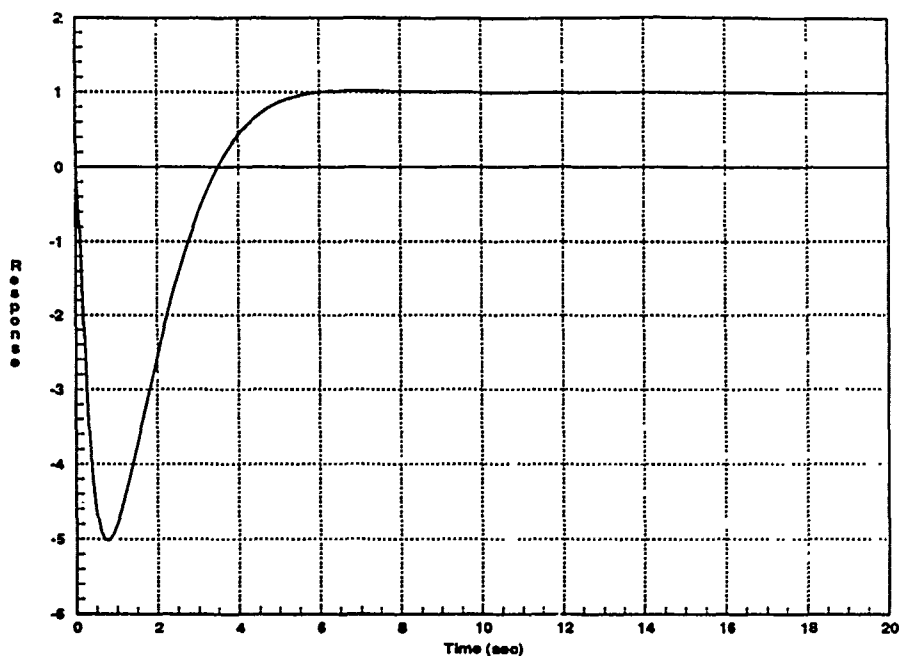


Figure 4.43. Pitch Rate Step Response - Prefilter Design 2 ($\alpha = 50$)

Finally, for the 60 degree flight condition, the closed-loop response shown in Figure 4.23 is analyzed. It is noted that a more complex prefilter is required, since the response magnitude requires lowering only for frequencies below 0.1 radians/second. Also, the initial roll-off frequency is over 200 radians/second. The prefilter design specified in Equation 4.21 results in the frequency response shown in Figure 4.44.

$$F_{60-1} = \frac{1.6574(s + 0.05)}{(s + 0.3318)(s + 0.56)} \quad (4.21)$$

The corresponding time response is shown in Figure 4.45. As with the 50 degree case, the region of negative response cannot be used for the desired transient response region. With a reverse region magnitude of one, the crossover time is approximately five seconds and the settling time is a relatively slow 20 seconds.

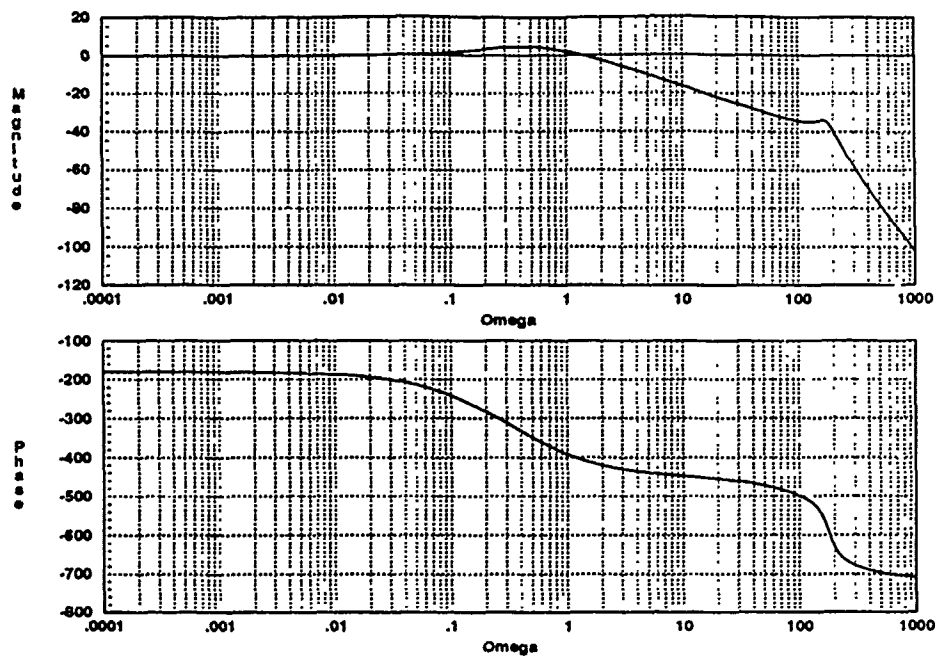


Figure 4.44. Bode Plot - Pitch Rate with Prefilter Design 1 ($\alpha = 60$)

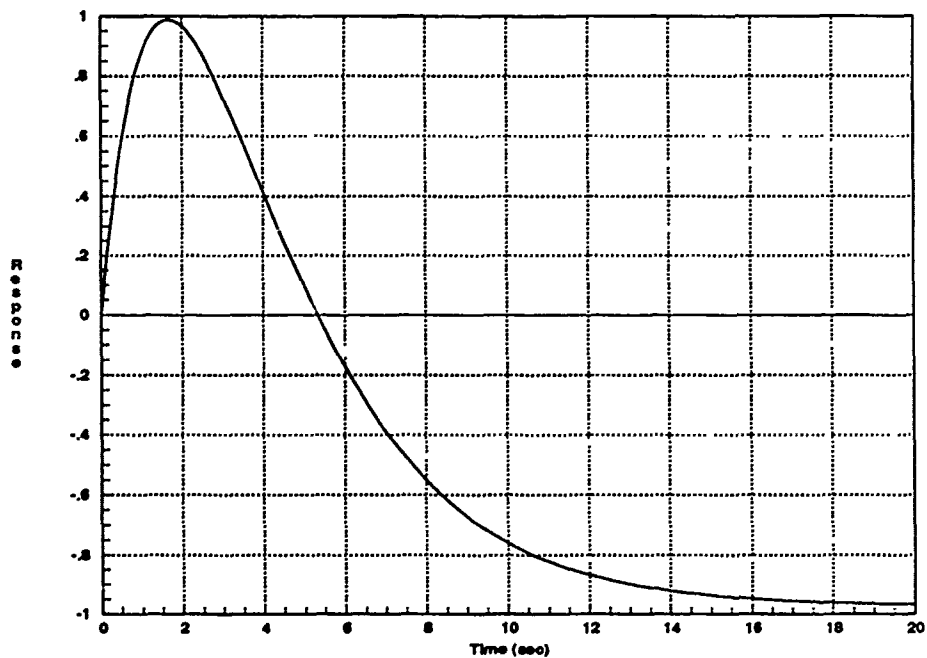


Figure 4.45. Pitch Rate Step Response - Prefilter Design 1 ($\alpha = 60$)

Like the 50 degree condition, it is now shown that an alternate prefilter design can improve the system time response characteristics. The alternate design prefilter for this flight condition is given by Equation 4.22.

$$F_{60-2} = \frac{3.5234(s + 0.042)}{(s + 0.3318)(s + 1)} \quad (4.22)$$

The frequency response resulting from this design is shown in Figure 4.46. Note that the roll-off frequency has been increased slightly. In this case, even using the technique of optimizing the prefilter parameters while examining the time response, the best that can be obtained is shown in Figure 4.47. This response is seen to be only slightly faster than the one obtained with the first prefilter design for this flight condition.

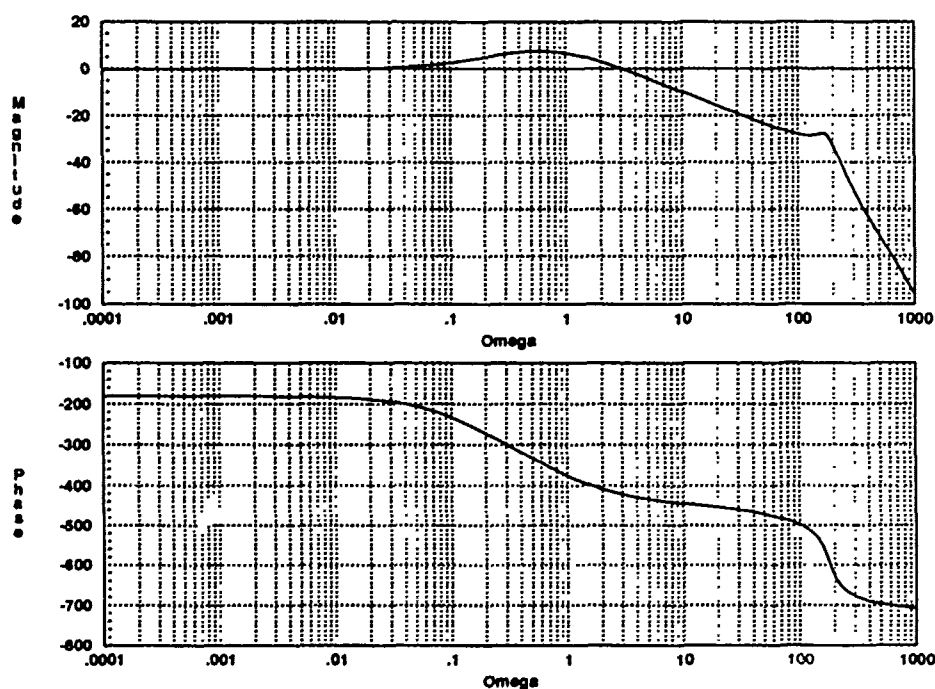


Figure 4.46. Bode Plot - Pitch Rate with Prefilter Design 2 ($\alpha = 60$)

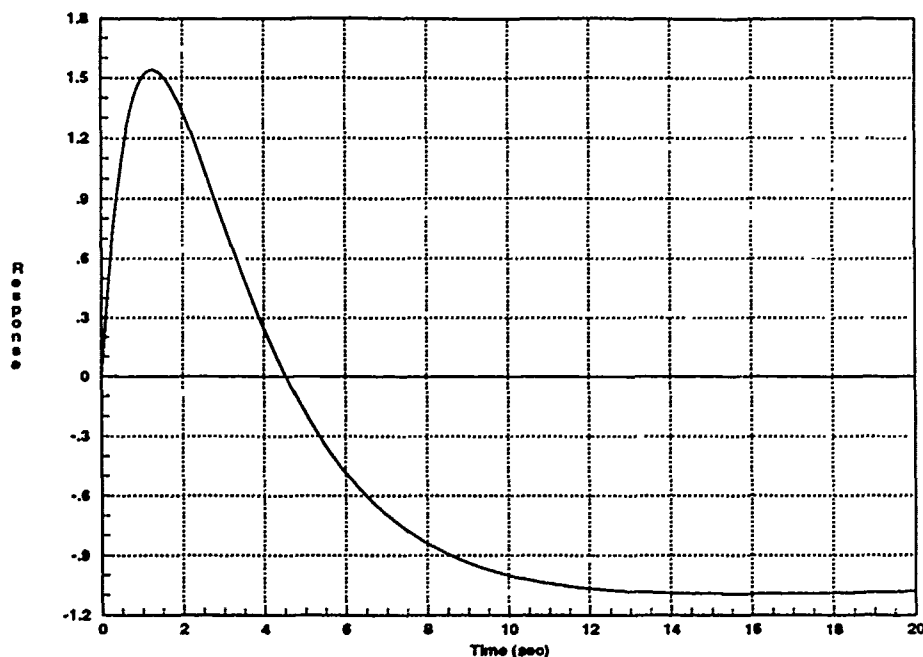


Figure 4.47. Pitch Rate Step Response - Prefilter Design 2 ($\alpha = 60$)

Once again, the response reverses too quickly to allow using the reverse response region. With this prefilter design, the negative response magnitude is approximately 1.5, and the crossover time has only been lowered to 4.5 seconds. The settling time is approximately ten seconds with a slight overshoot.

It is also noted that for both of the 60 degree cases the desired response region, after the crossover, has a negative magnitude. This is easily corrected with a negative gain in the prefilter, but both of the 60 degree responses are too slow to be practical, so as pointed out before, this problem is purely academic. The limitations imposed by the non-minimum phase zeros force the designer to work with a response that initially goes in a negative direction, thus making it virtually impossible to obtain the exact response desired [15].

4.5 Summary

This chapter presents the design procedures for the longitudinal (SISO) pitch rate controllers. After defining some key terms, the effective plants are shown for each flight condition. In addition to listing the polynomial forms, the roots of each effective plant are listed in tabular form for easy reference. Based on these roots, the loop transmission functions for each flight condition are developed. These functions are plotted on both Nichols and Bode charts to show the relative magnitude and phase characteristics as a function of the frequency. The gain and phase margins are listed in each case, and in all but the 50 degree flight condition, the stability margins are reasonable.

An alternate loop transmission function is designed for the 20 and 40 degree cases, to demonstrate some of the possible design trade-offs. The 50 degree case presents some unusual problems and requires the use of the optimal blending method to achieve stability. This system is made stable, but with unacceptably low stability margins. Also discussed is the effect of non-minimum phase zeros on loop transmission gain, and why that gain must be maximized in the frequency range of interest. The loop transmission function and the resulting compensator transfer function is shown for each of the cases.

Finally, the design of the longitudinal prefilters is presented. The responses are analyzed in detail and a novel idea is proposed to use the non-minimum phase induced region of negative response as the desired transient control region. This is reasonable for the extremely slow responses of the 20 and 40 degree cases. For the 50 and 60 degree cases, this is not a reasonable approach. However, for each of those cases, an alternate prefilter design is presented to demonstrate how optimizing the prefilter can improve the time response characteristics. Even though these designs are not acceptable, this discussion presents several analytical design techniques that may be useful in similar situations. Chapter V addresses the design issues surrounding the lateral-directional (MIMO) flight control systems.

V. Lateral-Directional Control System Design

5.1 Introduction

In this chapter, the lateral-directional control systems are examined in detail, and variations of QFT are applied. The chapter begins with a look at the roots of each effective plant. After pointing out some of the problems with these particular unstable non-minimum phase plants, the *Singular-G* method is presented and used to modify the plants. For each flight condition, the 2x2 MIMO plant is temporarily converted into an equivalent SISO plant by use of a singular compensator. The goal is to use the compensator elements to separate the RHP poles and zeros as much as possible. This is done to expand the range of loop transmission gain that can be used for the stable closed-loop system. The modified effective plants are listed in factored form and the root-loci are shown to provide a graphic look at the relative positions of the RHP poles and zeros.

Following this, the design process is carried on for one of the flight conditions. The optimal blending method is applied to design a stable loop transmission function for the chosen case. At this point, the loop transmission function is a SISO transfer function, based on the SISO plant obtained from the Singular-G method. Next, a procedure for determining the compensator transfer function is presented. Time constraints, as well as limitations in the LTI techniques used, prevent completion of the lateral-directional controller designs. However, the general procedure that can be used to obtain the MIMO compensators and prefilters is discussed.

5.2 Analysis of Effective Plants

As with the longitudinal case, the lateral-directional effective plants are each presented in factored form, to facilitate analysis of the system roots. Appendix H shows the block diagram representation of each of the 16 lateral-directional effective plants. Using the *MatrixX* linearization command *lin*, the systems transfer functions are obtained. The factored results are listed in Tables 5.1 through 5.15.

In each case, the unstable poles and non-minimum phase zeros are readily apparent. In a few of the cases, there is a zero far to the right of the origin. These

particular non-minimum phase zeros are not a significant problem, since they contribute minimal amounts of additional phase lag and they are not near any RHP poles [15]. The real concern is with the RHP poles and zeros near the origin, and in particular, those in close proximity to each other. This is discussed further in the next section.

roots(num20)-(1,1)	roots(den20)-(1,1)
0.0384	0.0058
-0.0919	-0.1000
-0.0577±j1.3866	-0.3239
-8.8395	-0.0500±j1.3919
9.2676	0.1288±j2.7262
-20.0000	-20.0000
-20.0000	-20.0000
	-20.0000

Table 5.1. Roots of Lateral-Directional $P_{eff}(1,1)$ ($\alpha = 20$)

roots(num20)-(1,2)	roots(den20)-(1,2)
0.0367	0.0058
-0.9720	0.2000
0.1478±j1.5669	-0.3239
-3.0167	-0.0000±j2.3979
3.0865±j4.8059	0.1288±j2.7262
-20.0000	0.3200±j3.6011
-20.0000	-20.0000
31.5050	-20.0000
	-20.0000

Table 5.2. Roots of Lateral-Directional $P_{eff}(1,2)$ ($\alpha = 20$)

roots(num20)-(2,1)	roots(den20)-(2,1)
-0.1937±j0.0661	0.0058
0.9568±j2.1320	-0.1000
-0.9451±j2.2835	-0.3239
-20.0000	-0.0500±j1.3919
-20.0000	0.1288±j2.7262
	-20.0000
	-20.0000
	-20.0000

Table 5.3. Roots of Lateral-Directional P_{eff} (2,1) ($\alpha = 20$)

roots(num20)-(2,2)	roots(den20)-(2,2)
0.2023	0.0058
-0.3074	0.2000
0.0631±j2.4406	-0.3239
0.3459±j3.5946	-0.0000±j2.3979
-20.0000	0.1288±j2.7262
-20.0000	0.3200±j3.6011
-25.6236	-20.0000
28.8912	-20.0000
	-20.0000

Table 5.4. Roots of Lateral-Directional P_{eff} (2,2) ($\alpha = 20$)

roots(num40)-(1,1)	roots(den40)-(1,1)
-0.0453	0.0000
0.0603	-0.0808±j0.1561
-0.0860±j1.2477	-0.1000±j1.2610
0.2528±j2.9088	0.2500±j2.9047
-20.0000	0.7098±j3.0081
-20.0000	-20.0000
-65.1516	-20.0000
85.9709	-20.0000

Table 5.5. Roots of Lateral-Directional P_{eff} (1,1) ($\alpha = 40$)

roots(num40)-(1,2)	roots(den40)-(1,2)
-0.0020±j0.1080	-0.0808±j0.1561
2.1000±j3.8974	0.7098±j3.0081
2.2013±j3.9426	2.1000±j3.8974
13.9264	2.1000±j3.8974
-20.0000	2.2010±j3.9192
-20.0000	-20.0000
	-20.0000
	-20.0000

Table 5.6. Roots of Lateral-Directional P_{eff} (1,2) ($\alpha = 40$)

roots(num40)-(2,1)	roots(den40)-(2,1)
0.0300	0.0000
-0.1800	-0.0808±j0.1561
-0.1200±j2.1700	-0.1000±j1.2610
-0.7000±j3.1900	0.2500±j2.9047
-20.0000	0.7098±j3.0081
-20.0000	-20.0000
60.0000	-20.0000
-115.2900	-20.0000

Table 5.7. Roots of Lateral-Directional P_{eff} (2,1) ($\alpha = 40$)

roots(num40)-(2,2)	roots(den40)-(2,2)
-0.5054	-0.0808±j0.1561
-0.2903±j1.4951	0.7098±j3.0081
2.1000±j3.8974	2.1000±j3.8974
2.1748±j309188	2.1000±j3.8974
-20.0000	2.2000±j3.9192
-20.0000	-20.0000
-5.3859E12	-20.0000
	-20.0000

Table 5.8. Roots of Lateral-Directional P_{eff} (2,2) ($\alpha = 40$)

roots(num50)-(1,1)	roots(den50)-(1,1)
0.1686	-0.0190±j0.0977
-0.3493	-0.3668
-0.2167±j0.5889	-0.5000
-14.4886	0.7143±j3.8832
-20.0000	-13.6332
-20.0000	-20.0000
-44.5691	-20.0000
53.0418	-20.0000
	-29.0000

Table 5.9. Roots of Lateral-Directional P_{eff} (1,1) ($\alpha = 50$)

roots(num50)-(1,2)	roots(den50)-(1,2)
0.1443	-0.0190±j0.0977
-0.4062	0.4500±j3.1141
0.1173±j2.8344	0.7143±j3.8832
4.4312	-1.0000±j4.0000
-2.3445±j5.6225	-19.0000
-7.6311	-20.0000
-20.0000	-20.0000
-20.0000	-20.0000

Table 5.10. Roots of Lateral-Directional P_{eff} (1,2) ($\alpha = 50$)

roots(num50)-(2,1)	roots(den50)-(2,1)
-0.0163	-0.0190±j0.0977
-0.3421	-0.3668
-0.3541±j2.4034	-0.5000
-13.5556	0.7143±j3.8832
-19.7248±j29.2216	-13.6332
-20.0000	-20.0000
-20.0000	-20.0000
	-20.0000
	-29.0000

Table 5.11. Roots of Lateral-Directional P_{eff} (2,1) ($\alpha = 50$)

roots(num50)-(2,2)	roots(den50)-(2,2)
-0.0073	-0.0190±j0.0977
0.3469±j3.0648	0.4500±j3.1141
-1.7457±j4.0933	0.7143±j3.8832
-11.3331	-1.0000±j4.0000
12.7288	-19.0000
-20.0000	-20.0000
-20.0000	-20.0000
-24.3445	-20.0000

Table 5.12. Roots of Lateral-Directional P_{eff} (2,2) ($\alpha = 50$)

roots(num60)-(1,1)	roots(den60)-(1,1)
0.1219	0.0459
-0.1972	-0.1554
-0.2112	-1.0000
0.2868±j3.1245	0.0477±j3.1259
0.5345±j3.1569	0.3000±j3.1225
-20.0000	0.5500±j3.1524
-20.0000	-20.0000
35.0285	-20.0000
	-20.0000

Table 5.13. Roots of Lateral-Directional P_{eff} (1,1) ($\alpha = 60$)

roots(num60)-(1,2)	roots(den60)-(1,2)
0.1485	0.0459
-0.2962	-0.1554
-0.0227±j1.8979	0.1000±j2.2716
-1.9099±j4.7794	-2.7000±j1.0000
18.4115	0.0477±j3.1259
-20.0000	-0.7000±j4.5826
-20.0000	-20.0000
	-20.0000
	-20.0000

Table 5.14. Roots of Lateral-Directional P_{eff} (1,2) ($\alpha = 60$)

roots(num60)-(2,1)	roots(den60)-(2,1)
-0.0113	0.0459
-0.1983	-0.1554
-2.3432±j1.4216	-1.0000
0.2873±j3.1215	0.0477±j3.1259
0.5385±j3.1607	0.3000±j3.1225
-20.0000	0.5500±j3.1524
-20.0000	-20.0000
	-20.0000
	-20.0000

Table 5.15. Roots of Lateral-Directional P_{eff} (2,1) ($\alpha = 60$)

roots(num60)-(2,2)	roots(den60)-(2,2)
0.0048	0.0459
0.1432±j2.2750	-0.1554
-2.5675±j1.1827	0.1000±j2.2716
-0.7026±j4.6553	-2.7000±j1.0000
-20.0000	0.0477±j3.1259
-20.0000	-0.7000±j4.5826
-3.0275E12	-20.0000
	-20.0000
	-20.0000

Table 5.16. Roots of Lateral-Directional P_{eff} (2,2) ($\alpha = 60$)

5.3 Singular-G Modification of Effective Plants

As previously mentioned, the RHP poles and zeros in close proximity to each other limit the range of loop transmission gain that results in a stable closed-loop system. In this section, each of the MIMO effective plants is transformed into an effective SISO plant by use of a singular compensation matrix. The elements of the compensation matrix are then used to separate the RHP poles and zeros of the equivalent plant as much as possible. By separating the RHP poles and zeros, the range of allowable gain for closed-loop stability is increased.

Figure 5.1 shows the general form of the singular-G compensator, and the feedback paths from the MIMO effective plant. The next several equations are used to derive the expression for the equivalent SISO plant. The expression for the compensator matrix can be derived from the figure, and is given by Equation 5.1. By post multiplying the effective plant by the compensator, the expression for the forward gain, or equivalent loop transmission, is given by Equation 5.2.

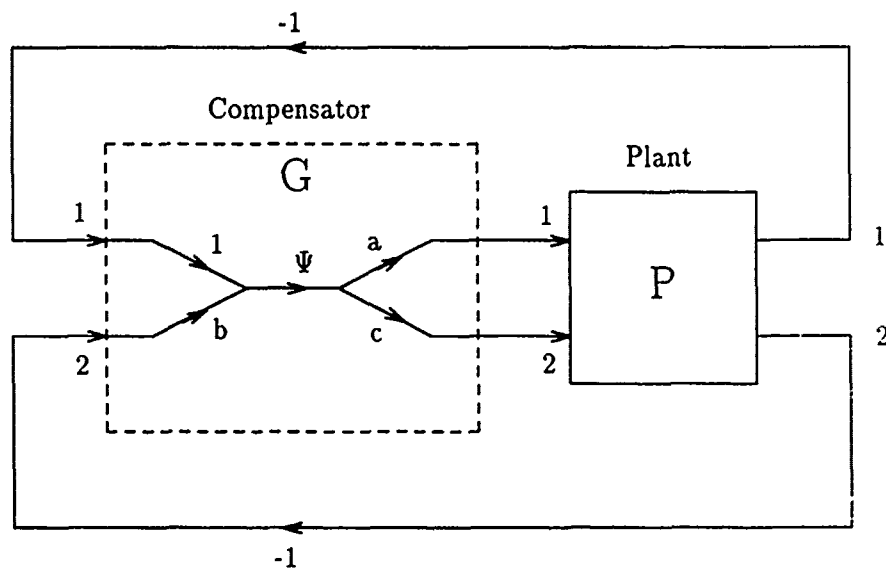


Figure 5.1. Singular-G Compensator [15]

$$G = \Psi \begin{bmatrix} a & ba \\ c & bc \end{bmatrix} \quad (5.1)$$

$$\mathbf{PG} = \Psi \begin{bmatrix} a & ba \\ c & bc \end{bmatrix} \begin{bmatrix} P_{(1,1)} & P_{(1,2)} \\ P_{(2,1)} & P_{(2,2)} \end{bmatrix} \quad (5.2)$$

In general, the elements a , b , and c may be either scalars or frequency dependent functions. For this study, they are chosen to be scalars. It is these elements that are used to modify the effective plant. The common element (Ψ) is the compensator transfer function and is determined in the usual manner by dividing the determined loop transmission function by the effective plant.

The transfer function for the system shown in Figure 5.1 is given by:

$$\frac{\mathbf{PG}}{\mathbf{I} + \mathbf{PG}} = \left[\frac{1}{\mathbf{I} + \mathbf{PG}} \right] \mathbf{PG} \quad (5.3)$$

The stability of this system is determined by the poles of Equation 5.3, which come from the determinant of $[\mathbf{I} + \mathbf{PG}]$. Substituting Equation 5.2 into the expression $[\mathbf{I} + \mathbf{PG}]$ results in Equation 5.4.

$$[\mathbf{I} + \mathbf{PG}] = \begin{bmatrix} 1 + \Psi (P_{(1,1)} a + P_{(1,2)} c) & \Psi (P_{(1,1)} ab + P_{(1,2)} bc) \\ \Psi (P_{(2,1)} a + P_{(2,2)} c) & 1 + \Psi (P_{(2,1)} ab + P_{(2,2)} bc) \end{bmatrix} \quad (5.4)$$

Taking the determinant of Equation 5.4 yields Equation 5.5.

$$\begin{aligned} \text{Det}[\mathbf{I} + \mathbf{PG}] &= [1 + \Psi (P_{(1,1)} a + P_{(1,2)} c) + (P_{(2,1)} ab + P_{(2,2)} bc) \\ &\quad + \Psi^2 (P_{(1,1)} a + P_{(1,2)} c)(P_{(2,1)} ab + P_{(2,2)} bc)] \\ &\quad - [\Psi^2 (P_{(1,1)} ab + P_{(1,2)} bc)(P_{(2,1)} a + P_{(2,2)} c)] \end{aligned} \quad (5.5)$$

When the factors of the positive and negative Ψ^2 terms are multiplied out, they are seen to be equal. Thus, the Ψ^2 terms cancel out and the resulting determinant expression is given by Equation 5.6.

$$\text{Det}[I + PG] = 1 + \Psi (P_{(1,1)} a + P_{(1,2)} c) + \Psi (P_{(2,1)} ab + P_{(2,2)} bc) \quad (5.6)$$

Defining Ψ as the compensator transfer function, the expression for the SISO equivalent plant, here defined as (Λ) , is obtained from Equation 5.6, and shown explicitly in Equation 5.7. The usage of the word *equivalent* in this situation refers to the stability characteristics only. Recall that the primary goal in this section is to achieve stability over some range of gain values.

$$\Lambda \equiv P_{(1,1)} a + P_{(1,2)} c + P_{(2,1)} ab + P_{(2,2)} bc \quad (5.7)$$

It is now desired to use a , b , and c to modify the expression for the SISO equivalent plant. Ideally, one would like to make the expression minimum phase (i.e. no RHP zeros). In this situation, however, the *best* that can be done is to separate the right half plane poles and zeros as much as possible, as discussed above [15]. Also, while performing the search, it is possible to move some of the RHP poles and/or zeros into the LHP, with careful selection of the compensator parameters. Even with a computer, this is a painstaking process requiring careful examination of the root locus plot for each combination of the variable parameters. To reduce the amount of searching to a manageable level, c is chosen to be unity. Thus, the SISO equivalent plant is now a function of the compensator parameters a and b . A commented listing of the *MatrixX* commands used to accomplish such a task is shown in Appendix I.

Initially, large search patterns across positive and negative values are used and the roots of the equation are examined. As trends point toward optimal search regions, the patterns are successively narrowed until none of the RHP poles and zeros are *close* to each other. *Close* in this sense is a relative term, with no set criteria available for use as a benchmark. For this task, the designer must visually optimize the pole zero pattern by striking a blend between maximum separation and minimum number of RHP poles and zeros. That is, in some cases, it may be

desirable to sacrifice some amount of separation, if by so doing some of the RHP poles and/or zeros can be forced into the LHP.

For the 20 degree case, the final values of a and b are determined to be -1 and $+1$, respectively. The root locus of the modified plant for this flight condition is shown in Figure 5.2. Examination of the figure reveals that no effort has been made to separate the left half plane poles and zeros. This is because they do not result in unstable closed-loop system poles. However, the RHP poles all now have a *reasonable* amount of separation. Again, there is no set criteria for determining what is reasonable separation, other than to say that the system is improved.

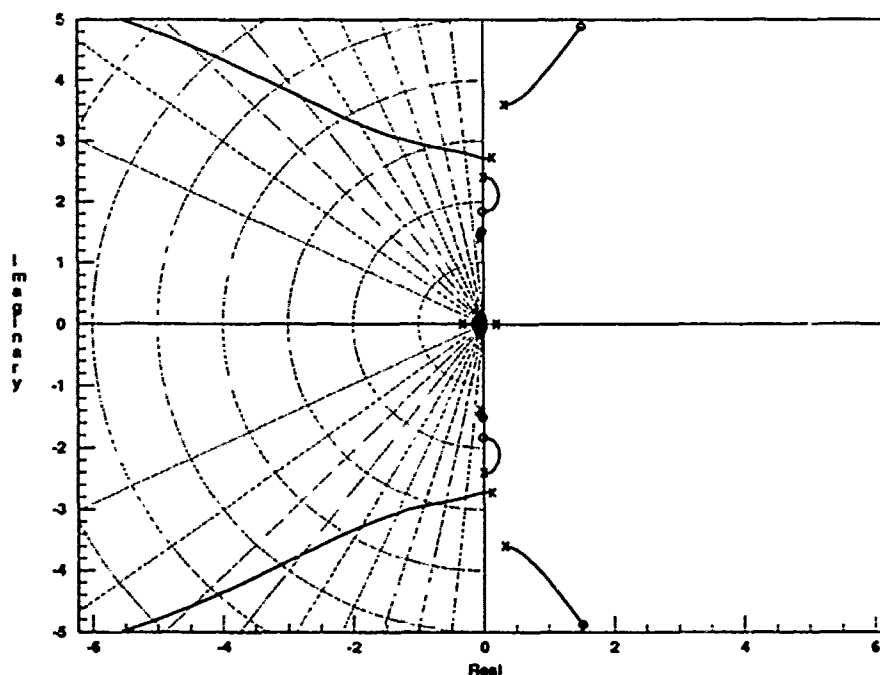


Figure 5.2. Root Locus of Modified Effective Plant ($\alpha = 20$)

The roots of this modified plant are listed in table 5.17. Finally, it should be remembered that the modified plant has only been temporarily converted from a MIMO to a SISO plant as defined by Equation 5.6. The actual lateral-directional plant is still a 2×2 MIMO system. The next section discusses this further.

roots(num-modplnt20)	roots(den-modplnt20)
-0.0335	0.0058
-0.0362±j0.1047	-0.1000
-0.0313±j1.5069	-0.3239
-0.0169±j1.8413	-0.0500±j1.3919
1.5161±j4.8876	0.1288±j2.7262
-6.7782	-20.0000
-20.0000	-20.0000
-20.0000	-20.0000
34.2306	0.2000
	0.0000±j2.3979
	0.3200±j3.6011

Table 5.17. Roots of Modified Lateral-Directional Effective Plant ($\alpha = 20$)

Figure 5.3 shows the root locus for the modified 40 degree effective plant. The optimal values of a and b for this case are found to be +13 and -13, respectively. It is noted that there is a greater number of RHP poles and zeros in this case than was seen in the 20 degree case. Close examination of Figure 5.3 reveals that two pairs of RHP poles are extremely close to each other. This poses no problem, since the system closed-loop poles migrate *away* from the open-loop poles and *toward* the zeros. Also note that one pair of RHP poles migrates into the LHP. Table 5.18 lists the roots of this equivalent plant.

The root locus of the 50 degree equivalent plant is shown in Figure 5.4. It is interesting to note that this flight condition proved to be the most troublesome in the longitudinal mode, but turns out to be the *best* of the lateral-directional cases. By setting the value of a to -0.001 and b to -3.5, the equivalent plant has only four right half plane poles and two RHP zeros. Further, it is noted that two of these poles migrate into the stable LHP and the remaining RHP poles and zeros are widely separated. The roots of this equivalent plant are listed in Table 5.19.

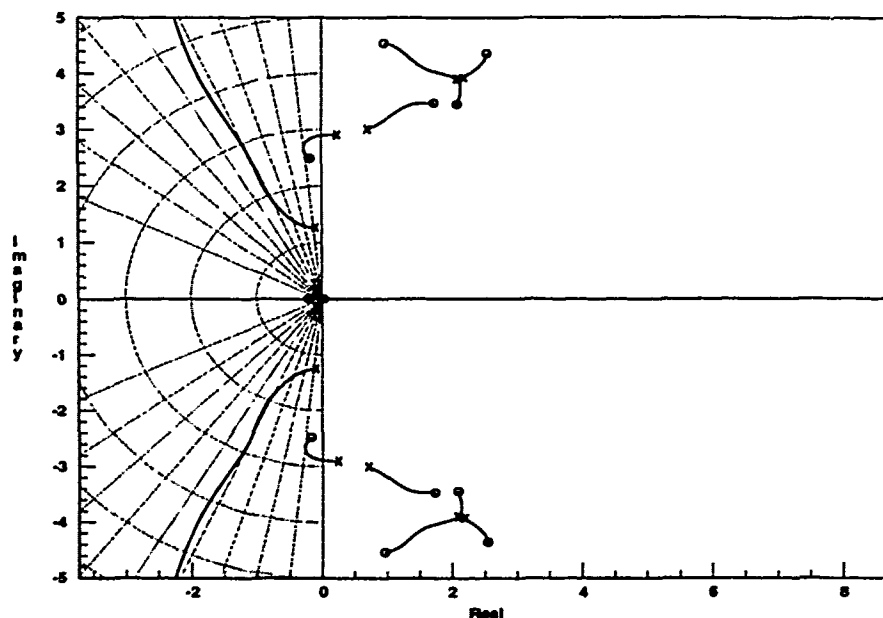


Figure 5.3. Root Locus of Modified Effective Plant ($\alpha = 40$)

roots(num-modplnt40)	roots(den-modplnt40)
0.0286	0.0000
-0.2115	-0.0808±j0.1561
-0.1785±j2.4879	-0.1000±j1.2610
1.7341±j3.4741	0.2500±j2.9047
2.0896±j3.4452	0.7098±j3.0081
0.9627±j4.5355	-20.0000
2.5424±j4.3558	-20.0000
-15.2233	-20.0000
-77.8939	2.1000±j3.8974
	2.1000±j3.8974
	2.2000±j3.9192

Table 5.18. Roots of Modified Lateral-Directional Effective Plant ($\alpha = 40$)

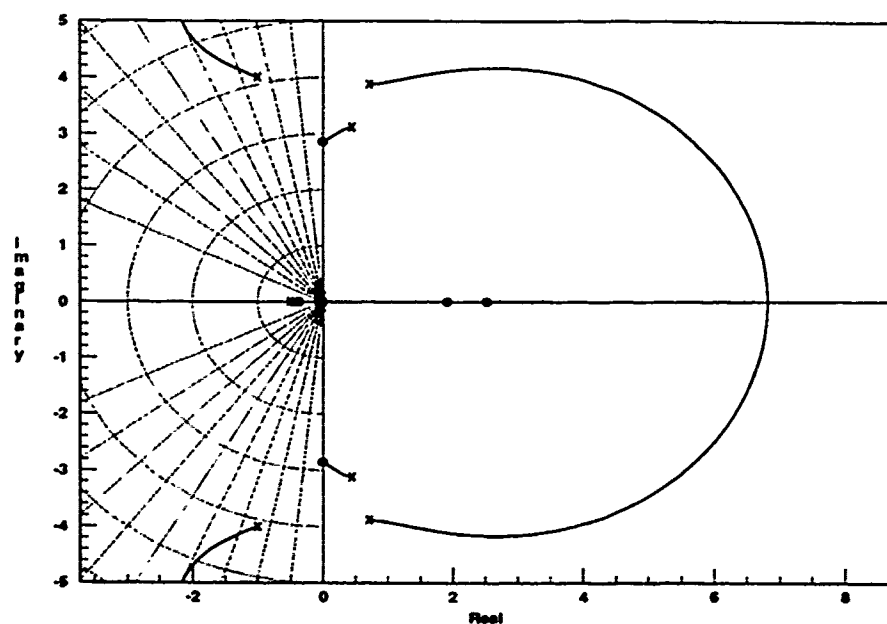


Figure 5.4. Root Locus of Modified Effective Plant ($\alpha = 50$)

roots(num-modplnt50)	roots(den-modplnt50)
-0.0569	-0.0190±j0.0977
-0.3769	-0.3668
-0.4623	-0.5000
1.9130	0.7143±j3.8832
2.5237	-13.6332
-0.0100±j2.8632	-20.0000
-2.1180±j5.7859	-20.0000
-7.7142	-20.0000
-13.6449	-29.0000
-20.0000	0.4500±j3.1141
-20.0000	-1.0000±j4.0000
-29.9804	-19.0000

Table 5.19. Roots of Modified Lateral-Directional Effective Plant ($\alpha = 50$)

The equivalent plant for the 60 degree flight condition is shown in Figure 5.5. With the values of a and b chosen as $+180$ and -11 , respectively, the RIIP roots are separated as much as possible. By adjusting the two parameters while observing the root locus plots, it is possible to pull two pairs of complex zeros into the stable LIIP. Table 5.20 lists the roots of the modified effective plant for this flight condition.

Finally, it should be noted that this procedure worked fairly well in achieving the desired objective in each case. However, it is possible that by varying the c parameter, along with a and b , the results could have been better. Further, recall that the a , b , and c parameters need not be scalars. By allowing these parameters to be frequency dependent transfer functions, it *may* even be possible to stabilize the effective plants, or at least make them minimum phase. However, such a determination would be extremely time consuming, even with a computer, and is beyond the scope of this effort.

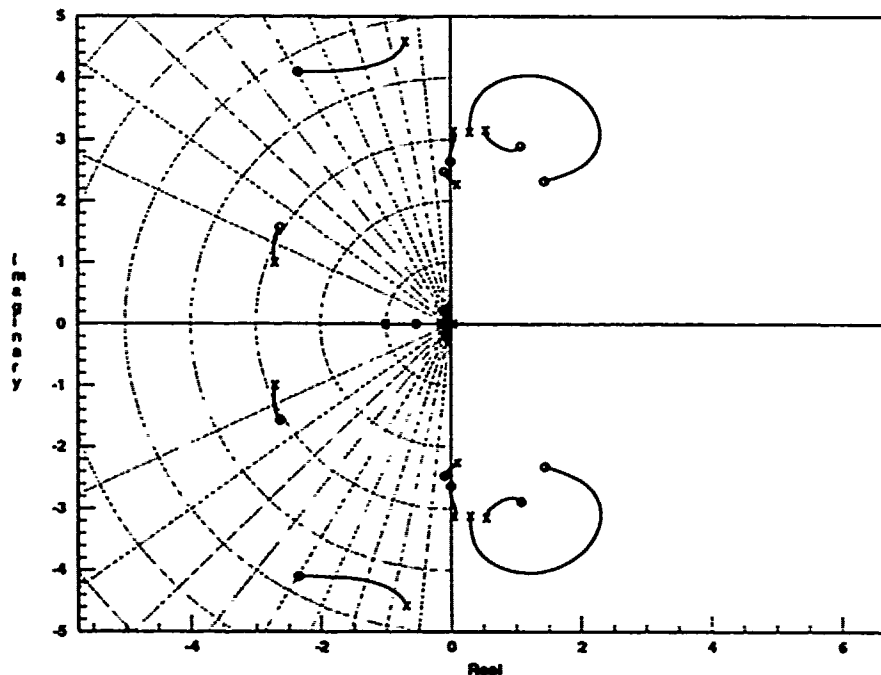


Figure 5.5. Root Locus of Modified Effective Plant ($\alpha = 60$)

roots(num-modplnt60)	roots(den-modplnt60)
-0.0201	0.0459
-0.5359	-0.1554
-0.1014±j2.4721	-1.0000
-0.0014±j2.6429	0.0477±j3.1259
1.4473±j2.3231	0.3000±j3.1225
-2.6296±j1.5661	0.5500±j3.1524
1.0852±j2.8870	-20.0000
-2.3487±j4.0988	-20.0000
	-29.0000
	0.1000±j2.2716
	-2.7000±j1.0000
	-0.7000±j4.5826

Table 5.20. Roots of Modified Lateral-Directional Effective Plant ($\alpha = 60$)

5.4 Application of Optimal Blending to One Case

The lateral-directional design procedure is now carried further for one of the flight conditions. The 50 degree flight condition is chosen, since its equivalent plant has the least number of RHP poles and zeros. The optimal blending method is used to obtain a loop transmission function which for a specified range of gain can result in a stable closed-loop system. Following this, the procedure to obtain the overall compensator transfer function (Ψ) is presented. Finally, the general procedure for designing the MIMO system, complete with prefilters, is discussed.

The design proceeds with a step-by-step method for developing an *optimum* loop transmission function. The RHP poles and zeros in the plant may *not* be cancelled due to the uncertainties in the exact values. Therefore, the loop transmission function must contain the RHP poles and zeros of the effective plant (see Table 5.19). The optimal blending design procedure is based on *only* the RHP poles and zeros of the effective plant, since the stable LHP roots are not a concern for stability. The LHP roots may be cancelled with additional compensator terms, if desired.

The optimal blending method is now applied to this particular case. The general procedure is derived in reference [12]. The numbers of RHP poles (δ_p) and zeros (δ_z) in the effective plant determine the order of the balanced loop transmission function. Equations 5.8 and 5.9 are used to determine the number of compensator poles (δ_{pc}) and zeros (δ_{zc}) required to ensure the necessary symmetry.

$$\delta_{pc} = \delta_p + 2\delta_z - 2 \quad (5.8)$$

$$\delta_{zc} = 2\delta_p + \delta_z - 2 \quad (5.9)$$

In this case, with $\delta_p = 4$ and $\delta_z = 2$, the compensator must have six poles and eight zeros. The balanced portion of the loop transmission function must contain ten poles and ten zeros. Note that this is an improper transfer function, so additional far off poles must be added later.

An optimal blending function $[\phi(s)]$ is now defined as one side of the balanced portion of the loop transmission function. Thus, $\phi(s)$ is a function with five zeros and five poles. In this case, two zeros and four poles result from the effective plant. The values of the remaining roots must be determined. The optimal blending function is defined in Equation 5.10.

$$\phi(s) = \left[\frac{(s - 1.9130)(s - 2.5237)}{(s - 0.7143 \pm j3.8832)(s - 0.4500 \pm j3.1141)} \right] \left[\frac{(s^3 + As^2 + Bs + C)}{(s + D)} \right] \quad (5.10)$$

Proceeding with a design based on Equation 5.10 would result in a symmetric function about the $j\omega$ axis (i.e. marginal stability). To ensure stability, the $j\omega$ axis is offset into the left half plane by replacing s with $v - 2$. The *left* side offset blending function is given by Equation 5.11.

$$\phi(v) = \left[\frac{(v + 3.9130)(v + 4.5237)}{(v + 2.7143 \pm j2.8832)(v + 2.4500 \pm j3.1141)} \right] \left[\frac{(v^3 + Av^2 + Bv + C)}{(v + D)} \right] \quad (5.11)$$

Convolving the known roots from the effective plant yields Equation 5.12.

$$\phi(v) = \left[\frac{(v^2 + 8.4367v + 17.7012)}{(v^4 + 10.3286v^3 + 64.7469v^2 + 195.2183v + 352.4153)} \right] \left[\frac{(v^3 + Av^2 + Bv + C)}{(v + D)} \right] \quad (5.12)$$

The next step involves expanding the numerator and denominator into even and odd monic polynomials, respectively. This is done in Equations 5.13 and 5.14.

$$\begin{aligned} o_n + c_n e_n &= v^5 + (8.4367A + B + 17.7012)v^3 + (17.7012B + 8.4367C)v \\ &+ (8.4367 + A) \left(v^4 + \frac{(8.4367B + 17.7012A + C)v^2}{(8.4367 + A)} + \frac{(17.7012C)}{(8.4367 + A)} \right) \end{aligned} \quad (5.13)$$

$$\begin{aligned} o_d + c_d e_d &= v^5 + (64.7469 + 10.3286D)v^3 + (352.4153 + 195.2183D)v \\ &+ (10.3286 + D) \left(v^4 + \frac{(195.2183 + 64.7469D)v^2}{(10.3286 + D)} + \frac{(352.4153D)}{(10.3286 + D)} \right) \end{aligned} \quad (5.14)$$

Now the odd numerator and denominator coefficients are equated. Likewise, the even numerator and denominator coefficients are equated. The resulting four equations contain the four unknowns (Equations 5.15 through 5.18).

$$8.4367A + B + 17.7012 = 64.7469 + 10.3286D \quad (5.15)$$

$$17.7012B + 8.4367C = 352.4153 + 195.2183D \quad (5.16)$$

$$\frac{8.4367B + 17.7012A + C}{8.4367 + A} = \frac{195.2183 + 64.7469D}{10.3286 + D} \quad (5.17)$$

$$\frac{17.7012C}{8.4367 + A} = \frac{352.4153D}{10.3286 + D} \quad (5.18)$$

Since the last two equations are non-linear, the solution involves considerable algebraic manipulation. Without reproducing all the steps, it should be noted that the first variable isolated is D , which is the solution to a cubic equation. Engineering judgement is required to select the most sensible root. In this case, one root is negative, and another is very large. The third root, a small positive value, is the sensible choice. After making this selection, the other coefficients are obtained by solving the above equations. The values are:

$$\begin{aligned} A &= 4.2770 & B &= 25.1603 \\ C &= 20.7992 & D &= 1.3750 \end{aligned}$$

Factoring the cubic numerator roots, the shifted blending function is given by:

$$\phi(v) = \left[\frac{(v + 3.9130)(v + 4.5237)}{(v + 2.7143 \pm j3.8832)(v + 2.4500 \pm j3.1141)} \right] \left[\frac{(v + 0.9449)(v + 1.6660 \pm j4.3859)}{(v + 1.3750)} \right] \quad (5.19)$$

The roots are now shifted back by adding two to the real portions of each, resulting in:

$$\phi(s) = \left[\frac{(s + 5.9130)(s + 6.5237)}{(s + 4.7143 \pm j3.8832)(s + 4.4500 \pm j3.1141)} \right] \left[\frac{(s + 2.9449)(s + 3.6660 \pm j4.3859)}{(s + 3.3750)} \right] \quad (5.20)$$

Finally, the *mirror image* of $\phi(s)$ about the chosen line of symmetry ($s = -2$) is given by:

$$\phi(s)_{im} = \left[\frac{(s - 1.9130)(s - 2.5237)}{(s - 0.7143 \pm j3.8832)(s - 0.4500 \pm j3.1141)} \right] \left[\frac{(s + 1.0051)(s + 0.3340 \pm j4.3859)}{(s + 0.6250)} \right] \quad (5.21)$$

Equations 5.20 and 5.21 are now combined into a single transfer function (the symmetric loop transmission function) and plotted on a root locus, as shown in Figure 5.6. The symmetry about $s = -2$ is readily apparent. It should be noted that Equations 5.20 and 5.21 result in this root locus pattern *only* for negative gain values.

The reason for plotting this function is to determine the range of loop transmission gain for which the closed-loop system is stable (i.e. no RHP closed-loop poles). As the gain magnitude is increased, the system becomes stable at $K = -0.82$ and again goes unstable at $K = -0.98$. A reasonable choice for the loop transmission

gain is the midpoint, $K = -0.90$. Close examination of Figure 5.6 reveals the locations of the *closed-loop* poles with this gain value. The closed-loop poles are denoted by small stars on the plot. All ten closed-loop poles are in the LHP; two on the real axis and eight on the $s = -2$ line of symmetry (two are just off the plot with the selected scaling).

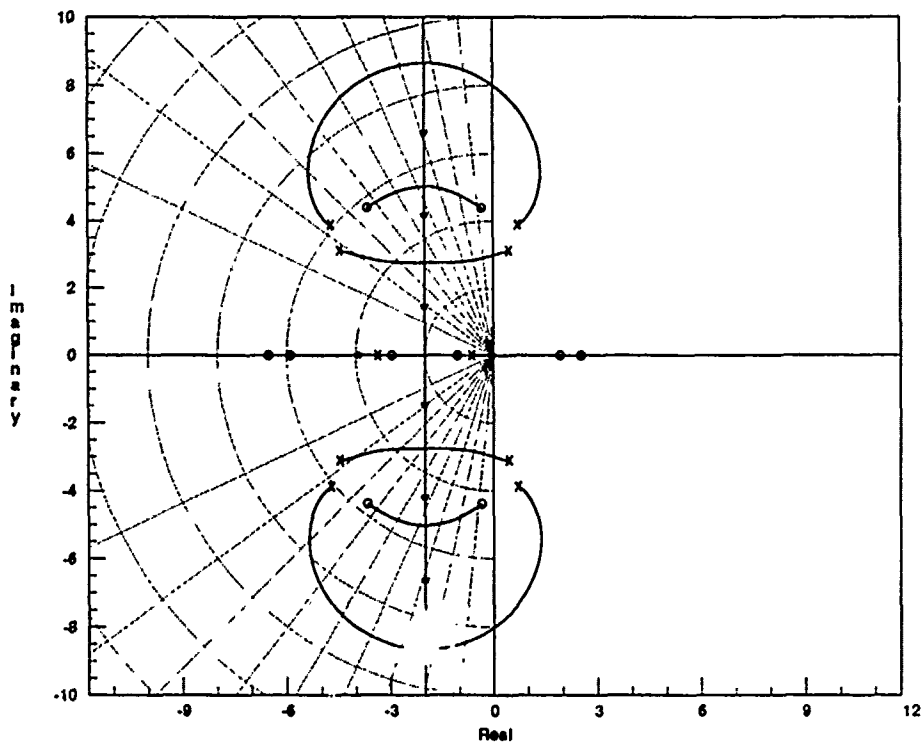


Figure 5.6. Initial Optimal Blending Loop Transmission ($\alpha = 50$)

As mentioned previously, additional poles are required to make the loop transmission function a *proper* transfer function. The effective plant has an excess of two poles over zeros, and that excess must be maintained. Three poles are added to the loop transmission function to ensure that the compensator is also a proper transfer function. The three LHP poles are added far off ($s = -10000$) so that the symmetry near the origin is not disturbed greatly.

Even with such far off poles, it is seen in Figure 5.7 that the symmetric pattern is disturbed somewhat. However, the closed-loop poles are still in the stable region of the s -plane with the loop transmission gain set at -0.9 . It is found that the addition of the far off poles causes a *slight* degradation in the range of allowable gain for stability. The range is now from $K = -0.83$ to $K = -0.97$; still centered about $K = -0.9$.

Table 5.1 lists the roots of the equivalent loop transmission function with the far off poles added. This technique results in achieving a stable loop transmission function with at least some degree of gain insensitivity. Although the insensitivity is rather low, this approach results in achieving the stability goal where conventional methods would fail when applied to a problem such as this [15].

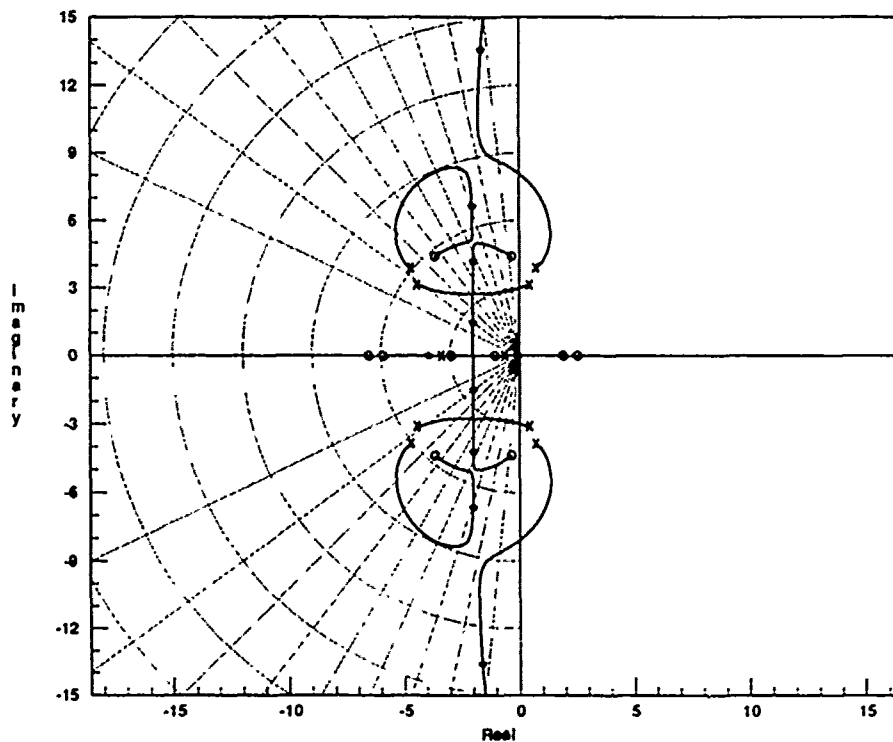


Figure 5.7. Final Optimal Blending Loop Transmission ($\alpha = 50$)

roots(num50equiv)	roots(den50equiv)
-1.0551	-0.6250
1.9130	$0.4500 \pm j3.1141$
2.5237	-3.3750
-2.9449	$0.7143 \pm j3.8832$
$-0.3340 \pm j4.3859$	$-4.4500 \pm j3.1141$
$-0.3660 \pm j4.3859$	$-4.7143 \pm j3.8832$
-5.9130	-10000
-6.5237	-10000
	-10000

Table 5.21. Roots of Equivalent Loop Transmission Function ($\alpha = 50$)

Lack of time prevents carrying this design any further. However, with the equivalent loop transmission function defined, the compensator transfer function (Ψ) may be obtained as before. Dividing the equivalent loop transmission function by the equivalent effective plant (Equation 5.7) results in a fairly high order compensator. Recall that the effective plant still has many LHP roots that are not addressed in the above optimal blending procedure. The compensator transfer function could be used to cancel out the LHP roots of the effective plant, if desired.

Although time constraints prevented completion of this design, the procedure for transforming the system back to a MIMO system and designing the prefilter matrix is discussed for reference and possible follow-on work. Figure 5.8 shows the arrangement of the complete MIMO system, with the prefilter matrix [15]. Note that the prefilter affects only the commanded input signals and the compensator affects only the fed-back output states. The summation of these signals is the input to the effective plant. At this point one might ask if the control surfaces would still work together. The answer is yes. The weighting matrix terms that ensure this are embedded in the effective plant, and the compensator will affect all plant inputs equally.

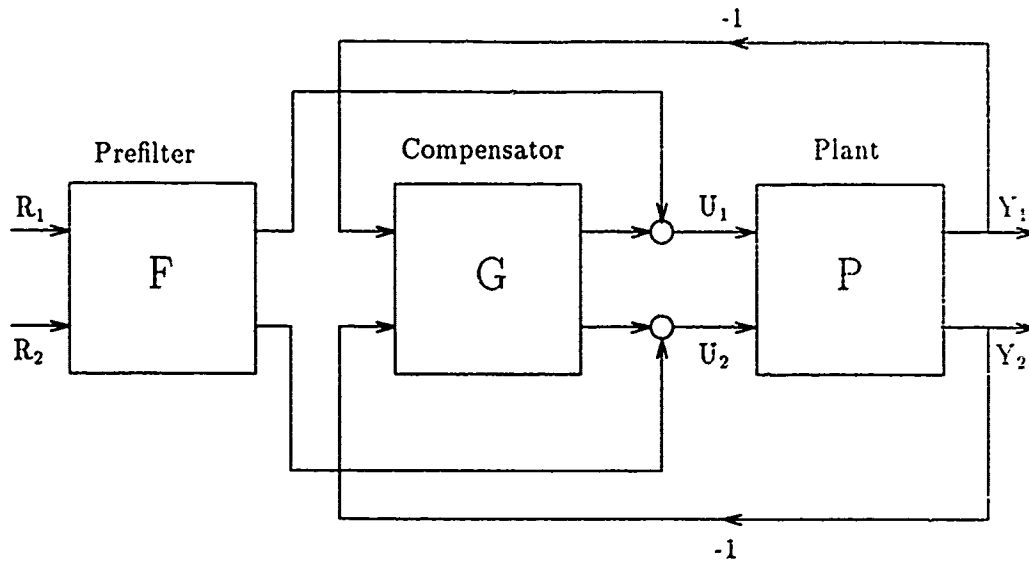


Figure 5.8. Singular-G Compensator with Prefilter [15]

The inputs to the effective plant (u_1 and u_2), are functions of the *compensated* output states (y_1 and y_2) and the *filtered* commanded inputs (r_1 and r_2). Equation 5.22 expresses this relation, and Equation 5.23 expresses the input/output relationship of the effective plant. These two equations are combined into the closed-loop control ratio as given by Equation 5.24.

$$\mathbf{u} = -\mathbf{G}\mathbf{y} + \mathbf{F}\mathbf{r} \quad (5.22)$$

$$\mathbf{y} = \mathbf{P}\mathbf{u} \quad (5.23)$$

$$\frac{\mathbf{y}}{\mathbf{r}} = \left[\frac{\mathbf{I}}{\mathbf{I} + \mathbf{P}\mathbf{G}} \right] \mathbf{P}\mathbf{F} \quad (5.24)$$

When the individual *original* $P_{i,j}$ transfer functions (each an element of a 2x2 matrix) are combined with the compensator transfer function (Ψ) in Equation 5.24, the 2x2 matrix of system transfer functions is obtained. Each element of this matrix can then be equated to a desired transfer function and the elements of the prefilter matrix can be obtained by algebraic methods. The desired transfer functions are typically developed by choosing dominant poles and zeros to obtain the desired time response characteristics. The procedure is discussed in ref [8]. Also, the cross coupling effects, represented by the off-diagonal elements in the transfer function matrix, can be eliminated by proper selection of the prefilter terms. With the prefilter matrix defined, the MIMO design is complete.

5.5 Summary

This chapter presents some specialized design techniques that are useful when one is forced to work with unstable non-minimum phase plants. Several tasks are defined and their importance is explained. After defining each of the individual effective plants in factored form, the roots are analyzed. Specifically, the concern is with right half plane poles and zeros that are in close proximity to each other. The singular-G method is presented and used to modify the effective MIMO plants by converting them to equivalent SISO plants (with respect to stability). Compensation parameters are then used to separate the RHP poles and zeros as much as possible, to maximize the range of loop transmission gain over which the closed-loop system would be stable.

Then, for one flight condition the optimal blending method is used to develop the balanced stable loop transmission function. A root locus plot is used to determine the range of gain over which the closed-loop system would be stable, and an optimal value is chosen. After adding the necessary far off poles, the loop transmission function is again plotted on a root locus to verify that the system would still be stable for the chosen gain value.

Following this is a brief discussion of how to obtain the overall compensator transfer function. Finally, the general procedure is discussed that would be required to complete the MIMO design, with the appropriate prefilter matrix for ensuring the desired system time response characteristics. Chapter VI presents the conclusions and recommendations for related efforts.

VI. Conclusions and Recommendations

6.1 Conclusions

This thesis discusses a variety of separate but related tasks pertaining to control law development for an unstable, non-minimum phase aircraft. Variations of the Quantitative Feedback Technique are discussed and applied to the design problem. Although time did not permit the completion of the lateral-directional control system designs, a substantial amount of material is presented that may be useful to flight control engineers pursuing similar development efforts. This problem is considered *extremely* challenging [15], due to the large number of RHP poles and zeros in the effective plants and the wide plant variations across the different flight conditions.

This research breaks new ground in several areas:

- Develops new aircraft models based on existing models that incorporate additional control capability.
- Develops frequency dependent compensation for multi-variable, unstable, non-minimum phase open-loop dynamics models.
- Proposes using the non-minimum phase reverse response region as the transient control region of interest when the non-minimum phase zeros are sufficiently small.
- Presents the first combined application of optimal blending and the singular-G method to a non-minimum phase, unstable MIMO plant.

The thesis starts by defining a problem experienced by the X-29A research aircraft. While flying at extreme AOAs, the aircraft in its present configuration uses most of its available control authority to control wing rock and yaw oscillations, leaving little maneuvering capability. The use of differential canards is one proposed solution. It is decided to investigate this idea by developing and modifying existing aircraft dynamics models and developing flight control laws that incorporate the additional control capability. Due to limited amounts of differential canard wind tunnel data, the linearized aircraft models developed here only *approximate* the performance of the original aircraft. Development of aircraft models that represent the

actual performance of the X-29A with differential canards would require substantial additional wind tunnel testing, but a general procedure to develop such models is presented in this thesis.

Four flight conditions with varying AOAs are chosen based on a speed of 0.3 Mach and an altitude of 20,000 feet. The four AOAs are 20, 40, 50, and 60 degrees. The aircraft model development begins by defining the control surface configurations and their representative transfer functions. Next, after a brief description of linearized aircraft models in general, the state vectors are defined. The control vectors are modified to account for the differential canard effects and the development of the new control matrices is presented. The control variables are chosen to be pitch rate, roll rate, and yaw rate. After re-defining the output matrices to specify these state variables, the final linearized state space models are presented for the four chosen flight conditions.

The weighting matrix development begins with a detailed look at the purpose of a weighting matrix and a discussion of why the development is especially challenging for this type of problem. Considerable time was expended on trying conventional design techniques to develop the frequency dependent compensation required for the lateral-directional channels. Due to the effects of unstable RHP poles, a root shifting method is applied and found to yield acceptable results. With this method, frequency dependent compensation terms are developed for each of the cases in the frequency domain and then *fine-tuned* as necessary in the time domain. The resulting open-loop step responses clearly show the desired results; that the control surfaces are all working in phase with each other continuously. The results of this development are perhaps best summarized by comparing the uncompensated open-loop responses for the 50 degree yaw case (Figure 3.3), with the unsuccessful compensated responses (Figures 3.7 & 3.9), and the successful compensated responses (Figure 3.63).

Due to extreme variations in the effective plants, it is decided to design four separate controllers for the longitudinal flight control system. Following a brief overview of QFT terms, the roots of the longitudinal effective plants are analyzed and the effects of RHP poles and zeros are discussed. The actual control design centers on developing optimal loop transmission functions that maximize the feedback benefits over the frequency range of interest while maintaining acceptable gain and phase margins for stability. The development uses Nichols and Bode plots, since each has advantages over the other in terms of usefulness. In each case, the loop

transmission function is used to obtain the compensator functions. Following this, the prefilter design process is discussed and it is shown how the prefilter is used to modify the closed-loop system time response. Also shown is how an otherwise undesirable non-minimum phase characteristic (the region of reverse response) may be used to advantage in some situations, as is shown in Figures 4.25 through 4.27.

The lateral-directional designs commence with an analysis of the effective plants. It is noted that due to the large number of RHP poles and zeros in close proximity to each other the achievable stability margins are *severely* limited. In an effort to improve this situation, the singular-G method is presented and used to transform the effective MIMO plant into an equivalent (with respect to stability) SISO plant. The form of the singular-G compensator is shown (Figure 5.1) and its parameters are used to modify the equivalent SISO plant in such a way that the RHP poles and zeros are separated as much as possible. The results are shown on root locus plots for clarity. Next, the optimal blending method is discussed in detail, and applied to one case to develop an optimal loop transmission function for the equivalent SISO plant. The resulting function is shown to result in a stable closed-loop system over a specified range of gain (Figure 5.7). Although time constraints prevented completion of the lateral-directional controllers, the remaining steps are discussed as an aid to engineers interested in performing related design efforts.

Finally, one overall conclusion is worth mentioning. Throughout the effort, *MatrixX* (with *SystemBuild*) has proven to be an extremely effective computer aided design and analysis package. Also, the Sun *Sparc - II* workstations, with their *multiple window* capabilities and many useful features, have made both the design and the write-up tasks considerably easier than they might have been on a less capable system.

6.2 Recommendations

Several recommendations come to mind as this research is concluded. These recommendations may be useful to anyone continuing this research or pursuing similar development studies. While this thesis presents a great deal of information on how to work with unstable, non-minimum phase plants, it is shown that the *best* results obtained are only marginally acceptable for a practical design.

As alluded to earlier, the correct choice of control variables is critical for a MIMO design problem such as this. By choosing the three angular rates as control

variables, the output matrix is quite simple, as these rates are direct state variables. However, such a choice clearly results in effective plants that have very undesirable characteristics in the form of numerous RHP poles and zeros in close proximity to each other. With such limitations, the designer is limited in what he can do to develop some sort of optimal control system. In this case, all that can be hoped for is to achieve *marginal* stability [15].

It is interesting to note that the idea of re-defining a problem such as this is not new. Normal acceleration and pitch rate were originally defined by the manufacturer as the two outputs to be independently controlled in the X-29A longitudinal flight control system. The resulting effective plant had RHP poles and zeros so close to each other that designers could achieve only very small stability margins, even with scheduling. In that case, the problem was abandoned and different variables were defined as outputs, for which the effective plant was minimum phase [13]. Thus, the recommendation here is to carefully choose the control variables in such a way that the open-loop plants are at least minimum-phase, even if unstable.

Another recommendation pertains to the lateral-directional control system design. The singular-G method is seen to be somewhat effective in improving the effective plant characteristics by increasing the separation of RHP poles and zeros. However, in this thesis, the choice is made to use only two of the singular-G parameters and to constrain them to be scalars. Perhaps by using all three parameters and allowing them to be frequency dependent terms, the singular-G method would result in equivalent effective plants with desirable characteristics. Also, it is recommended that after applying the singular-G compensation, the control surfaces be checked once again to ensure that they are still working together as effectively as they were before the compensation was added.

Finally, one over-riding recommendation is to attack a problem such as this with non-linear QFT theory, and allow for time-varying dynamics. The use of linear time-invariant design techniques, while somewhat better proven and more easily understood, limits the designer in unusual problems such as this [15]. Further, non-linear mathematical aircraft models are likely to better approximate the aircraft's dynamics at high AOAs. A non-linear model of the basic X-29 aircraft has been developed for the AFIT *SIMSTAR* computer by Captain Cox [6].

In closing, as an aid to related follow-on research efforts, the following additional references may be useful [7],[17],[18],[25],[28].

Bibliography

1. Barfield, Finley, A., "Head Control Engineer AFTI/F-16. Personal Interviews." Flight Dynamics Directorate, Wright Labs, Wright-Patterson AFB, OH, December 1990 through December 1991.
2. Blakelock, John H. *Automatic Control of Aircraft and Missiles* (Second Edition). Wiley & Sons, 1991.
3. Bosworth, John T. *Linearized Aerodynamic and Control Law Models of the X-29A Airplane and Comparison with Flight Data*. Technical Report, Edwards AFB, CA: NASA Ames Research Center / Dryden Flight Research Facility, September 1989.
4. Bosworth, John T. and Timothy H. Cox. *A Design Procedure for the Handling Qualities Optimization of the X-29A Aircraft*. Technical Report, Edwards AFB, CA: NASA Ames Research Center / Dryden Flight Research Facility.
5. Christian, Terry V., "Group Leader for Simulation Programs. Personal Interviews." Flight Dynamics Directorate, Wright Labs, Wright-Patterson AFB, OH, December 1990 through December 1991.
6. Cox, Thomas J. *Development of a High Fidelity Non-linear Simulation of the X-29 Aircraft on the Simstar Computer*. MS thesis, Air Force Institute of Technology, Wright-Patterson AFB, OH, March 1991.
7. Crosby, Kenneth A. *Quantitative Feedback Theory Application to Flight Control System Design for the AFTI/F-16*. MS thesis, Air Force Institute of Technology, Wright-Patterson AFB, OH, December 1990.
8. D'Azzo, John J. and Constantine H. Houpis. *Linear Control System Analysis & Design —Conventional and Modern* (Third Edition). McGraw-Hill, 1988.
9. Gillard, William, "Flight Control Systems Engineer. Personal Interviews." X-29 Program Office, Wright Labs, Wright-Patterson AFB, OH, December 1990 through December 1991.
10. Gunston, Bill. *Grumman X-29*. Aeolus Publishing Limited, 1985.
11. Hicks, John W. and Neil W. Matheny. *Preliminary Flight Assessment of the X-29A Advanced Technology Demonstrator*. Technical Report NASA TM-100407, Edwards AFB, CA: NASA Ames Research Center / Dryden Flight Research Facility, September 1987.
12. Horowitz, Isaac. "Design of Feedback Systems with Non-minimum Phase Unstable Plants," *International Journal of Systems Sciences*, 10:1025-1040 (September 1979).
13. Horowitz, Isaac. "Survey of Quantitative Feedback Theory," *International Journal of Control*, 53:255-291 (February 1991).

14. Horowitz, Isaac and Yin-Kuei Liao. "Limitations of Non-minimum Phase Feedback Systems," *International Journal of Control*, 40:1003-1013 (May 1984).
15. Horowitz, Isaac M., "Personal Conversation and Correspondance." Distinguished Visiting Professor of Electrical Engineering, Air Force Institute of Technology, Wright-Patterson AFB, OH, May 1991 through December 1991.
16. Houpis, Constantine H., "Personal Conversation, Correspondance and Class Notes." Professor of Electrical Engineering, Air Force Institute of Technology, Wright-Patterson AFB, OH, May 1990 through December 1991.
17. Houpis, Constantine H. *Quantitative Feedback Theory (QFT)—Technique for Designing Multivariable Control Systems*. Technical Report AFWAL-TR-86-3107, Wright-Patterson AFB, OH: Flight Dynamics Laboratory, January 1987.
18. Miller, Russel B. *Multi-Input Multi-Output Flight Control System Design for the YF-16 Using Non-Linear QFT and Pilot Compensation*. MS thesis, Air Force Institute of Technology, Wright-Patterson AFB, OH, December 1990.
19. Matrix, CAD/CAE Program, Integrated Systems Inc., Santa Clara, CA, 95054-1215.
20. Nelson, Robert C. *Flight Stability and Automatic Control*. McGraw-Hill, 1989.
21. Pace, Steve. *The Grumman X-29*. Tab Books, 1991.
22. Pachter, Meir, "Personal Conversation, Correspondance and Class Notes." Distinguished Visiting Professor of Electrical Engineering, Air Force Institute of Technology, Wright-Patterson AFB, OH, January 1991 through December 1991.
23. Paschall, Randall N., "Personal Conversation, Correspondance and Class Notes." Associate Professor of Electrical Engineering, Air Force Institute of Technology, Wright-Patterson AFB, OH, May 1990 through December 1991.
24. Pellicano, Paul and others. *X-29 High Angle of Attack Flight Test Procedures, Results, and Lessons Learned*. Technical Report, Edwards AFB, CA: Grumman Systems Division and Air Force Flight Test Center, 1990.
25. Phillips, William D. *Frequency Sensitive QFT Weighting Matrix*. MS thesis, Air Force Institute of Technology, Wright-Patterson AFB, OH, December 1988.
26. Raney, David L. and James G. Batterson. *Lateral Stability Analysis for the X-29A Drop Model Using System Identification Methodology*. Technical Report NASA TM-4108, Hampton, VA: NASA Langley Research Center, 1989.
27. Walke, Jon G. *Design of Longitudinal Flight Control System Using Singular-G Method*. MS thesis, Air Force Institute of Technology, Wright Patterson AFB, OH, December 1983.
28. Wheaton, David G. *Automatic Flight Control System Design for an Unmanned Research Vehicle Using Discrete Quantitative Feedback Theory*. MS thesis, Air Force Institute of Technology, Wright-Patterson AFB, OH, December 1990.

Appendix A. Original State Space Matrices

This appendix lists the original state space matrices (both longitudinal and lateral-directional) for each of the four flight conditions. These matrices were generated by the NASA Ames-Dryden non-linear simulation program and do not include differential canard effects.

$$A_{lon20} = \begin{bmatrix} -6.7320D - 02 & -1.9190D + 01 & -5.8320D - 01 & -3.2110D + 01 \\ -6.0200D - 04 & -1.4980D - 01 & 9.9480D - 01 & -3.9770D - 09 \\ 4.9390D - 04 & 7.3440D - 01 & -1.4560D - 01 & -2.2720D - 09 \\ 0.0000D + 00 & 0.0000D + 00 & 1.0000D + 00 & 0.0000D + 00 \end{bmatrix}$$

$$B_{lon20} = \begin{bmatrix} -8.8250D - 02 & -8.5710D - 02 & -2.3390D - 02 & 1.0280D - 01 \\ -3.3100D - 04 & -3.4930D - 04 & -2.1030D - 04 & -1.2020D - 04 \\ 1.2410D - 02 & -2.7310D - 03 & -9.6810D - 03 & -9.0470D - 04 \\ 0.0000D + 00 & 0.0000D + 00 & 0.0000D + 00 & 0.0000D + 00 \end{bmatrix}$$

$$C_{lon20} = \begin{bmatrix} 1.0000D + 00 & 0.0000D + 00 & 0.0000D + 00 & 0.0000D + 00 \\ 0.0000D + 00 & 5.7300D + 01 & 0.0000D + 00 & 0.0000D + 00 \\ 0.0000D + 00 & 0.0000D + 00 & 5.7300D + 01 & 0.0000D + 00 \\ 0.0000D + 00 & 0.0000D + 00 & 0.0000D + 00 & 5.7300D + 01 \\ 6.7000D - 03 & 1.4100D + 00 & 5.9590D - 02 & -6.0660D - 04 \\ 6.7000D - 03 & 1.4100D + 00 & 5.9590D - 02 & -6.0660D - 04 \end{bmatrix}$$

$$D_{lon20} = \begin{bmatrix} 0.0000D + 00 & 0.0000D + 00 & 0.0000D + 00 & 0.0000D + 00 \\ 0.0000D + 00 & 0.0000D + 00 & 0.0000D + 00 & 0.0000D + 00 \\ 0.0000D + 00 & 0.0000D + 00 & 0.0000D + 00 & 0.0000D + 00 \\ 0.0000D + 00 & 0.0000D + 00 & 0.0000D + 00 & 0.0000D + 00 \\ 3.4850D - 03 & 4.1870D - 03 & 2.5190D - 03 & 3.3150D - 05 \\ 3.4850D - 03 & 4.1870D - 03 & 2.5190D - 03 & 3.3150D - 05 \end{bmatrix}$$

$$A_{lat20} = \begin{bmatrix} -6.8010D - 02 & 3.4030D - 01 & -9.3810D - 01 & 9.7000D - 02 \\ -1.8850D + 01 & 1.4380D - 02 & 1.2860D - 01 & 1.4200D - 06 \\ 1.0090D + 00 & -3.3750D - 02 & -1.3520D - 02 & 4.3340D - 07 \\ 0.0000D + 00 & 1.0000D + 00 & 3.6400D - 01 & 6.6800D - 03 \end{bmatrix}$$

$$B_{lat20} = \begin{bmatrix} -8.8650D - 05 & 2.0300D - 04 \\ 1.3280D - 01 & 1.0630D - 02 \\ 7.1400D - 03 & -9.8750D - 03 \\ 0.0000D + 00 & 0.0000D + 00 \end{bmatrix}$$

$$C_{lat20} = \begin{bmatrix} 5.7300D + 01 & 0.0000D + 00 & 0.0000D + 00 & 0.0000D + 00 \\ 0.0000D + 00 & 5.7300D + 01 & 0.0000D + 00 & 0.0000D + 00 \\ 0.0000D + 00 & 0.0000D + 00 & 5.7300D + 01 & 0.0000D + 00 \\ 0.0000D + 00 & 0.0000D + 00 & 0.0000D + 00 & 5.7300D + 01 \\ -1.0800D + 03 & 8.2390D - 01 & 7.3660D + 00 & 8.1380D - 05 \\ 5.7800D + 01 & -1.9340D + 00 & -7.7450D - 01 & 2.4830D - 05 \\ 7.3500D - 03 & -1.6550D - 02 & 1.2130D - 02 & -1.6670D - 03 \end{bmatrix}$$

$$D_{lat20} = \begin{bmatrix} 0.0000D + 00 & 0.0000D + 00 \\ 0.0000D + 00 & 0.0000D + 00 \\ 0.0000D + 00 & 0.0000D + 00 \\ 0.0000D + 00 & 0.0000D + 00 \\ 7.6080D + 00 & 6.0910D - 01 \\ 4.0910D - 01 & -5.6580D - 01 \\ -5.5480D - 03 & 1.9680D - 03 \end{bmatrix}$$

$$A_{lon40} = \begin{bmatrix} -1.8900D - 01 & -4.4710D + 01 & -1.0960D + 00 & -3.2110D + 01 \\ -6.6150D - 04 & -8.2400D - 02 & 9.9580D - 01 & -1.2670D - 08 \\ 4.7760D - 04 & 3.0720D - 01 & -2.7990D - 01 & 1.5050D - 07 \\ 0.0000D + 00 & 0.0000D + 00 & 1.0000D + 00 & 0.0000D + 00 \end{bmatrix}$$

$$B_{lon40} = \begin{bmatrix} -2.1920D - 01 & -5.1610D - 02 & -5.1690D - 02 & 8.3780D - 02 \\ -7.4030D - 04 & 3.4270D - 05 & -2.0890D - 04 & -2.2590D - 04 \\ 1.4130D - 02 & -2.9220D - 03 & -8.6820D - 03 & -9.0290D - 04 \\ 0.0000D + 00 & 0.0000D + 00 & 0.0000D + 00 & 0.0000D + 00 \end{bmatrix}$$

$$C_{lon40} = \begin{bmatrix} 1.0000D + 00 & 0.0000D + 00 & 0.0000D + 00 & 0.0000D + 00 \\ 0.0000D + 00 & 5.7300D + 01 & 0.0000D + 00 & 0.0000D + 00 \\ 0.0000D + 00 & 0.0000D + 00 & 5.7300D + 01 & 0.0000D + 00 \\ 0.0000D + 00 & 0.0000D + 00 & 0.0000D + 00 & 5.7300D + 01 \\ 9.9490D - 03 & 1.5930D + 00 & 6.6880D - 02 & -1.1400D - 03 \\ 9.9490D - 03 & 1.5930D + 00 & 6.6880D - 02 & -1.1400D - 03 \end{bmatrix}$$

$$D_{lon40} = \begin{bmatrix} 0.0000D + 00 & 0.0000D + 00 & 0.0000D + 00 & 0.0000D + 00 \\ 0.0000D + 00 & 0.0000D + 00 & 0.0000D + 00 & 0.0000D + 00 \\ 0.0000D + 00 & 0.0000D + 00 & 0.0000D + 00 & 0.0000D + 00 \\ 0.0000D + 00 & 0.0000D + 00 & 0.0000D + 00 & 0.0000D + 00 \\ 9.3380D - 03 & 8.8570D - 04 & 2.9020D - 03 & 3.2710D - 05 \\ 9.3380D - 03 & 8.8570D - 04 & 2.9020D - 03 & 3.2710D - 05 \end{bmatrix}$$

$$A_{lat40} = \begin{bmatrix} 4.7370D - 02 & 6.3860D - 01 & -7.6430D - 01 & 7.9080D - 02 \\ -1.4260D + 01 & 1.3430D + 00 & -1.1530D + 00 & -1.0300D - 04 \\ 3.9610D - 01 & 6.3430D - 02 & -1.7800D - 01 & -2.4160D - 05 \\ 0.0000D + 00 & 1.0000D + 00 & 8.3910D - 01 & 4.5550D - 02 \end{bmatrix}$$

$$B_{lat40} = \begin{bmatrix} -9.3770D - 05 & 3.6380D - 05 \\ 2.3610D - 02 & -4.3660D - 03 \\ 2.5790D - 03 & -3.3690D - 03 \\ 0.0000D + 00 & 0.0000D + 00 \end{bmatrix}$$

$$C_{lat40} = \begin{bmatrix} 5.7300D + 01 & 0.0000D + 00 & 0.0000D + 00 & 0.0000D + 00 \\ 0.0000D + 00 & 5.7300D + 01 & 0.0000D + 00 & 0.0000D + 00 \\ 0.0000D + 00 & 0.0000D + 00 & 5.7300D + 01 & 0.0000D + 00 \\ 0.0000D + 00 & 0.0000D + 00 & 0.0000D + 00 & 5.7300D + 01 \\ -8.1720D + 02 & 7.6960D + 01 & -6.6050D + 01 & -5.8990D - 03 \\ 2.2690D + 01 & 3.6340D + 00 & -1.0200D + 01 & -1.3840D - 03 \\ 3.4950D - 01 & -9.0060D - 02 & 6.3870D - 02 & -1.3570D - 03 \end{bmatrix}$$

$$D_{lat40} = \begin{bmatrix} 0.0000D + 00 & 0.0000D + 00 \\ 0.0000D + 00 & 0.0000D + 00 \\ 0.0000D + 00 & 0.0000D + 00 \\ 0.0000D + 00 & 0.0000D + 00 \\ 1.3530D + 00 & -2.5010D - 01 \\ 1.4780D - 01 & -1.9300D - 01 \\ -1.7890D - 03 & 6.2030D - 04 \end{bmatrix}$$

$$A_{lon50} = \begin{bmatrix} -2.5560D - 01 & -4.0360D + 01 & -1.3060D + 00 & -3.2110D + 01 \\ -6.4510D - 04 & 8.9490D - 03 & 9.9650D - 01 & -4.8610D - 08 \\ 4.8980D - 04 & 5.4140D - 02 & -3.9930D - 01 & 1.6800D - 06 \\ 0.0000D + 00 & 0.0000D + 00 & 1.0000D + 00 & 0.0000D + 00 \end{bmatrix}$$

$$B_{lon50} = \begin{bmatrix} -2.7550D - 01 & -5.4060D - 02 & -4.8730D - 02 & 7.0310D - 02 \\ -6.7650D - 04 & 1.0800D - 04 & -1.5410D - 04 & -2.6920D - 04 \\ 1.8180D - 02 & -3.2690D - 03 & -8.6100D - 03 & -9.0220D - 04 \\ 0.0000D + 00 & 0.0000D + 00 & 0.0000D + 00 & 0.0000D + 00 \end{bmatrix}$$

$$C_{lon50} = \begin{bmatrix} 1.0000D + 00 & 0.0000D + 00 & 0.0000D + 00 & 0.0000D + 00 \\ 0.0000D + 00 & 5.7300D + 01 & 0.0000D + 00 & 0.0000D + 00 \\ 0.0000D + 00 & 0.0000D + 00 & 5.7300D + 01 & 0.0000D + 00 \\ 0.0000D + 00 & 0.0000D + 00 & 0.0000D + 00 & 5.7300D + 01 \\ 1.1230D - 02 & 1.0780D + 00 & 7.1520D - 02 & -1.3580D - 03 \\ 1.1230D - 02 & 1.0780D + 00 & 7.1520D - 02 & -1.3580D - 03 \end{bmatrix}$$

$$D_{lon50} = \begin{bmatrix} 0.0000D + 00 & 0.0000D + 00 & 0.0000D + 00 & 0.0000D + 00 \\ 0.0000D + 00 & 0.0000D + 00 & 0.0000D + 00 & 0.0000D + 00 \\ 0.0000D + 00 & 0.0000D + 00 & 0.0000D + 00 & 0.0000D + 00 \\ 0.0000D + 00 & 0.0000D + 00 & 0.0000D + 00 & 0.0000D + 00 \\ 1.0090D - 02 & 7.3700D - 04 & 2.4380D - 03 & 3.2530D - 05 \\ 1.0090D - 02 & 7.3700D - 04 & 2.4380D - 03 & 3.2530D - 05 \end{bmatrix}$$

$$A_{lat50} = \begin{bmatrix} 1.1860D - 01 & 7.5760D - 01 & -6.3960D - 01 & 6.6350D - 02 \\ -2.1300D + 01 & 1.1930D + 00 & 1.2230D + 00 & 3.3230D - 05 \\ -1.0910D + 00 & 1.1400D - 01 & 1.0400D - 02 & -2.5620D - 05 \\ 0.0000D + 00 & 1.0000D + 00 & 1.1920D + 00 & 6.8560D - 02 \end{bmatrix}$$

$$B_{lat50} = \begin{bmatrix} -9.3770D - 05 & 3.2810D - 06 \\ 2.2790D - 02 & -1.1010D - 02 \\ 2.5430D - 03 & -6.6130D - 05 \\ 0.0000D + 00 & 0.0000D + 00 \end{bmatrix}$$

$$C_{lat50} = \begin{bmatrix} 5.7300D + 01 & 0.0000D + 00 & 0.0000D + 00 & 0.0000D + 00 \\ 0.0000D + 00 & 5.7300D + 01 & 0.0000D + 00 & 0.0000D + 00 \\ 0.0000D + 00 & 0.0000D + 00 & 5.7300D + 01 & 0.0000D + 00 \\ 0.0000D + 00 & 0.0000D + 00 & 0.0000D + 00 & 5.7300D + 01 \\ -1.2200D + 03 & 6.8330D + 01 & 7.0070D + 01 & 1.9040D - 03 \\ -6.2480D + 01 & 6.5310D + 00 & 5.9610D - 01 & -1.4680D - 03 \\ 9.7070D - 01 & -1.2790D - 01 & -8.3360D - 03 & -1.1450D - 03 \end{bmatrix}$$

$$D_{lat50} = \begin{bmatrix} 0.0000D + 00 & 0.0000D + 00 \\ 0.0000D + 00 & 0.0000D + 00 \\ 0.0000D + 00 & 0.0000D + 00 \\ 0.0000D + 00 & 0.0000D + 00 \\ 1.3060D + 00 & -6.3070D - 01 \\ 1.4570D - 01 & -3.7890D - 03 \\ -1.7600D - 03 & 4.0140D - 04 \end{bmatrix}$$

$$A_{lon60} = \begin{bmatrix} -2.9390D - 01 & -2.7690D + 01 & -1.4770D + 00 & -3.2110D + 01 \\ -5.6540D - 04 & 9.5210D - 02 & 9.9730D - 01 & -2.0250D - 08 \\ 4.7520D - 04 & -1.0640D + 00 & -1.6620D - 01 & 7.0730D - 07 \\ 0.0000D + 00 & 0.0000D + 00 & 1.0000D + 00 & 0.0000D + 00 \end{bmatrix}$$

$$B_{lon60} = \begin{bmatrix} -2.2010D - 01 & -1.3380D - 01 & -3.4770D - 02 & 5.4700D - 02 \\ -2.3780D - 04 & -2.7180D - 04 & -7.3550D - 05 & -3.0430D - 04 \\ 8.2980D - 03 & -5.7350D - 03 & -9.5570D - 03 & -9.0160D - 04 \\ 0.0000D + 00 & 0.0000D + 00 & 0.0000D + 00 & 0.0000D + 00 \end{bmatrix}$$

$$C_{lon60} = \begin{bmatrix} 1.0000D + 00 & 0.0000D + 00 & 0.0000D + 00 & 0.0000D + 00 \\ 0.0000D + 00 & 5.7300D + 01 & 0.0000D + 00 & 0.0000D + 00 \\ 0.0000D + 00 & 0.0000D + 00 & 5.7300D + 01 & 0.0000D + 00 \\ 0.0000D + 00 & 0.0000D + 00 & 0.0000D + 00 & 5.7300D + 01 \\ 1.1290D - 02 & 5.5020D - 01 & 6.1940D - 02 & -1.5350D - 03 \\ 1.1290D - 02 & 5.5020D - 01 & 6.1940D - 02 & -1.5350D - 03 \end{bmatrix}$$

$$D_{lon60} = \begin{bmatrix} 0.0000D + 00 & 0.0000D + 00 & 0.0000D + 00 & 0.0000D + 00 \\ 0.0000D + 00 & 0.0000D + 00 & 0.0000D + 00 & 0.0000D + 00 \\ 0.0000D + 00 & 0.0000D + 00 & 0.0000D + 00 & 0.0000D + 00 \\ 0.0000D + 00 & 0.0000D + 00 & 0.0000D + 00 & 0.0000D + 00 \\ 6.7670D - 03 & 5.1280D - 03 & 1.6460D - 03 & 3.2380D - 05 \\ 6.7670D - 03 & 5.1280D - 03 & 1.6460D - 03 & 3.2380D - 05 \end{bmatrix}$$

$$A_{lat60} = \begin{bmatrix} 1.3450D - 01 & 8.6190D - 01 & -4.9850D - 01 & 5.1610D - 02 \\ -1.1630D + 01 & -2.2140D - 01 & 1.6470D + 00 & 1.9310D - 04 \\ -6.3660D - 01 & -5.2130D - 02 & -1.5140D - 03 & -5.3250D - 05 \\ 0.0000D + 00 & 1.0000D + 00 & 1.7320D + 00 & 7.4330D - 02 \end{bmatrix}$$

$$B_{lat60} = \begin{bmatrix} -9.3770D - 05 & 1.2120D - 05 \\ 2.2100D - 02 & -9.1430D - 03 \\ 2.5130D - 03 & 3.2340D - 04 \\ 0.0000D + 00 & 0.0000D + 00 \end{bmatrix}$$

$$C_{lat60} = \begin{bmatrix} 5.7300D + 01 & 0.0000D + 00 & 0.0000D + 00 & 0.0000D + 00 \\ 0.0000D + 00 & 5.7300D + 01 & 0.0000D + 00 & 0.0000D + 00 \\ 0.0000D + 00 & 0.0000D + 00 & 5.7300D + 01 & 0.0000D + 00 \\ 0.0000D + 00 & 0.0000D + 00 & 0.0000D + 00 & 5.7300D + 01 \\ -6.6650D + 02 & -1.2690D + 01 & 9.4350D + 01 & 1.1060D - 02 \\ -3.6470D + 01 & -2.9870D + 00 & -8.6720D - 02 & -3.0510D - 03 \\ 5.4660D - 01 & -3.2430D - 02 & -3.8710D - 02 & -8.9560D - 04 \end{bmatrix}$$

$$D_{lat60} = \begin{bmatrix} 0.0000D + 00 & 0.0000D + 00 \\ 0.0000D + 00 & 0.0000D + 00 \\ 0.0000D + 00 & 0.0000D + 00 \\ 0.0000D + 00 & 0.0000D + 00 \\ 1.2660D + 00 & -5.2390D - 01 \\ 1.4400D - 01 & 1.8530D - 02 \\ -1.7360D - 03 & 4.1050D - 04 \end{bmatrix}$$

Appendix B. Open-Loop System Eigenvalues

This appendix lists the open-loop system Eigenvalues for each of the four flight conditions. The Eigenvalues given in this appendix are obtained from the corresponding A matrices listed in Appendix A. The positive Eigenvalues are unstable open-loop right half plane poles. The complex conjugate pairs possess oscillatory characteristics, while the purely real unstable roots have an exponential growth characteristic. This can be seen in the uncompensated step response diagrams in Chapter III.

$$\lambda_{lon20} = \begin{bmatrix} -0.0203 + 0.1257j \\ -0.0203 - 0.1257j \\ 0.7080 + 0.0000j \\ -1.0302 + 0.0000j \end{bmatrix}$$

$$\lambda_{lon40} = \begin{bmatrix} -0.0534 + 0.1193j \\ -0.0534 - 0.1193j \\ 0.3756 + 0.0000j \\ -0.8200 + 0.0000j \end{bmatrix}$$

$$\lambda_{lon50} = \begin{bmatrix} 0.0785 + 0.0000j \\ -0.0377 + 0.1528j \\ -0.0377 - 0.1528j \\ -0.6490 + 0.0000j \end{bmatrix}$$

$$\lambda_{lon60} = \begin{bmatrix} -0.0677 + 0.0000j \\ -0.2586 + 0.0000j \\ -0.0193 + 1.0103j \\ -0.0193 - 1.0103j \end{bmatrix}$$

$$\lambda_{lat20} = \begin{bmatrix} 0.0058 + 0.0000j \\ -0.3239 + 0.0000j \\ 0.1288 + 2.7262j \\ 0.1288 - 2.7262j \end{bmatrix}$$

$$\lambda_{lat40} = \begin{bmatrix} -0.0808 + 0.1561j \\ -0.0808 - 0.1561j \\ 0.7098 + 3.0081j \\ 0.7098 - 3.0081j \end{bmatrix}$$

$$\lambda_{lat50} = \begin{bmatrix} -0.0190 + 0.0977j \\ -0.0190 - 0.0977j \\ 0.7143 + 3.8832j \\ 0.7143 - 3.8832j \end{bmatrix}$$

$$\lambda_{lat60} = \begin{bmatrix} 0.0459 + 0.0000j \\ -0.1554 + 0.0000j \\ 0.0477 + 3.1259j \\ 0.0477 - 3.1259j \end{bmatrix}$$

Appendix C. Differential Canard Stability Derivatives

This appendix lists the matrices of symmetric canard coefficients, and differential canard coefficients, each taken about nominal symmetric canard settings of -25 and -40 degrees, respectively. Following this, the calculated stability derivative matrices are listed, each preceded by its respective *MatrixX* command line.

In each of the matrices, the 13 rows correspond to the angle of attack (α) varying from zero to sixty degrees in five degree increments. The six columns correspond to the coefficients of lift, drag, pitching moment, side force, yawing moment, and rolling moment, respectively.

SIM25 =						
CL	CD	CM	CY	CN	CL	AOA
4.9200D-01	1.3280D-01	-6.9310D-01	3.9000D-03	1.1000D-03	-9.0000D-04	0
8.2300D-01	1.5980D-01	-5.1460D-01	-7.6000D-03	3.4000D-03	2.0000D-04	5
1.1429D+00	2.6080D-01	-3.7700D-01	-1.2800D-02	5.8000D-03	1.7200D-03	10
1.3452D+00	4.0180D-01	-2.8640D-01	-5.6000D-03	5.3000D-03	1.3000D-03	15
1.4423D+00	5.5790D-01	-2.0230D-01	-3.7000D-03	4.9000D-03	4.7000D-03	20
1.5829D+00	7.3880D-01	-1.1930D-01	4.1000D-03	5.7000D-03	3.7000D-03	25
1.6977D+00	9.4520D-01	-3.9800D-02	1.6000D-02	8.2000D-03	2.0000D-03	30
1.8673D+00	1.2308D+00	3.9200D-02	3.7200D-02	7.1000D-03	-3.9000D-04	35
1.9713D+00	1.5244D+00	1.0690D-01	2.6000D-02	6.0000D-04	-1.1000D-03	40
1.9774D+00	1.7967D+00	1.7250D-01	-1.1200D-02	3.0000D-04	-3.9000D-03	45
1.9065D+00	2.0442D+00	1.8510D-01	-5.0000D-04	5.6000D-03	-2.8000D-03	50
1.7491D+00	2.2246D+00	1.8420D-01	2.0700D-02	1.8500D-02	-7.0000D-03	55
1.5072D+00	2.3065D+00	1.4920D-01	1.5200D-02	9.1000D-03	-4.0000D-04	60

SIM40 =						
CL	CD	CM	CY	CN	CL	AOA
3.5240D-01	2.4410D-01	-7.5000D-01	9.9000D-03	-2.0000D-04	-1.6000D-03	0
6.5630D-01	2.9650D-01	-7.5620D-01	2.8000D-03	1.1000D-03	3.9000D-03	5
8.7640D-01	3.5700D-01	-6.3300D-01	-1.0300D-02	1.8000D-03	3.5000D-03	10
1.0526D+00	4.4210D-01	-4.6310D-01	-9.4000D-03	2.8000D-03	-1.2000D-03	15
1.2245D+00	5.7370D-01	-3.7440D-01	5.0000D-03	3.5000D-03	-1.8000D-03	20
1.4137D+00	7.3830D-01	-3.0340D-01	7.2000D-03	5.5000D-03	-1.6000D-03	25
1.5258D+00	9.2110D-01	-2.4730D-01	1.6600D-02	6.3000D-03	-2.3000D-03	30
1.6222D+00	1.1320D+00	-1.7530D-01	1.2900D-02	1.2400D-02	-3.7000D-03	35
1.7680D+00	1.4235D+00	-1.0290D-01	1.6000D-03	7.1000D-03	3.1000D-03	40
1.7943D+00	1.6511D+00	-1.6300D-02	-1.5000D-02	7.5000D-03	3.9000D-03	45
1.7644D+00	1.8685D+00	3.8700D-02	8.2000D-03	6.8000D-03	2.0000D-04	50
1.6573D+00	2.0337D+00	7.5100D-02	1.2900D-02	8.7000D-03	-4.2000D-03	55
1.5108D+00	2.1930D+00	9.0300D-02	2.1200D-02	7.3000D-03	-4.0000D-04	60

DIFF25 =						
CL	CD	CM	CY	CN	CL	AOA
5.3890D-01	1.6740D-01	-5.4800D-01	-4.2100D-02	-1.3800D-02	-7.5000D-03	0
7.7050D-01	2.2950D-01	-4.9040D-01	-6.5600D-02	-1.0000D-02	-1.2900D-02	5
1.0388D+00	3.2270D-01	-3.9430D-01	-9.2400D-02	-7.5000D-03	-2.4800D-02	10
1.2587D+00	4.6430D-01	-3.0300D-01	-1.0170D-01	8.0000D-04	-3.2400D-02	15
1.4415D+00	6.2900D-01	-2.0760D-01	-1.0870D-01	1.3000D-02	-4.1400D-02	20
1.6005D+00	8.2080D-01	-1.3710D-01	-1.0260D-01	2.1800D-02	-4.6600D-02	25
1.7209D+00	1.0382D+00	-8.3100D-02	-6.0600D-02	2.0900D-02	-4.0800D-02	30
1.7963D+00	1.2676D+00	-2.1700D-02	-5.1500D-02	2.0800D-02	-3.7000D-02	35
1.8340D+00	1.5137D+00	2.9200D-02	-9.5500D-02	1.2500D-02	-2.3500D-02	40
1.8170D+00	1.7461D+00	7.6100D-02	-1.3170D-01	2.1200D-02	-2.9200D-02	45
1.7380D+00	1.9547D+00	1.1410D-01	-8.6000D-02	2.2300D-02	-3.7300D-02	50
1.5782D+00	2.0936D+00	1.0720D-01	-5.5400D-02	2.3500D-02	-2.7300D-02	55
1.4051D+00	2.2224D+00	6.6200D-02	-7.9100D-02	2.8900D-02	-1.6000D-02	60

DIFF40 =							
CL	CD	CM	CY	CN	Cl	AOA	
5.1290D-01	1.9550D-01	-5.7610D-01	-2.0900D-02	-1.0200D-02	-3.9000D-03	0	
7.6870D-01	2.4190D-01	-4.6270D-01	-4.7100D-02	-8.8000D-03	-4.4000D-03	5	
1.0628D+00	3.4860D-01	-3.9310D-01	-6.5700D-02	-5.2000D-03	-1.7100D-02	10	
1.1942D+00	4.9400D-01	-3.6080D-01	-6.5400D-02	2.0000D-04	-3.2000D-02	15	
1.3467D+00	6.7850D-01	-3.5970D-01	-1.0120D-01	1.7000D-03	-3.5600D-02	20	
1.4547D+00	8.3380D-01	-2.9650D-01	-1.0560D-01	4.6000D-03	-3.3400D-02	25	
1.5839D+00	1.0232D+00	-2.0200D-01	-9.2800D-02	3.3000D-03	-3.5400D-02	30	
1.6891D+00	1.2395D+00	-1.2650D-01	-9.5500D-02	3.2000D-03	-3.3300D-02	35	
1.7768D+00	1.4919D+00	-5.6000D-02	-1.2680D-01	4.0000D-03	-2.7500D-02	40	
1.7414D+00	1.6860D+00	-1.9200D-02	-1.2830D-01	1.3200D-02	-3.3200D-02	45	
1.6759D+00	1.8853D+00	2.3300D-02	-6.5300D-02	1.3100D-02	-4.2700D-02	50	
1.5616D+00	2.0679D+00	2.1500D-02	-2.7000D-02	6.3000D-03	-3.4600D-02	55	
1.3978D+00	2.1980D+00	1.9200D-02	-4.4600D-02	1.6400D-02	-2.2900D-02	60	

<> stabder25=(diff25-sim25)/20

STABDER25

=

CL	CD	CM	CY	CN	C1	AOA
2.3450D-03	1.7300D-03	7.2550D-03	-2.3000D-03	-7.4500D-04	-3.3000D-04	0
-2.6250D-03	3.4850D-03	1.2100D-03	-2.9000D-03	-6.7000D-04	-6.5500D-04	5
-5.2050D-03	3.0950D-03	-8.6500D-04	-3.9800D-03	-6.6500D-04	-1.3260D-03	10
-4.3250D-03	3.1250D-03	-8.3000D-04	-4.8050D-03	-2.2500D-04	-1.6850D-03	15
-4.0000D-05	3.5550D-03	-2.6500D-04	-5.2500D-03	4.0500D-04	-2.3050D-03	20
8.8000D-04	4.1000D-03	-8.9000D-04	-5.3350D-03	8.0500D-04	-2.5150D-03	25
1.1600D-03	4.6500D-03	-2.1650D-03	-3.8300D-03	6.3500D-04	-2.1400D-03	30
-3.5500D-03	1.8400D-03	-3.0450D-03	-4.4350D-03	6.8500D-04	-1.8350D-03	35
-6.8650D-03	-5.3500D-04	-3.8850D-03	-6.0750D-03	5.9500D-04	-1.1200D-03	40
-8.0200D-03	-2.5300D-03	-4.8200D-03	-6.0250D-03	1.0450D-03	-1.2650D-03	45
-8.4250D-03	-4.4750D-03	-3.5500D-03	-4.2750D-03	8.3500D-04	-1.7250D-03	50
-8.5450D-03	-6.5500D-03	-3.8500D-03	-3.8050D-03	2.5000D-04	-1.0150D-03	55
-5.1050D-03	-4.2050D-03	-4.1500D-03	-4.7150D-03	9.9000D-04	-7.8000D-04	60

<> stabder40=(diff40-sim40)/20

STABDER40

=

CL	CD	CM	CY	CN	C1	AOA
8.0250D-03	-2.4300D-03	8.6950D-03	-1.5400D-03	-5.0000D-04	-1.1500D-04	0
5.6200D-03	-2.7300D-03	1.4675D-02	-2.4950D-03	-4.9500D-04	-4.1500D-04	5
9.3200D-03	-4.2000D-04	1.1995D-02	-2.7700D-03	-3.5000D-04	-1.0300D-03	10
7.0800D-03	2.5950D-03	5.1150D-03	-2.8000D-03	-1.3000D-04	-1.5400D-03	15
6.1100D-03	5.2400D-03	7.3500D-04	-5.3100D-03	-9.0000D-05	-1.6900D-03	20
2.0500D-03	4.7750D-03	3.4500D-04	-5.6400D-03	-4.5000D-05	-1.5900D-03	25
2.9050D-03	5.1050D-03	2.2650D-03	-5.4700D-03	-1.5000D-04	-1.6550D-03	30
3.3450D-03	5.3750D-03	2.4400D-03	-5.4200D-03	-4.6000D-04	-1.4800D-03	35
4.4000D-04	3.4200D-03	2.3450D-03	-6.4200D-03	-1.5500D-04	-1.5300D-03	40
-2.6450D-03	1.7450D-03	-1.4500D-04	-5.6650D-03	2.8500D-04	-1.8550D-03	45
-4.4250D-03	8.4000D-04	-7.7000D-04	-3.6750D-03	3.1500D-04	-2.1450D-03	50
-4.7850D-03	1.7100D-03	-2.6800D-03	-1.9950D-03	-1.2000D-04	-1.5200D-03	55
-5.6500D-03	2.5000D-04	-3.5550D-03	-3.2900D-03	4.5500D-04	-1.1250D-03	60

Appendix D. Translation of Longitudinal Stability Derivatives

This appendix lists the differential canard stability derivatives obtained from the calculations shown in Appendix C. The first two of the six derivatives in each case are based on the coefficients of lift and drag. As shown in Figure 2.5, these stability derivatives are now transformed into the **Z** and **X** force derivatives. The *Matrix_X* command lines are shown for each calculation, and are readily derived from Figure 2.5.

STABDER20 =

-4.0000D-05 3.5550D-03 -2.6500D-04 -5.2500D-03 4.0500D-04 -2.3050D-03

STABDER40 =

4.4000D-04 3.4200D-03 2.3450D-03 -6.4200D-03 -1.5500D-04 -1.5300D-03

STABDER50 =

-4.4250D-03 8.4000D-04 -7.7000D-04 -3.6750D-03 3.1500D-04 -2.1450D-03

STABDER60 =

-5.6500D-03 2.5000D-04 -3.5550D-03 -3.2900D-03 4.5500D-04 -1.1250D-03

<> // CZ=-CLcos(alpha)-CDsin(alpha)

<> // CX=CLsin(alpha)-CDcos(alpha)

<> CZ20=4.0000D-05*cos(20)-3.5550D-03*sin(20)

CZ20 =

-3.2292D-03

<> CX20=-4.0000D-05*sin(20)-3.5550D-03*cos(20)

CX20 =

-1.4872D-03

<> CZ40=-4.4000D-04*cos(40)-3.4200D-03*sin(40)

CZ40 =

-2.2548D-03

<> CX40=4.4000D-04*sin(40)-3.4200D-03*cos(40)

CX40 =

2.6088D-03

<> CZ50=4.4250D-03*cos(50)-8.4000D-04*sin(50)

CZ50 =

4.4904D-03

<> CX50=-4.4250D-03*sin(50)-8.4000D-04*cos(50)

CX50 =

3.5044D-04

<> CZ60=5.6500D-03*cos(60)-2.5000D-04*sin(60)

CZ60 =

-5.3049D-03

<> CX60=-5.6500D-03*sin(60)-2.5000D-04*cos(60)

CX60 =

1.9603D-03

Appendix E. Modified B Matrices

This appendix lists the modified **B** matrices, after the incorporation of the differential canard wind tunnel data. The longitudinal and lateral-directional matrices are shown for the all four flight conditions.

$$\tilde{\mathbf{B}}_{lon20} = \begin{bmatrix} -8.8250D - 02 & -1.4872D - 03 & -8.5710D - 02 & -2.3390D - 02 \\ -3.3100D - 04 & -3.2292D - 03 & -3.4930D - 04 & -2.1030D - 04 \\ 1.2410D - 02 & -2.6500D - 04 & -2.7310D - 03 & -9.6810D - 03 \\ 0.0000D + 00 & 0.0000D + 00 & 0.0000D + 00 & 0.0000D + 00 \end{bmatrix}$$

$$\tilde{\mathbf{B}}_{lat20} = \begin{bmatrix} -8.8650D - 05 & 2.0300D - 04 & -5.2500D - 03 \\ 1.3280D - 01 & 1.0630D - 02 & -2.3050D - 03 \\ 7.1400D - 03 & -9.8750D - 03 & 4.0500D - 04 \\ 0.0000D + 00 & 0.0000D + 00 & 0.0000D + 00 \end{bmatrix}$$

$$\tilde{\mathbf{B}}_{lon40} = \begin{bmatrix} -2.1920D - 01 & 2.6088D - 03 & -5.1610D - 02 & -5.1690D - 02 \\ -7.4030D - 04 & -2.2548D - 03 & 3.4270D - 05 & -2.0890D - 04 \\ 1.2410D - 02 & 2.3450D - 03 & -2.9220D - 03 & -8.6820D - 03 \\ 0.0000D + 00 & 0.0000D + 00 & 0.0000D + 00 & 0.0000D + 00 \end{bmatrix}$$

$$\tilde{\mathbf{B}}_{lat40} = \begin{bmatrix} -9.3770D - 05 & 3.6380D - 05 & -6.4200D - 03 \\ 2.3610D - 02 & -4.3660D - 03 & -1.5300D - 03 \\ 2.5790D - 03 & -3.3690D - 03 & -1.5500D - 04 \\ 0.0000D + 00 & 0.0000D + 00 & 0.0000D + 00 \end{bmatrix}$$

$$\tilde{\mathbf{B}}_{lon50} = \begin{bmatrix} -2.7550D-01 & 3.5044D-04 & -5.4060D-02 & -4.8730D-02 \\ -6.7650D-04 & 4.4904D-03 & 1.0800D-03 & -1.5410D-04 \\ 1.8180D-02 & -7.7000D-04 & -3.2000D-03 & -8.0100D-03 \\ 0.0000D+00 & 0.0000D+00 & 0.0000D+00 & 0.0000D+00 \end{bmatrix}$$

$$\tilde{\mathbf{B}}_{lat50} = \begin{bmatrix} -9.3770D-05 & 3.2810D-06 & -3.6750D-03 \\ 2.2790D-02 & -1.1010D-02 & -2.1450D-03 \\ 2.5430D-03 & -6.6130D-05 & 3.1500D-04 \\ 0.0000D+00 & 0.0000D+00 & 0.0000D+00 \end{bmatrix}$$

$$\tilde{\mathbf{B}}_{lon60} = \begin{bmatrix} -2.2010D-01 & 1.9603D-03 & -1.3380D-01 & -3.4770D-02 \\ -2.3780D-04 & -5.3049D-03 & -2.7180D-04 & -7.3550D-05 \\ 1.8180D-02 & -3.5550D-03 & -5.7350D-03 & -9.5570D-03 \\ 0.0000D+00 & 0.0000D+00 & 0.0000D+00 & 0.0000D+00 \end{bmatrix}$$

$$\tilde{\mathbf{B}}_{lat60} = \begin{bmatrix} -9.3770D-05 & 1.2120D-05 & -3.2900D-03 \\ 2.2100D-02 & -9.1430D-03 & -1.1250D-03 \\ 2.5130D-03 & 3.2340D-04 & 4.5500D-04 \\ 0.0000D+00 & 0.0000D+00 & 0.0000D+00 \end{bmatrix}$$

Appendix F. Final State Space Models

This appendix lists the final state space models (S matrices) for each of the four flight conditions. These models have been modified to include differential canard aerodynamic effects. The reader is reminded that no changes have been made to the A matrices.

$$S_{lon20} =$$

Columns	1 thru	6			
-6.7320D-02	-1.9190D+01	-5.8320D-01	-3.2110D+01	-8.8250D-02	-1.4872D-03
-6.0200D-04	-1.4980D-01	9.9480D-01	-3.9770D-09	-3.3100D-04	-3.2292D-03
4.9390D-04	7.3440D-01	-1.4560D-01	-2.2720D-09	1.2410D-02	-2.6500D-04
0.0000D+00	0.0000D+00	1.0000D+00	0.0000D+00	0.0000D+00	0.0000D+00
0.0000D+00	0.0000D+00	0.0000D+00	0.0000D+00	0.0000D+00	0.0000D+00
0.0000D+00	0.0000D+00	0.0000D+00	0.0000D+00	0.0000D+00	0.0000D+00
0.0000D+00	0.0000D+00	1.0000D+00	0.0000D+00	0.0000D+00	0.0000D+00
0.0000D+00	0.0000D+00	0.0000D+00	0.0000D+00	0.0000D+00	0.0000D+00

Columns	7 thru	8
-8.5710D-02	-2.3390D-02	
-3.4930D-04	-2.1030D-04	
-2.7310D-03	-9.6810D-03	
0.0000D+00	0.0000D+00	
0.0000D+00	0.0000D+00	
0.0000D+00	0.0000D+00	
0.0000D+00	0.0000D+00	
0.0000D+00	0.0000D+00	

$$S_{lat20} =$$

Columns	1 thru	6				
-6.8010D-02	3.4030D-01	-9.3810D-01	9.7000D-02	-8.8650D-05	2.0300D-04	
-1.8850D+01	1.4380D-02	1.2860D-01	1.4200D-06	1.3280D-01	1.0630D-02	
1.0090D+00	-3.3750D-02	-1.3520D-02	4.3340D-07	7.1400D-03	-9.8750D-03	
0.0000D+00	1.0000D+00	3.6400D-01	6.6800D-02	0.0000D+00	0.0000D+00	
0.0000D+00	0.0000D+00	0.0000D+00	0.0000D+00	0.0000D+00	0.0000D+00	
0.0000D+00	1.0000D+00	0.0000D+00	0.0000D+00	0.0000D+00	0.0000D+00	
0.0000D+00	0.0000D+00	1.0000D+00	0.0000D+00	0.0000D+00	0.0000D+00	
0.0000D+00	0.0000D+00	0.0000D+00	0.0000D+00	0.0000D+00	0.0000D+00	

Columns	7 thru	7
-5.2500D-03		
-2.3050D-03		
4.0500D-04		
0.0000D+00		
0.0000D+00		
0.0000D+00		
0.0000D+00		
0.0000D+00		

$S_{lon40} =$

Columns	1 thru	6
-1.8900D-01	-4.4710D+01	-1.0960D+00 -3.2110D+01 -2.1920D-01 2.6088D-03
-6.6150D-04	-8.2400D-02	9.9580D-01 -1.2670D-08 -7.4030D-04 -2.2548D-03
4.7760D-04	3.0720D-01	-2.7990D-01 1.5050D-07 1.2410D-02 2.3450D-03
0.0000D+00	0.0000D+00	1.0000D+00 0.0000D+00 0.0000D+00 0.0000D+00
0.0000D+00	0.0000D+00	0.0000D+00 0.0000D+00 0.0000D+00 0.0000D+00
0.0000D+00	0.0000D+00	0.0000D+00 0.0000D+00 0.0000D+00 0.0000D+00
0.0000D+00	0.0000D+00	1.0000D+00 0.0000D+00 0.0000D+00 0.0000D+00
0.0000D+00	0.0000D+00	0.0000D+00 0.0000D+00 0.0000D+00 0.0000D+00

Columns	7 thru	8
-5.1610D-02	-5.1690D-02	
3.4270D-05	-2.0890D-04	
-2.9220D-03	-8.6820D-03	
0.0000D+00	0.0000D+00	
0.0000D+00	0.0000D+00	
0.0000D+00	0.0000D+00	
0.0000D+00	0.0000D+00	
0.0000D+00	0.0000D+00	

$$S_{lat40} =$$

Columns	1 thru	6
4.7370D-02	6.3860D-01	-7.6430D-01 7.9080D-02 -9.3770D-05 3.6380D-05
-1.4260D+01	1.3430D+00	-1.1530D+00 -1.0300D-04 2.3610D-02 -4.3660D-03
3.9610D-01	6.3430D-02	-1.7800D-01 -2.4160D-05 2.5790D-03 -3.3690D-03
0.0000D+00	1.0000D+00	8.3910D-01 4.5550D-02 0.0000D+00 0.0000D+00
0.0000D+00	0.0000D+00	0.0000D+00 0.0000D+00 0.0000D+00 0.0000D+00
0.0000D+00	1.0000D+00	0.0000D+00 0.0000D+00 0.0000D+00 0.0000D+00
0.0000D+00	0.0000D+00	1.0000D+00 0.0000D+00 0.0000D+00 0.0000D+00
0.0000D+00	0.0000D+00	0.0000D+00 0.0000D+00 0.0000D+00 0.0000D+00

Columns	7 thru	7
-6.4200D-03		
-1.5300D-03		
-1.5500D-04		
0.0000D+00		
0.0000D+00		
0.0000D+00		
0.0000D+00		
0.0000D+00		

$S_{ion50} =$

Columns	1 thru	6
-2.5560D-01	-4.0360D+01	-1.3060D+00 -3.2110D+01 -2.7550D-01 3.5044D-04
-6.4510D-04	8.9490D-03	9.9650D-01 -4.8610D-08 -6.7650D-04 4.4904D-03
4.8980D-04	5.4140D-02	-3.9930D-01 1.6800D-06 1.8180D-02 -7.7000D-04
0.0000D+00	0.0000D+00	1.0000D+00 0.0000D+00 0.0000D+00 0.0000D+00
0.0000D+00	0.0000D+00	0.0000D+00 0.0000D+00 0.0000D+00 0.0000D+00
0.0000D+00	0.0000D+00	0.0000D+00 0.0000D+00 0.0000D+00 0.0000D+00
0.0000D+00	0.0000D+00	1.0000D+00 0.0000D+00 0.0000D+00 0.0000D+00
0.0000D+00	0.0000D+00	0.0000D+00 0.0000D+00 0.0000D+00 0.0000D+00

Columns	7 thru	8
-5.4060D-02	-4.8730D-02	
1.0800D-04	-1.5410D-04	
-3.2690D-03	-8.6100D-03	
0.0000D+00	0.0000D+00	
0.0000D+00	0.0000D+00	
0.0000D+00	0.0000D+00	
0.0000D+00	0.0000D+00	
0.0000D+00	0.0000D+00	

$$S_{lat50} =$$

Columns	1 thru	6				
1.1860D-01	7.5760D-01	-6.3960D-01	6.6350D-02	-9.3770D-05	3.2810D-06	
-2.1300D+01	1.1930D+00	1.2230D+00	3.3230D-05	2.2790D-02	-1.1010D-02	
-1.0910D+00	1.1400D-01	1.0400D-02	-2.5620D-05	2.5430D-03	-6.6130D-05	
0.0000D+00	1.0000D+00	1.1920D+00	6.8560D-02	0.0000D+00	0.0000D+00	
0.0000D+00	0.0000D+00	0.0000D+00	0.0000D+00	0.0000D+00	0.0000D+00	
0.0000D+00	1.0000D+00	0.0000D+00	0.0000D+00	0.0000D+00	0.0000D+00	
0.0000D+00	0.0000D+00	1.0000D+00	0.0000D+00	0.0000D+00	0.0000D+00	
0.0000D+00	0.0000D+00	0.0000D+00	0.0000D+00	0.0000D+00	0.0000D+00	

Columns	7 thru	7
-3.6750D-03		
-2.1450D-03		
3.1500D-04		
0.0000D+00		
0.0000D+00		
0.0000D+00		
0.0000D+00		
0.0000D+00		

$$S_{lon60} =$$

Columns	1 thru	6			
-2.9390D-01	-2.7690D+01	-1.4770D+00	-3.2110D+01	-2.2010D-01	1.9603D-03
-5.6540D-04	9.5210D-02	9.9730D-01	-2.0250D-08	-2.3780D-04	-5.3049D-03
4.7520D-04	-1.0640D+00	-1.6620D-01	7.0730D-07	1.8180D-02	-3.5550D-03
0.0000D+00	0.0000D+00	1.0000D+00	0.0000D+00	0.0000D+00	0.0000D+00
0.0000D+00	0.0000D+00	0.0000D+00	0.0000D+00	0.0000D+00	0.0000D+00
0.0000D+00	0.0000D+00	0.0000D+00	0.0000D+00	0.0000D+00	0.0000D+00
0.0000D+00	0.0000D+00	1.0000D+00	0.0000D+00	0.0000D+00	0.0000D+00
0.0000D+00	0.0000D+00	0.0000D+00	0.0000D+00	0.0000D+00	0.0000D+00

Columns	7 thru	8
-1.3380D-01	-3.4770D-02	
-2.7180D-04	-7.3550D-05	
-5.7350D-03	-9.5570D-03	
0.0000D+00	0.0000D+00	
0.0000D+00	0.0000D+00	
0.0000D+00	0.0000D+00	
0.0000D+00	0.0000D+00	
0.0000D+00	0.0000D+00	

$$S_{lat60} =$$

Columns	1 thru	6			
1.3450D-01	8.6190D-01	-4.9850D-01	5.1610D-02	-9.3770D-05	1.2120D-05
-1.1630D+01	-2.2140D-01	1.6470D+00	1.9310D-04	2.2100D-02	-9.1430D-03
-6.3660D-01	-5.2130D-02	-1.5140D-03	-5.3250D-05	2.5130D-03	3.2340D-04
0.0000D+00	1.0000D+00	1.7320D+00	7.4330D-02	0.0000D+00	0.0000D+00
0.0000D+00	0.0000D+00	0.0000D+00	0.0000D+00	0.0000D+00	0.0000D+00
0.0000D+00	1.0000D+00	0.0000D+00	0.0000D+00	0.0000D+00	0.0000D+00
0.0000D+00	0.0000D+00	1.0000D+00	0.0000D+00	0.0000D+00	0.0000D+00
0.0000D+00	0.0000D+00	0.0000D+00	0.0000D+00	0.0000D+00	0.0000D+00

Columns	7 thru	7
-3.2900D-03		
-1.1250D-03		
4.5500D-04		
0.0000D+00		
0.0000D+00		
0.0000D+00		
0.0000D+00		
0.0000D+00		

Appendix G. *Matrix_x* Executable Files - Weighting Matrix

This appendix details three abbreviated *Matrix_x* executable files that may be useful in developing frequency sensitive compensation elements for a control system such as this. This procedure is discussed in detail in Section 3.4. As stated in the text, what follows is *not* software code. It is simply a commented listing of useful *Matrix_x* commands that may save the reader some time if he chooses to perform a similar operation.

G.1 Development of Frequency Dependent Terms

```
diary('rol20')
```

```
// Executable file for shifting roots to eliminate right half plane  
// poles for phase compensation.
```

```
// Generate the state space (S,NS) for each transfer function from  
// system build.
```

```
// Include actuators.
```

```
// Generate N1, N2, N3 , & D from each system build state space.
```

```
[n1,d]=tform(s1,ns1);  
[n2,d]=tform(s2,ns2);  
[n3,d]=tform(s3,ns3);
```

```
// Obtain roots.
```

```
rn1=roots(n1)  
rn2=roots(n2)  
rn3=roots(n3)  
rd=roots(d)
```

```
// Shift roots.
```

```
srn1=rn1-.2
```

```
srn2=rn2-.2
```

```
srn3=rn3-.2
```

```
srd=rd-.2
```

```
// Obtain shifted transfer functions for use in Bode commands.
```

```
psrn1=poly(srn1)
```

```
psrn2=poly(srn2)
```

```
psrn3=poly(srn3)
```

```
psrd=poly(srd)
```

```
// Generate uncompensated composite Bode plots.
```

```
[w,db1,ph1]=bode(psrn1,psrd,.001,100,400);
```

```
[w,db2,ph2]=bode(psrn2,psrd,.001,100,400);
```

```
[w,db3,ph3]=bode(psrn3,psrd,.001,100,400);
```

```
plot(w,[db1,db2,db3],'ylab/Magnitude/xlab/Omega/upper/logx')
```

```
plot(w,[ph1,ph2,ph3],'ylab/Phase/xlab/Omega/title/Composite Bode ...  
Plot of Uncompensated Shifted Transfer Functions <Roll 20>/lower/...  
logx/keep')
```

```
hard('p20uncomp')
```

```
pause
```

```

// Iteratively run this portion of the program and fine-tune the
// necessary compensation terms to achieve the desired composite
// Bode Phase plots.

// Read the final compensation terms from the highlighted section.

// *****

nc1=convolve(psrn1,[2]);

nc2=convolve(psrn2,[-1]);

nc3=convolve(psrn3,[-1/40,-1]);

dc1=convolve(psrdr,[1,.5,2]);

dc2=convolve(psrdr,[1]);

dc3=convolve(psrdr,[1/.3,1]);

// *****

// Generate compensated composite Bode plots.

[w,db1,ph1]=bode(nc1,dc1,.001,100,400);
pause

[w,db2,ph2]=bode(nc2,dc2,.001,100,400);
pause

[w,db3,ph3]=bode(nc3,dc3,.001,100,400);
pause

```

```

plot(w,[db1,db2,db3], 'ylab/Magnitude/xlab/Omega/upper/logx')

plot(w,[ph1,ph2,ph3], 'ylab/Phase/xlab/Omega/title/Composite Bode ...
Plot of Compensated Shifted Transfer Functions <Roll 20>/lower/...
logx/keep')

hard('p20comp')

pause

// Obtain compensated roots in shifted domain.

rsnc1=roots(nc1);
rsnc2=roots(nc2);
rsnc3=roots(nc3);
rsdc1=roots(dc1);
rsdc2=roots(dc2);
rsdc3=roots(dc3);

// Shift jw axis back to original value.

rnc1=rsnc1+.2
rnc2=rsnc2+.2
rnc3=rsnc3+.2
rdc1=rsdc1+.2
rdc2=rsdc2+.2
rdc3=rsdc3+.2

// Obtain polynomial forms, and redefine them to be real.

pnc1=poly(rnc1);pnc1=real(pnc1);
pnc2=poly(rnc2);pnc2=real(pnc2);
pnc3=poly(rnc3);pnc3=real(pnc3);
pdc1=poly(rdc1);pdc1=real(pdc1);

```

```
pdc2=poly(rdc2);pdc2=real(pdc2);
```

```
pdc3=poly(rdc3);pdc3=real(pdc3);
```

```
// Generate step response data and plots.
```

```
[t,y1]=step(pnc1,pdc1,8,200);
```

```
[t,y2]=step(pnc2,pdc2,8,200);
```

```
[t,y3]=step(pnc3,pdc3,8,200);
```

```
plot(t,[y1,y2,y3],'strip/ylab/Dif Flp|Rudder|Dif Can/xlab/Time ...  
(sec)/title/Compensated Open Loop Step Responses <Roll 20>')
```

```
pause
```

```
hard('resp1')
```

```
// Correct rudder and differential canards for sign conventions.
```

```
[t,y2]=step(-pnc2,pdc2,8,200);
```

```
[t,y3]=step(-pnc3,pdc3,8,200);
```

```
plot(t,[y1,y2,y3],'strip/ylab/Dif Flp|Rudder|Dif Can/xlab/Time ...  
(sec)/title/Compensated Open Loop Step Responses with Sign ...  
Corrections <Roll 20>')
```

```
pause
```

```
hard('p20resp2')
```

```
diary(0)
```

```
*****
```

G.2 Verification of Phase Compensation

```
// Executable file for verifying lateral-directional phase
// compensation using system build.

// Obtain phase compensation terms from appropriate 'shift.mxx'
//files by comparing rnc* with rn* and rdc* with d for each case.

// Include phase compensation blocks into system build diagrams.

// Initially leave gains at unity, but include appropriate
// negative signs.

// Generate compensated state space (sc,nsc) for each
// transfer function.

sim('anal/pcomp20_1');
[s1c,ns1c]=lin(.001);

sim('anal/pcomp20_2');
[s2c,ns2c]=lin(.001);

sim('anal/pcomp20_3');
[s3c,ns3c]=lin(.001);

// Obtain phase compensated step response data and plot.

[t,y1c]=step(s1c,ns1c,8,200);
[t,y2c]=step(s2c,ns2c,8,200);
[t,y3c]=step(s3c,ns3c,8,200);
```

```
plot(t,[y1c,y2c,y3c],'strip/ylab/Dif Flp|Rudder|Dif Can/xlab/Time ...  
(sec)/title/Phase Compensated Open Loop Step Responses <Roll 20>')
```

```
pause
```

```
hard('comp')
```

```
*****
```


G.3 Inclusion of Gain Compensation

```
// Executable file for including gain compensation in the
// lateral-directional channels.

// Determine desired relative weights as discussed in the text.

// Dif Flp - 40%
// Rudder - 20%
// Dif Can - 40%

// Multiply these percentages by the gains required to normalize
// each of the responses to unity.

// Insert the resulting gains into system build to obtain desired
// composite time response plots.

// Generate compensated state space (sc,nsc) from system build.

sim('anal/pcomp20_1');
[s1c,ns1c]=lin(.001);

sim('anal/pcomp20_2');
[s2c,ns2c]=lin(.001);

sim('anal/pcomp20_3');
[s3c,ns3c]=lin(.001);

// Obtain gain and phase compensated step response data and plot.

[t,y1c]=step(s1c,ns1c,8,200);
[t,y2c]=step(s2c,ns2c,8,200);
[t,y3c]=step(s3c,ns3c,8,200);
```

```
plot(t,[y1c,y2c,y3c],'name/ylab/Responses/xlab/Time (sec)/...  
legend/Dif Flp|Rudder|Dif Can/title/Final Compensated ...  
Open Loop Step Responses <Roll 20>')
```

```
hard('p20finalresp')
```

```
pause
```

```
// Generate system build hardcopy file of final compensated system.  
// (pcomp20.bd).
```

```
*****
```

Appendix H. Lateral-Directional Effective Plants

This appendix shows the *System Build* block diagrams of the lateral-directional effective plants, including final gain compensation as discussed in Section 3.6

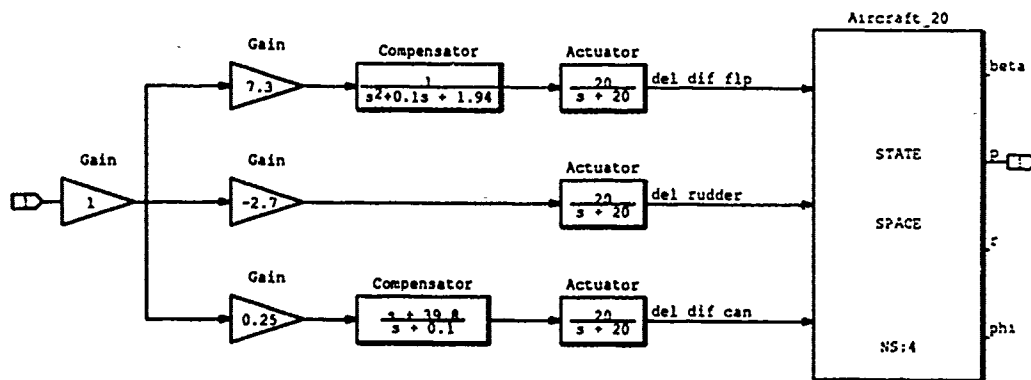


Figure H.1. $P_{eff}(1,1)$ Final Compensation Block Diagram ($\alpha = 20$)

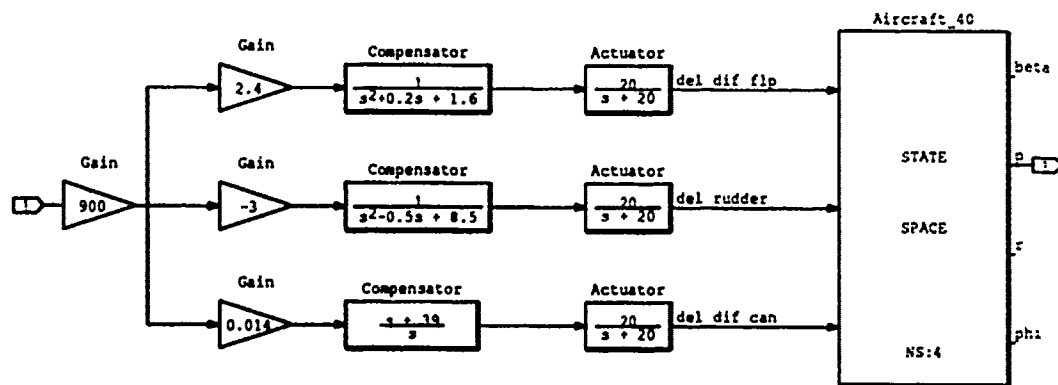


Figure H.2. $P_{eff}(1,1)$ Final Compensation Block Diagram ($\alpha = 40$)

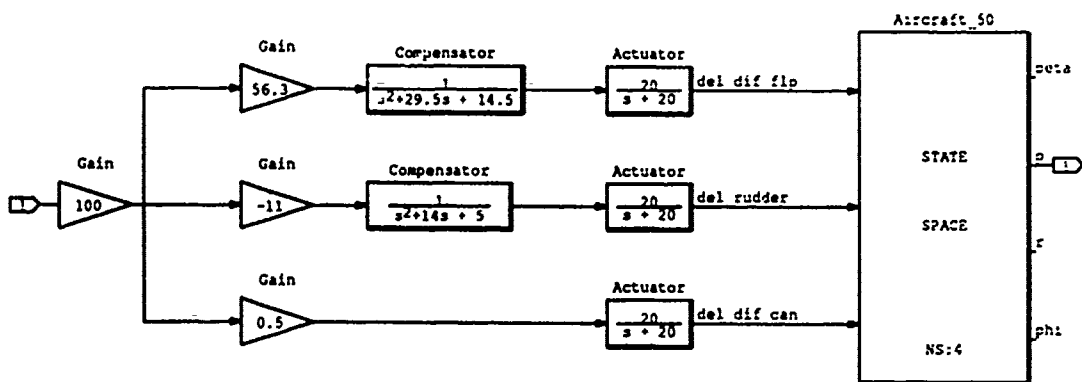


Figure H.3. $P_{eff}(1,1)$ Final Compensation Block Diagram ($\alpha = 50$)

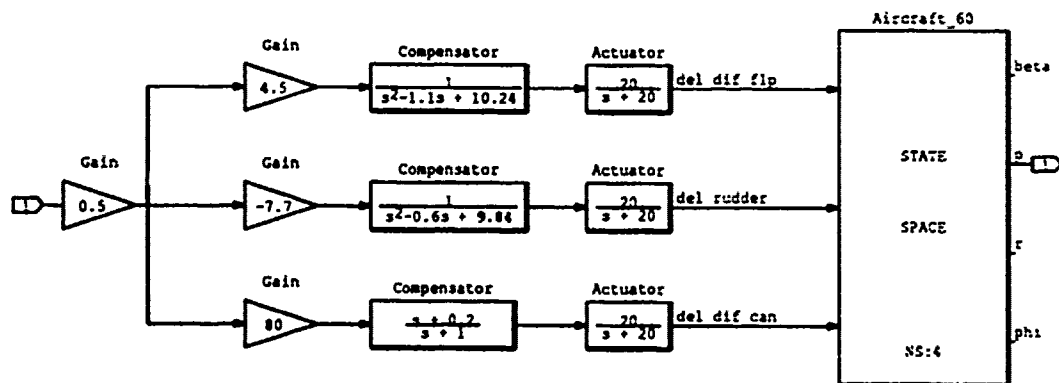


Figure H.4. $P_{eff}(1,1)$ Final Compensation Block Diagram ($\alpha = 60$)

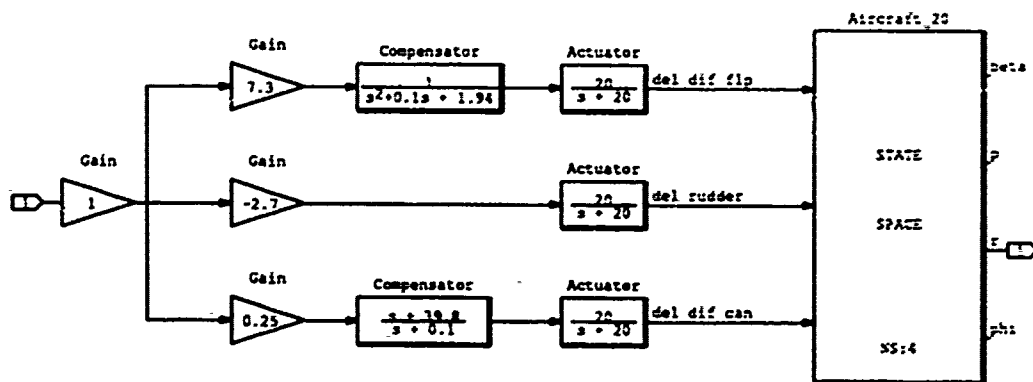


Figure H.5. $P_{eff}(2,1)$ Final Compensation Block Diagram ($\alpha = 20$)

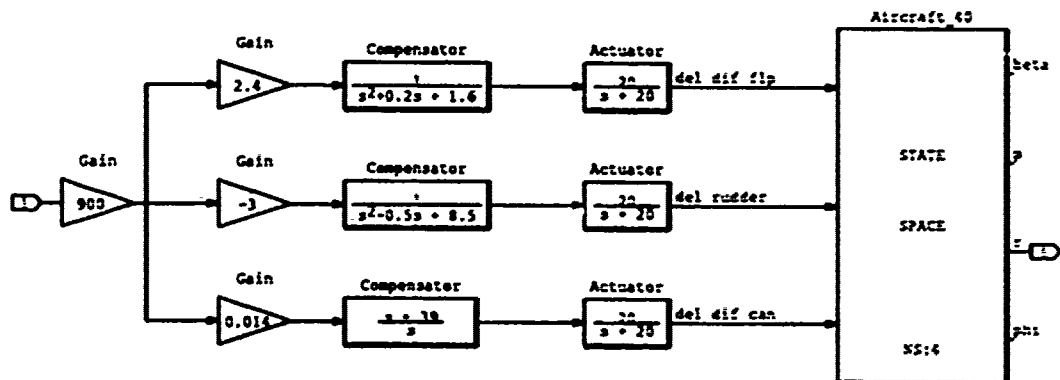


Figure H.6. $P_{eff}(2,1)$ Final Compensation Block Diagram ($\alpha = 10$)

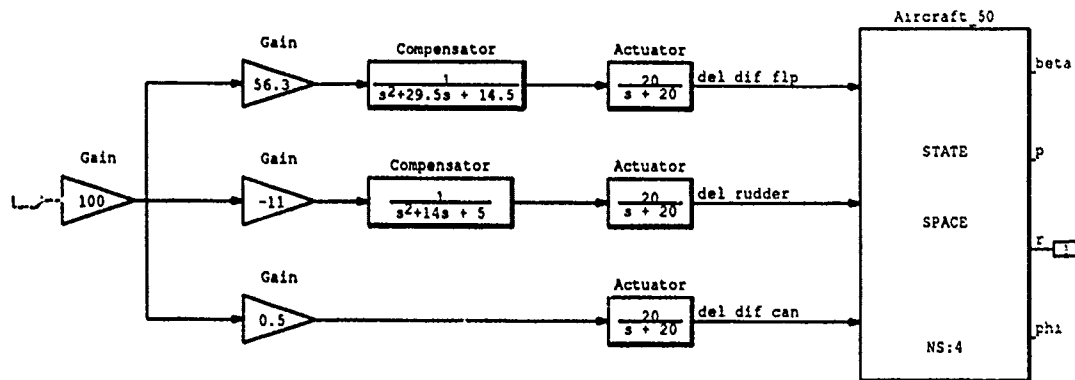


Figure H.7. $P_{eff}(2,1)$ Final Compensation Block Diagram ($\alpha = 50$)

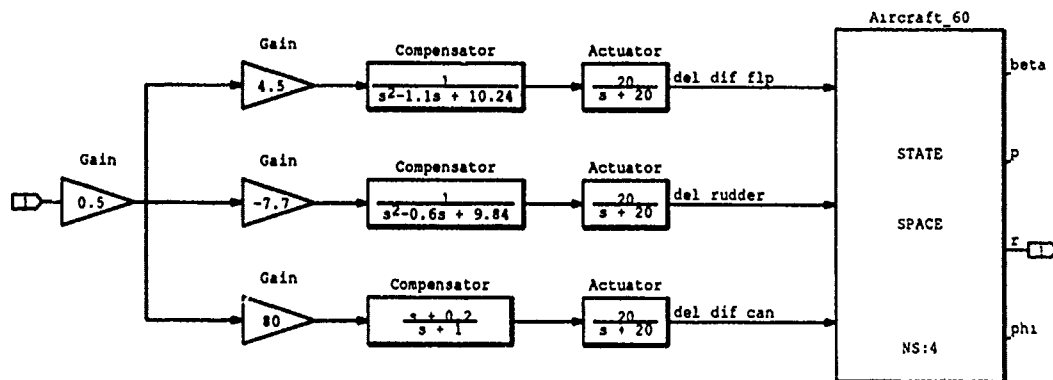


Figure H.8. $P_{eff}(2,1)$ Final Compensation Block Diagram ($\alpha = 60$)

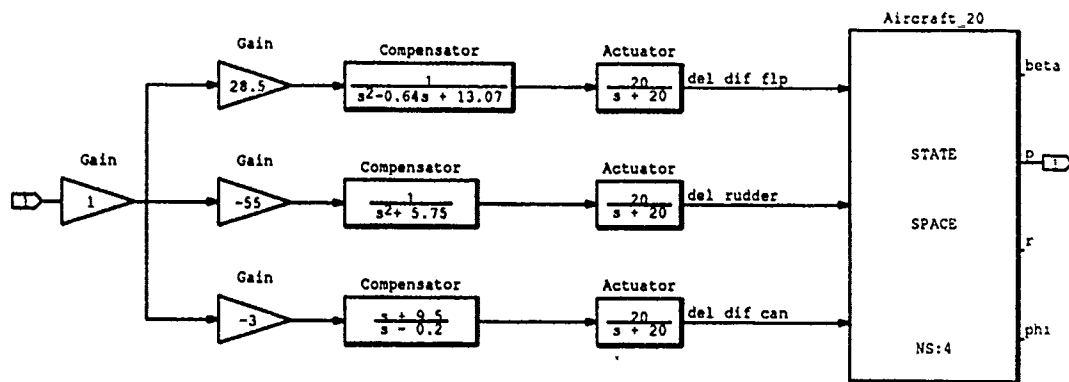


Figure H.9. $P_{eff}(1,2)$ Final Compensation Block Diagram ($\alpha = 20$)

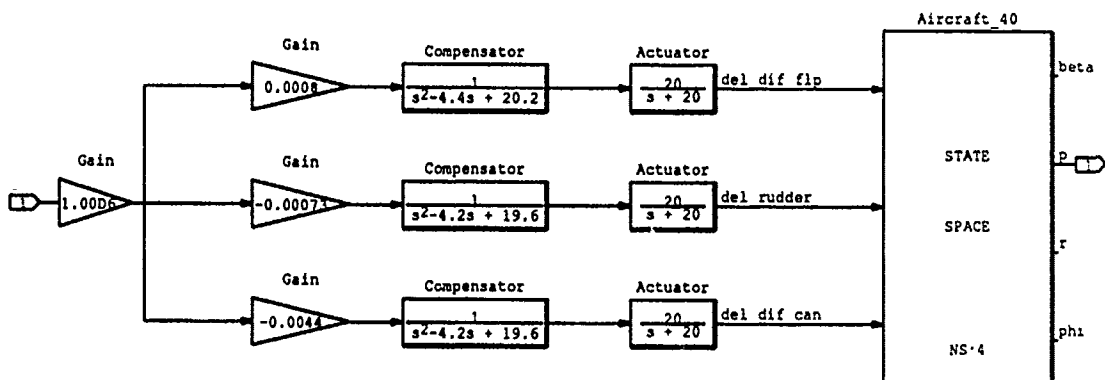


Figure H.10. $P_{eff}(1,2)$ Final Compensation Block Diagram ($\alpha = 40$)

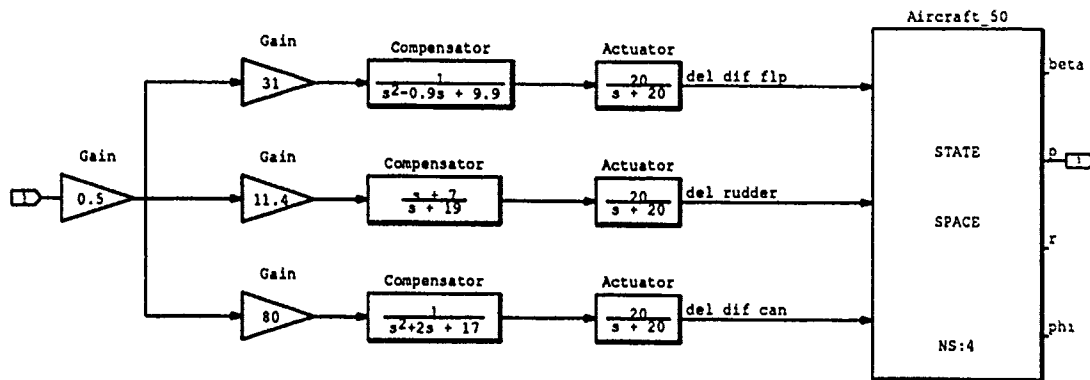


Figure H.11. $P_{eff}(1,2)$ Final Compensation Block Diagram ($\alpha = 50$)

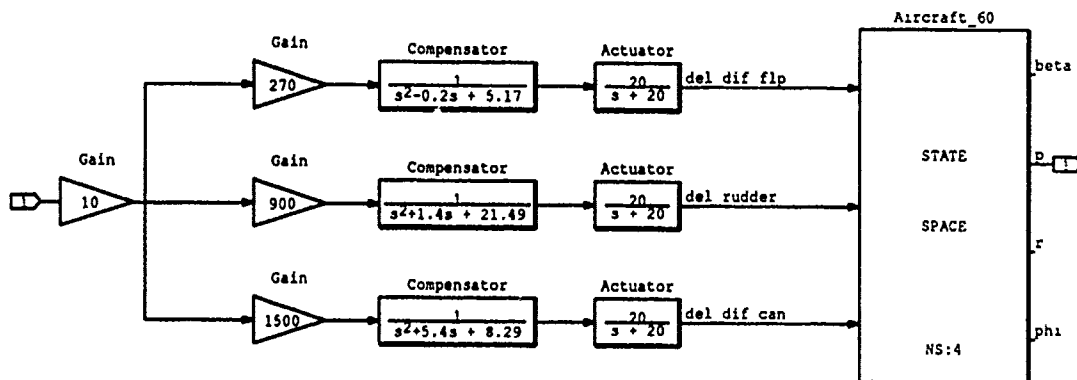


Figure H.12. $P_{eff}(1,2)$ Final Compensation Block Diagram ($\alpha = 60$)

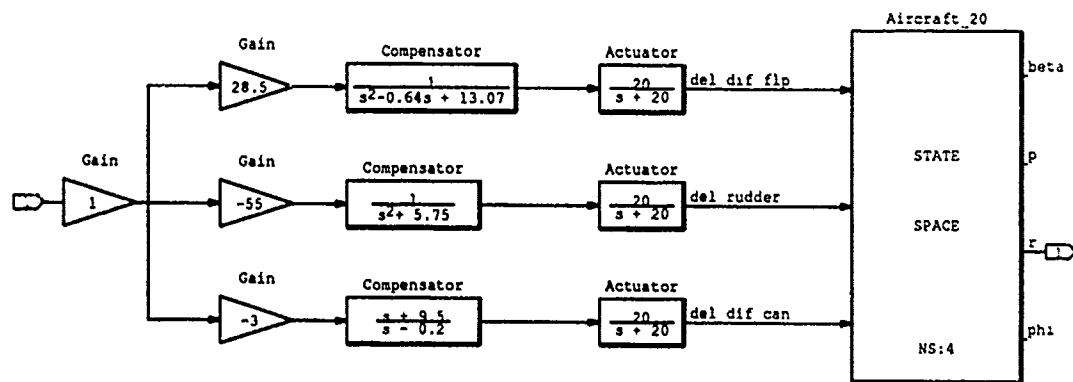


Figure H.13. $P_{eff}(2,2)$ Final Compensation Block Diagram ($\alpha = 20$)

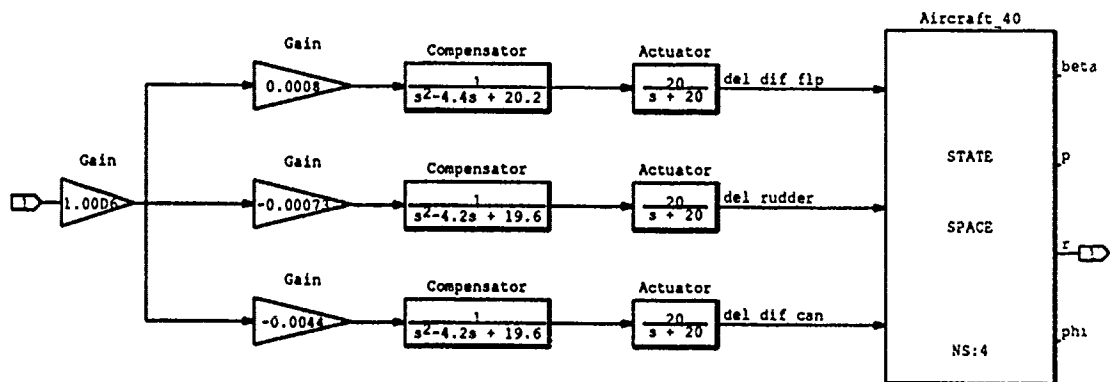


Figure H.14. $P_{eff}(2,2)$ Final Compensation Block Diagram ($\alpha = 40$)

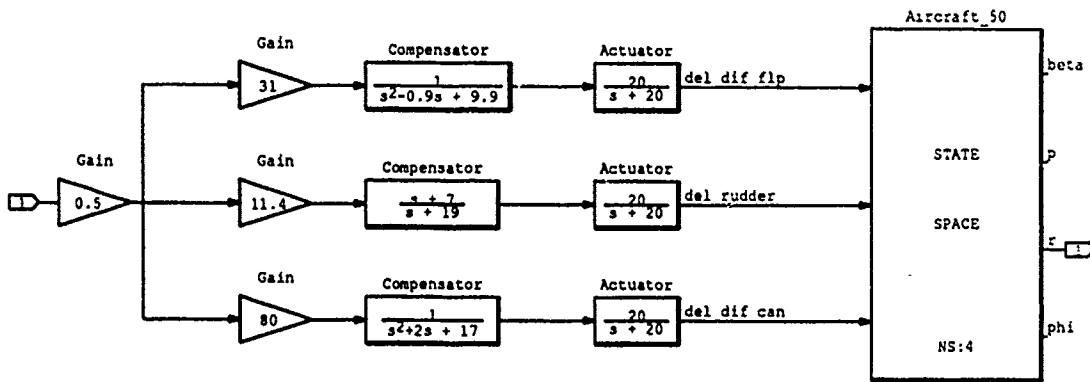


Figure H.15. $P_{eff}(2,2)$ Final Compensation Block Diagram ($\alpha = 50$)

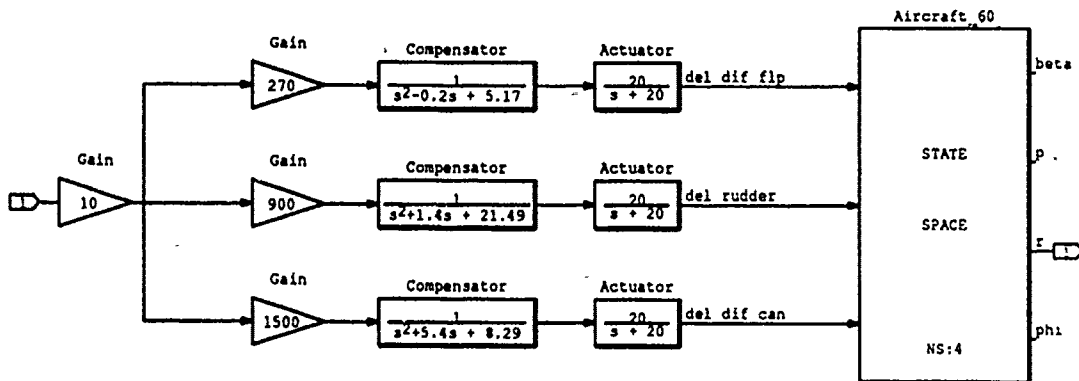


Figure H.16. $P_{eff}(2,2)$ Final Compensation Block Diagram ($\alpha = 60$)

Appendix I. *Matrix_X* Executable Files - Singular-G

This appendix lists the *Matrix_X* executable file that was used to iteratively find the values of the a and b elements of the singular-G compensation matrix. The goal was to separate, as much as possible, the right half plane poles and zeros of the effective (SISO converted) lateral-directional plants. This procedure is discussed in detail in Section 5.3. One again, this is *not* software code. It is only a listing of comments and recommended command lines that may be useful to the reader.

```
// Singular-G-20.mxx

// Executable file for finding the 'Singular G' compensator
// coefficients for the lateral-directional controllers.

// Desire RHP zeros of 1 + G*Peff to be separated as much as
// possible from the RHP poles.

// Peff = A*D2(N11+B*N21)+D1(N12+B*N22)

// P11 = N11/DD1
// P12 = N12/DD2
// P21 = N21/DD1
// P22 = N22/DD2

// D = common portion of denominators.
// D1,D2 = unique portions of denominators.
// A,B = coefficients allowed to vary.

load '~/thesis/lateral/lat20/lat20.mat'

diary('Sin-G20.dy')
```

N11=PN20P;

N12=PN20PR;

N21=PN20RP;

N22=PN20R;

RN11=roots(N11)

RN12=roots(N12)

RN21=roots(N21)

RN22=roots(N22)

DEN11=PD20P;

DEN12=PD20PR;

DEN21=PD20RP;

DEN22=PD20R;

RDEN11=Roots(DEN11)

RDEN12=Roots(DEN12)

RDEN21=Roots(DEN21)

RDEN22=Roots(DEN22)

// Note that DEN11=DEN21 & DEN12=DEN22.

// Common portion of denominator is not used to find zeros.

// Compare RDEN11 & RDEN12 and cross out common roots.

// Convolve remaining roots of DEN11 to form D1.

D1a=convolve([1,.05+1.3919*jay],[1,.05-1.3919*jay]);

D1=convolve(D1a,[1,.1])

RD1=roots(D1)

```
// Convolve remaining roots of DEN12 to form D2.
```

```
D2a=convolve([1,2.3979*jay],[1,-2.3979*jay]);  
D2b=convolve([1,-.32+3.6011*jay],[1,-.32-3.6011*jay]);  
D2c=convolve(D2a,D2b);  
D2=convolve(D2c,[1,-.2])  
RD2=roots(D2)
```

```
diary(0)
```

```
// Find combination of values for A & B that separate RHP  
// zeros of Peff as much as possible from its RHP poles.
```

```
//*****
```

```
//diary('modroots20')  
for a=-2:1:4;...  
for b=-3:1:3;...  
Peff=convolve(a*d2,(n11+b*n21))+convolve(d1,(n12+b*n22));...  
R=roots(Peff);...  
R,a,b,...  
end,...  
end  
//diary(0)
```

```
//*****
```

```

// Now plot root locus of effective plant <lat20>, and list
// roots of modified plant.

diary('modroots20.list')

a=-1
b=1

Peff=convolve(a*d2,(n11+b*n21))+convolve(d1,(n12+b*n22));

rtnumplnt20=roots(Peff)

// Add roots of two denominators, then remove duplicated roots.

rtldenplnt20=RD1+RD2-d

diary(0)

// Generate poly form for root locus command.

pd=poly(rtndenplnt20);

k=rlocus(Peff,pd,'xmax=5/xmin=-5/ymax=5/ymin=-5/...
title/Root Locus of Effective Plant <Lat 20> a=-1,b=1')

```

Bibliography

1. Barfield, Finley, A., "Head Control Engineer AFTI/F-16. Personal Interviews." Flight Dynamics Directorate, Wright Labs, Wright-Patterson AFB, OH, December 1990 through December 1991.
2. Blakelock, John H. *Automatic Control of Aircraft and Missiles* (Second Edition). Wiley & Sons, 1991.
3. Bosworth, John T. *Linearized Aerodynamic and Control Law Models of the X-29A Airplane and Comparison with Flight Data*. Technical Report, Edwards AFB, CA: NASA Ames Research Center / Dryden Flight Research Facility, September 1989.
4. Bosworth, John T. and Timothy H. Cox. *A Design Procedure for the Handling Qualities Optimization of the X-29A Aircraft*. Technical Report, Edwards AFB, CA: NASA Ames Research Center / Dryden Flight Research Facility.
5. Christian, Terry V., "Group Leader for Simulation Programs. Personal Interviews." Flight Dynamics Directorate, Wright Labs, Wright-Patterson AFB, OH, December 1990 through December 1991.
6. Cox, Thomas J. *Development of a High Fidelity Non-linear Simulation of the X-29 Aircraft on the Simstar Computer*. MS thesis, Air Force Institute of Technology, Wright-Patterson AFB, OH, March 1991.
7. Crosby, Kenneth A. *Quantitative Feedback Theory Application to Flight Control System Design for the AFTI/F-16*. MS thesis, Air Force Institute of Technology, Wright-Patterson AFB, OH, December 1990.
8. D'Azzo, John J. and Constantine H. Houpis. *Linear Control System Analysis & Design — Conventional and Modern* (Third Edition). McGraw-Hill, 1988.
9. Gillard, William, "Flight Control Systems Engineer. Personal Interviews." X-29 Program Office, Wright Labs, Wright-Patterson AFB, OH, December 1990 through December 1991.
10. Gunston, Bill. *Grumman X-29*. Aeolus Publishing Limited, 1985.
11. Hicks, John W. and Neil W. Matheny. *Preliminary Flight Assessment of the X-29A Advanced Technology Demonstrator*. Technical Report NASA TM-100407, Edwards AFB, CA: NASA Ames Research Center / Dryden Flight Research Facility, September 1987.
12. Horowitz, Isaac. "Design of Feedback Systems with Non-minimum Phase Unstable Plants," *International Journal of Systems Sciences*, 10:1025-1040 (September 1979).
13. Horowitz, Isaac. "Survey of Quantitative Feedback Theory," *International Journal of Control*, 53:255-291 (February 1991).

14. Horowitz, Isaac and Yin-Kuei Liao. "Limitations of Non-minimum Phase Feedback Systems," *International Journal of Control*, 40:1003-1013 (May 1984).
15. Horowitz, Isaac M., "Personal Conversation and Correspondance." Distinguished Visiting Professor of Electrical Engineering, Air Force Institute of Technology, Wright-Patterson AFB, OH, May 1991 through December 1991.
16. Houpis, Constantine H., "Personal Conversation, Correspondance and Class Notes." Professor of Electrical Engineering, Air Force Institute of Technology, Wright-Patterson AFB, OH, May 1990 through December 1991.
17. Houpis, Constantine H. *Quantitative Feedback Theory (QFT)—Technique for Designing Multivariable Control Systems*. Technical Report AFWAL-TR-86-3107, Wright-Patterson AFB, OH: Flight Dynamics Laboratory, January 1987.
18. Miller, Russel B. *Multi-Input Multi-Output Flight Control System Design for the YF-16 Using Non-Linear QFT and Pilot Compensation*. MS thesis, Air Force Institute of Technology, Wright-Patterson AFB, OH, December 1990.
19. Matrix_x CAD/CAE Program, Integrated Systems Inc., Santa Clara, CA, 95054-1215.
20. Nelson, Robert C. *Flight Stability and Automatic Control*. McGraw-Hill, 1989.
21. Pace, Steve. *The Grumman X-29*. Tab Books, 1991.
22. Pachter, Meir, "Personal Conversation, Correspondance and Class Notes." Distinguished Visiting Professor of Electrical Engineering, Air Force Institute of Technology, Wright-Patterson AFB, OH, January 1991 through December 1991.
23. Paschall, Randall N., "Personal Conversation, Correspondance and Class Notes." Associate Professor of Electrical Engineering, Air Force Institute of Technology, Wright-Patterson AFB, OH, May 1990 through December 1991.
24. Pellicano, Paul and others. *X-29 High Angle of Attack Flight Test Procedures, Results, and Lessons Learned*. Technical Report, Edwards AFB, CA: Grumman Systems Division and Air Force Flight Test Center, 1990.
25. Phillips, William D. *Frequency Sensitive QFT Weighting Matrix*. MS thesis, Air Force Institute of Technology, Wright-Patterson AFB, OH, December 1988.
26. Raney, David L. and James G. Batterson. *Lateral Stability Analysis for the X-29A Drop Model Using System Identification Methodology*. Technical Report NASA TM-4108, Hampton, VA: NASA Langley Research Center, 1989.
27. Walke, Jon G. *Design of Longitudinal Flight Control System Using Singular-G Method*. MS thesis, Air Force Institute of Technology, Wright Patterson AFB, OH, December 1983.
28. Wheaton, David G. *Automatic Flight Control System Design for an Unmanned Research Vehicle Using Discrete Quantitative Feedback Theory*. MS thesis, Air Force Institute of Technology, Wright-Patterson AFB, OH, December 1990.